PB2000-105936

DOT/FAA/AR-00/14

Office of Aviation Research
Washington, D.C. 20591

Effects of Large-Droplet Ice Accretion on Airfoil and Wing Aerodynamics and Control

April 2000

Final Report

U.S. Department of Transportation
Federal Aviation Administration

NOTICE

This document is disseminated under the sponsorship of the U.S. Department of Transportation in the interest of information exchange. The United States Government assumes no liability for the contents or use thereof. The United States Government does not endorse products or manufacturers. Trade or manufacturer's names appear herein solely because they are considered essential to the objective of this report. This document does not constitute FAA certification policy. Consult your local FAA aircraft certification office as to its use.

Technical Report Documentation Page

1. Report No.	2. Government Accession No.	3. Recipient's Catalog No.
DOT/FAA/AR-00/14		

4. Title and Subtitle	5. Report Date
EFFECTS OF LARGE-DROPLET ICE ACCREATION ON AIRFOIL AND WING AERODYNAMICS AND CONTROL	April 2000
	6. Performing Organization Code

7. Author(s)	8. Performing Organization Report No.
Michael B. Bragg and Eric Loth	

9. Performing Organization Name and Address	10. Work Unit No. (TRAIS)
University of Illinois at Urbana-Champaign Aeronautical and Astronautical Engineering Urbana, IL 61801	11. Contract or Grant No.

12. Sponsoring Agency Name and Address	13. Type of Report and Period Covered
U.S. Department of Transportation Federal Aviation Administration Office of Aviation Research Washington, DC 20591	Final Report
	14. Sponsoring Agency Code AIR-100

15. Supplementary Notes

The Federal Aviation Administration William J. Hughes Technical Center technical manager was James Riley.

16. Abstract

An integrated experimental and computational investigation was conducted to determine the effect of simulated ridge ice shapes on airfoil aerodynamics. These upper-surface shapes are representative of those which may form aft of protected surfaces in super-cooled large droplet conditions. The simulated ice shapes were experimentally tested on a modified National Advisory Committee for Aeronautics (NACA) 23012 (23012m) airfoil and Natural Laminar Flow (NLF) 0414 airfoil at Reynolds numbers of 1.8 million for a range of protuberance locations, sizes, and shapes. The computational study investigated the cases encompassed by the experimental study but in addition included higher Reynolds numbers and other airfoils from the NASA Commuter Airfoil Program.

The simulated ice shapes produced very different results on the NACA 23012m and the NLF airfoils, which was primarily attributed to their very different pressure distributions without ice. The effects of the simulated ice shapes were much more severe on the forward-loaded NACA 23012m, with a measured $C_{\ell,max}$ as low as 0.25 from the ice shape with a height-to-chord ratio of 0.0139 and an x/c of 0.12. The lowest true $C_{\ell,max}$ measured for the NLF 0414 with the same ice shape was 0.68. Various simulated ice shape sizes and geometries were also investigated on both airfoils. Aerodynamic penalties became more severe as the height-to-chord ratio of the simulated ice shape was increased from 0.0056 to 0.0139. The variation in the simulated ice shape geometry had only minor effects on the airfoil aerodynamics.

The numerical investigation included steady-state simulations with a high-resolution full Navier-Stokes solver using a solution-adaptive unstructured grid for both non-iced and iced configurations. The effect of ice shape size, geometry, location, Reynolds number, flap deflection and airfoil geometry was reasonably reproduced by computational methodology for a wide range of the experimental conditions. The airfoil shape sensitivity studies indicated that the NACA 23012m exhibited the most detrimental performance with respect to lift loss, which tended to be greatest around x/c of about 0.1 which also corresponds to the location of minimum pressure coefficient (C_p). However, the more evenly loaded NLF 0414 tended to have less separation for equivalent clean airfoil lift conditions and did not exhibit a unique critical ice shape location. Both the business jet model and the large horizontal tailplane airfoils had very high suction peaks near the leading edge ($x/c = 0.02$), closest to the location of its minimum C_p. Finally, Reynolds number effects for the iced airfoil cases were found to be negligible (unlike that for the clean airfoil cases.)

17. Key Words	18. Distribution Statement
Super-cooled large droplets, Ridge ice accretion, Airfoil, Aerodynamic penalty	This document is available to the public through the National Technical Information Service (NTIS), Springfield, Virginia 22161.

19. Security Classif. (of this report)	20. Security Classif. (of this page)	21. No. of Pages	22. Price
Unclassified	Unclassified	195	

TABLE OF CONTENTS

LIST OF FIGURES

LIST OF TABLES

LIST OF ABBREVIATIONS AND SYMBOLS

LETTERS

A	Area of the element
C_d	Drag coefficient, $D'/(q_\infty c)$
C_f	Skin friction coefficient
C_h	Flap hinge moment coefficient, $H'/(q_\infty c_f^2)$
$C_{h,\alpha}$	Flap hinge moment curve slope
C_ℓ	Lift coefficient, $L'/(q_\infty c)$
$C_{\ell max}$	Maximum lift coefficient
$C_{\ell\alpha}$	Lift curve slope
$C_{\ell\delta f}$	Change in lift with flap deflection
C_m	Pitching moment coefficient, $M'/(q_\infty c^2)$
$C_{m,\alpha}$	Pitching moment curve slope
$C_{m,\delta f}$	Change in pitching moment with flap deflection
C_n	Normal force coefficient, $N'/(q_\infty c)$
C_p	Pressure coefficient, $(p-p_\infty)/q_\infty$
CFL	Inviscid Courant Number
D'	Drag per unit span
E'	Fluid total energy
$\mathbf{F}_c$	Convective flux
$\mathbf{F}_v$	Viscous flux
H	Step height
H'	Flap hinge moment per unit span
LWC	Liquid water content
L'	Lift per unit span
L_{AB}	Length of edge AB
M	Mach number
MVD	Mean volumetric diameter
M'	Pitching moment per unit span
N	Normal force per unit span
N_i	Linear shape function of node I
Pr	Prandtl number
Pr_t	Turbulent Prandtl number
Re	Chord-based Reynolds number, $(\rho V_\infty c)/\mu$
T	Fluid temperature
V_∞	Freestream velocity
a	Speed of sound
c	Airfoil chord
c_f	Flap chord
f_c, g_c	Cartesian components of convective flux
f_v, g_v	Cartesian components of viscous flux
k	Protuberance height
$\hat{\mathbf{n}}$	Unit normal vector
p	Fluid static pressure
p_0	Total pressure in the wake
$p_{\infty,0}$	Freestream total pressure
p_∞	Freestream static pressure
$\mathbf{q}$	Heat flux vector
q_w	Dynamic pressure in the wake
q_∞	Freestream dynamic pressure
$u.v$	Cartesian components of the velocity vector
u_e	Edge velocity

u^+	Law of the wall inner variable, u/v^*
v^*	Wall friction velocity, $(\tau_w/\rho)^{1/2}$
w	Solution vector of the conservative variables
x	Airfoil coordinate in chordwise direction
x_R	Reattachment length
x_r	Reattachment location
y	Airfoil coordinate perpendicular to chord
y^+	Law of the wall inner variable, $(yv^*)/v$
z	Airfoil coordinate in spanwise direction

SYMBOLS

ΔC_d	Drag increase due to ice accretion, $C_d - C_{d,clean}$
ΔC_ℓ	Lift loss due to ice accretion, $C_{\ell clean} - C_\ell$
Δt	Local time step
Ω	Area of the domain
α	Angle of attack
δ	Top wall deflection angle
δ_f	Flap deflection
ϕ	Galerkin test function
γ	Specific heat ratio
ε	Blasius similarity variable
μ	Molecular viscosity
μ_t	Eddy viscosity
ν	Kinematic viscosity
$\tilde{\nu}$	Spalart-Allmaras working variable
ν_t	Turbulent kinematic viscosity
ρ	Fluid density
σ	Stress tensor
τ_w	Wall shear stress, $\mu(du/dy)_w$

SUBSCRIPTS

x,y	Components in x,y directions
∞	Freestream value

SUPERSCRIPTS

^	Dimensional variable

EXECUTIVE SUMMARY

An integrated experimental and computational investigation was conducted to determine the effect of simulated ridge ice shapes on airfoil aerodynamics. These upper-surface shapes are representative of those which may form aft of protected surfaces in super-cooled large droplet (SLD) conditions. The simulated ice shapes were experimentally tested on a modified National Advisory Committee for Aeronautics (NACA) 23012 (23012m) airfoil and the Natural Laminar Flow (NLF) 0414 airfoil at Reynolds number Re = 1.8 million for a range of protuberance locations, sizes, and shapes. The computational study investigated the cases encompassed by the experimental study but in addition included higher Reynolds numbers and other airfoils from the NASA Commuter Airfoil Program.

The simulated ice shapes produced very different results on the NACA 23012m and the NLF airfoils, which was primarily attributed to their very different pressure distributions without ice. The effects of the simulated ice shapes were much more severe on the forward-loaded NACA 23012m, with a measured maximum coefficient lift ($C_{\ell,max}$) as low as 0.25 from the ice shape with a height-to-chord ratio of 0.0139 and an x/c of 0.12. The lowest true $C_{\ell,max}$ measured for the NLF 0414 with the same ice shape was 0.68. The effect of simulated ice shape on the flap hinge moment was also much more severe on the NACA 23012m than on the NLF 0414. Various simulated ice shape size and geometries were also investigated on the NLF 0414. The aerodynamic penalties (in C_ℓ, C_d, C_m, and C_h (flap hinge moment coefficient)) became more severe as the height-to-chord ratio of the simulated ice shape was increased from 0.0056 to 0.0139. The variation in the simulated ice shape geometry (from forward-facing to aft-facing quarter rounds) had only minor effects on the airfoil aerodynamics.

The numerical investigation included steady-state simulations with a high-resolution full Navier-Stokes solver using a solution-adaptive unstructured grid for both non-iced and ice configurations. Code validation was first performed with backward-facing step and Mach number and Reynolds number sensitivity studies on various clean airfoils. The effect of ice shape size, geometry, location, Reynolds number, flap deflection and airfoil geometry was reasonably reproduced by computational methodology for a wide range of the experimental conditions. Agreement was particularly good for pressure and hinge moment distributions (including the nonlinear break points); whereas, lift was predicted reasonably well up to (but not past) fully separated flow conditions. The airfoil shape sensitivity studies indicated that the NACA 23012m exhibited the most detrimental performance with respect to lift loss, which tended to be greatest around x/c of about 0.1 which also corresponds to the location of minimum pressure coefficient (C_p). However, the more evenly loaded NLF 0414 tended to have less separation for equivalent clean airfoil lift conditions and did not exhibit a unique critical ice shape location. Both the business jet model and the large transport horizontal stabilizer (LTHS) airfoils had very high suction peaks near the leading edge (x/c = 0.02), closest to the location of its minimum C_p. Finally, Reynolds number effects for the iced airfoil cases were found to be negligible (unlike that for the clean airfoil cases.)

1. INTRODUCTION.

Aircraft can accrete ice on its aerodynamic surfaces when flying through clouds of super-cooled water droplets. The size and shape of the ice accretion on unprotected aerodynamic surfaces depend primarily on airspeed, temperature, water droplet size, liquid water content, and the period of time the aircraft has operated in the icing condition.

Under a normal icing encounter, most of the ice accretion would occur over the active portion of the wing deicing system. When the deicing system is activated, almost all of the ice will be removed. However, this is not the case in the presence of super-cooled large droplets (SLD), where the droplet sizes are much larger than those in the Federal Aviation Administration (FAA) 14 Code of Federal Regulations (CFR) Part 25, Appendix C icing envelopes used in aircraft certification. Because of their larger size, the droplets can impinge and accrete as ice downstream of the deicing system. When the deicing system is activated, a ridge ice accretion can occur on the aircraft wing behind the leading edge deicing system [1]. In the literature, this type of accretion has been referred to as a spanwise-step ice accretion, a SLD ice accretion, and a large-droplet ice accretion. All refer to a ridge, usually forming aft of the protected region. Although such ice accretions have been observed in SLD icing conditions, they can also occur in other icing conditions. Figure 1 shows a ridge ice accretion, measured in SLD conditions, on a National Advisory Committee for Aeronautics (NACA) 23012 airfoil from the NASA Glenn Icing Research Tunnel (IRT) [2]. This model had an operational pneumatic deicing boot that extended to $x/c = 0.06$ on the upper surface. The ridge ice accretion shown is approximately two dimensional (2-D) and forms just behind the boot. This type of accretion presents both a forward- and aft-facing step to the flow and is essentially 2-D, extending spanwise on the wing.

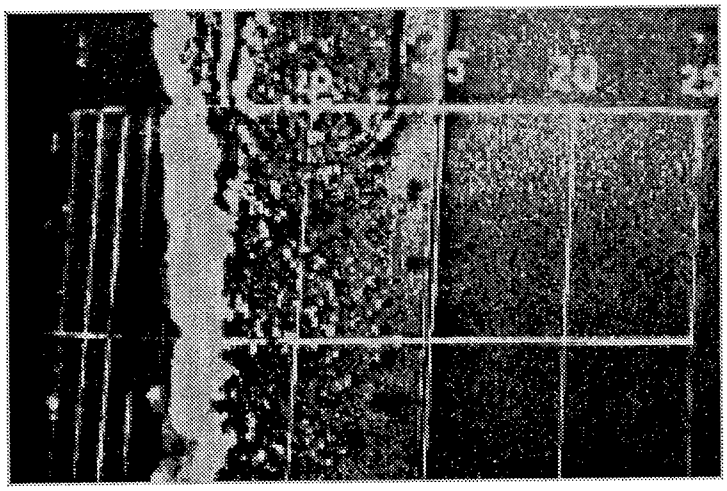

FIGURE 1. LARGE-DROPLET ICE ACCRETION ON A NACA 23012 AIRFOIL IN THE NASA GLENN ICING RESEARCH TUNNEL
(V = 195mph, MVD = 160 μm, LWC = 0.82g/m^3, $\alpha = 0°$,
BOOT CYCLE = 3 min, SPRAY = 18 min, T_0 = 26°F)

This type of accretion can lead to large changes in the lateral control (and the associated aileron hinge moments) by severely altering the flow over the ailerons. This is thought to have caused the crash of an ATR-72 commuter aircraft near Roselawn, Indiana, on October 31, 1994 [3]. A

ridge ice accretion can also occur in super-cooled droplet clouds, of Appendix C size, at air temperatures near freezing. This occurs when the surface water runs back and freezes. The understanding of the effects of ridge ice accretions on aircraft aerodynamics and control is still rather limited. Aircraft icing research prior to this study has concentrated primarily on ice accretion from Appendix C conditions that forms near the leading edge of the wing. The purpose of this study is to develop an understanding of the aerodynamics of ridge ice accretions.

1.1 REVIEW OF LITERATURE–EXPERIMENTAL.

The influence of ice accretion behind deicing boots on aircraft performance has long been recognized. Wind tunnel measurements by Johnson [4] in 1940 showed a 36% reduction in maximum roll control power due to ice accretion with full aileron deflection. As a response to a Viking aircraft incident, Morris [5] in 1947, reported wind tunnel results of the effect of simulated ice shapes on the leading edge of the aircraft horizontal tail. The objective was to propose a fix for the elevator control. One of the simulated ice shapes resembled a ridge accretion and was intended to represent ice formed downstream of a deicing system. Hinge moment results were summarized and design guidelines were presented. In 1948 Thoren [6] documented a 2-hour test flight in freezing rain with a Lockheed P2V aircraft. During this encounter, runback and freezing were observed behind the boots. A considerable increase in section drag and a reduction in lift were noted—but no serious degradation in lateral control was experienced. Thus, by 1950, it was established that ice accretion aft of the boots could affect aircraft control.

Insight into the effect of ridge ice accretion on aircraft control can also be found in the excellent report on horizontal tail stall by Trunov and Ingelman-Sundberg [7]. The combination of increased downwash due to main wing flap deflection and decreased maximum lift and stall angle due to ice on the horizontal tail can lead to horizontal tail stall. They reported hinge moment data on airfoils and tail sections with simulated Appendix C ice accretions and argued that the change in airfoil pressure distribution over the elevator due to the ice-induced separation led to altered hinge moments and pilot control forces.

A recent study at the University of Wyoming, which examined the effects of various types of icing conditions on a King Air aircraft, found that the freezing drizzle exposure resulted in the most severe performance degradation [8]. Under this icing condition, a ridge ice accretion was observed. In low Reynolds number wind tunnel tests with simulated ice shapes, Ashenden, Lindberg, and Marwitz [9] found that a computer-predicted freezing drizzle ice shape with a simulated deicing boot operation resulted in a more severe performance degradation than one without the deicing boot operation. According to this study, when the deicing boot is not in use (in SLD icing conditions), the ice accretion occurs around the leading edge of the wing and tends to conform to the geometry of the wing. No ridge is formed. However, when the deicing system is in use, the ridge shape forms immediately downstream of the boot, which typically extends to 5-10% chord on the upper surface.

In 1996, Bragg [10, 11] reviewed the aerodynamic effects of the ridge ice accretion and showed that the ridge accretion not only degraded lift and drag, but also adversely affected the aileron hinge moment. This was thought to be the result of a large separation bubble that formed downstream of the accretion, which severely altered the pressure distribution over the aileron.

Bragg reviewed NACA data on airfoils with 2-D protuberances to provide a useful background. In 1932, Jacobs [12] tested a series of protuberances of different heights at various chordwise locations on a NACA 0012 airfoil. The test revealed that the 5% and 15% chord locations on the airfoil's upper surface were the most critical in terms of lift and drag penalties for the large protuberance ($k/c = 0.0125$). This protuberance resulted in reductions in lift by as much by as 68% and a large change in the pitching moment. However, no locations between 5% and 15% were tested. For smaller protuberances, ($k/c < 0.005$), the effects were much less severe, and the most critical location was the leading edge.

In 1956, Bowden [13] tested a spanwise spoiler-type step protuberance of $k/c = 0.00286$ and 0.00572 on a NACA 0011 airfoil at $x/c = 0.01$, 0.025, and 0.05. The test showed that the effects of the protuberance on lift and pitching moment became more severe as it was moved closer to the leading edge. The reduction in lift was as high as 25%. At angles of attack greater than 4°, the maximum increase in the drag was observed to occur when the protuberance was placed near the location of maximum local velocity. Calay, Holdo and Mayman [14] tested three different small simulated runback ice shapes ($k/c = 0.0035$) at 5%, 15% and 25% chord on a NACA 0012 airfoil. The shapes at 5% chord had the largest effect on lift and drag, with penalties similar to those seen by Bowden [13]. The reports described do not provide the reasons why one protuberance size, shape, and location produced a more severe degradation in aerodynamic performance and control than another. This may have been due to the limited scope of the work that did not provide the authors enough information to draw any definitive conclusions. Indeed, the details of how a specific ice shape size and location systematically affect the aerodynamic performance in terms of pressure distributions, forces and moments has not been investigated experimentally prior to this study.

1.2 REVIEW OF LITERATURE–COMPUTATIONAL.

Although experimentation continues to be an important aspect of aerodynamic research, especially for complex flow problems, the trend has been to move toward a greater reliance on computer-based predictions in design and analysis. One of the areas that can benefit from computational modeling is aircraft icing. Evaluation of the aerodynamic response of an aircraft to the full envelope of icing conditions requires the determination of performance changes for a wide variety of ice accretion shapes and flow conditions. Therefore, an extensive number of tests must be performed, either in a wind tunnel or through flight testing. Computational modeling could reduce the number of tests and, therefore, decrease the cost and time required to perform them. This is especially true for high Reynolds number conditions. The following sections will discuss simulations of leading-edge ice shapes followed by the less common upper surface, ridge ice accretions.

1.2.1 Leading-Edge Ice Shapes.

Recently, sophisticated computer models have been applied to the problem of predicting the aerodynamics of iced airfoils. Similar to experimental studies, previous computational studies of aircraft icing have primarily concentrated on the more common leading-edge ice shapes. Both 2-D and three-dimensional (3-D) flow fields have been studied. Several approaches have been used to study the iced airfoil flow field. One approach is to use a full Navier-Stokes analysis, which has been performed on both structured and unstructured grids. A less computationally

intensive approach is to utilize the interactive boundary layer (IBL) technique, which couples the inviscid panel method solution to the solution of the boundary layer equations.

Potapczuk [15, 16] used the ARC2D code to study the aerodynamic effects of leading-edge ice. The ARC2D code solves the thin-layer Navier-Stokes equations, with turbulence simulated with the Baldwin-Lomax algebraic two-layer eddy-viscosity model [17]. This code was used in conjunction with the GRAPE grid generation code.

Potapczuk studied the effects of both rime and glaze ice accretion on a variety of airfoil geometries. One of the geometries studied was a NACA 0012 airfoil with a leading-edge glaze ice accretion. Predictions for angles of attack of 0° to 10° were presented and compared to the experimental data of Bragg and Spring [18]. The lift, drag, and moment computations show good agreement for angles of attack below stall. The predicted pressure distribution showed good agreement for locations aft of the ice shape. However, near the ice shape the computations contained large pressure spikes not present in the experiments. This was attributed to overly coarse grid spacing in the region. The structure of the recirculation zone was also studied using velocity profile plots that revealed significant differences between the computations and measurements. This suggested that the use of more appropriate grid spacing or an alternative turbulence model may have been required.

Recently, Caruso et al. [19, 20] used an unstructured mesh flow code and demonstrated high resolution of the detailed flow field around a leading-edge iced airfoil. Both Euler and Navier-Stokes computations were performed. The predicted flow field of the unstructured grid solutions compared well with predictions obtained on structured grids, although much larger computer requirements were noted for the unstructured methodology. Although several calculations were performed, the study focused primarily on the grid generation procedure and no comparisons with experiment were given. The study demonstrated a method for which ice growth could be calculated as a function of time while simultaneously solving for the flow field.

Another method for studying the flow about an iced airfoil was used by Cebeci [21]. He used an IBL method to predict the aerodynamic characteristics of a glaze iced NACA 0012. Results for lift and drag were presented for computations with and without modeling the wake. Lift was predicted better with the wake, while drag was predicted better without the wake. Velocity profile comparisons were also presented and large discrepancies were found within the separation region. The computations underpredicted the size of the experimentally measured separation bubble. Caruso and Farschi [22] later extended this methodology to 3-D calculations.

Kwon and Sankar [23, 24, 25] studied the flow about a 3-D finite wing with simulated leading-edge glaze ice. Wings with a NACA 0012 airfoil section were studied for both rectangular and swept wing configurations. The computational study solved the full unsteady 3-D Navier-Stokes equations on a structured algebraic C-grid. Turbulent flow was described with the Baldwin-Lomax model. Pressure distributions along spanwise locations were presented for 4° and 8°, which showed reasonable agreement with experimental data. However, it was shown that the boundary conditions of the sidewall played an important role in prediction accuracy. Euler solutions were also presented, but did not agree well with the experiments or the Navier-Stokes solutions.

1.2.2 Upper-Surface Ridge Ice Shapes.

One of the few relevant computational studies on large-droplet ice accretion (upper surface ridge ice shapes) was presented by Wright and Potapczuk [26]. The study was performed to gain a better understanding of the aerodynamics of large-droplet iced airfoils. Comparison of the aerodynamics of real ice accretion shapes and artificial shapes was one of the objectives. This study used the LEWICE ice accretion computer code to calculate large droplet icing conditions.

The study also performed computations to simulate the aerodynamic impact of large-droplet ice formations. The study used the ARC2D structured Navier-Stokes code with an algebraic turbulence model. The mesh was created using a hyperbolic grid generator. A variety of airfoil configurations and ice shapes were studied. The simulated ice shapes were obtained from IRT icing tests, LEWICE predicted ice shapes, and an artificial shape which was used in flight tests. Although no experimental data were presented for comparison, Mach number contours of the flow field were presented for each of the cases considered.

The first test case was an MS-317 airfoil with an ice shape generated in the IRT. The computations were performed at $M = 0.28$, Reynolds number (Re) $= 9 \times 10^6$, and $\alpha = 4°$. The ice shape had large-scale roughness over the front portion of the airfoil, with the most pronounced roughness occurring at approximately 10% chord on the upper surface. Flow field analysis revealed a trailing-edge separation bubble at lower angles of attack than for the clean airfoil. This was caused by the momentum loss in the boundary layer through the rough ice region.

The second case studied was representative of a regional transport wing section. A quarter-round simulated ice shape was placed on the upper surface at 6% chord. The computations were performed at $M = 0.28$, $Re = 9 \times 10^6$, and $\alpha = 6°$. Both clean and iced predictions were presented. The quarter-round obstruction caused a completely different flow field compared with the clean results. The iced case flow field was very unsteady with considerable vortex shedding forming off the quarter-round shape.

The final case considered was a NACA 23012 airfoil section. The computations were performed at $M = 0.28$, $Re = 9 \times 10^6$, and $\alpha = 6°$. Two ice shapes were studied: a shape obtained from IRT tracings and a shape predicted by LEWICE. Although the shapes were very similar geometrically, computed it was found that the two shapes resulted in very different computed flow fields. Similar to the MS-317 results, the LEWICE-predicted shape resulted in premature trailing-edge separation. The IRT shape, however, encountered a leading-edge stall with unsteady vortex shedding.

Recently, Dompierre et al. [27] reported results of computations about iced airfoils using adaptive meshing techniques. An efficient remeshing technology was employed such that the Navier-Stokes equations could be solved on a grid with a uniform distribution of error. The study utilized a Navier-Stokes finite-volume Galerkin method for the large-scale icing calculations. The k-ε turbulence model with wall functions was used for turbulence modeling. This code was used to demonstrate solver-independent solutions.

In this study a number of icing conditions were studied on the surface of a NACA 0012 airfoil. Computations for airfoils with leading-edge horns, an upper surface quarter-round ridge, and small-scale roughness were made. The upper surface ice ridge was similar to ice accretions resulting from large droplet icing conditions. The quarter-round ridge had a height of 0.0125 chords and was located at 5% chord. The computations were performed at $M = 0.15$ and $Re = 3.1 \times 10^6$. The mesh is shown to appropriately adapt to the predicted viscous regions. Although flow fields and a lift curve are plotted, no experimental data was available for comparison. The computations revealed a very large loss of lift. A much greater loss of lift was seen in the computations for the ridge ice than in the computations for the leading-edge ice horns.

None of these studies of airfoils with upper surface ridge ice accretions examined the pressure distributions and moments as will be considered herein. Also, none of the studies provided detailed comparison with experimental data, as it was not available at the time.

1.3 RESEARCH OBJECTIVES.

The objective of this study was to obtain an understanding of the effects of ridge ice accretions on subsonic aircraft aerodynamics and control. This overall objective can be broken down into four parts:

a. Measure the effect of simulated ridge ice accretions on airfoil performance and flap hinge moment over a range of conditions. Determine the most critical size and location for the ice accretion as well as the critical airfoil angle of attack and control surface deflections.

b. Determine how the ice accretion alters the airfoil aerodynamics by studying the boundary layer interaction between the ice accretion and the airfoil flow field.

c. Understand the effect of Reynolds number and airfoil geometry over a range applicable to subsonic aircraft.

d. Understand how the ice accretion affects aircraft control and what combination of ice shape and position, angle of attack, control deflection, airfoil geometry, and Reynolds number represent the most critical condition in terms of flight safety.

These objectives have been addressed by conducting wind tunnel tests on airfoils with a control surface using simulated ridge ice accretions and carrying out a parallel computational study to extend the applicability of the experimental data to higher Reynolds numbers and different airfoil geometries.

1.4 RESEARCH OVERIEW.

An experimental program was conducted in the University of Illinois' low-speed wind tunnel using simulated ice accretions to determine the sensitivity of ice shape and location on airfoil performance and control surface hinge moment as a function of angle of attack and flap deflection. The NACA 23012 airfoil section was used as it is representative of current commuter aircraft. Limited testing was also performed on the Natural Laminar Flow (NLF) 0414 airfoil to

better understand the role of airfoil geometry in aerodynamic performance of airfoils with ice. By identifying the airfoil sensitivity to ridge ice accretions and understanding the aerodynamic causes, better engineering decisions can be made with regards to these types of ice accretions.

To support the experimental study, an accompanying high-resolution computational investigation was performed for the ridge of accretion which had three primary objectives: (1) to provide additional details of the flow field (especially at critical conditions); (2) to predict any changes which result from increasing the Reynolds number to full-scale conditions; and (3) to predict changes which result from different airfoil configurations. In order to meet these objectives with well-characterized numerical fidelity, a detailed validation study was conducted to predict both separated flow behavior and Reynolds number effects on airfoils with these ice accretions.

The section that follows summarizes the experimental and computational research performed to study these ridge ice accretions. Preliminary papers on this research can be found in three AIAA papers [28, 29, 30] and two journal articles by the authors [31, 32].

2. RESEARCH METHODOLOGY.

2.1 EXPERIMENTAL METHODOLOGY.

The experiment was conducted in the low-turbulence subsonic wind tunnel in the Subsonic Aerodynamics Laboratory at the University of Illinois at Urbana-Champaign. The overall schematic of the experimental setup is shown in figure 2. The airfoil model was mounted in the test section on a three-component force balance, which was also used to set the model angle of attack. A traverseable wake rake was mounted downstream of the model and was used to measure drag. The airfoil models were instrumented for surface pressure measurements. The models were also flapped so that hinge moments could be measured and measurements could be taken with the flap deflected. A single IBM-compatible Pentium computer was used for all data acquisition and was used to control all of the experimental hardware.

2.1.1 Wind Tunnel.

The wind tunnel used was a conventional, open-return type and is shown in figure 3. The inlet settling chamber contained a 4-inch honeycomb, which was immediately followed downstream by four stainless steel antiturbulence screens. The test section measured $2.8 \times 4.0 \times 8.0$ ft and the side walls expanded 0.5 inch over its length to accommodate the growing boundary layer. The inlet had a 7.5:1 contraction ratio. The test section turbulence intensity was measured to be less than 0.1% at all operating speeds. The tunnel contained a 5-bladed fan that was driven by a 125-hp AC motor controlled by a variable frequency drive. The maximum speed attainable in the test section was 160 mph (235 ft/sec) which corresponded to a Reynolds number of 1.5 million per foot under standard conditions. The tunnel speed was controlled by the ABB ACS-600 frequency drive that was connected to the data acquisition computer by a serial RS-232 interface. During the data acquisition, the tunnel velocity was iterated until the Reynolds number was within 2%.

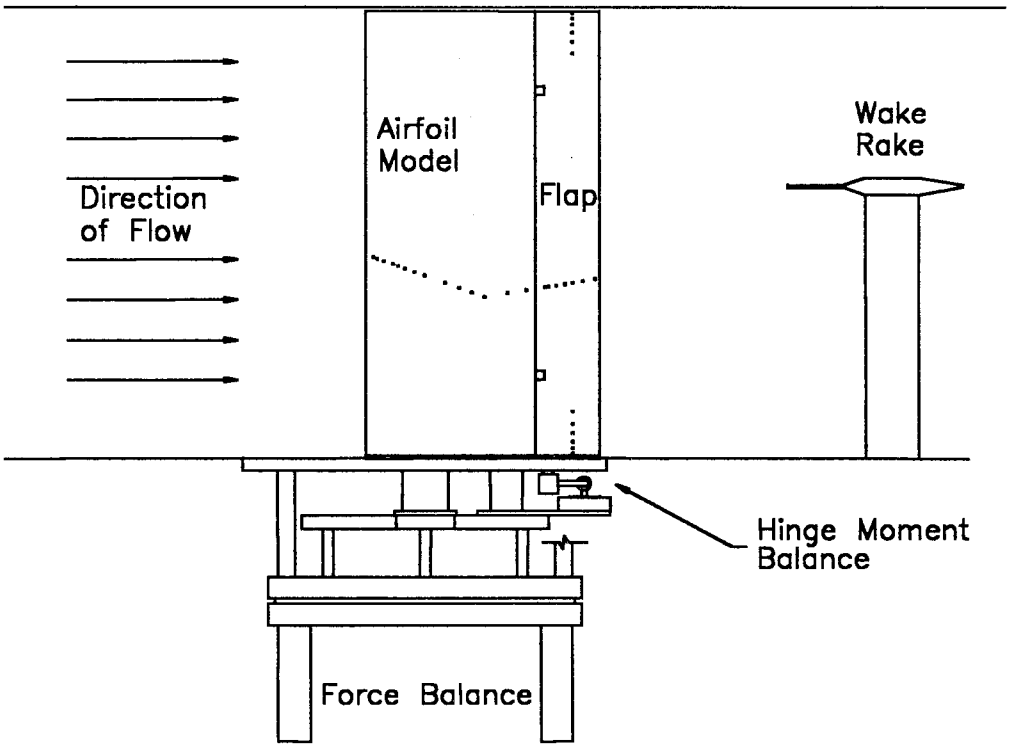

FIGURE 2. SCHEMATIC OF THE EXPERIMENTAL SETUP

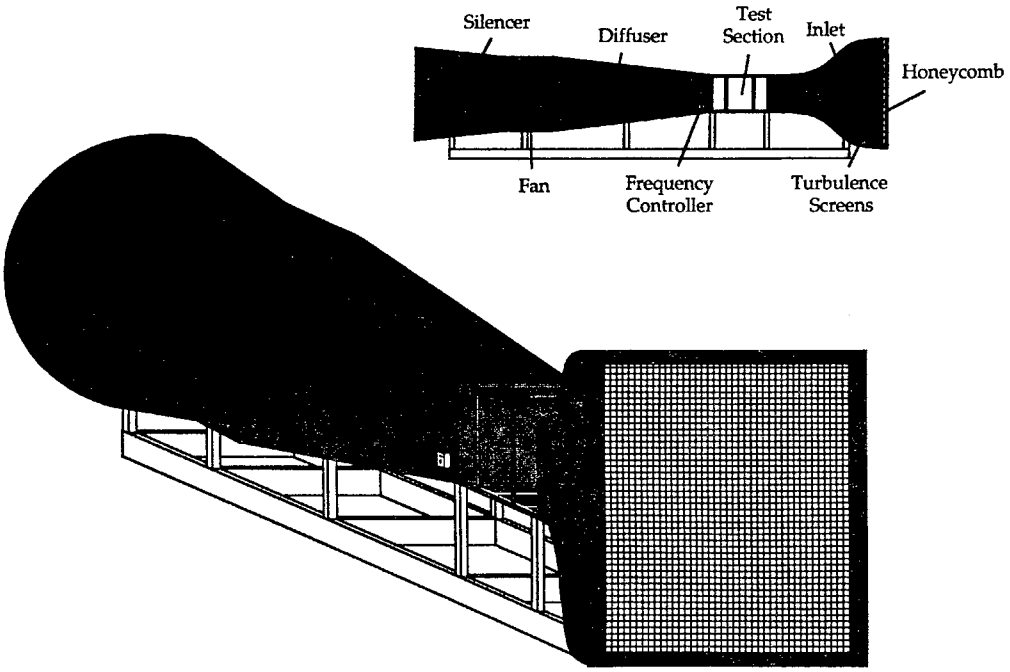

FIGURE 3. UNIVERSITY OF ILLINOIS 3′ × 4′ SUBSONIC WIND TUNNEL

2.1.2 Airfoil Models.

There were two airfoils studied in this investigation, a modified NACA 23012 designated NACA 23012m in this report, and a NLF 0414 model (borrowed from NASA/AGATE tests). The nature of the NACA 23012m modification (and its impact on the airfoil aerodynamics) will be discussed later in section 3.1. The NACA 23012 airfoil was chosen because it has aerodynamic characteristics that are typical of the current commuter aircraft fleet. The NLF 0414 airfoil was chosen because, as a natural laminar flow airfoil, it has aerodynamic characteristics that are quite different from the NACA 23012. The differences will be explained in more detail in section 4.1.7.1.

Both of the models had 18-inch chord with 25% chord simple flaps. The leading edge of the flap was located at $x/c = 0.75$ on both of the models. The flap hinge line was located at $x/c = 0.779$ on both of the models. The models were constructed of a carbon fiber skin surrounding a foam core. Two rectangular steel spars were located at $x/c = 0.25$ and 0.60 and were supported by wooden ribs. The spars extended 4 inches past one end of the model. This allowed it to be attached to the metric force plate of the three-component force balance using custom-built mounting supports. The flap gap was sealed on the model lower surface using a 1-inch-wide Mylar strip that was taped only on the main element side. At positive angles of attack, the high pressure on the lower surface of the model pushed the Mylar strip against the flap gap, effectively sealing it without adversely affecting the measurements from the flap hinge balance.

The airfoil models were equipped with surface pressure taps in order to measure the surface pressure distribution. The NACA 23012m model had 50 surface pressure taps on the main element and 30 taps on the flap (including 12 spanwise taps). The NLF 0414 had 75 taps on the main element (including 17 spanwise taps) and 22 taps on the flap. This arrangement is shown in figure 4. The main tap line was angled at 15 degrees with respect to the direction of the flow in order to put the pressure taps out of a possible turbulent wedge generated by the taps preceding them. The spanwise taps were used to measure spanwise flow nonuniformity near the walls.

2.1.3 Force and Moment Balance.

An Aerotech three-component force and moment balance (shown in figure 5) was primarily used to set the model angle of attack. However, it was also used to measure the lift, drag, and pitching moment for comparisons to the pressure and wake measurements. The model was mounted on the metric force plate of the balance with mounting supports. The signals from the load cells on the balance were gained by a factor of 250, low-pass filtered at 1 Hz and converted to normal, axial, and pitching moment components. The balance did not directly measure lift and drag because the load cells turned with the model. The force balance was equipped with a position encoder that precisely measured the angle of attack. The turntable portion of the balance (including the encoder) was interfaced to the data acquisition computer through the RS-232 serial connection. A more detailed description of the force balance can be found in Noe [33].

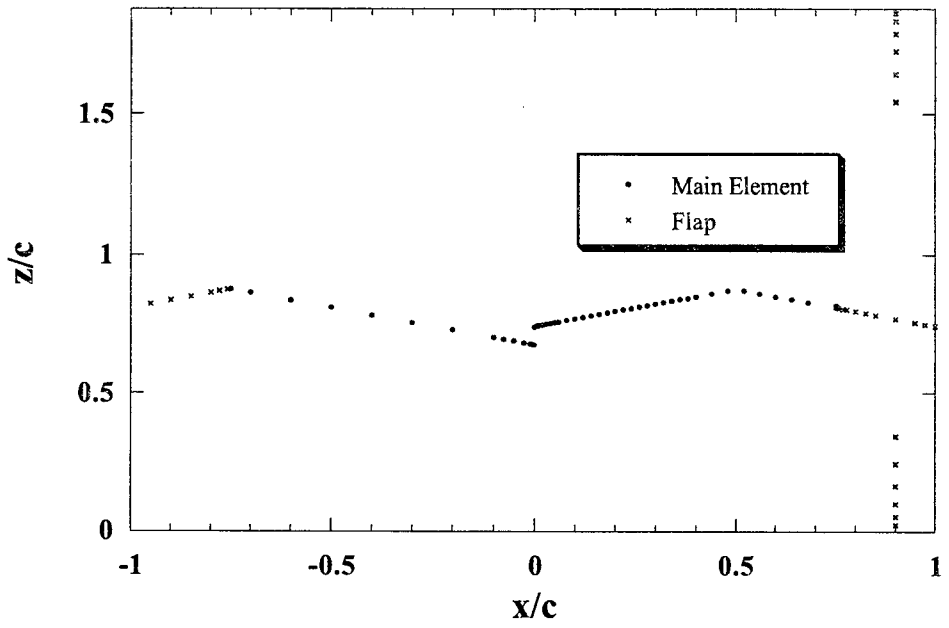

(a) NACA 23012m

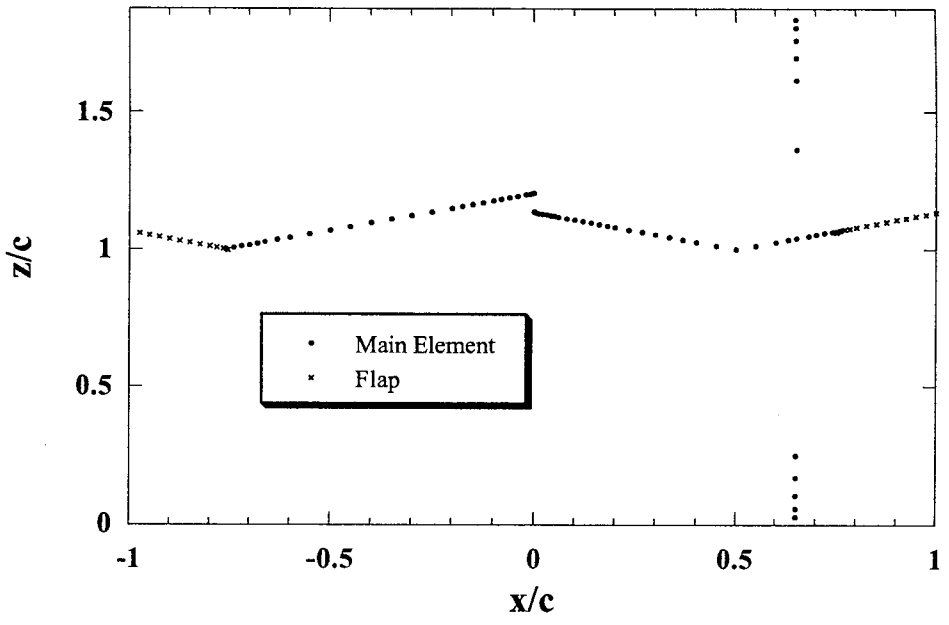

(b) NLF 0414

FIGURE 4. SURFACE PRESSURE TAP LOCATIONS FOR THE NACA 23012m AND NLF 0414 AIRFOIL MODELS
(Negative chordwise locations indicate lower surface)

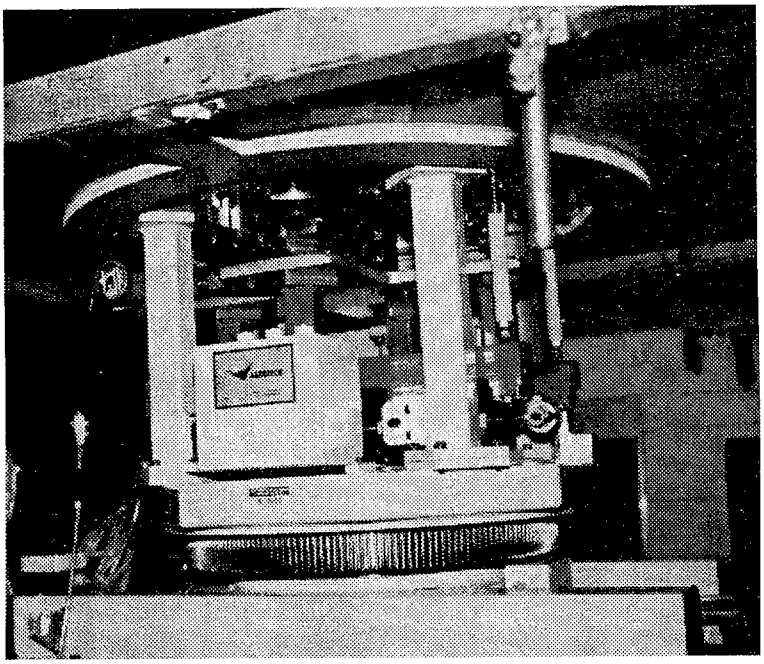

FIGURE 5. THREE-COMPONENT FORCE BALANCE

2.1.4 Flap Actuator and Balance.

The flap was actuated by a two-arm linkage system, which was driven by a Velmex linear traverse. An Omega LCF-50 load cell with 50 lb range was attached to one of the arms and was used to measure the flap hinge moments. The traverse was mounted on the metric force plate of the force balance. Thus, the entire load on the flap was eventually transferred to the force balance.

The flap load cell was calibrated by directly applying loads to the flap by using weights and pulley. The flap was calibrated up to 20 ft-lbs (which was 50% over the maximum moment it was expected to encounter) with 15 points and was linearly curve fit. The flap was calibrated at five flap deflection angles (-10, -5, 0, 5, and 10), providing a separate calibration curve for each flap angle that was to be tested.

2.1.5 Wake Survey System.

The primary drag measurements were recorded using a wake rake system (figure 6). It contained 59 total pressure probes aligned horizontally. The wake rake was traversed by a Velmex traverse system. The outer six ports on each side of the wake rake were spaced 0.27″ apart and the inner 47 ports were spaced 0.135″ apart. The total width of the wake rake was 9.75″. This was wide enough to capture the entire wake when the flow over the model was attached. However, when there was a very large wake due to flow separation, two or three spans of the wake rake were needed to capture the entire wake. There was a 0.27″ overlap between the successive spans in order to not to leave any gaps in the wake. The pressures from the wake rake were measured using two PSI EPS-32 units with 0.35″ psid range. The total pressures measured from the wake rake were referenced to the atmospheric pressure.

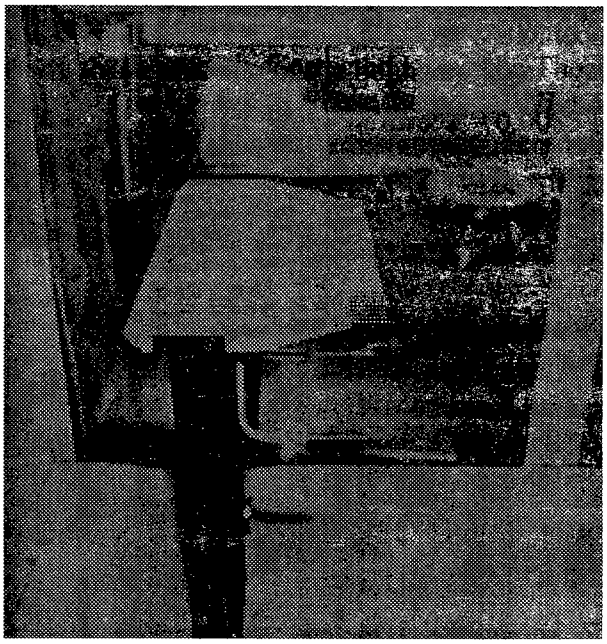

FIGURE 6. WAKE RAKE

The drag from the wake rake was determined using the method described in Jones [34]. The drag per unit span was calculated using the following equation:

$$D = \int \left(\sqrt{q_w q_\infty} - q_w \right) dy \tag{1}$$

It was necessary to modify the above equation to use terms that were directly measured. This resulted in equation 2.

$$D' = \int \left(\sqrt{q_\infty^2 - q_\infty \left(P_{0_\infty} - P_{0_w} \right)} - \left[q_\infty - \left(P_{0_\infty} - P_{0_w} \right) \right] \right) dy \tag{2}$$

2.1.6 Digital Pressure Acquisition System.

The PSI 8400 digital pressure system was used to measure all of the pressures except for the ambient pressure. Five electronically scanned pressure (ESP) modules with 32 ports each were used in this investigation. Two 0.35 psid ESP modules were used to measure the drag from the wake rake with the reference ports open to the atmosphere. Two 1 psid and one 5 psid modules were used to measure the surface pressures on the airfoil models and were referenced to the tunnel static pressure port. A port on the 1 psid module also measured the tunnel settling section static pressure from which the test section dynamic pressure was derived.

The PSI 8400 system had two built-in pressure calibration units (PCU). The 0.35 psid modules were calibrated by the 1 psid PCU and the 1 psid and 5 psid modules were calibrated by the 5 psid PCU. The calibration employed a three-point (2^{nd} order) curve fit. The ESP modules were calibrated before each run and during the runs when the temperature drifted by more than 2°F.

2.1.7 Ice Simulation.

The ridge ice accretions were simulated using several basic geometries as shown in figure 7. The baseline ridge ice accretions were simulated with wooden forward-facing quarter-round shapes of 0.10″, 0.15″, and 0.25″ heights. This geometry was used because it has a vertical step facing the flow, which is consistent with the shape of the residual ice that forms just aft of the wing ice protection system in an SLD encounter. The forward-facing quarter round is also the geometry used by the FAA during aircraft certification. Finally, a simple geometry, such as the forward-facing quarter round, allowed a much easier implementation for the numerical modeling aspect of this investigation.

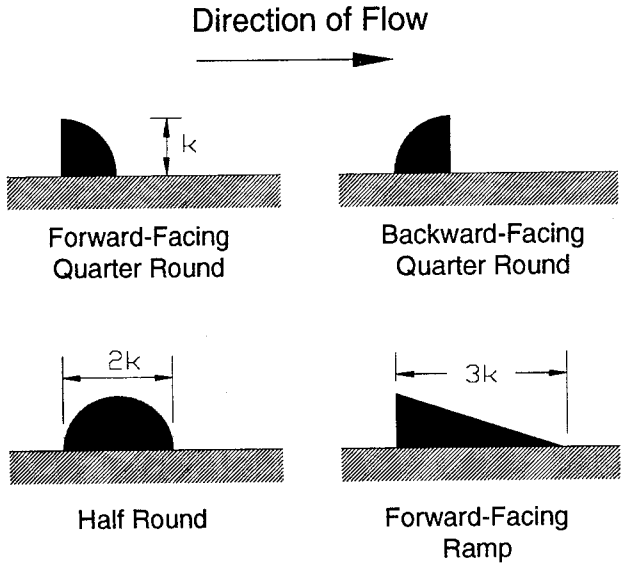

FIGURE 7. ICE SHAPE SIMULATION GEOMETRY

The other geometries tested consisted of backward-facing quarter round, half round, and forward-facing ramp (all with 0.25″ height and made of wood). The ramp shape was machined from aluminum and had a base length to height ratio of 3. The 0.25″ forward-facing quarter round was also tested with spanwise gaps (the detailed geometry of the spanwise gaps is provided in the results and discussions section). The simulated ice shapes were attached to the model using clear Scotch tape.

Roughness was also used both in place of, and in addition to, the simulated ice shape. When it was used in place of the ice shape, the roughness had a 0.5″ chordwise extent. When used with the ice shape, the roughness extended upstream and/or downstream from the ice shape. The chordwise extent of the upstream roughness varied from 0.25″ to 2″, and the extent of the downstream roughness was 2″. The roughness was simulated using 16-grit aluminum carbide attached to a double-sided tape. This resulted in 0.025″ roughness height, with k/c = 0.0014. The roughness density in terms of the coverage area was estimated to be about 30%.

The 0.25″ height of the baseline shapes was obtained from scaling the actual 0.75″ ridge ice accretion observed during tanker and icing wind tunnel tests. A survey of various commuter-

type aircraft by the authors showed that the average chord at the aileron section was roughly 5 feet [35]. The airfoil models used in the current investigation had 1.5-ft chord. Thus, when the actual 0.75″ ice accretion was scaled by the ratio of the University of Illinois at Urbana-Champaign (UIUC) airfoil model and the full size chord (1.5/5), a scaled height of 0.225″ resulted. This was rounded up to 0.25″ to provide a convenient number. Two other heights (0.10″ and 0.15″) were also tested in order to determine the effects of ice accretion height.

For most of the cases tested, the boundary layer was tripped at $x/c = 0.02$ on the upper surface and at $x/c = 0.05$ on the lower surface. The trip consisted of 0.012-inch-diameter microbeads that were applied onto a 0.003-inch-thick and 0.25-inch-wide double-sided tape. The models were tripped for two reasons. When the leading-edge deicing boot is activated, it usually does not remove all of the ice accretion. Instead, a residual ice roughness is usually left behind which causes the flow to be turbulent (or at least transitional) from the leading edge. Another reason for the trip was to provide a fixed transition location for the Computational Fluid Dynamics (CFD) simulations. Figure 8 shows the NACA 23012 model with the baseline 0.25″ forward-facing quarter round at $x/c = 0.10$.

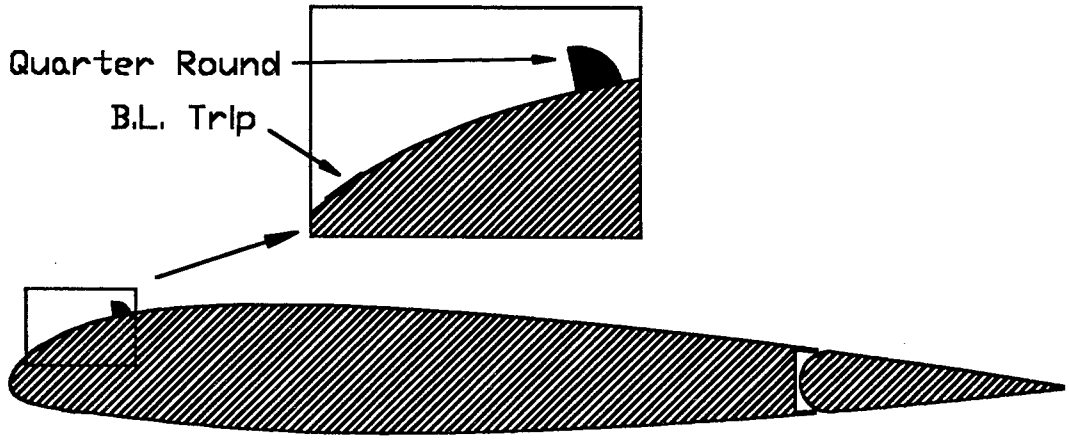

FIGURE 8. NACA 23012 MODEL WITH QUARTER-ROUND ICE SIMULATION
(0.25″ quarter round at $x/c = 0.10$ shown)

2.1.8 Data Acquisition and Reduction.

A typical run consisted of sweeping the angle of attack from negative stall to a few degrees past positive stall in 1° increments. At each angle of attack, the flap was swept from -10° to 10° in 5° increments. Before each run, the digital pressure system was calibrated and the force and hinge moment balance tares were measured.

The lift coefficient (C_ℓ) and pitching moment coefficient (C_m) measurements were derived from both the force balance and the surface pressure measurements. In this report, the C_ℓ and C_m data were taken from the pressure measurements unless indicated otherwise. The primary drag coefficient (C_d) measurements were taken with the wake rake and confirmed with the force balance. The flap hinge moment coefficients (C_h) were measured with the flap hinge load cell and confirmed with the surface pressure measurements. The surface pressure measurements and

fluorescent oil flow visualization were used for flow diagnostics. The C_ℓ, C_m, C_d, and C_h values were calculated using standard methods with conventional definitions:

$$C_\ell = \frac{L'}{q_\infty c} \tag{3a}$$

$$C_d = \frac{D'}{q_\infty c} \tag{3b}$$

$$C_m = \frac{M'}{q_\infty c^2} \tag{3c}$$

$$C_h = \frac{H'}{q_\infty c_f^{\,2}} \tag{3d}$$

All of the aerodynamic coefficients were corrected for wall effects using the method described by Rae and Pope [36].

The surface pressure coefficients were defined as:

$$C_p = \frac{p - p_\infty}{q_\infty} \tag{4}$$

In addition to providing the lift and pitching moment, the surface pressure measurements provided the reattachment locations for small separation bubbles that formed downstream of the ice shape simulations. For cases with large separation bubbles, the fluorescent oil flow visualization method [37] was used for determining the locations of flow reattachment.

All measurements were taken at 50 Hz and averaged over 2 seconds. The force balance data were low-pass filtered at 1 Hz. None of the other measurements were filtered. Shown in table 1 are the uncertainty estimates of the aerodynamic coefficients for a typical data point. The case shown is that of the clean NACA 23012m model $\alpha = 5°$ with zero flap deflection and $Re = 1.8$ million. The relative uncertainties for C_m and C_h appear to be rather large, but this was due to relatively small reference values at this point.

TABLE 1. EXPERIMENTAL UNCERTAINTIES FOR THE CLEAN NACA 23012m MODEL AT $\alpha = 5°$, $Re = 1.8$ MILLION

Aerodynamic Coefficient	Reference Value	Absolute Uncertainty	Relative Uncertainty
C_ℓ Pressure	0.633	2.11×10^{-03}	0.33%
C_d Wake	0.01022	1.43×10^{-04}	1.40%
C_m Pressure	-0.00894	3.49×10^{-04}	3.90%
C_h Balance	-0.0157	3.55×10^{-03}	9.70%

2.2 COMPUTATIONAL METHODOLOGY.

The science of CFD has made great strides in recent years. Many new flow solving and grid generating techniques have been developed. Tremendous improvements in computing capabilities have significantly contributed to the field as well. These advancements have facilitated the solution of many complex flow fields that had been previously impossible. In particular, advanced grid generation techniques and high-capacity computers have enhanced our ability to compute flow fields around airfoils with simulated ice shapes.

Most aerodynamic simulations using computational fluid dynamics are performed using structured grids. Structured grids are very efficient and are very convenient for conventional airfoil with attached flow. However, airfoils with complex geometries, such as airfoils with significant ice acretions or multielement airfoils, are not easily mapped onto a conventional structured grid. One solution to this problem is to use a multiblock structured grid. This involves tessellating the domain between the body and far field into simple rectangular blocks. The grid can then easily be generated within each block. This process is very difficult to automate and thus requires much interaction with the user. Another method is using overlapping (chimera) grids. Here, structured grids are generated about each component in the flow field. These grids are allowed to overlap. This method is also difficult to automate, and the flow solver requires overhead for interpolating between grids.

Recently another solution to this problem has prompted a surge of activity: unstructured grids. Unstructured grids have been very popular for use in solid modeling and structural mechanics for many years. It is only recently that they have received considerable attention within the field of fluid dynamics. For use in fluid dynamics, unstructured grids are traditionally composed of simplices (triangles in 2-D and tetrahedra in 3-D) and do not possess any coherent structure. Hence, they can provide flexibility for tessellating about 88 complex geometries and adapting to flow features. Generating unstructured grids is also much more automatable than conventional multiblock structured grid generation. This allows the user to dedicate much less time to grid generation. Although much of the fluid dynamics research using unstructured grids has concentrated on inviscid flow problems, recently much progress has been made for high Reynolds number viscous flows, which are of much greater practical interest. Currently, unstructured grid technology requires additional memory and computational costs for the same number of nodes (often an order of magnitude less). Thus, for complex flows, unstructured grids are often much more efficient. This, however, is balanced with the ability to compute flows about complex geometries and with the ease of adaption, thus, typically requiring fewer nodes.

This chapter describes the various pieces of software that constitute the complete unstructured CFD package used for the present study. The package was authored and supported by Dimitri Mavriplis at *Scientific Simulations* and was based on extensive work completed at NASA Langley. It is described in references 38, 39, 40, 41, 42, and 43. The package was developed such that the user could proceed step by step, beginning from a simple coordinate description of the geometry, and resulting in the fully turbulent steady-state solution of the Navier-Stokes equations about the geometry at the given conditions.

The current computational methodology consists of four stages:

- Flow Solution
- Grid Generation
- Grid Adaption
- Postprocessing

Each stage represents a separate portion of the package's overall methodology. The algorithm is presented in the flowchart in figure 9, which is provided as an overview for the following sections.

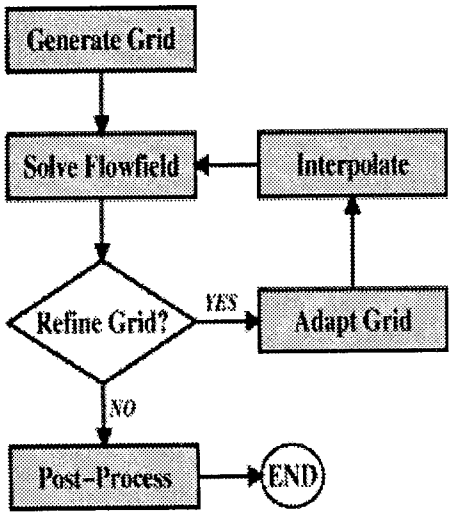

FIGURE 9. FLOWCHART OF THE OVERALL COMPUTATIONAL STRATEGY

2.2.1 Flow Solution.

The flow solution is obtained with a code called NSU2D (Version 5.0.b). This code takes a discretized mesh of the flow field and obtains a steady-state solution of the governing equations. The detailed methodology used in NSU2D is described in the following sections.

2.2.1.1 Governing Equations.

The flow solver obtains the steady-state solution of the full two-dimensional compressible Reynolds (Favre) Averaged Navier-Stokes equations (without a thin-layer assumption), which can be written in conservative form as

$$\frac{\partial w}{\partial t}+\frac{\partial f_c}{\partial x}+\frac{\partial g_c}{\partial y}=\frac{\sqrt{\gamma}M}{Re}\left(\frac{\partial f_v}{\partial x}+\frac{\partial g_v}{\partial y}\right) \tag{5}$$

where w is the solution vector of the conserved variables

$$w = \begin{bmatrix} \rho \\ \rho u \\ \rho v \\ \rho E \end{bmatrix} \tag{6}$$

and ρ is the fluid density, u and v are the cartesian velocity components, and E is the total energy. The pressure, p, can be calculated from the equation of state for a perfect gas

$$p = (\gamma - 1)\rho\left(E - \frac{(u^2 + v^2)}{2}\right) \tag{7}$$

The $\sqrt{\gamma}\, M/Re$ term results from employing the following nondimensional variables

$$\rho = \frac{\hat{\rho}}{\hat{\rho}_\infty} \quad u = \frac{\hat{u}}{\hat{a}_\infty / \sqrt{\gamma}} \quad x = \frac{\hat{x}}{c} \quad t = \frac{\hat{t}}{\frac{c}{\hat{a}_\infty / \sqrt{\gamma}}}$$

$$p = \frac{\hat{p}}{\hat{p}_\infty} \quad v = \frac{\hat{v}}{\hat{a}_\infty / \sqrt{\gamma}} \quad y = \frac{\hat{y}}{c}$$

where the ($\wedge$) denotes dimensional variables, and the infinity (∞) refers to freestream values. Using the components of w along with the pressure, the cartesian components of the convective fluxes (f_c,g_c) are given as

$$f_c = \begin{bmatrix} \rho u \\ \rho u^2 + p \\ \rho uv \\ \rho uE + up \end{bmatrix} \quad g_c = \begin{bmatrix} \rho v \\ \rho vu \\ \rho v^2 + p \\ \rho vE + vp \end{bmatrix} \tag{8}$$

and the components of the viscous fluxes (f_v,g_v) are given by

$$f_v = \begin{bmatrix} 0 \\ \sigma_{xx} \\ \sigma_{xy} \\ u\sigma_{xx} + v\sigma_{xy} - q_x \end{bmatrix} \quad g_v = \begin{bmatrix} 0 \\ \sigma_{xy} \\ \sigma_{yy} \\ u\sigma_{xy} + v\sigma_{yy} - q_y \end{bmatrix} \tag{9}$$

Using Stokes' hypothesis and modeling the Reynolds stress and heat flux terms with the Boussinesq assumption, the components of the stress tensor, σ, and heat flux vector, q, are given by

$$\begin{aligned}
\sigma_{xx} &= 2(\mu+\mu_t)\frac{\partial u}{\partial x} - \frac{2}{3}(\mu+\mu_t)\left(\frac{\partial u}{\partial x}+\frac{\partial v}{\partial y}\right) \\
\sigma_{yy} &= 2(\mu+\mu_t)\frac{\partial v}{\partial y} - \frac{2}{3}(\mu+\mu_t)\left(\frac{\partial u}{\partial x}+\frac{\partial v}{\partial y}\right) \\
\sigma_{xy} &= \sigma_{yx} = (\mu+\mu_t)\left(\frac{\partial u}{\partial y}+\frac{\partial v}{\partial x}\right)
\end{aligned} \tag{10}$$

and

$$\begin{aligned}
q_x &= -\frac{\gamma}{\gamma-1}\left(\frac{\mu}{Pr}+\frac{\mu_t}{Pr_t}\right)\frac{\partial \frac{p}{\rho}}{\partial x} \\
q_y &= -\frac{\gamma}{\gamma-1}\left(\frac{\mu}{Pr}+\frac{\mu_t}{Pr_t}\right)\frac{\partial \frac{p}{\rho}}{\partial y}
\end{aligned} \tag{11}$$

respectively. Note, all solutions presented here assume adiabatic wall conditions. Here the molecular viscosity, μ, is a function of temperature, such that

$$\mu = K_1 T^{K_2} \tag{12}$$

where K_1 and K_2 are constants and μ_t is the turbulent eddy viscosity, which must be calculated with a suitable turbulence model. Pr is the laminar Prandtl number taken as 0.7, and Pr_t is the turbulent Prandtl number taken as 0.9. The ratio of specific heats, γ, is taken as 1.4 for air.

The above equations represent a set of partial differential equations in space and time. These can be discretized in space in order to obtain a set of coupled ordinary differential equations. They can then be integrated in time to find the steady-state solution.

2.2.1.2 Spatial Discretization.

In the current methodology, the space domain is discretized by subdividing the continuum into 2-D triangular elements. The code uses a vertex-based discretization where the flow variables are stored at the triangle vertices. These field variables are approximated by a linear combination of basis functions, such that

$$w \approx \sum_i w_i N_i(x,y) \tag{13}$$

where the summation is performed over each node in the mesh. w_i is the value of the conserved variables evaluated at vertex i, and $N_i(x,y)$ is the standard locally defined linear shape function where

$$N_i(x_j,y_j) = \begin{cases} 0 & \text{if } i=j \\ 1 & \text{if } i\neq j \end{cases} \tag{14}$$

Since the convective fluxes are algebraic functions of the conserved variables, they can also be computed at the element vertices and vary linearly with the basis functions. However, the viscous terms are functions of the gradients in the conserved variables. Therefore, the gradients required for the stress tensor and the heat flux vector are calculated at the centers of the triangles. These first derivatives are constant over each element and can be computed as

$$\frac{\partial w}{\partial x} = \frac{1}{A}\iint \frac{\partial w}{\partial x} dxdy = \frac{1}{A}\int w dy = \frac{1}{A}\sum_{k=1}^{3} \frac{(w_{k+1} + w_k)}{2}(y_{k+1} - y_k) \tag{15}$$

$$\frac{\partial w}{\partial y} = \frac{1}{A}\iint \frac{\partial w}{\partial y} dxdy = \frac{1}{A}\int w dx = \frac{1}{A}\sum_{k=1}^{3} \frac{(w_{k+1} + w_k)}{2}(x_{k+1} - x_k) \tag{16}$$

where the summation is performed over the three vertices of the triangle.

The flux terms are evaluated using a Galerkin based finite-element formulation. To derive the Galerkin formulation, equation 5 is first rewritten in vector notation

$$\frac{\partial w}{\partial t} + \nabla \cdot \mathbf{F}_c = \frac{\sqrt{\gamma} M}{Re} \nabla \cdot \mathbf{F}_v \tag{17}$$

Next, a weak formulation is obtained using the method of weighted residuals. This is done by multiplying the above differential system by a test function, ϕ, and integrating over the entire domain

$$\frac{\partial}{\partial t}\iint_\Omega \phi w dxdy + \iint_\Omega \phi \nabla \cdot \mathbf{F}_c dxdy = \frac{\sqrt{\gamma} M}{Re}\iint_\Omega \phi \nabla \cdot \mathbf{F}_v dxdy \tag{18}$$

Using integration by parts to integrate the flux integrals and neglecting the boundary terms yields

$$\frac{\partial}{\partial t}\iint_\Omega \phi w dxdy = \iint_\Omega \mathbf{F}_c \cdot \nabla \phi dxdy - \frac{\sqrt{\gamma} M}{Re}\iint_\Omega \mathbf{F}_v \cdot \nabla \phi dxdy \tag{19}$$

This equation must be evaluated at each node in the domain. To evaluate the above equation at a node P, the test function is taken as a linear combination of the same basis functions used in equation 13.

$$\phi = \sum_i \phi_i N_i(x, y) \tag{20}$$

Therefore, the flux integrals in equation 19 are zero for all elements which do not contain the vertex P. Thus, a domain of influence is defined as the union of all triangles with a vertex P. Knowing that $\nabla\phi$ is constant over a triangle and each triangle is fully enclosed, the flux integrals over the domain of influence can be evaluated for node P to obtain

$$\frac{\partial}{\partial t}\iint_{\Omega} N_p w dx dy = \frac{1}{6}\sum_{e=1}^{n} L_{AB}\left(\mathbf{F}_C^A + \mathbf{F}_C^B\right)\cdot\hat{\mathbf{n}} - \frac{\sqrt{\gamma}M}{2Re}\sum_{e=1}^{n} L_{AB}\mathbf{F}_v^e\cdot\hat{\mathbf{n}} \tag{21}$$

where the summation is over all triangles in the domain of influence. Here L_{AB} refers to the length of the edge, $\hat{\mathbf{n}}$ is the unit vector normal to the edge, $\mathbf{F}_C^A$ and $\mathbf{F}_C^B$ are the convective fluxes computed at vertices A and B respectively, and $\mathbf{F}_v^e$ is the viscous flux over triangle e.

Performing a similar analysis to evaluate the left-hand side of equation 21 results in a coupling of the time and space derivatives. This makes the set of equations difficult to solve efficiently. Since time-accuracy is not an issue while computing steady-state solutions, the conserved variables are set to a constant, w_p, over the domain of influence. Therefore, w_p can be pulled out of the integral to obtain

$$\Omega_p \frac{\partial w_p}{\partial t} = \frac{1}{2}\sum_{e=1}^{n} L_{AB}\left(\mathbf{F}_c^A + \mathbf{F}_c^B\right)\cdot\hat{n} - \frac{3\sqrt{\gamma}M}{2Re}\sum_{e=1}^{n} L_{AB}\mathbf{F}_v^e\cdot\hat{\mathbf{n}} \tag{22}$$

where Ω_p is the surface area of the domain of influence.

For certain conditions, the above formulation can be shown to be equivalent to a finite-volume formulation. It is also analogous to a central differencing scheme on a structured, quadrilateral mesh. As such, artificial dissipation terms must be incorporated for stability. A blend of a Laplacian and biharmonic operators are used. These simulate the blended second and fourth differences commonly used with structured grids. The biharmonic dissipation provides second-order accurate background dissipation in regions of smooth flow. The Laplacian dissipation provides first-order accurate smoothing in the vicinity of shock waves to reduce numerical oscillations.

2.2.1.3 Time Discretization.

The spatial discretization represented by equation 22 is a set of coupled ordinary differential equations and can be written as

$$\Omega\frac{dw_p}{dt} + \left[Q\left(w_p\right) - D\left(w_p\right)\right] = 0 \tag{23}$$

where the discrete approximation to the convective and dissipative terms for node P are represented by Q(wp) and D(wp) respectively. The dissipative terms contain both the viscous fluxes and the artificial dissipation terms. This set of equations is integrated in time using an explicit five-stage Runge-Kutta time-stepping scheme given by

$$
\begin{aligned}
w^{(0)} &= w^n \\
w^{(1)} &= w^{(0)} - \alpha_1 \frac{\Delta t}{\Omega_p}\left[Q\left(w^{(0)}\right) - D_0\right] \\
w^{(2)} &= w^{(0)} - \alpha_2 \frac{\Delta t}{\Omega_p}\left[Q\left(w^{(1)}\right) - D_1\right] \\
w^{(3)} &= w^{(0)} - \alpha_3 \frac{\Delta t}{\Omega_p}\left[Q\left(w^{(2)}\right) - D_2\right] \\
w^{(4)} &= w^{(0)} - \alpha_4 \frac{\Delta t}{\Omega_p}\left[Q\left(w^{(3)}\right) - D_3\right] \\
w^{(5)} &= w^{(0)} - \alpha_5 \frac{\Delta t}{\Omega_p}\left[Q\left(w^{(4)}\right) - D_4\right] \\
w^{n+1} &= w^{(5)}
\end{aligned}
\tag{24}
$$

where

$$
\begin{aligned}
D_0 &= D_1 = D\left(w^{(0)}\right) \\
D_2 &= D_3 = \beta_1 D\left(w^{(2)}\right) + \left(1 - \beta_1\right) D_0 \\
D_4 &= \beta_2 D\left(w^{(4)}\right) + \left(1 - \beta_2\right) D_2
\end{aligned}
$$

and the coefficients are given as

$$
\alpha_1 = 1/4 \qquad \alpha_2 = 1/6 \qquad \alpha_3 = 3/8 \qquad \alpha_4 = 1/2 \qquad \alpha_5 = 1
$$

$$
\beta_1 = 0.56 \qquad \beta_2 = 0.44
$$

Here w^n represents the solution vector at the nth time step, and $w^{(q)}$ represents the solution at the qth stage within the time step. Notice that the convective terms are evaluated at every stage, while the dissipation terms are only evaluated at the first, third, and fifth stages. This scheme was designed to obtain the best balance of efficiency and robustness for viscous flows with the algebraic multigrid algorithm.

Although the turbulence equations could be integrated in time with this same procedure, it would impose a more restrictive time-step limitation and lead to slower convergence. Since the turbulence equations are only loosely coupled to the governing equations, it is possible to use a different integration strategy when solving them. Therefore, the turbulence model is integrated using a point-implicit or Jacobi iteration strategy. The implicit strategy allows a larger time step to be used on the turbulence equations than would be possible using an explicit scheme, therefore allowing the turbulence quantities to be advanced at the same rate as the governing equations. One Jacobi iteration is performed during each stage of the time-stepping scheme. The details associated with the actual method used in NSU2D are described in reference 42.

2.2.1.4 Convergence Acceleration Techniques.

The NSU2D program has been primarily designed to obtain steady-state solutions, i.e., time-stepping until all time derivatives are reduced to an acceptably small level. Therefore, the time-accuracy of the solution can be compromised in order to accelerate convergence. Various convergence accelerating techniques are used in the code, such as local time-stepping, residual smoothing, and an algebraic multigrid algorithm.

Local time-stepping advances the equations at each grid point by the maximum permissible time-step at that point as determined by stability analysis. This ensures stability as calculated from local grid and flow properties. Both convective and diffusive characteristics of the Navier-Stokes equations must be considered. Therefore, the local time-step is taken as a weighted combination of the inviscid and viscous time-step limits

$$\Delta t = CFL\left(\frac{\Delta t_c \Delta t_v}{\Delta t_c + \Delta t_v}\right) \tag{25}$$

where CFL is the inviscid Courant number. Here

$$\Delta t_c = \frac{\Omega}{\lambda_c} \qquad \Delta t_c = K_v \frac{\Omega}{\lambda_v} \tag{26}$$

where Ω denotes the control volume area, K_v is a coefficient which determines the relative importance of the viscous and inviscid contribution to the time-step limit, and the eigen values are given by

$$\begin{aligned} \lambda_c &= \sum_{e=1}^{n} \left| U_{AB}\Delta y_{AB} - v_{AB}\Delta x_{AB} \right| + c_{AB}\sqrt{\Delta x_{AB}^2 + \Delta y_{AB}^2} \\ \lambda_v &= \frac{\gamma^{3/2} M}{RePr\Omega} \sum_{e=1}^{n} \frac{\mu_{AB}}{\rho_{AB}} \left[\Delta x_{AB}^2 + \Delta y_{AB}^2 \right] \end{aligned} \tag{27}$$

The above formulation is a simplified version of the actual method used in NSU2D since the stability of the turbulence equations must also be taken into account.

Residual smoothing is also employed to accelerate convergence by allowing the use of larger Courant numbers and, hence, larger time-steps. Residual smoothing is a technique which involves implicitly averaging the residuals in order to increase the stability limit of the discretized equations. The original residuals, R, may be replaced by the smoothed residuals, $\overline{R}$, by solving the implicit equation

$$\overline{R}_i = R_i + \varepsilon \nabla^2 \overline{R}_i \tag{28}$$

at each node, i, in the mesh. Here ε is the smoothing coefficient. The above equation is solved using an iterative Jacobi scheme.

The main technique used in NSU2D to accelerate the convergence is the multigrid algorithm. This method performs time-steps on a sequence of progressively coarser grid levels. This method accelerates convergence by damping out low-frequency errors on the coarser grids where these errors can manifest themselves as high frequencies. In the NSU2D methodology, the coarse grid levels are not physical grids which must be generated separately, rather, they are created automatically prior to the flow solution through agglomeration. Here the fine grid control volumes are fused together to form complex polyhedral coarse grid control volumes. NSU2D uses an algebraic multigrid algorithm (AMG), as opposed to a geometric algorithm, and therefore operates on the matrix of the discrete operator, rather than on the grid of the discretization. The formulation of the algebraic algorithm can be found in reference 44.

The present research used a W-cycle to traverse the various grid levels during the multigrid cycle. Here a time-step is first performed on the finest grid. Then, the flow variables are interpolated to the next coarser grid, on which a time-step is performed. This process is repeated recursively until the coarsest mesh has been reached. The flow solution is then interpolated back to the finer grids and the grid levels are marched in a W pattern.

Five grid levels were typically used for the current computations. However, for grids constrained by the outer boundary, such as when modeling wind-tunnel walls, fewer grid levels needed to be used since the control volumes of the coarse grid levels were wider than the flow field. Also, for flows with large separation regions, it was found that numerical instabilities developed in the coarse grid levels, therefore preventing convergence. Reducing the number of grid levels eliminated these instabilities and allowed convergence. For these cases, three grid levels were used.

2.2.1.5 Turbulence Model.

The NSU2D code supports the computation of inviscid flows, laminar viscous flows, and turbulent viscous flows. For practical flows at large Reynolds numbers, turbulence must be simulated. This is done through an appropriate turbulence model which computes the turbulent eddy viscosity, μ_t, found in the viscous flux terms of the Reynolds averaged equations (equations 10 and 11). There are many eddy-viscosity models in use today. Algebraic turbulence models such as the Baldwin-Lomax [17] model have been very popular for use with structured grids and have been used for studying iced airfoil aerodynamics [16]. Although it has been done [45], these models are difficult to implement on unstructured grids since the solution at one node depends on the solution at neighboring nodes. Therefore, the recent trend is towards simple one- and two-equation models. NSU2D supports the Baldwin-Barth [46] and Spalart-Allmaras [47] one-equation models along with the k-ε (with or without wall functions) [42] and the k-Ω [48] two-equation models. The Spalart-Allmaras model is used exclusively in this research.

The Spalart-Allmaras model has many similarities to the Baldwin-Barth model. However, unlike the Baldwin-Barth model which was derived from a simplified form of the $k-\varepsilon$ model, the Spalart-Allmaras model was developed separately and uses arguments of dimensional analysis, Galilean invariance, and selective dependence on the molecular viscosity. The model is computationally local in that the equation at one point does not depend on the solution at other points and is, therefore, well suited for unstructured grids. The model was designed and

calibrated for use with mixing layers, wakes, and boundary layers. It therefore appears to be a good candidate for predicting the flow field around iced airfoils. Recently, Spalart et al. [49] modified the original Spalart-Allmaras model to account for system rotation and streamline curvature. Although this alteration was found to improve predictions for many types of flows, it was found to have very little effect on the prediction of backward-facing step flows, which are similar to flows encountered around an ice-accreted airfoil. Therefore, the modified version was not pursued in this study.

2.2.1.5.1 Description of the Spalart-Allmaras Formulation.

Using dimensional variables for simplicity for the standard Spalart-Allmaras model as described in reference 50 the kinematic eddy viscosity ($\nu_t = \mu_t/\rho$) is related to a working variable, $\tilde{\nu}$, by

$$\nu_t = \tilde{\nu} f_{v1} \tag{29}$$

where

$$f_{v1} = \frac{\chi^3}{\chi^3 + c_{v1}^3} \tag{30}$$

and

$$\chi \equiv \frac{\tilde{\nu}}{\nu} \tag{31}$$

The working variable, $\tilde{\nu}$, obeys the transport equation

$$\frac{D\tilde{\nu}}{Dt} = c_{b1}\tilde{S}\tilde{\nu} + \frac{1}{\sigma}\left[\nabla\cdot\left((\nu+\tilde{\nu})\nabla\tilde{\nu}\right) + c_{b2}(\nabla\tilde{\nu})^2\right] - c_{w1}f_w\left[\frac{\tilde{\nu}}{d}\right]^2 \tag{32}$$

Where $\frac{D}{Dt}$ denotes the substantial derivative and d is the distance to the closest wall. The quantity $\tilde{S}$ in the production term is given by

$$\tilde{S} \equiv S + \frac{\tilde{\nu}}{\kappa^2 d^2} f_{v2} \tag{33}$$

where the source term, S, is modeled with the magnitude of the vorticity

$$S = |\omega| \equiv \left|\frac{\partial v}{\partial x} - \frac{\partial u}{\partial y}\right| \tag{34}$$

The closure functions appearing in the above equation are defined as

$$
\begin{aligned}
f_{v2} &= 1 - \frac{\chi}{1 + \chi f_{v1}} \\
f_w &= g\left[\frac{1 + c_{w3}^6}{g^6 + c_{w3}^6}\right]^{1/6} \\
g &= r + c_{w2}\left(r^6 - r\right) \\
r &\equiv \frac{\tilde{\nu}}{\tilde{S}\kappa^2 d^2}
\end{aligned}
\tag{35}
$$

The constants, as specified in reference 47, are given as follows: $\kappa = 0.41$, $\sigma = 2/3$, $c_{b1} = 0.1355$, $c_{b2} = 0.622$, $c_{v1} = 7.1$, $c_{w1} = c_{b1}/\kappa^2 + \left(1 + c_{b2}\right)/\sigma$, $c_{w2} = 0.3$, and $c_{w3} = 2$.

2.2.1.5.2 Transition Specification.

Within the turbulent flow field, the NSU2D code provides a procedure to establish transition points, or more precisely, to define laminar regions which run along the airfoil surface and extend into the flow field. This laminar region is modeled by turning off the source terms in the turbulent transport equations. This produces a laminar effect but does not eliminate the possibility of turbulent eddy viscosity being convected or diffused into these regions from the neighboring turbulent regions.

Although the code allows prescription of the laminar to turbulent transition location, the code itself does not predict the location of transition. Therefore, the transition points must be user specified. In this research the transition points are predicted *a priori* using the integral boundary layer program of XFOIL [51]. This program incorporates an e^N-type amplification formulation for determining the transition location. The e^N method is based on the Orr-Sommerfeld equation and assumes that transition occurs when the most unstable Tollmien-Schlichting wave in the boundary layer has grown by some factor, taken here as e^9. A detailed description of this method as used in XFOIL can be found in reference 52. To account for variations in the predicted lift of XFOIL, a lift-corrected angle of attack is used when the transition point is being computed. When comparing against experimental tests which have a boundary layer trip placed on the airfoil, the transition is assumed to occur at which ever comes first: the trip location or the transition location predicted by XFOIL.

The presence of the quarter-round ice shape on the airfoil required additional consideration while determining whether to model laminar or turbulent flow. The protuberance can cause a large separation bubble that will initiate at the top of the shape due to its sharp corner. This configuration fortunately eliminates the problem of predicting the separation point of the free-shear layer, which can be difficult to accurately simulate on smooth surfaces. For entrainment along the free-shear layer itself, the flow can be considered fully developed turbulent in a small fraction of a step height downstream of the separation point for the Reynolds numbers

considered herein [53]. Therefore, the entire free-shear layer and reattachment region were modeled as turbulent.

All experimental results considered in the icing results (section 4.2) use trip strips placed at 2% chord on the upper surface and 5% chord on the lower surface. Due to the complex geometry and large separation regions, XFOIL cannot accurately predict the flow about an iced airfoil. Therefore, for all positive angles of attack, the upper surface transition point for the iced airfoil was always taken as the trip location. This is because the iced case was limited to low lift coefficients such that the lift-corrected non-iced XFOIL transition was never further upstream than the trip location. Computations where the upper surface trip location was moved further upstream did not change the results significantly. However, for negative angles of attack, the transition location on the lower surface moved forward of the transition trip. Therefore, the transition position for the lower surface was taken at the leading edge for all negative angles of attack.

2.2.2 Grid Generation.

The grid is generated using an interactive program for Silicon Graphics (SGI) workstations called UMESH2D (Version 3.0.a). The code creates an unstructured (triangular) discretization of the entire flow field from an initial coordinate definition of the geometry. The code was designed with emphasis on multielement, high-lift viscous airfoil configurations. The resulting grid contains highly stretched elements within the boundary layers and wakes and is therefore suitable for high Reynolds number viscous flows.

The grid is generated in six independent stages:

- Geometry
- Wake Generation
- Surface Grid Spacing Specification
- Interior Grid Spacing Specification
- Grid Generation
- Mesh Postprocessing and Output

In the first stage, the user provides a pointwise geometry description of the airfoil and all boundaries. Figure 10(a) shows an example geometry definition for a typical three-element airfoil configuration. Next, a spline curve is generated from these coordinates and a wake is generated by a simple panel method (figure 10(b)). Then the boundary point distribution is determined as specified in a user-supplied input file, and a field function is created for the spacing within the domain. The actual grid generation is performed in two stages. First a semistructured mesh within the viscous regions near the walls and wakes are discretized with an advancing-layers algorithm (figures 10(c) and 10(d)). Then the grid within the remaining inviscid regions is generated using an advancing-front Delaunay method (figures 10(e) and 10(f)). These two grid generation procedures are described in detail in the following sections. Finally, optional mesh smoothing (using a Laplacian operator) and edge swapping are performed. In general, edge swapping was not used for this research as it can lead to poor connectivity in the boundary layer and wake.

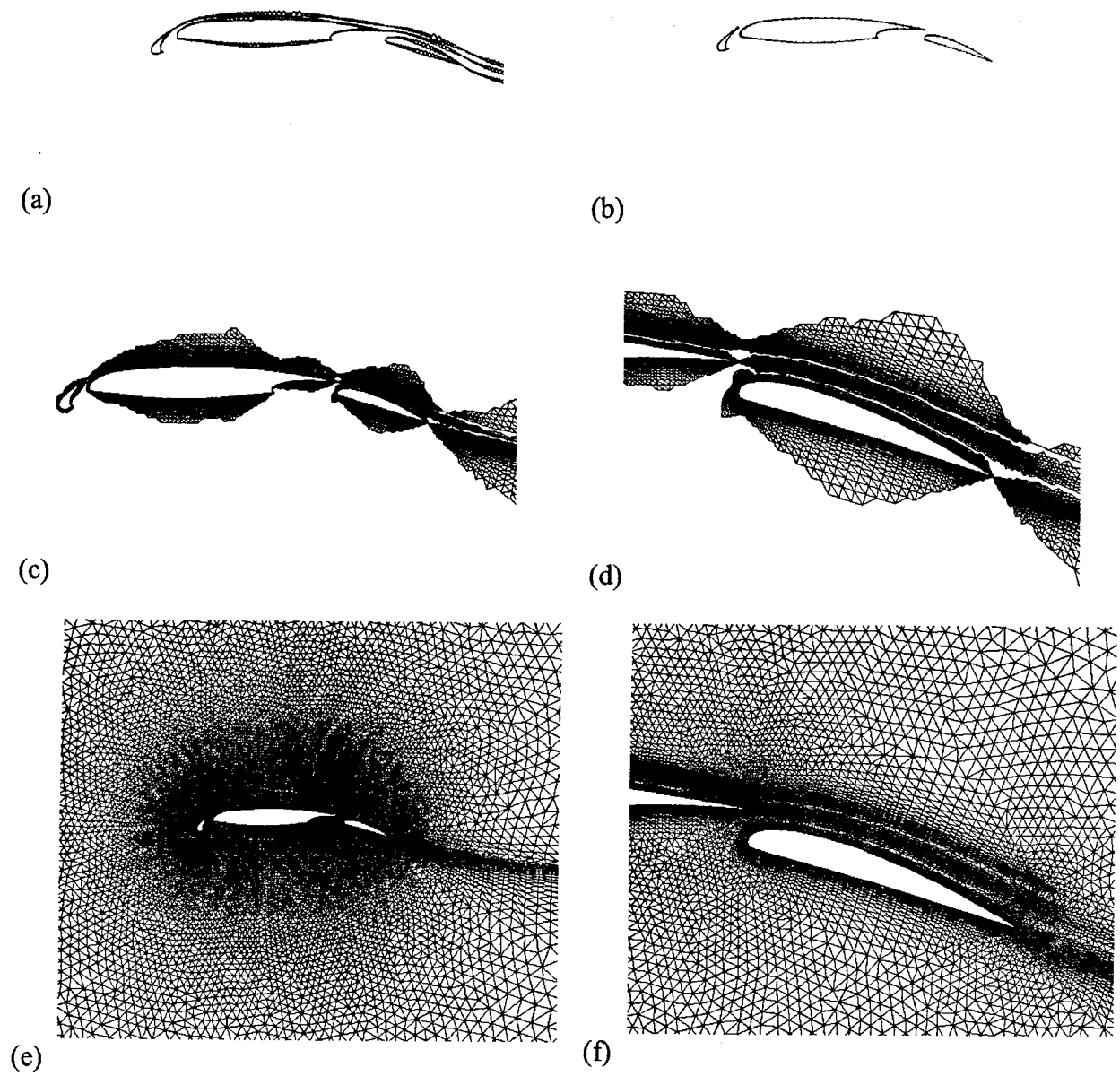

FIGURE 10. MESH GENERATION STAGES, (a) GEOMETRY, (b) SPLINE AND WAKE, (c) VISCOUS GRID (FAR FIELD), (d) VISCOUS GRID (CLOSEUP), (e) FINAL GRID (FAR FIELD), AND (f) FINAL GRID (CLOSEUP)

2.2.2.1 Commonly Used Grid Generation Techniques.

To understand the techniques used within UMESH2D, it is useful to first examine the advantages and disadvantages of the more general grid generation algorithms. Two approaches which have received much attention in the CFD community are the advancing-front and Delaunay triangulation techniques.

2.2.2.1.1 Advancing-Front Approach.

Advancing-front techniques begin with a discretization of the boundaries as a set of edges which form the initial front. An edge of the front is selected, then a new triangle is formed with this edge and a new point or an existing point on the front. The current edge is then removed from the front and the new edges are added to the front (or removed if they are hidden). The process stops when all fronts have merged and the domain is covered. New points are selected/ positioned such that the new triangle has an optimal size and shape as determined by a field function. The new point is rejected if it is located near an existing point on the front or if the resulting triangle crosses over an existing front.

The advancing-front method has many advantages. The method usually produces very high quality elements. The operations are all local in nature which reduces round-off error. Also, boundary integrity is guaranteed. Computationally the algorithm is not very complex and requires low storage since only the front is active.

There are also many disadvantages. Due to the amount of time required to check for intersections and locate near points, the algorithm is not very efficient. The method generates the grid one element at a time; whereas, it would be faster to generate one node at a time since there are roughly twice as many triangles as nodes. The method also runs into robustness problems caused by the merging fronts.

2.2.2.1.2 Delaunay Triangulation Approach.

Strictly speaking, a Delaunay triangulation is not a grid generation procedure but merely refers to a unique triangulation of a set of points which exhibits well-defined properties. The Bowyer/Watson algorithm is one of the most common sets of properties. It states that no triangle in the Delaunay triangulation can contain a point other than its own three vertices within its circumcircle. This gives rise to what is known as a point insertion scheme. This type of algorithm is useful when the mesh points have been predetermined. An initial mesh which completely covers the entire domain is created. Given this initial triangulation, new points may be inserted one at a time by locating and deleting all existing triangles whose circumcircles contain the newly inserted point. New triangles are then formed with the new point.

There are many advantages to such a scheme. It is a very simple algorithm since there are no complex data structures associated with locating neighboring points and fronts. The mesh is generated point by point, rather than one triangle at a time.

There are also some disadvantages to this type of scheme. The final mesh does not have the element quality and the grid is not as smooth as grids generated by advancing-front methods. During the insertion process, nonlocal operations may be required which can lead to round-off errors. Also, boundary integrity is not guaranteed.

2.2.2.2 Grid Generation Techniques Used in UMESH2D.

Grid generation within UMESH2D is separated into two stages. First the viscous mesh is generated, then the rest of the mesh is filled in. The algorithms used are described in the following sections.

2.2.2.2.1 Viscous Grid Generation—Advancing-Layers Method.

The first phase of the grid generation process utilizes the advancing-layers method as described by Pirzadeh [54]. This stage creates a highly stretched semistructured grid within the viscous regions around the airfoil geometry and wakes. This method is based on the advancing-front technique, and as such, it tries to keep many of the desirable features: a high degree of flexibility, robustness, and good grid quality. As in the standard advancing-front method, grid cells begin from the boundaries and march into the domain. However, unlike the conventional method where individual cells are added in no particular order, the advancing-layers method advances an entire layer at a time. This minimizes front congestion, minimizes complexity of search-and-check operations, evenly distributes cells on all solid boundaries as much as possible, provides less complicated operation, and improves efficiency.

To ensure high grid quality, new grid points are positioned along a set of predetermined vectors which are normal to the boundary surfaces. The distribution along the vectors is prescribed by a stretching function. As the positions of the new points are determined, they are added and deleted from the current front in a method which is similar to the standard advancing front. The layers continue to form and advance until two opposing fronts approach or grid quality becomes unacceptable. In order to control how far the layers advance into the field, a background spacing function is used. The advancing process for a face terminates when the local characteristics of the grid no longer match the background spacing function. The current front is then stored and used as the initial front for the next stage in the grid generation process. The grid resulting from this stage in the grid generation process is seen in figures 10(c) and 10(d). Notice that the grid has been generated around each airfoil element and the wake regions. Note that although the mesh is composed of unstructured triangular elements, the grid in this region is generated in a semi-structured manner, as is evident in the rows and columns of node points.

2.2.2.2.2 Inviscid Grid Generation—Advancing-Front Delaunay Triangulation Method.

The second phase of the grid generation process uses the method of Mavriplis. This stage creates isotropic elements within the inviscid regions of the flow field. This hybrid technique is essentially an advancing-front algorithm which adds new points ahead of the front and triangulates them using the Delaunay criterion. It therefore combines the efficiency and mathematical elegance of Delaunay triangulation with the point placement features, robustness, and boundary integrity of the advancing-front method.

Similar to the standard advancing-front technique, the current methodology begins with an initial set of edges which forms a front. An edge along the front is selected. If none of the points located on the front can combine with the selected edge to form an acceptable Delaunay triangle then a new point is created. The new point is inserted along the median of the edge at a distance which results in the desired circumradius. A field function is used to determine the maximum allowable circumradius for a triangle as a function of its position. This point is then checked to make sure that it does not lie inside an existing triangle's circumcircle or violate the boundary. If the point is acceptable then an appropriate Delaunay triangulation is formed with the surrounding points. Another edge along the front is then selected, and the process continues until the entire domain has been discretized. The resulting grid (after smoothing) is shown in figures 10(e) and

10(f). Notice the smooth transition from the highly stretched grid elements in the viscous region to the isotropic elements in the outer regions of the flow.

Overall, the two-staged approach described above creates a quality grid throughout the entire domain. The two methods are coupled together such that the semi structured mesh in the viscous region merges with the isotropic grid in the far field with a smooth transition. In many instances however, the grid generation procedure itself cannot provide adequate resolution within some of the more complex areas of the flow field. Therefore, grid adaptivity is employed.

2.2.3 Grid Adaptivity, Refinement, and Interpolation.

After an initial unstructured grid has been generated and a flow solution has been obtained on this mesh, an adaptively refined mesh can be constructed by adding new points in regions of large flow gradients and discretization errors. Figure 11 shows a closeup of the initial grid generated by UMESH2D near the quarter-round simulated ice shape for $\alpha = 0°$. Although this grid is highly refined, it was deemed insufficient with respect to the resolution of the resulting free-shear layer. Therefore, grid adaptivity was employed.

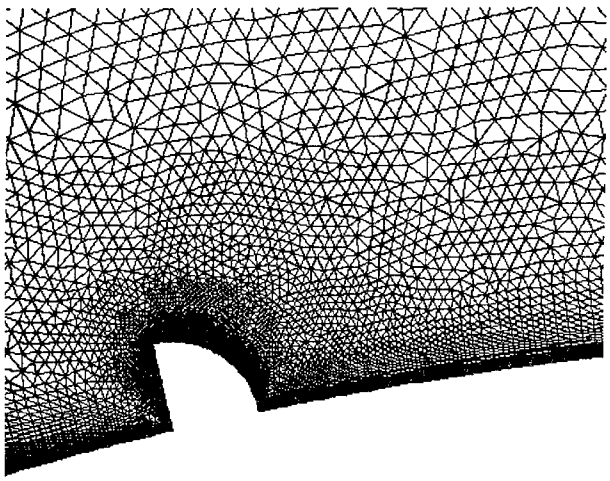

FIGURE 11. ORIGINAL GRID NEAR QUARTER-ROUND SHAPE

Solution adaptive grids are becoming increasingly common for computing complex flows. This is especially true within the finite element community due to the ease in which adaption can be performed on unstructured grids. There are three distinct methods which are commonly used to adapt the grid: r-refinement, p-refinement, and h-refinement. The simplest concept is probably refinement in which existing nodes are redistributed to more important areas. However, this method runs into some practical difficulties when dealing with highly stretch meshes. In p-refinement, the degree of the basis functions is adjusted locally to improve accuracy of the solution within regions of interest. This method is not practical for many types of problems and is, therefore, not as commonly used. The most common technique is h-refinement or mesh enrichment. In this method cells are locally subdivided or merged, and in some cases, a complete remeshing is performed to reduce the grid spacing. Regions of interest are identified by some kind of heuristic criteria such as gradients in the flow variables or an estimation of the truncation error. The third technique (h-refinement) was chosen for the current research.

Unlike most of the software used in this research, the code used to generate adaptive grids was developed in-house. The grid refinement was performed by splitting edges in regions of high flow field gradients. If the gradient of a particular flow variable was larger than some prescribed tolerance, the edge was refined by adding a new point at the midpoint of the edge. Pressure gradients render good refinement of the inviscid flow features, such as shocks and expansions. Gradients in velocity and Mach number provide good refinement of the viscous phenomena within boundary layers, wakes, and shear layers. The refinement criteria was based on a first-order approximation to the error and was calculated along each edge from the flow variable gradients within each element. The error along an edge was taken as the average of the magnitude of the gradient for the two neighboring elements multiplied by the edge length. The technique essentially subdivides the elements with the largest flow field gradients. This approach is similar to the method of Mavriplis [42] which bases refinement on the undivided difference along an edge.

Figure 12 shows the grid resulting from one adaptation based on gradients in absolute velocity. Figure 13 shows the corresponding velocity contours of the initial solution. Note that additional grid points have been clustered around the separation point and along the high-velocity gradients of the downstream free-shear layer. The adaption increased the number of grid points by approximately 25%. It should be noted that in the present methodology, elements near the airfoil and within the boundary layer are not subdivided. This was done to limit the overall number of points and still allow adequate resolution within the shear layer. All computations with ridge ice shapes presented in section 4.2 used this same adaption strategy. Using additional refinement and adaption was also investigated, but there were no significant differences in flow prediction.

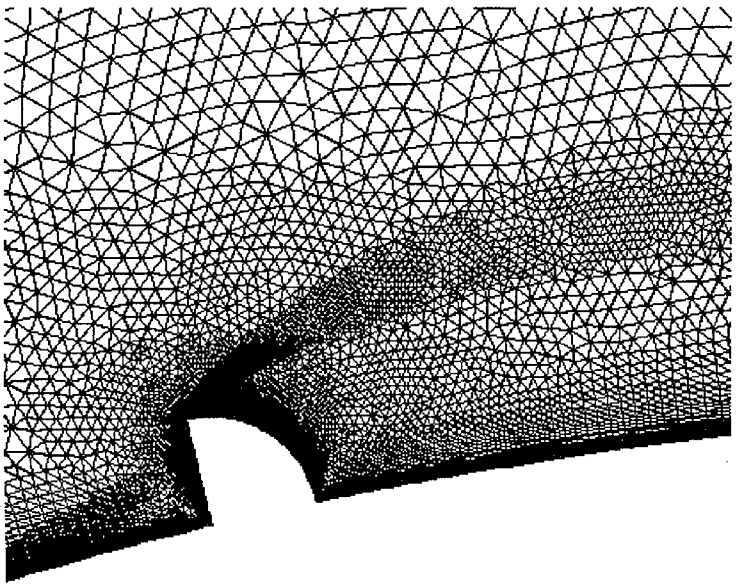

FIGURE 12. ADAPTED GRID NEAR QUARTER-ROUND SHAPE

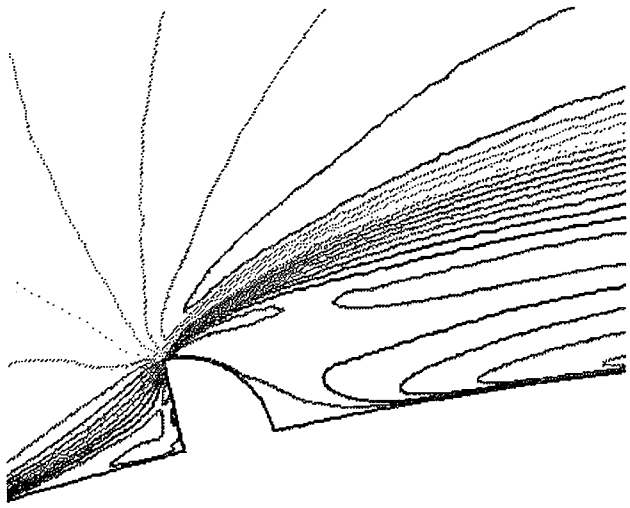

FIGURE 13. ABSOLUTE VELOCITY CONTOURS FOR ORIGINAL GRID

After the grid has been refined, a new flow field solution is obtained on the new adapted grid. To reduce the number of time cycles required for convergence, it is desirable to initialize the flow field with the previously computed solution. This is accomplished with a simple interpolation procedure from the original grid to the new grid by using shape functions. The difficulty lies in the determination of the coarse grid cell that encloses a particular fine grid node. A naïve search over all the coarse grid cells would require $O(n^2)$ operations, where n is on the order of the number of fine grid nodes and the number of coarse grid cells. This would be impractical since it would require more time to perform the search than it would take to compute the flow solution. Therefore, a more efficient search method is needed. This is accomplished in the current research by using a neighbor search. Interpolation to the adapted-grid node, N_1, is initiated by providing an initial guess, E_1, for the coarse grid element. This cell is then tested by its shape functions to see if it encloses N_1. If the test is positive, then the values at the vertices of are interpolated to N_1. If the test is negative, then the neighboring cell of E_1 with a centroid, which is closest to N_1, is the next cell tested. The algorithm then marches through the coarse grid until the enclosing cell is found. In many cases this strategy can run into problems with complex domains and boundary conditions. Therefore, the search must be checked to make sure that it is not going in circles. If this is the case, then a brute force check of all the coarse grid cells is performed for the current node. In some rare cases due to grid smoothing and point placement along the boundary, a node in the fine grid will actually lie outside the coarse grid domain, i.e., there is no enclosing cell. In this case, the closest coarse grid node is located and the flow variables are copied to the fine grid node.

2.2.4 Postprocessing and Data Reduction.

After the flow solution has been obtained, the solution is analyzed to determine the aerodynamic properties of the airfoil. The lift, drag, and moment coefficients are calculated by integrating the surface pressure and skin friction about the entire airfoil while the hinge moment coefficient is integrated about the flap only. Most experimental data presented here for comparison measure the momentum loss through the tunnel test section with a wake pressure survey to obtain the total (viscous and pressure) drag on the airfoil. The surface pressure taps are used to measure the

experimental lift and moment coefficients, and thus only include the inviscid force contributions. However, in the computational results, viscous forces are included in all force calculations. This is not expected to greatly influence the values of these coefficients. The shear stress at the wall used to calculate the skin friction is calculated using a linear approximation to the velocity derivative as determined from the first grid point normal to the airfoil surface. The reference length used to calculate the lift, drag, and moment coefficients is taken as the airfoil chord length. The hinge moment uses the flap chord length as the reference length. The pitching moments are taken about the quarter-chord location, and the hinge moments are taken about the flap's pivot location.

3. VALIDATION.

3.1 NACA 23012 COORDINATE MODIFICATION.

As stated in the previous section, the NACA 23012 airfoil that was used in this experiment did not have coordinates that are conventionally defined. The airfoil coordinates were generated through XFOIL [51] by selecting the standard NACA 23012 configuration. However, XFOIL generates thicknesses on a vertical plane instead of normal to the mean camber line, producing a small difference near the leading edge as compared to a conventionally defined NACA 23012. The result was a slightly drooped leading edge with a maximum vertical coordinate shift of 0.4% chord as compared to the conventional NACA 23012. In addition, because of errors in the manufacture of the model, the maximum was 12.2% instead of the standard 12%. The coordinates for the standard NACA 23012 and the modified NACA 23012m (as measured using a digital coordinate measurement machine) are shown in table 2. The leading edge geometry comparisons between the modified NACA 23012m and the standard NACA 23012 is shown in figure 14. Because of these differences, the airfoil model used in this study will be called NACA 23012m.

The slight change in the airfoil geometry did not significantly alter the airfoil aerodynamic characteristics. Figure 15 shows the lift curve comparison between the two airfoils. The results were obtained from XFOIL with both of the airfoils at the Reynolds number of 1.8 million. It shows nearly identical values of $C_{\ell,max}$ in the linear region of the lift curve. The NACA 23102m had a slightly higher $C_{\ell,max}$ (1.61) when compared to the standard NACA 23012 (1.57) due to increased camber.

Figure 16 shows the surface pressure distribution comparisons (again obtained using XFOIL at Re = 1.8 million). It shows nearly identical surface pressure distributions at angles of attack of 0° and 5°. At α = 5°, both the modified and the standard NACA 23012 surface pressure distributions contained a discontinuity between 15% and 20% chord which was caused by a laminar separation bubble. At α = 10° (where the lift curve started to become nonlinear), there were greater differences in the surface pressure distributions. The modified NACA 23012m airfoil had a $C_{p,min}$ of -4 while the standard NACA 23012 had a $C_{p,min}$ of -4.8. Also, the laminar separation bubble on the modified NACA 23012m is located near x/c = 0.10 while on the standard NACA 23012, it is located near x/c = 0.06. Figures 15 and 16 show that although the modification of the airfoil geometry cause changes in aerodynamic characteristics, they were not large and the distinctive aerodynamic characteristics of the NACA 23012 were maintained.

TABLE 2. STANDARD NACA 23012 AND MODIFIED NACA 23012m COORDINATES

Standard NACA 23012				Modified NACA 23012			
Upper Surface		Lower Surface		Upper Surface		Lower Surface	
x/c	*y/c*	*x/c*	*y/c*	*x/c*	*y/c*	*x/c*	*y/c*
0	0	0.00533	-0.01	0.00001	0.00037	0.00008	0
2E-04	0.00956	0.01557	-0.01	0.00011	0.00182	0.00017	0
0.006	0.0203	0.03029	-0.02	0.00094	0.00555	0.00054	0
0.019	0.03176	0.04915	-0.02	0.0017	0.00756	0.00117	-0.01
0.037	0.04324	0.07195	-0.03	0.00358	0.01142	0.00206	-0.01
0.062	0.05382	0.09868	-0.03	0.00381	0.01181	0.00337	-0.01
0.092	0.06265	0.12954	-0.03	0.00765	0.01738	0.00448	-0.01
0.127	0.06915	0.16483	-0.04	0.01109	0.02136	0.00567	-0.01
0.166	0.0732	0.20483	-0.04	0.01512	0.02536	0.00662	-0.01
0.207	0.07524	0.24869	-0.04	0.01961	0.02926	0.00716	-0.01
0.251	0.07597	0.29531	-0.04	0.02902	0.03613	0.00851	-0.01
0.298	0.07554	0.34418	-0.05	0.0347	0.03971	0.00989	-0.01
0.347	0.07402	0.39476	-0.04	0.03892	0.04217	0.01142	-0.02
0.397	0.0715	0.4465	-0.04	0.04236	0.04404	0.01308	-0.02
0.449	0.06811	0.49883	-0.04	0.05899	0.05188	0.01486	-0.02
0.501	0.06397	0.55117	-0.04	0.06478	0.05419	0.01584	-0.02
0.553	0.05924	0.60296	-0.04	0.07189	0.05679	0.02046	-0.02
0.605	0.05405	0.6536	-0.03	0.08701	0.06153	0.02497	-0.02
0.655	0.04854	0.70257	-0.03	0.09457	0.06356	0.0315	-0.02
0.704	0.04285	0.7493	-0.03	0.10486	0.06598	0.03617	-0.02
0.751	0.03712	0.7933	-0.02	0.11263	0.06757	0.04206	-0.02
0.794	0.03145	0.83407	-0.02	0.12141	0.06912	0.04908	-0.02
0.835	0.02597	0.87118	-0.02	0.12857	0.07023	0.05754	-0.03
0.872	0.02079	0.9042	-0.01	0.15473	0.07333	0.05988	-0.03
0.905	0.01602	0.93279	-0.01	0.16089	0.07388	0.06545	-0.03
0.933	0.01176	0.95661	-0.01	0.16252	0.07402	0.07327	-0.03
0.957	0.00812	0.97543	0	0.18336	0.07541	0.07788	-0.03
0.976	0.00518	0.98901	0	0.19975	0.07612	0.08615	-0.03
0.989	0.00302	0.99722	0	0.22696	0.07678	0.08891	-0.03
0.997	0.0017	0.99997	0	0.24468	0.07691	0.09796	-0.03
1	0.00126			0.26005	0.07687	0.10523	-0.03
				0.27779	0.07666	0.11551	-0.03
				0.31478	0.07576	0.11988	-0.03
				0.35461	0.07419	0.1268	-0.03
				0.37689	0.07311	0.13376	-0.03
				0.40376	0.07162	0.14312	-0.04
				0.42647	0.07021	0.15183	-0.04
				0.49844	0.06467	0.16268	-0.04
				0.55317	0.05977	0.18158	-0.04

TABLE 2. STANDARD NACA 23012 AND MODIFIED NACA 23012m COORDINATES (Continued)

Standard NACA 23012				Modified NACA 23012			
Upper Surface		Lower Surface		Upper Surface		Lower Surface	
x/c	*y/c*	*x/c*	*y/c*	*x/c*	*y/c*	*x/c*	*y/c*
				0.58462	0.05673	0.20329	-0.04
				0.60356	0.05479	0.23507	-0.04
				0.62187	0.05284	0.26035	-0.04
				0.63299	0.05162	0.33481	-0.05
				0.63913	0.05094	0.35556	-0.05
				0.64566	0.0502	0.40086	-0.05
				0.65571	0.04906	0.4402	-0.04
				0.66687	0.04778	0.47542	-0.04
				0.68282	0.04592	0.56559	-0.04
				0.70686	0.04307	0.59802	-0.04
				0.71858	0.04166	0.62621	-0.04
				0.72607	0.04075	0.66851	-0.03
				0.73215	0.04	0.69886	-0.03
				0.7452	0.03839	0.7345	-0.03
				0.74881	0.03794	0.75	-0.03
				0.8	0.03117	0.8	-0.02
				0.85	0.02425	0.85	-0.02
				0.9	0.01698	0.9	-0.01
				0.95	0.00933	0.95	-0.01
				1	0.00128	1	0

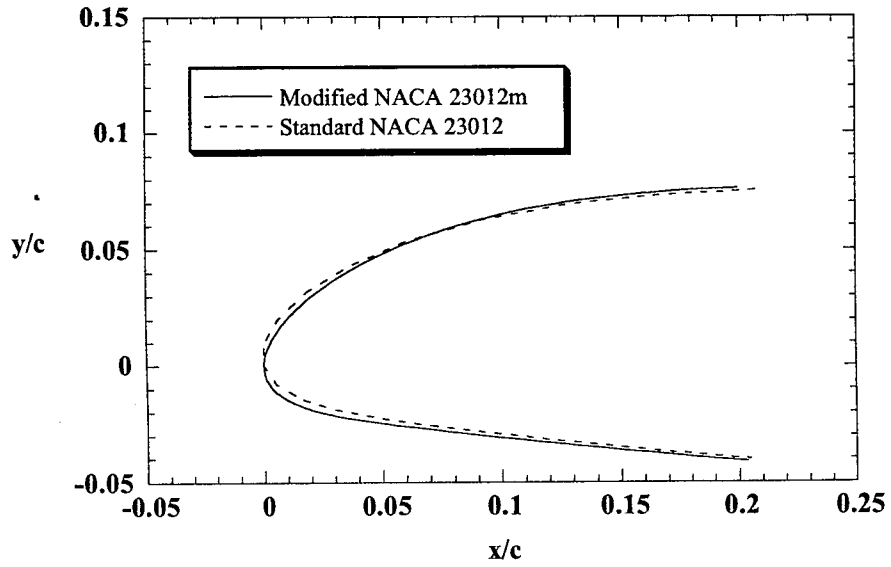

FIGURE 14. GEOMETRY COMPARISON BETWEEN MODIFIED NACA 23012m USED IN THIS STUDY AND STANDARD NACA 23012

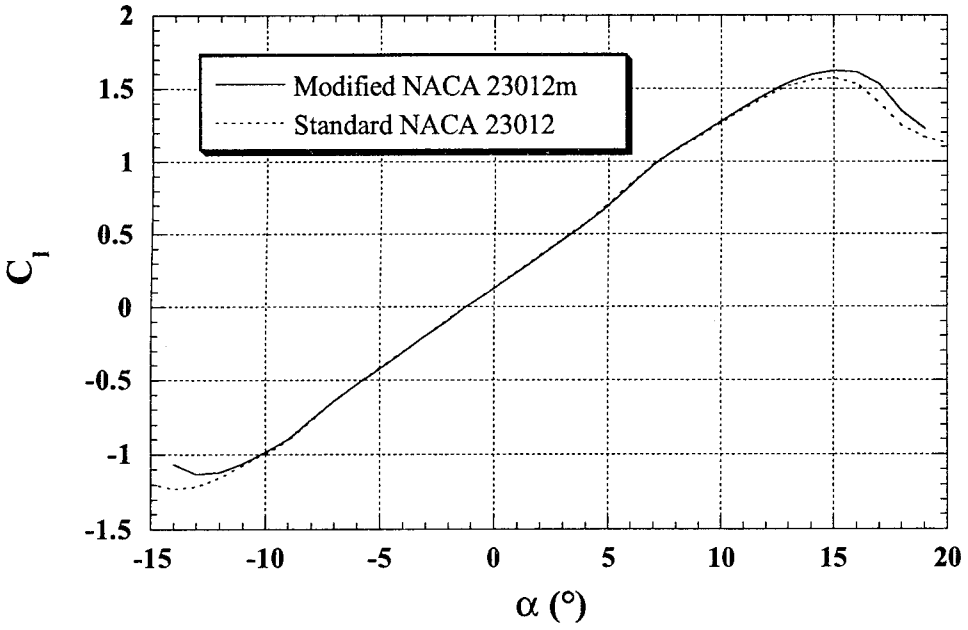

FIGURE 15. LIFT COMPARISON BETWEEN MODIFIED NACA 23012m USED IN THIS STUDY AND STANDARD NACA 23012, RESULTS FROM XFOIL, $Re = 1.8 \times 10^6$

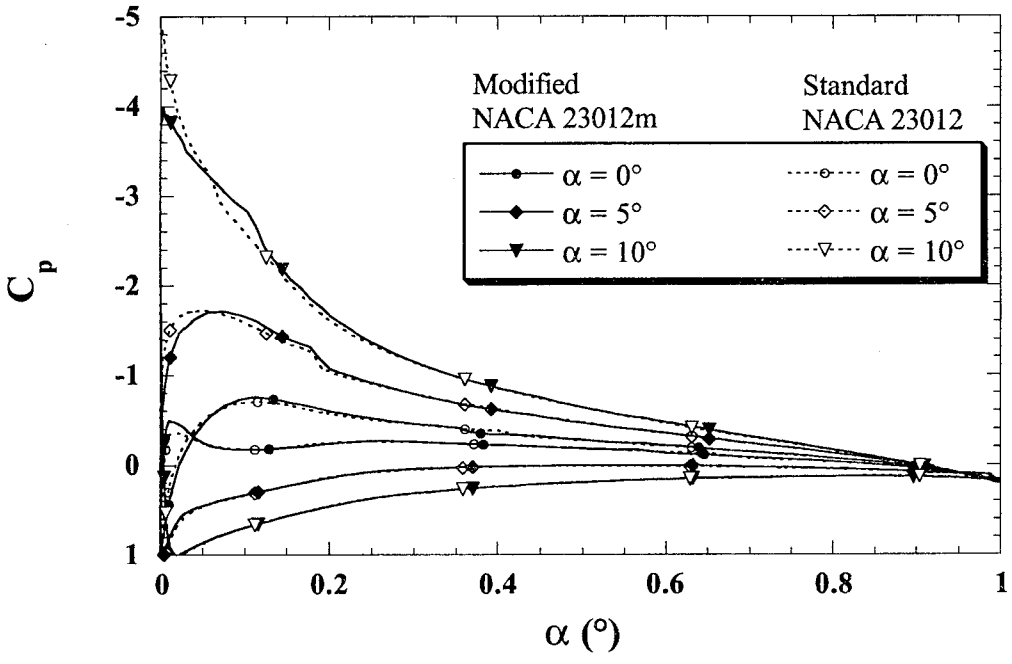

FIGURE 16. SURFACE PRESSURE COMPARISON BETWEEN MODIFIED NACA 23012m USED IN THIS STUDY AND STANDARD NACA 23012, RESULTS FROM XFOIL, $Re = 1.8 \times 10^6$

3.2 EXPERIMENTAL VALIDATION.

The clean baseline measurements were taken and compared to previously published data in order to validate the experimental apparatus and data reduction methods in figure 15. The measurements were also compared to the results from XFOIL [51], an airfoil analysis code that uses an integral boundary element method. The present UIUC data were obtained at a Reynolds number of 1.8 million. Figure 17(a) shows the lift curve comparisons, which indicate good agreement between the present UIUC experiment and Stuttgart data [55] (taken at Re = 2 million). The data of Abbott and von Doenhoff [56] showed a $C_{\ell max}$ that was approximately 8 percent higher which may have been due to their higher Reynolds number (Re = 3 million). All of the experimental data showed leading-edge stall, as expected for the NACA 23012 airfoil. XFOIL, which was not designed to predict large separated flow regions, showed a more gradual stall and a higher $C_{\ell max}$.

Figure 17(a) shows that end-wall effects were not significant as there was good agreement between the pressure data (which measured lift only near the model mid-chord) and the balance data (which measured the lift over the entire model). Had there been a significant wall-induced 3-D effect, the pressure and the balance data would have differed by a greater amount. This consistency was also verified by flow visualization, which showed that significant 3-D flow was not present until past stall. This is in agreement with the significant difference in the pressure and balance data only after stall at $\alpha = 17°$.

Figure 17(b) shows the drag comparisons. It shows slightly higher drag values for the UIUC data that may have been due to the flap gap discontinuity and leakage. Figure 17(c) shows reasonable pitching moment comparisons. No previous experimental results were found for flap hinge moment comparisons. Also, XFOIL cannot handle multielements and typically loses accuracy when predicting the thick boundary layer near the trailing edge; therefore, it was not used to generate a C_h. Thus, figure 17(d) shows only the comparison between the UIUC pressure and flap hinge balance data that agreed reasonably well.

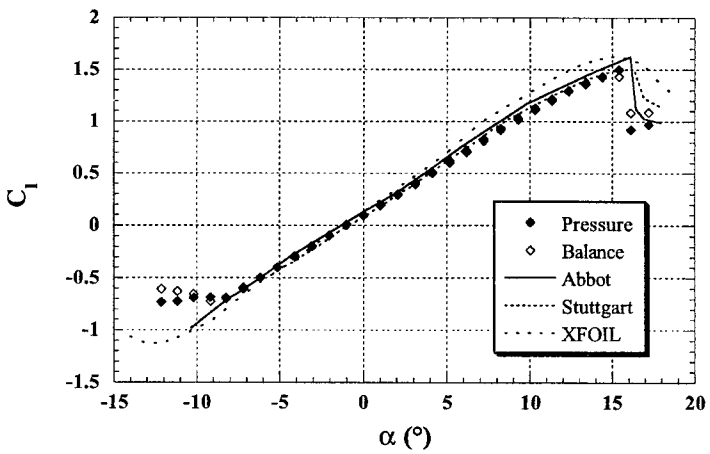

(a) Lift

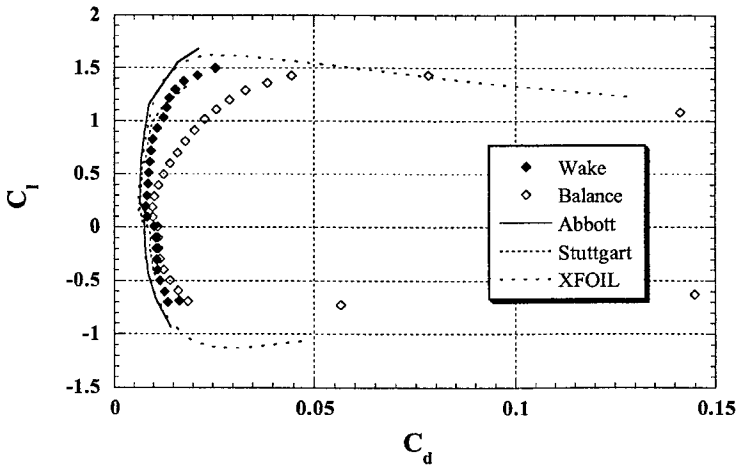

(b) Drag

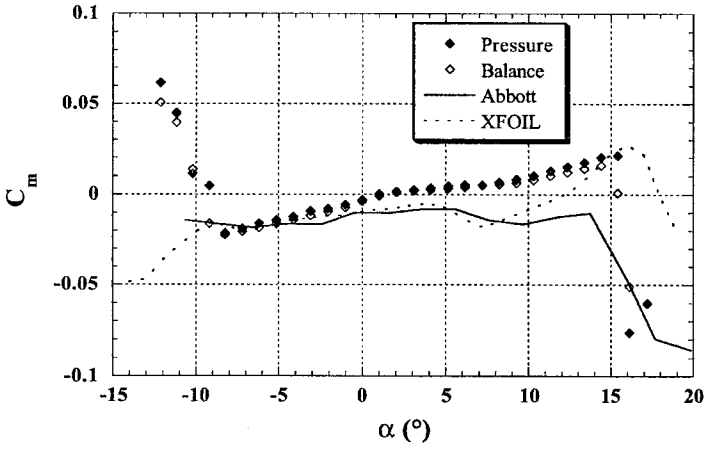

(c) Pitching Moment

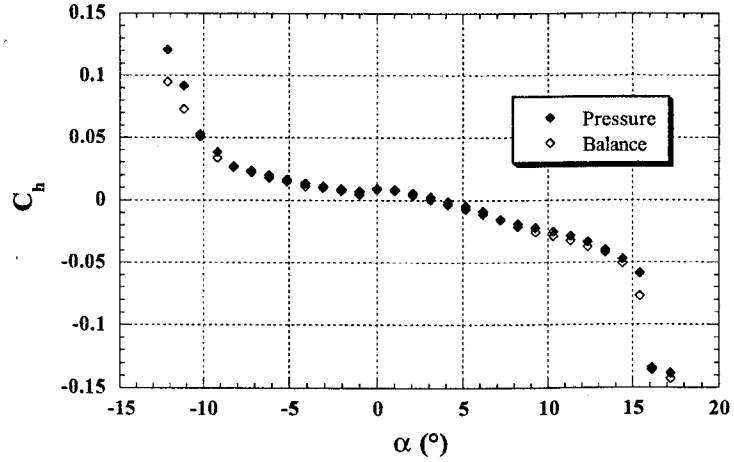

(d) Flap Hinge Moment

FIGURE 17. AERODYNAMIC COEFFICIENTS OF THE CLEAN NACA 23012m AIRFOIL
Comparisons of present UIUC data with existing data and foil numerical results.
(UIUC, XFOIL $Re = 1.8 \times 10^6$, ABBOT $Re = 3 \times 10^6$, STUTTGART $Re = 2 \times 10^6$)

Figure 18 shows the comparison between the experimental surface pressures and those predicted by XFOIL. The angles of attack for the experimental data and XFOIL were different by as much as 1°. This was done in order to match C_ℓ because XFOIL overpredicted lift, as shown in figure 17(a). At the matched lift coefficients, the surface pressure agreed reasonably well, including the location of the laminar separation bubble at $C_\ell = 0.65$ (located at $x/c = 0.19$).

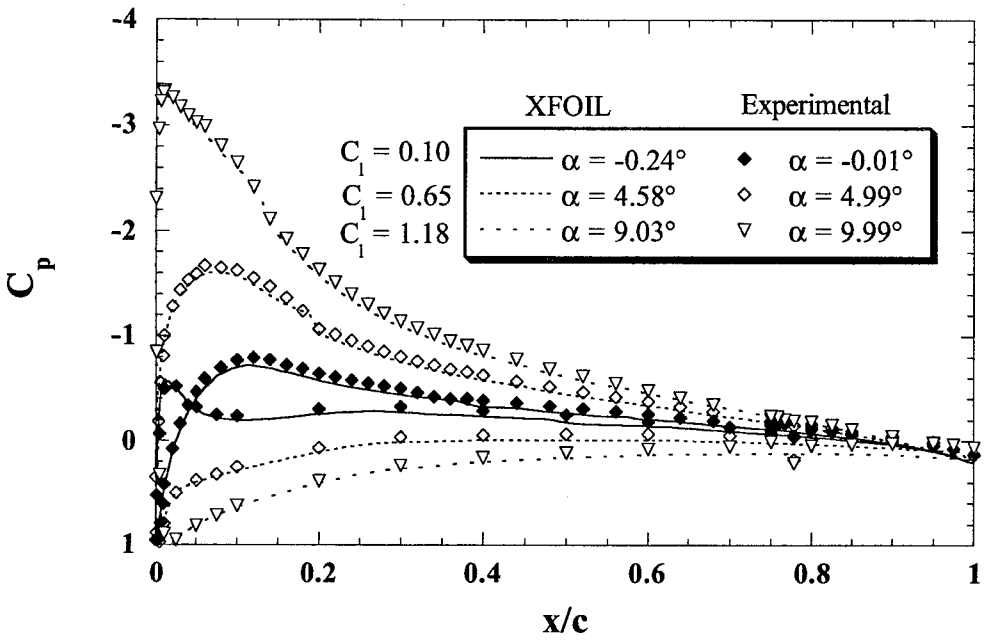

FIGURE 18. SURFACE PRESSURE OF THE CLEAN NACA 23012m AIRFOIL
Comparisons of experimental data and XFOIL at matched lift coefficients.

3.3 CODE VALIDATION.

Validation is the process of determining the degree to which a model is an accurate representation of the real world from the perspective of the intended uses of the model. The flow field about an iced airfoil contains many complicated flow features which are coupled in a very complex system. These complexities include Reynolds number effects, Mach number effects, separated flow features, adverse pressure gradient effects, etc. Therefore, it is important to understand the computational capabilities of the code with respect to predictive performance of the individual complexities of the code, with respect to predictive performance of the individual complexities of the system. Therefore, before results could be obtained for the primary icing study, a validation study was conducted to become acquainted with the code and determine the capabilities and limitations of the current computational methodology for each of the primary flow features. Once there is confidence in the solution for the individual flow physics, then the system can be analyzed as a whole more effectively and with greater confidence. In the following section, specific flow features which are consistent with the expected iced-airfoil flow field are analyzed individually and validated by comparison to theoretical or experimental data.

3.3.1 Simple Geometry Flow Simulation.

3.3.1.1 Flat-Plate Boundary Layer.

To assess the accuracy of NSU2D within the viscous regions near the wall boundaries, the code is first verified for a flat-plate boundary layer. This was done to determine an adequate level of grid resolution which was required near the airfoil surface. The NSU2D results were compared with analytical data obtained from classical incompressible flat-plate boundary layer analysis as found in White [57]. The compressible calculations were performed at a Mach number of 0.2, so compressibility effects are not expected to greatly influence the solution.

Since the code was designed to analyze airfoil configurations, the flat plate was modeled as a thin, flat airfoil. The thickness of the plate was 1% of the length, and the leading edge had an elliptical shape with an aspect ratio of 10:1. The trailing edge was modeled with a sharp drop-off. The total grid contained approximately 30,000 nodes, and the first node in the direction normal to the airfoil surface was located at approximately a y/c of 1×10^{-6} with a 15% successive increase in grid size away from the wall. This places the first grid point in the $y+ < 1$ region for the turbulent simulations performed, where yet is the nondimensional wall unit of the laminar sublayer.

The following sections present a small selection of the computations performed on the flat plate. A number of grid spacings were tested at a variety of Reynolds numbers for both laminar and turbulent flows. The results presented are considered representative of the findings.

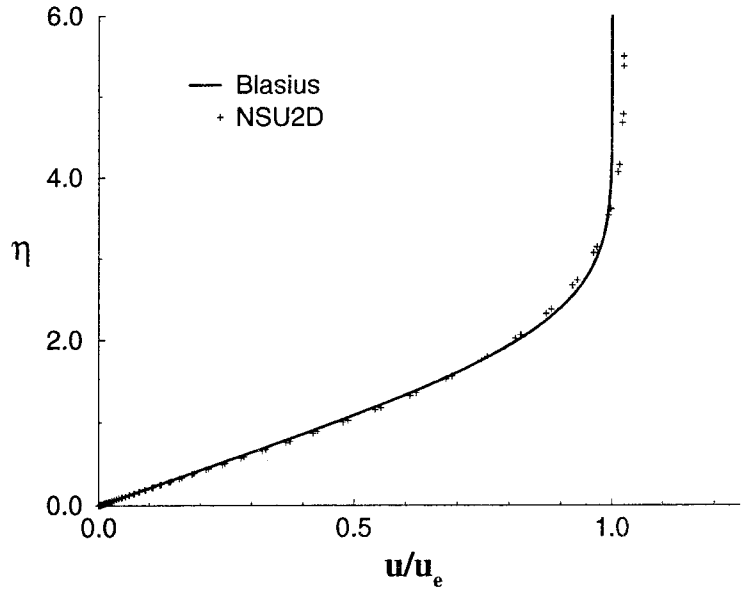

FIGURE 19. STREAMWISE VELOCITY IN LAMINAR BOUNDARY LAYER IN TERMS OF SIMILARITY COORDINATES

3.3.1.2 Laminar Boundary Layer.

The laminar boundary layer was set up such that the Reynolds number at the mid-chord of the plate was 10,000. This is a low value, but consistent with problems expecting laminar flow. Comparison of computed and *exact* boundary layer profiles is shown in figure 19 where the normalized streamwise velocity is plotted versus the similarity variable, $\eta = y\sqrt{U_\infty / (2\nu_\infty x)}$. The exact solution is given by the Blasius similarity solution [57]. Excellent agreement is observed between the computed and exact profiles, although NSU2D seems to overshoot the freestream velocity and slightly over predicts the boundary layer thickness.

3.3.1.3 Turbulent Boundary Layer.

The flat-plate turbulent boundary layer provides an excellent test of the accuracy of the turbulence model near the wall. The current test was set up such that the Reynolds number at the mid-chord of the plate was 10 million. The turbulent boundary layer is compared with the well known 1/7th power law in the outer regions of the boundary layer and the logarithmic law of the wall profile in the inner regions. Figure 20 shows the outer region velocity profile. NSU2D agreed very well with the power law theory throughout the entire profile. There was good correlation between the NSU2D predictions and the theoretical law of the wall profile. There was a slight wake in the NSU2D computations for $y^+ > 10^3$, which is consistent with experimental findings. Good agreement was found over the entire airfoil surface.

Overall, it is concluded that NSU2D adequately predicted the flow within the boundary layer over a flat plate.

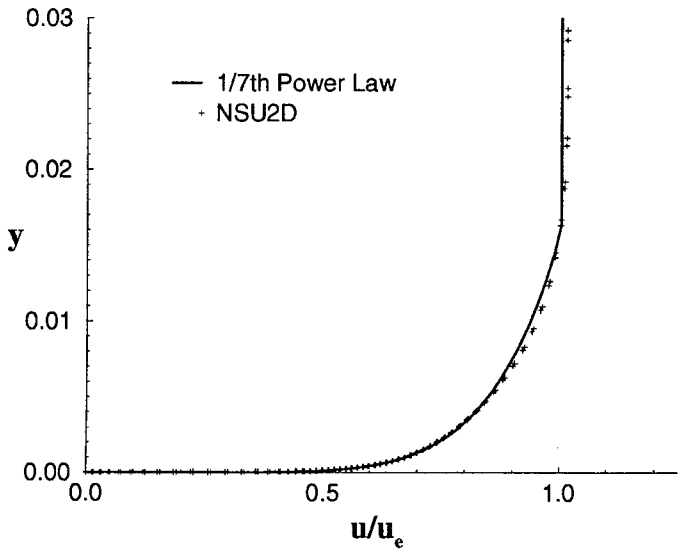

FIGURE 20. STREAMWISE VELOCITY PROFILE IN TURBULENT BOUNDARY LAYER IN TERMS OF PHYSICAL COORDINATES

3.3.1.4 Backward-Facing Step.

The ability to predict separating and reattaching shear flows is critical for accurately predicting iced-airfoil aerodynamics. The backward-facing step is one of the least complex geometries which provides this type of flow. Due to the extensive amount of experimental and computational research that has been conducted on step flows, it is an obvious choice for validation. An important aspect of an iced-airfoil flow field is the associated adverse pressure gradient throughout the separation region. To simulate this pressure gradient effect while keeping the simple geometry of the back-step, the channel wall opposite to the step can be diverged. The experimental data of Driver and Seegmiller [58] is of this form and is used herein for comparison.

Since NSU2D was designed to solve compressible flows around airfoils, conventional methods of setting up the backward-facing step problem are inconvenient. Therefore the back-step was modeled using an enclosed symmetric solid surface placed within a divergent channel. The surface was shaped to provide an upper surface back-step (as well as a lower surface back-step for flow symmetry) with long upstream and downstream extensions for boundary layer development and reattachment. The upstream length was determined such that the resulting boundary layer profile at the top of the step matched the experimental data. The solid surface was modeled with no-slip (Navier-Stokes) boundary conditions. The outside walls were modeled with slip (Euler) boundary conditions. Typical grids used for this study contained approximately 65,000 nodes. In the boundary layer normal to the solid surface, the first node was approximately at y/h of 5×10^{-4} with a 15% successive increase in grid size away from the wall.

Reattachment length was examined for prediction fidelity because it is a sensitive parameter of the flow behavior. Figure 21 plots the reattachment length versus the top-wall deflection angle, δ. Along with the experimental data, the NSU2D predictions are also compared with other computations presented by Driver and Seegmiller [58]. Overall, NSU2D appears to have reproduced the experimental reattachment lengths reasonably well, including the trend of increasing with greater pressure gradient. However, NSU2D slightly underpredicted the reattachment length as the deflection angle was increased.

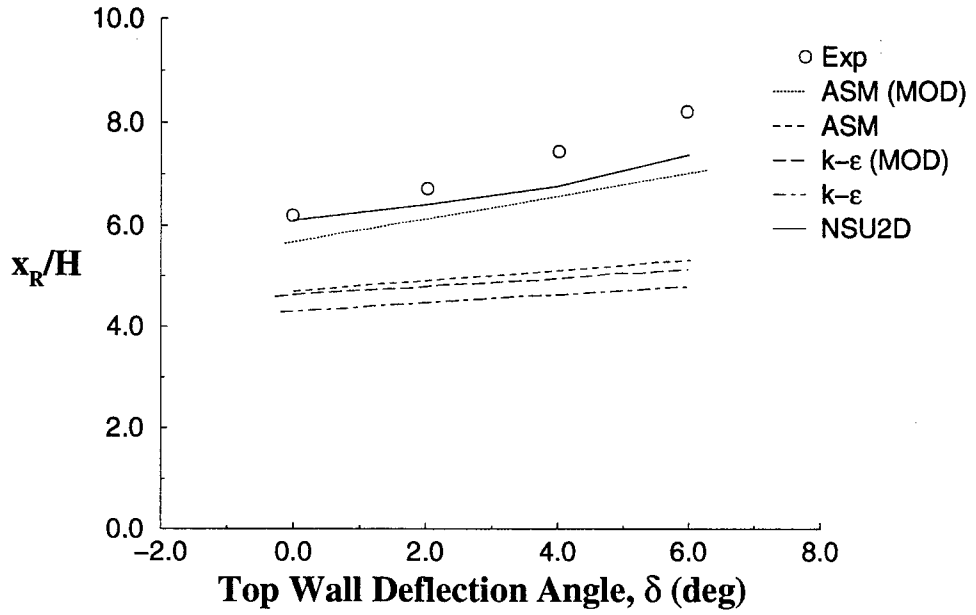

FIGURE 21. REATTACHMENT LENGTH PAST A BACKWARD-FACING STEP

Figure 22 shows the experimental and computational mean velocity profiles for a variety of streamwise positions. Results for top-wall deflection angles of 0 and 6 degrees are shown. The boundary layer ahead of the step was reasonably reproduced, indicating that the computational setup was appropriate for this problem. The general shape of the velocity profiles after the step was also well predicted. As mentioned by Driver and Seegmiller, the velocity profiles compared with the measured reattachment locations indicate that in the downstream portion of separation the flow reversal is confined to a long, thin region which cannot be resolved experimentally. This thin region of reverse flow was predicted by the current computations, although it was not adequately resolved. Far downstream of reattachment, the edge velocity of the computations was less than the edge velocity of the experiment, especially in the 6-degree deflection case. Once again, this was due to the higher numerical downstream pressure caused by the Euler boundary condition on the upper wall. Overall, NSU2D was able to reasonably predict the reattachment and flow field for the backward-facing step with a mild pressure gradient.

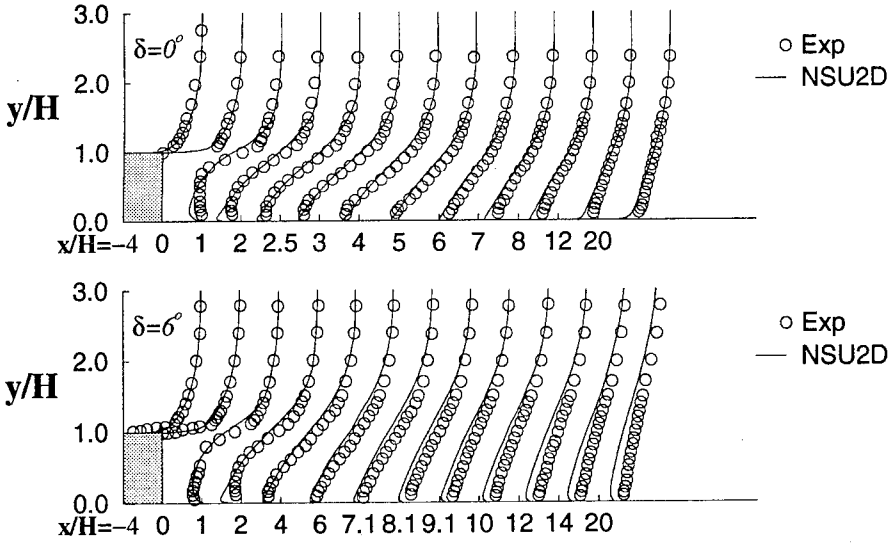

FIGURE 22. MEAN VELOCITY PROFILES PAST A BACKWARD-FACING STEP

3.3.2 Clean Airfoil Simulations.

In order to determine grid sensitivity/optimization and prediction robustness, the code was validated with some canonical experimental sets for non-iced NACA 0012 and NACA 23012 airfoils. The NACA 0012 is valuable as a standard because of the availability of both experimental and computational data for the clean and iced airfoil shapes. A standard and modified version of the NACA 23012 airfoil is also considered as it is relevant to the subject of the present investigations.

3.3.2.1 NACA 0012.

The predictions obtained from NSU2D are first compared with the experimental data of Harris [59]. This data set was chosen because of its accepted reliability [60] and due to the abundance of other CFD validations that have used the data [61]. The data were collected for a Mach number of 0.3 and a Reynolds number of 3×10^6 with transition trips placed at the 5% chord location on the upper and lower surfaces. The experimental data were corrected using the linear method for simulating wall interference provided by Harris [59].

For these simulations, the computational domain was a square region (40×40 chords) with the airfoil in the center. Far field boundary conditions were used on the outer boundary. The high-resolution grid contained approximately 50,000 nodes and 600 points on the airfoil surface. In the direction normal to the airfoil surface, there were approximately 50 nodes within the boundary layer with the first node approximately at a y/c of 2×10^{-6} and a 15% successive increase in grid size away from the wall.

3.3.2.1.1 Reynolds and Mach Number Effects for NACA 0012.

The second set of validation calculations on the NACA 0012 were intended to assess the ability of the code to predict chord Reynolds number (*Re*) and freestream Mach number (*M*) effects by comparing with the data of Ladson [62]. The tests were performed for Mach numbers of 0.15 and 0.30 and Reynolds numbers of 2, 4, and 6 million. A grid which was very similar to the one used in the previous section was used for all conditions in this study. The following data show that the code is generally able to predict trends due to both Mach number and Reynolds number variations in the aerodynamic coefficients of the non-iced NACA 0012 airfoil up to the maximum lift point.

3.3.2.1.2 Reynolds Number Effects.

The effect of Reynolds number variation on the NACA 0012 is shown in figures 23 to 25. Reynolds numbers of 2, 4, and 6 million are plotted for constant Mach number. Figure 23 shows the effects on the lift curve for Mach number 0.15. For this Mach number, we see that the code predicted the slight increases in both lift-curve slope and maximum lift for increases in Reynolds number. A similar trend was observed with Mach number 0.30. However, in all cases there was a slight overprediction of the lift, especially at the lower Mach number. Figure 24 shows the effects on drag. NSU2D reproduced the consistent decrease in drag as the Reynolds number was increased, although NSU2D overpredicted the drag at large angles of attack for the lower Reynolds numbers. Also, the computations did not predict the nonlinearity found in the experiment for Mach number 0.30 and Reynolds number 6 million. The effect of increasing the Reynolds number on pitching moment is plotted in figure 25. The very slight change in moment was predicted in the computations, although neither the computations nor the experiment revealed much influence due to variation in the Reynolds number on the pitching moment.

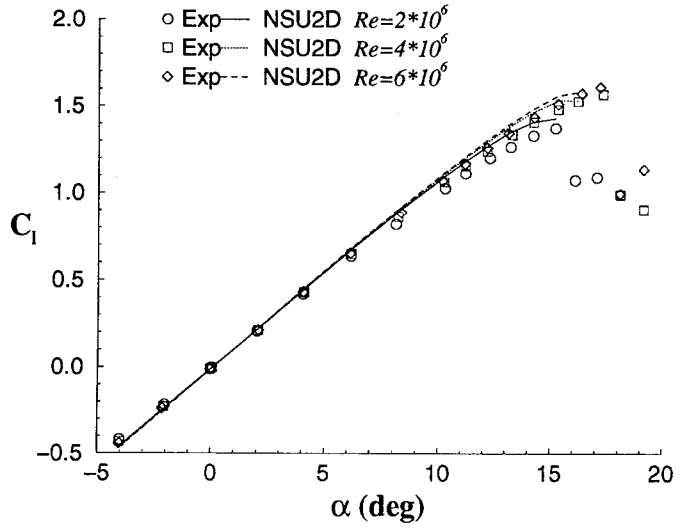

FIGURE 23. EFFECT OF VARIATION IN REYNOLDS NUMBER ON LIFT FOR A NACA 0012 AIRFOIL AT MACH NUMBER 0.15

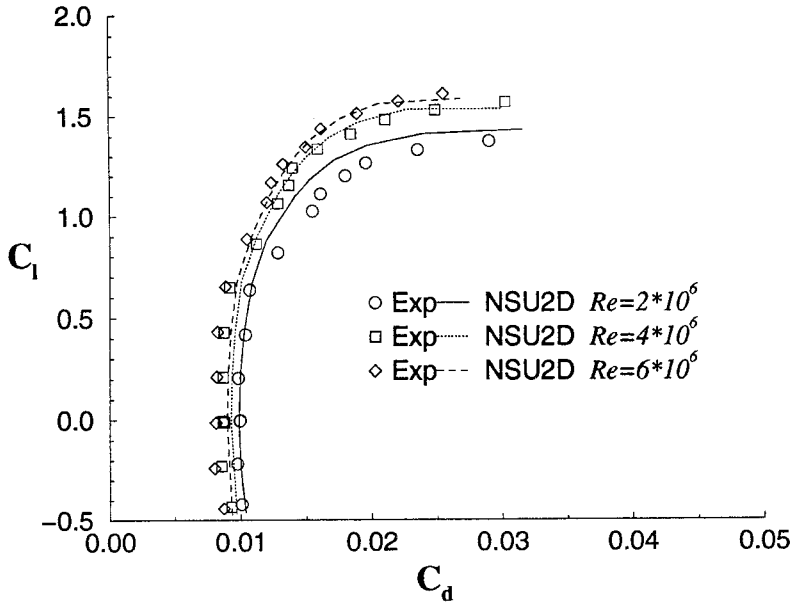

FIGURE 24. EFFECT OF VARIATION IN REYNOLDS NUMBER ON DRAG FOR A NACA 0012 AIRFOIL AT MACH NUMBER 0.15

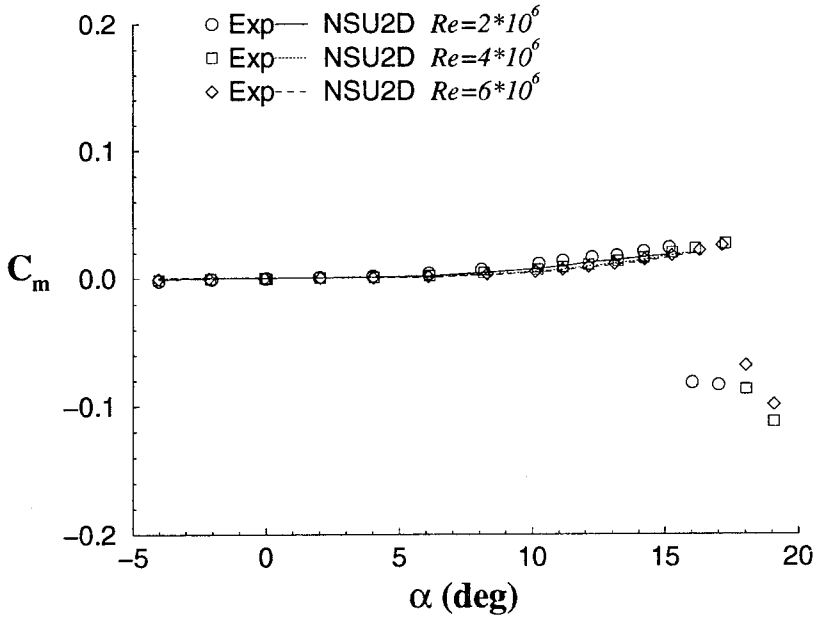

FIGURE 25. EFFECT OF VARIATION IN REYNOLDS NUMBER ON PITCHING MOMENT FOR A NACA 0012 AIRFOIL AT MACH NUMBER 0.15

3.3.2.1.3 Mach Number Effects.

The effect of Mach number variation on the NACA 0012 was studied for Mach numbers of 0.15 and 0.30 for constant Reynolds number. Only results for Reynolds number 6 million are shown in figures 26 to 28. Figure 26 shows the effects on the lift curve for Reynolds number 6 million. The figure reveals that the computations successfully predicted both the slight increase in slope and the significant decrease in maximum lift for an increase in Mach number. The effect on drag is plotted in figure 27. Most of the change in drag caused by Mach number variations occurred at the upper angles of attack and was a result of the decrease in stall angle as the Mach number was increased. This was predicted in the computations. However, for low angles of attack, the computations predicted a slight decrease in minimum drag; whereas, the experiment revealed very little Mach number dependence at these angles. Figure 28 plots the change in pitching moment. The computations accurately predicted the increase (nose up) in pitching moment with an increase in Mach number. This is again attributed to the early stall for high Mach numbers.

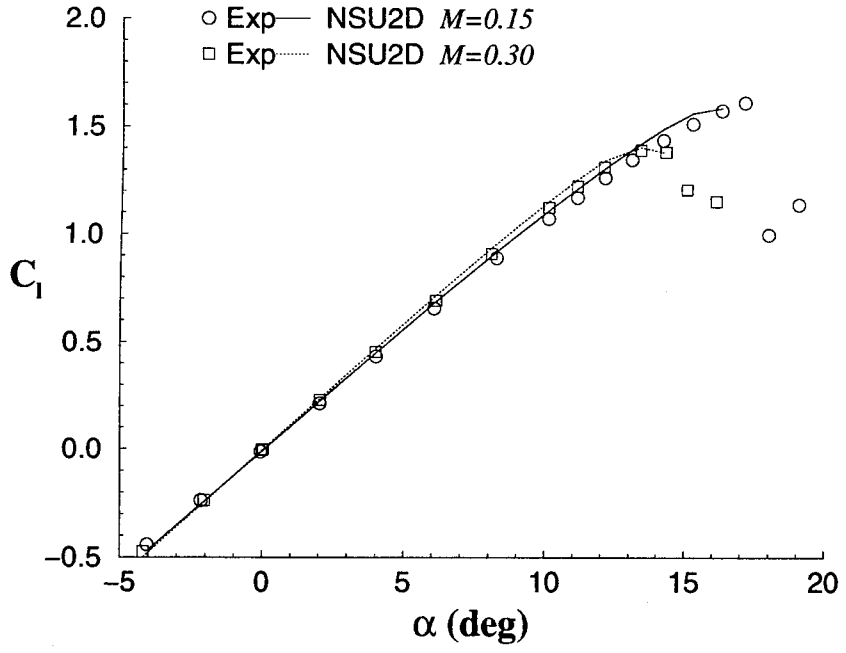

FIGURE 26. EFFECT OF VARIATION IN MACH NUMBER ON LIFT FOR A NACA 0012 AIRFOIL AT REYNOLDS NUMBER 6 MILLION

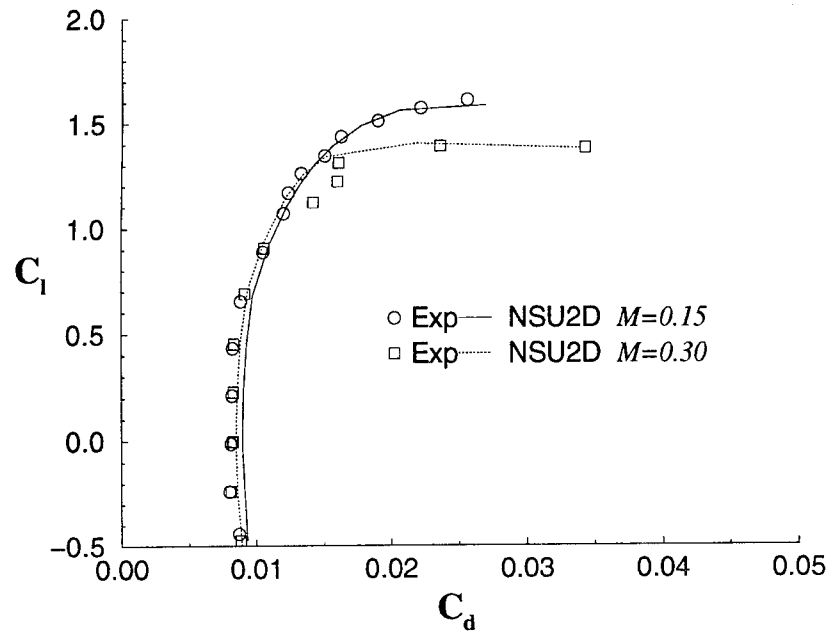

FIGURE 27. EFFECT OF VARIATION IN MACH NUMBER ON DRAG FOR A NACA 0012 AIRFOIL AT REYNOLDS NUMBER 6 MILLION

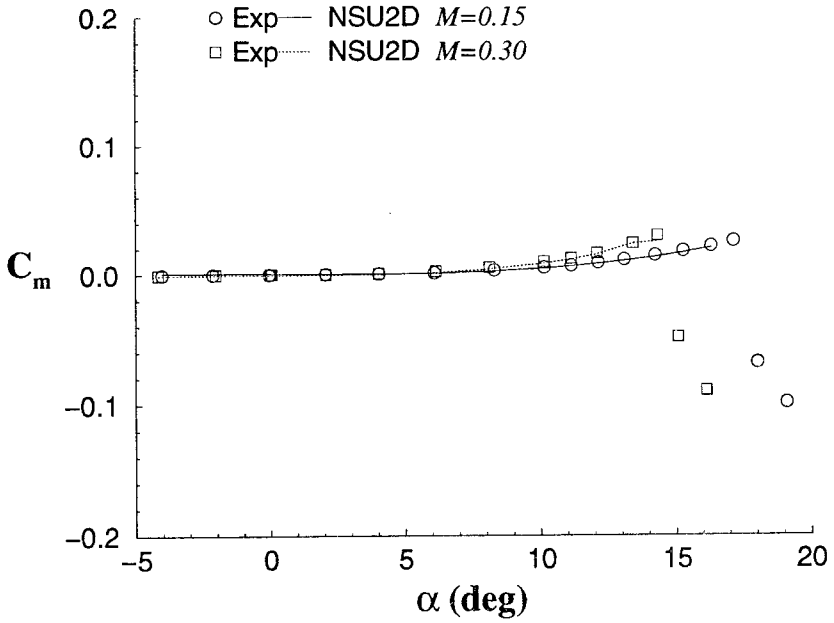

FIGURE 28. EFFECT OF VARIATION IN MACH NUMBER ON PITCHING MOMENT FOR A NACA 0012 AIRFOIL AT REYNOLDS NUMBER 6 MILLION

3.3.2.2 NACA 23012.

Validation of the code was also investigated with the NACA 23012 airfoil data set of Stuttgarter Profilkatalog I [55]. The measurements give the lift coefficient as a function of the angle of attack and the drag coefficient. Computational setups similar to those used for the above NACA 0012 cases were used. No transition trips were used in the experimental study, therefore the transition location predicted by XFOIL was used for all angles of attack. Figures 29 and 30 show lift and drag comparisons, at angles of attack ranging from -4 to 16 degrees, with a Mach number of 0.13 and a Reynolds number of 1.5 million. Figure 29 shows that NSU2D provided reasonable agreement for the airfoil lift but slightly overpredicted the lift curve slope. The angle of attack at maximum lift was also well predicted. The relation between the lift and drag coefficients shown in figure 30 indicates NSU2D generally provided good predictions of the Stuttgart experimental drag measurements. However, the drag was slightly underpredicted at the upper angles of attack which may have been due to inaccuracies in the XFOIL predicted transition point. Thus, the code reasonably characterized the aerodynamic features up to the point of maximum lift for the non-iced NACA 23012 airfoil.

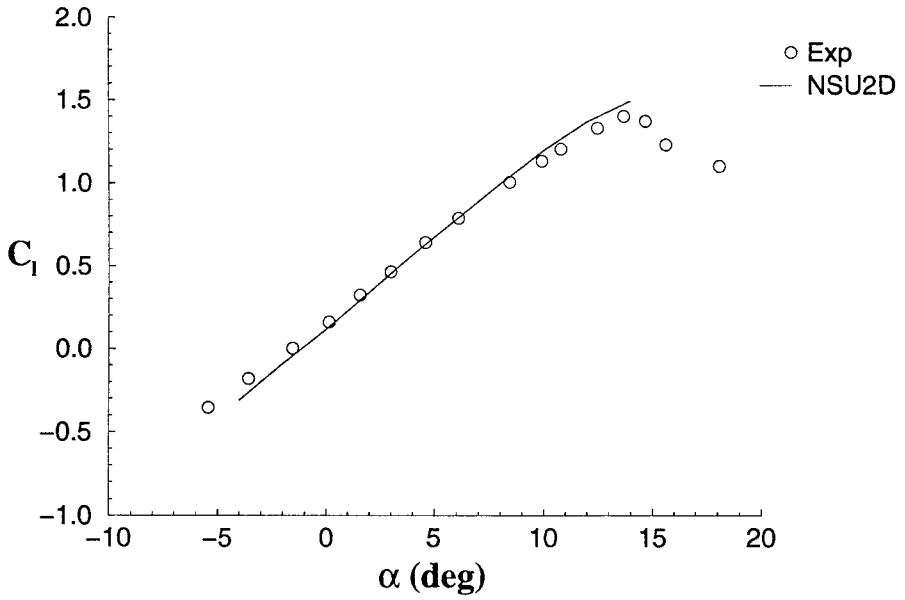

FIGURE 29. LIFT COEFFICIENTS FOR A NACA 23012 AIRFOIL

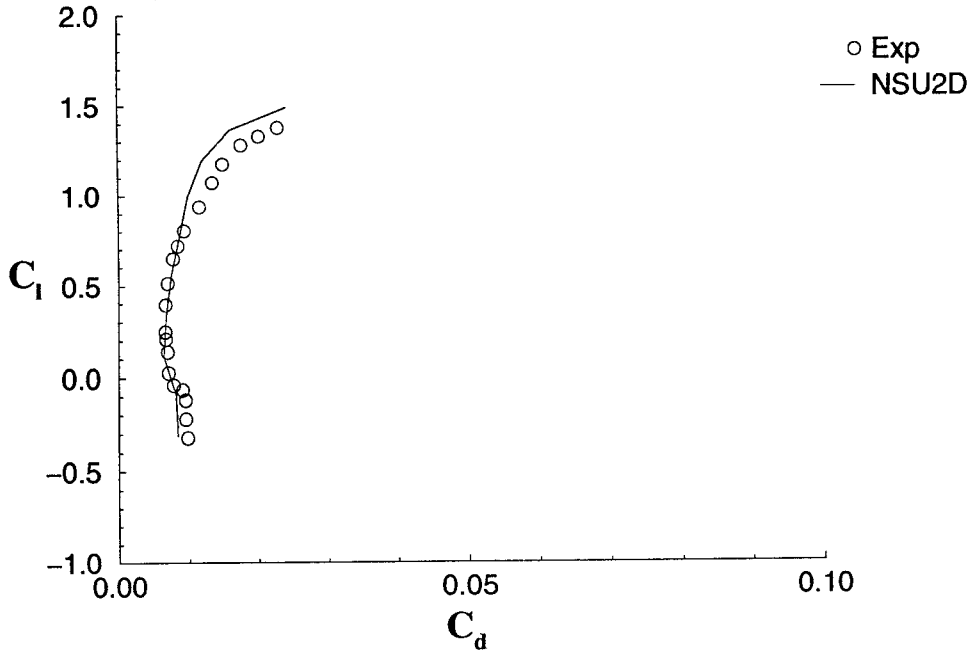

FIGURE 30. DRAG COEFFICIENTS FOR A NACA 23012 AIRFOIL

3.3.2.3 NACA 23012m With an Undeflected Flap.

The primary airfoil for the icing investigation was a modified version of the NACA 23012 with a 25 % chord simple flap. Therefore, simulations of the clean configuration (with boundary layer trip) for this model will be tested first. The NACA 23012 airfoil was chosen because it has aerodynamic characteristics that are typical of the current commuter aircraft fleet. Along with the addition of the simple flap, the actual airfoil tested had a few modifications from the standard NACA 23012. Refer to section 3.1 for the detailed explanation of the modifications to NACA 23012. Due to the variations, this model will be referred to as the NACA 23012m airfoil.

The predictions obtained from NSU2D are compared with the experimental data of Lee and Bragg [29]. The data were collected for a Mach number of 0.2 and a Reynolds number of 1.8×10^6 with transition trips placed at the 2% chord location on the upper surface and 5% on the lower surface. The experimental data have been corrected for wall interference.

Due to the added complexity of the flap element, the computational domain required slightly increased grid resolution. For these simulations, the computational domain was a square region, 50×50 chords, with the airfoil in the center. This domain is shown in figure 31. Far field boundary conditions were used on the outer boundary. The high-resolution grid contained approximately 70,000 nodes with 900 points distributed along the surface of the two elements. In the direction normal to the airfoil surface, the first node was located at approximately a y/c of 2×10^{-6} with a 15% successive increase in grid size away from the wall.

(a)

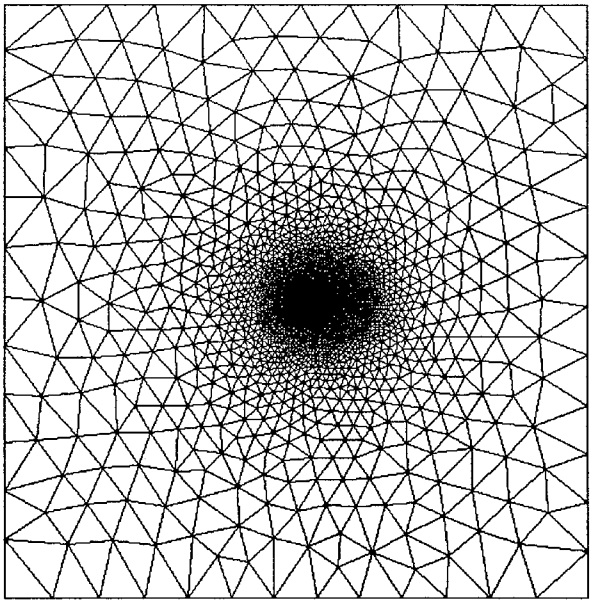

(b)

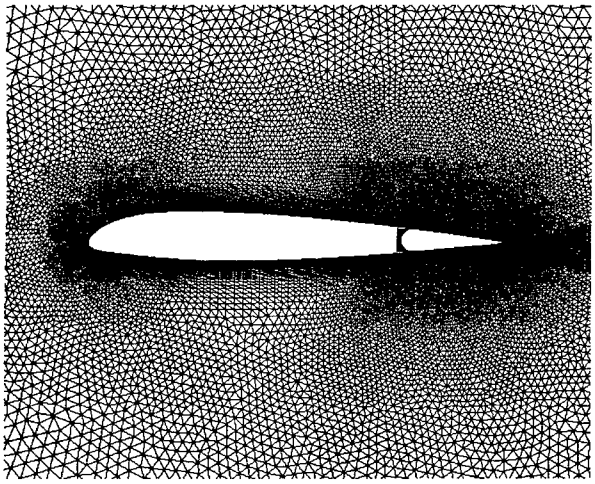

(c)

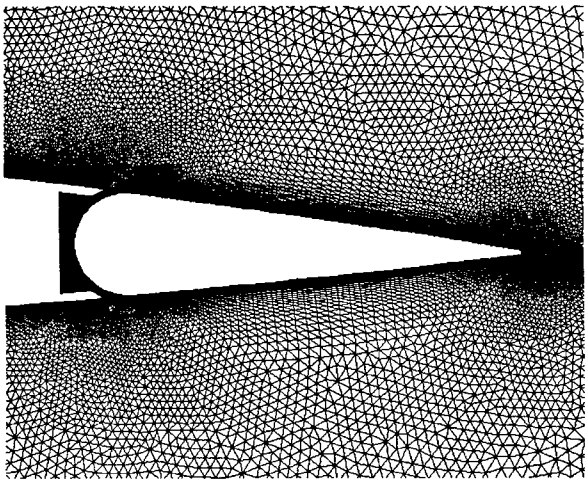

FIGURE 31. MESH FOR NACA 23012m, (a) FAR FIELD, (b) CLOSEUP, AND (c) FLAP

The condition of the flow through the flap gap (laminar, turbulent, or transitional) is difficult to judge because it contains two thin channels surrounding a cavity (figure 31) and can be subjected to a variety of pressure differences and Reynolds numbers. Fortunately, for cases with no flap deflection, only small changes were found if the gap was modeled as turbulent or laminar. Therefore, the region was always modeled as fully turbulent. However, it was noted that there was significant sensitivity of the flow solution to the width of the thin channel, where velocities of more than one-half of the freestream velocity can be found. This was unfortunate since the experimental setup made accurate measurement of the gap thickness difficult and there may have been some spanwise variation as well. Therefore, it is expected that some of the variation between the clean airfoil predictions and the experimental data was caused by an inaccurate geometry definition around the flap gap. However, this is not expected to have had a large effect on the iced airfoil predictions since no flap deflection cases were considered and the pressure gradient across the flap gap (from the upper to lower surfaces) was very small compared with that of the clean airfoil.

Figures 32 through 35 plot the aerodynamic coefficients for the clean NACA 23012m. Figure 32 shows the variation of lift coefficient as a function of angle of attack. In general, the NSU2D predictions exhibited good comparison with the experimental results, although the slope of the lift curve and maximum lift coefficient were overestimated. This is similar to the prediction of the low Reynolds number cases in the earlier validation studies (figures 23 and 29). A portion of this discrepancy can be attributed to the aforementioned difference in flap gap geometry between the experiment and computations. Additional discrepancies may be attributed to the difficulties associated with accurately measuring the dynamic pressure within the experiment. Figure 33 shows the drag predictions. The slight underprediction of the drag coefficient at higher lift conditions is also consistent with earlier validation computations. The coefficient for pitching moment is seen in figure 34 as a function of angle of attack, where close agreement between the predictions and the experiments is seen. The wall corrections were performed using classical methods. These methods are widely used, but known to have limitations and are unable to correct for all wall interference effects. Finally, the flap hinge moment was investigated as it is an important parameter with respect to aircraft control. NSU2D accurately predicted this coefficient as seen in figure 35.

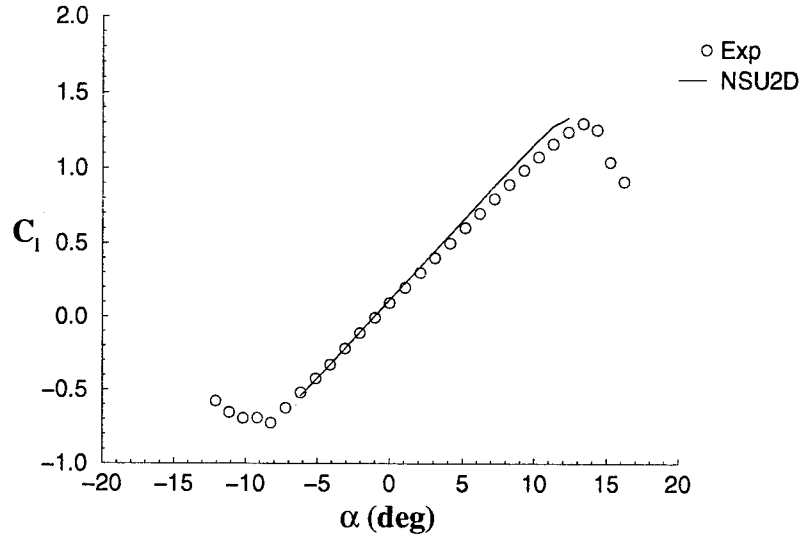

FIGURE 32. LIFT COEFFICIENTS FOR A NACA 23012m AIRFOIL

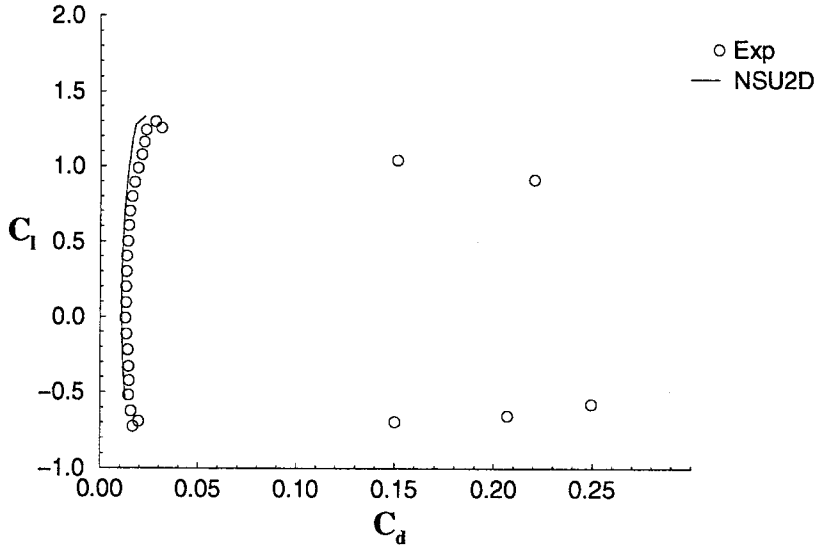

FIGURE 33. DRAG COEFFICIENTS FOR A NACA 23012m AIRFOIL

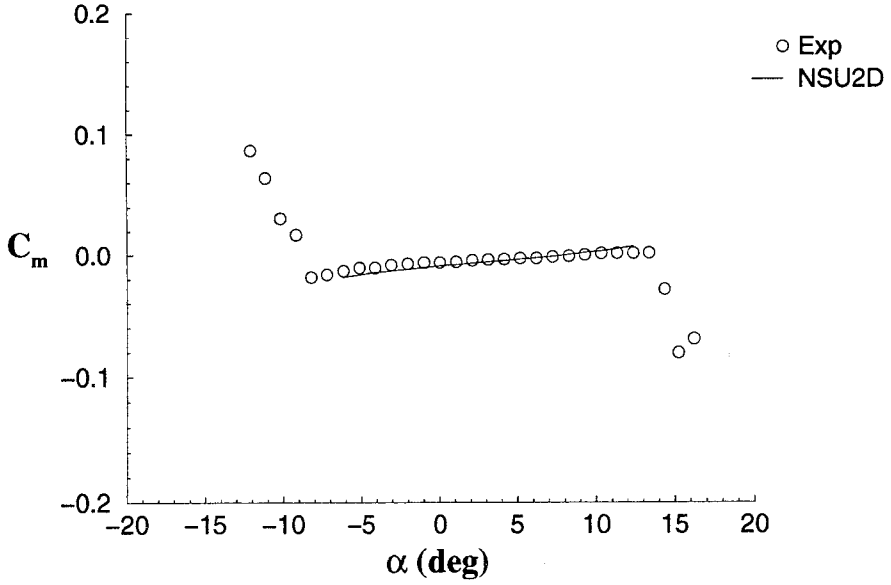

FIGURE 34. PICTCHING MOMENT COEFFICIENTS FOR A NACA 23012m AIRFOIL

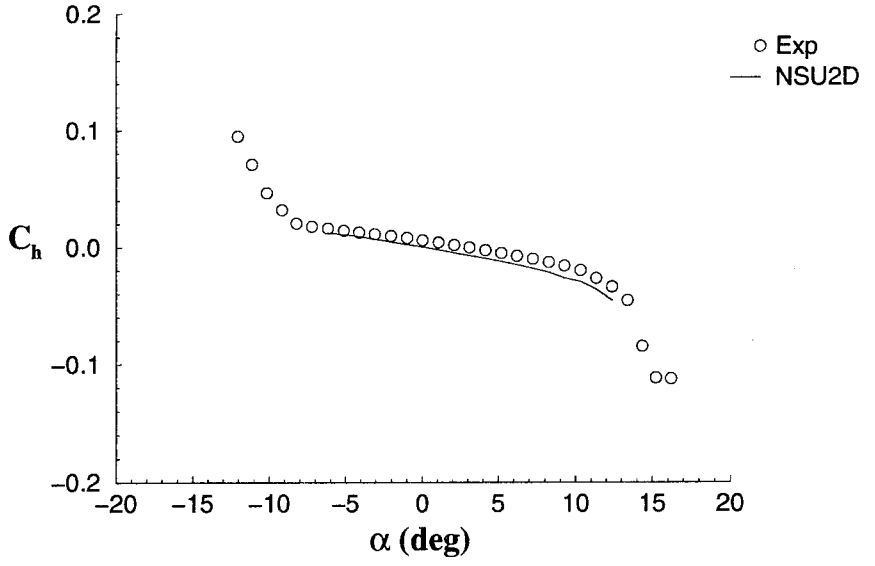

FIGURE 35. HINGE MOMENT COEFFICIENTS FOR A NACA 23012m AIRFOIL

Figures 36 and 37 show the surface pressure distribution for $\alpha = 4.14°$ and $\alpha = 12.36°$ respectively. The predictions for the low angle of attack generally showed good agreement about the entire surface. For the larger angle, NSU2D overpredicted the suction peak resulting in overpredicted lift.

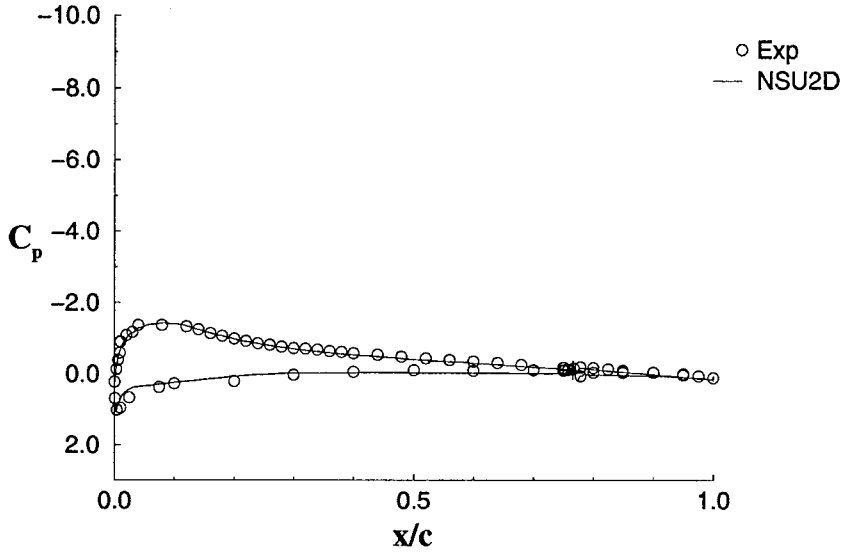

FIGURE 36. SURFACE PRESSURE DISTRIBUTION FOR A NACA 23012m AIRFOIL AT $\alpha = 4.14°$

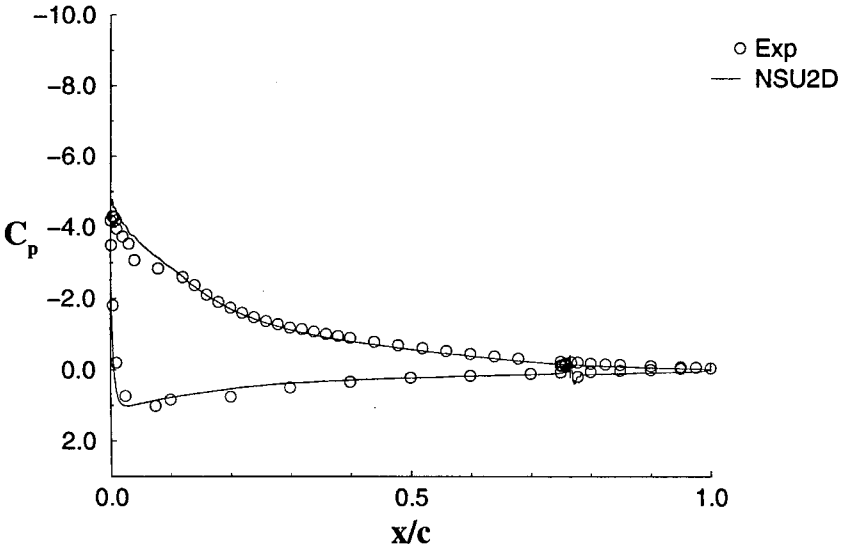

FIGURE 37. SURFACE PRESSURE DISTRIBUTION FOR A NACA 23012m AIRFOIL AT $\alpha = 12.36°$

3.3.2.4 NACA 23012m With Tunnel Walls.

For the present icing study, it was desired to employ a grid which formally included tunnel-wall effects. Therefore, the validation tests for the NACA 23012m were rerun with the upper and lower tunnel walls directly modeled within the computation. The tunnel height was 2.67 times the airfoil chord, and the model was placed slightly off the tunnel center line. The model was pivoted about its quarter-chord location. The tunnel walls were modeled with slip (Euler) boundary conditions, and the tunnel inlet and outlet were modeled as far-field boundaries. Due to the additional node points required along the outer boundary, a larger grid was used than in the earlier tests. The grid contained approximately 90,000 nodes with 1000 points distributed along the surface of the airfoil and approximately 500 points along the outer walls. The spacing of the first grid point normal to the airfoil surface was approximately 1×10^{-6} chord lengths with a 15% successive increase in grid size away from the wall. Since the tunnel walls must be parallel to the flow direction, each angle of attack required a separate grid. Rather than rotating the airfoil to change the angle of attack, the outer boundary was rotated. The grid used for $\alpha = 10.0°$ is given in figure 38.

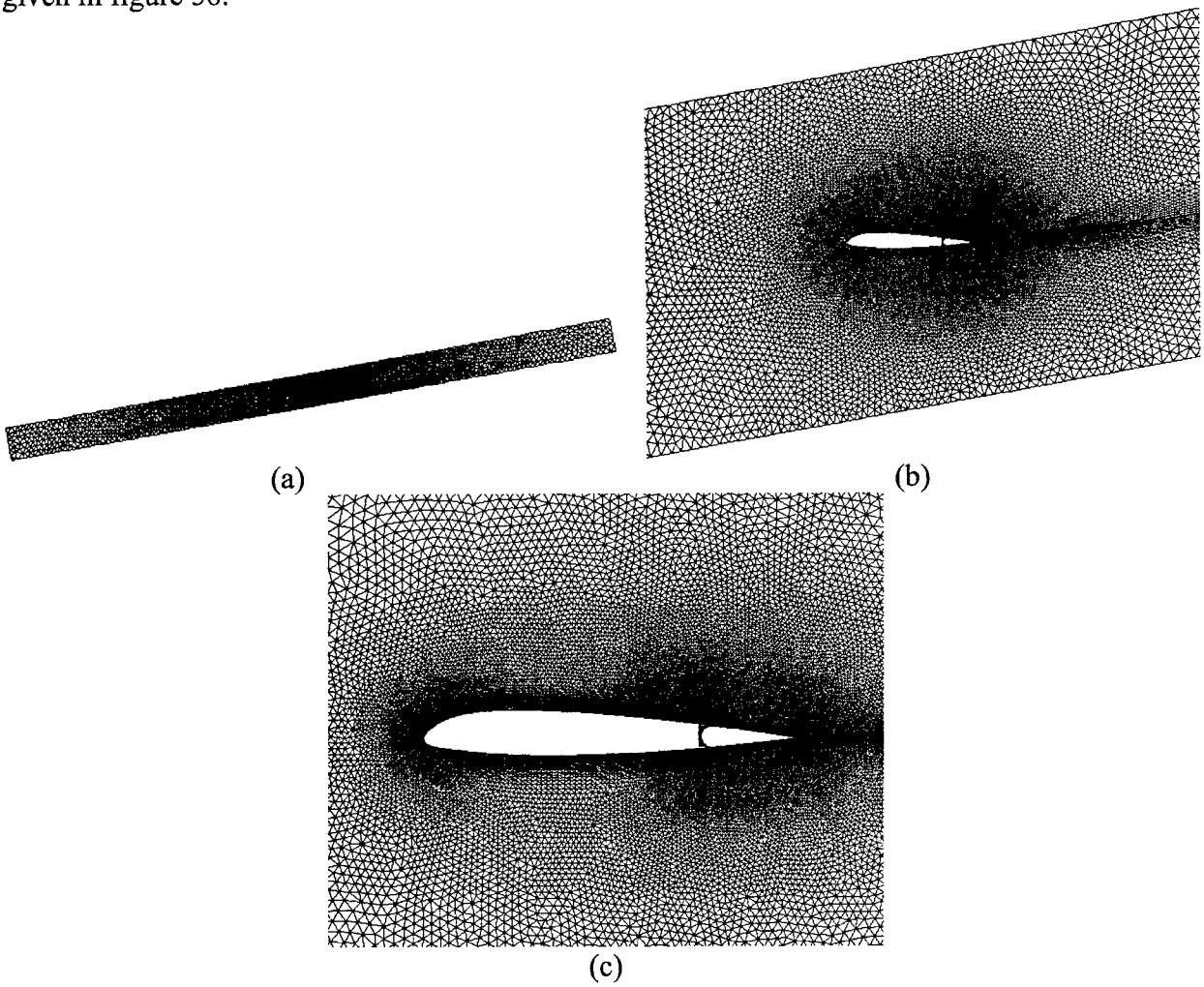

FIGURE 38. MESH FOR NACA 23012m IN TUNNEL AT $\alpha = 10.0°$, (a) OUTER BOUNDARY REGION, (b) FAR FIELD, AND (c) CLOSEUP

To verify this approach for NSU2D, the earlier simulations using free boundary conditions in the far field were compared with simulations where the tunnel walls were modeled directly. The aerodynamic coefficients computed in the simulations with tunnel walls were theoretically corrected *a posteriori* to an infinite domain using the theory of Rae and Pope [36]. These comparisons are found in figures 39 through 42. There was very little variation between the results obtained from the two simulation methods for lift (figure 39) and drag (figure 40), in fact the curves are barely distinguishable. However, the pitching moment (figure 41) did not have as good agreement. Simulating the tunnel walls predicted a curve which was much more flat than the computations without walls. It is assumed that this variation is caused in part by the inaccurate assumptions associated with using linear theory to determine the influence of tunnel walls. The two methods provided decent agreement for the hinge moment (figure 42), although the theoretical correction suffers from the same inadequacies as the pitching moment correction. Therefore, it is felt to be important to model tunnel walls directly when investigating aerodynamic moments.

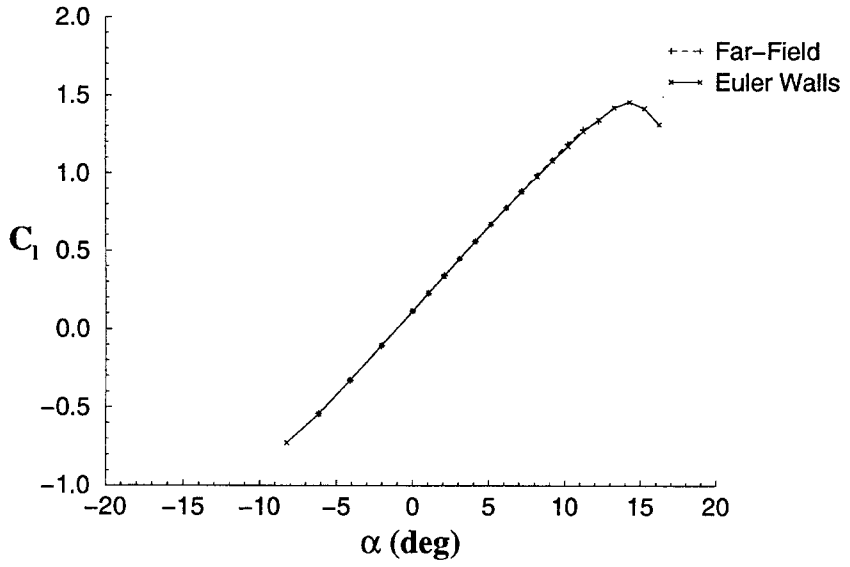

FIGURE 39. LIFT COEFFICIENTS FOR A NACA 23012m AIRFOIL MODELED FOR TWO METHODS (1) EULER-WALLS WHERE THE TUNNEL WALLS (AND CORRECTED USING THE THEORY OF RAE AND POPE) AND (2) FAR FIELD WHERE THE AIRFOIL WAS SIMULATED WITHOUT TUNNEL WALLS

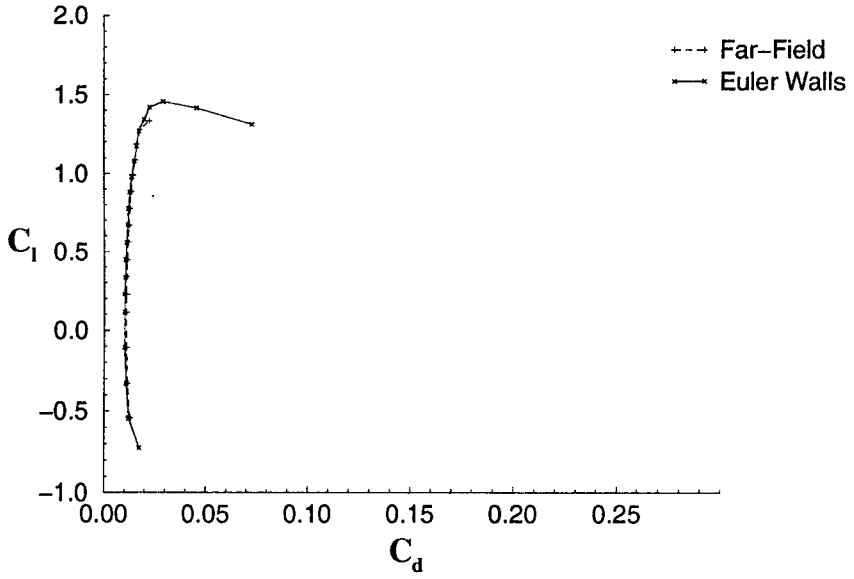

FIGURE 40. DRAG COEFFICIENTS FOR A NACA 23012m AIRFOIL MODELED WITH TUNNEL WALLS WERE SIMULATED DIRECTLY AND SUBSEQUENTLY CORRECTED USING THE THEORY OF RAE AND POPE TO FREE FLIGHT CONDITIONS AND FAR FIELD WHERE THE AIRFOIL WAS SIMULATED WITHOUT TUNNEL WALLS

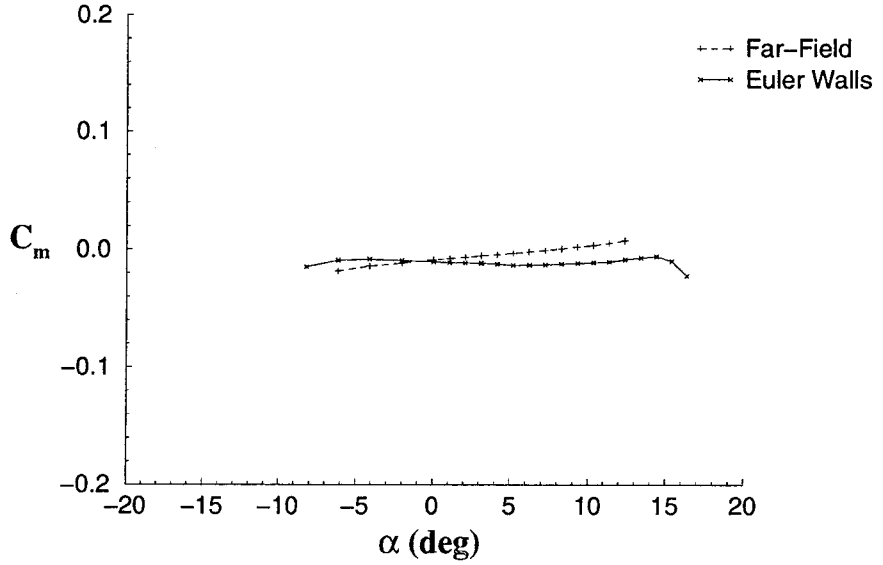

FIGURE 41. PITCHING MOMENT COEFFICIENTS FOR A NACA 23012m AIRFOIL MODELED WITH TUNNEL WALLS (AND CORRECTED USING THE THEORY OF RAE AND POPE) AND WITHOUT TUNNEL WALLS

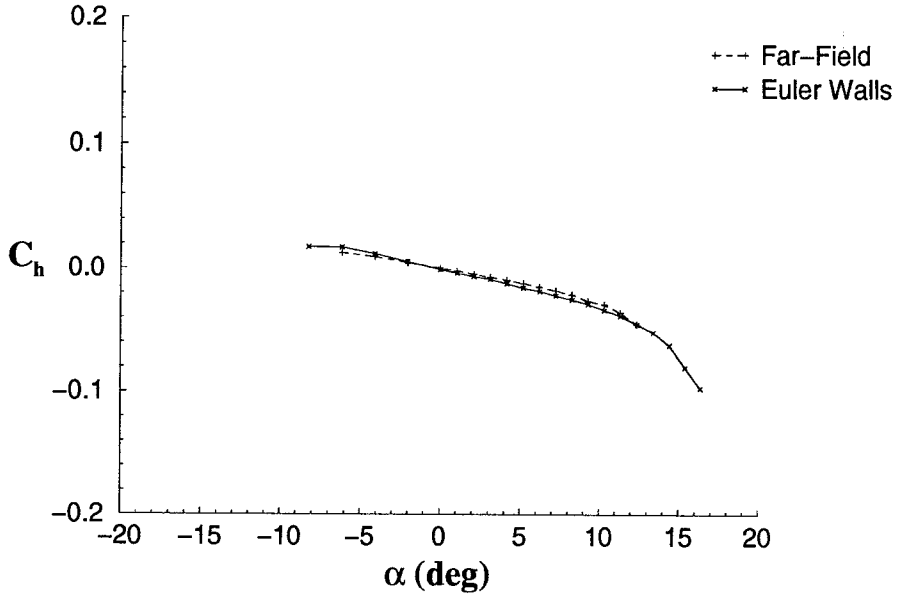

FIGURE 42. HINGE MOMENT COEFFICIENTS FOR A NACA 23012m AIRFOIL MODELED WITH TUNNEL WALLS (AND CORRECTED USING THE THEORY OF RAE AND POPE) AND WITHOUT TUNNEL WALLS

3.3.2.5 NLF 0414 Simulations.

The predictions obtained from NSU2D are compared with the experimental data of Lee and Bragg [29]. The data were collected for a Mach number of 0.2 and a Reynolds number of 1.8×10^6 with transition trips placed at the 2% chord location on the upper surface and 5% chord location on the lower surface. The experimental data has been corrected for wall interference. The simulations were carried out for the tunnel case with the same transition point specification technique used for the other airfoils.

Figures 43 through 46 plot the aerodynamic coefficients for the clean NLF 0414. Figure 43 shows the variation of lift coefficient as a function of angle of attack. The slope of the lift curve and maximum lift coefficient were overestimated by the computations. In fact, there are no comparisons of CFD solutions with experimental lift and pressure distributions in the open literature. It is well known that the flow field for this airfoil is difficult to predict with CFD techniques at these low Reynolds numbers. The differences are attributed to large regions of transitional flow (neither laminar nor turbulent) which the present methodology cannot predict. When simulations were run without the tunnel walls, there was a small improvement in the force and moment curves, but this approach was not used because of a desire to be consistent with all cases. Figure 44 shows the drag predictions. The slight underprediction of the drag coefficient at higher lift conditions is also consistent with earlier validation computations. The coefficient for pitching moment is seen in figure 45 as a function of angle of attack, where better agreement between the predictions and the experiments is seen. The flap hinge moment was investigated as

it is an important parameter with respect to aircraft control. NSU2D predicted this coefficient reasonably well as seen in figure 46.

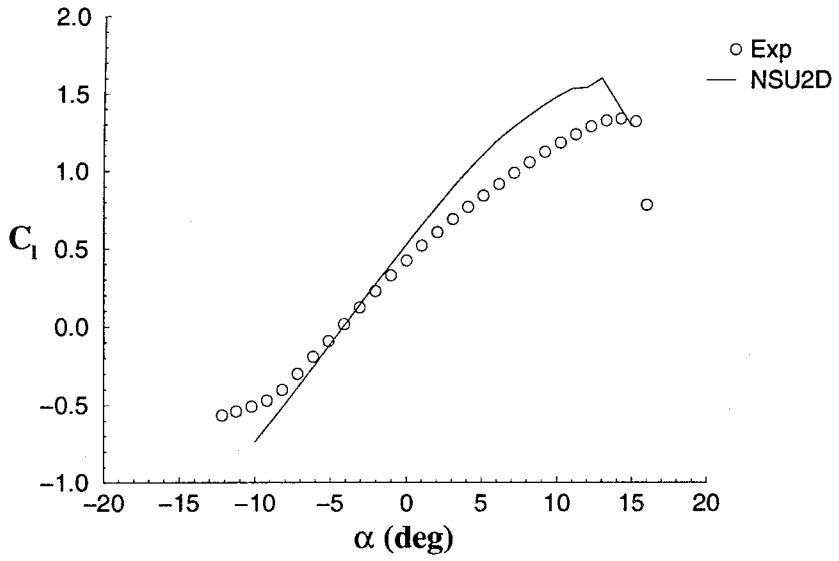

FIGURE 43. LIFT COEFFICIENTS FOR A NLF 0414 AIRFOIL MODELED WITH TUNNEL WALLS

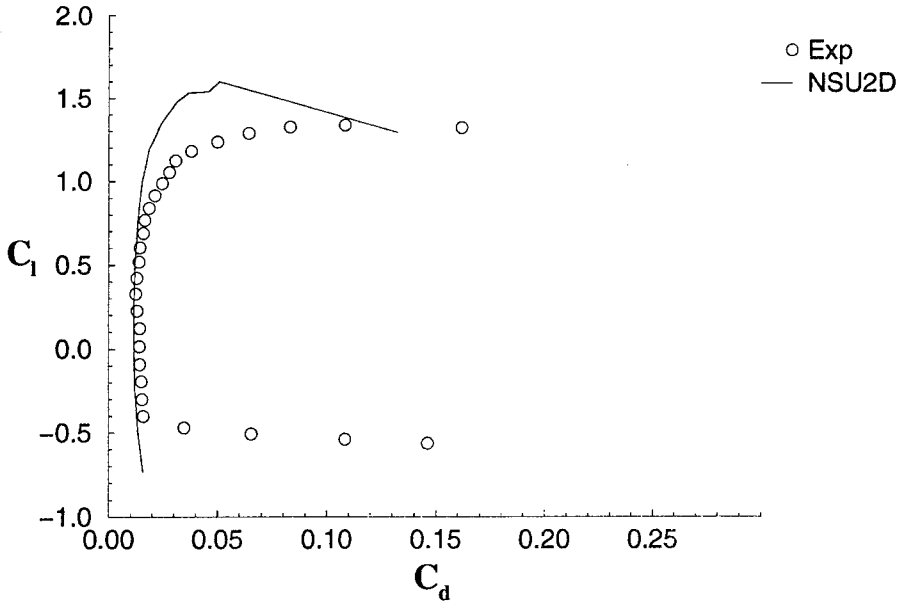

FIGURE 44. DRAG COEFFICIENTS FOR A NLF 0414 AIRFOIL MODELED WITH TUNNEL WALLS

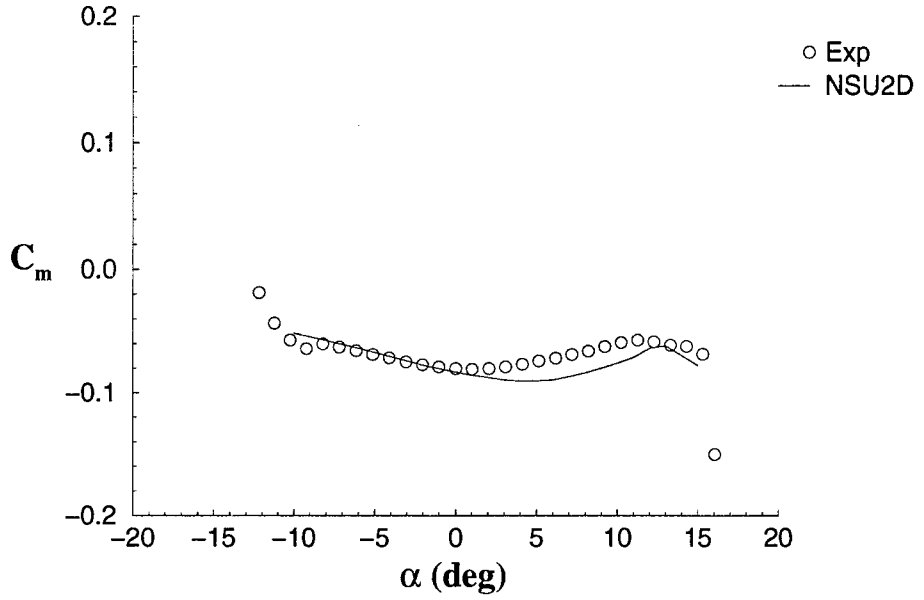

FIGURE 45. PITCHING MOMENT COEFFICIENTS FOR A NLF 0414 AIRFOIL MODELED WITH TUNNEL WALLS

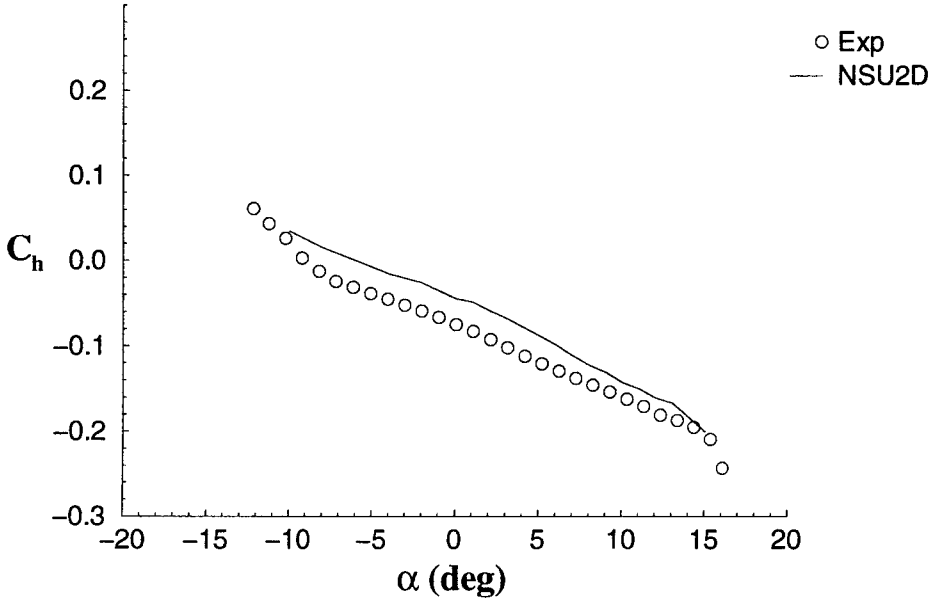

FIGURE 46. HINGE MOMENT COEFFICIENTS FOR A NLF 0414 AIRFOIL MODELED WITH TUNNEL WALLS

Figure 47 shows the surface pressure distributions for $\alpha = 6°$, $\alpha = 0°$, and $\alpha = 10°$. It is interesting to note that the disagreement with experimental pressure distribution is small, considering the comparison of lift coefficients at these angles. The main differences in the pressure distribution occur in the pressure recovery region and some differences exist on the lower surface.

In conclusion, NSU2D has been validated for basic fluid dynamic features associated with an iced airfoil: laminar and turbulent boundary layer flow, backward-facing step, and three markedly different clean airfoil shapes.

3.3.3 Iced Airfoil Simulations—NACA 0012 With Glaze Ice.

For further code validation, a leading-edge glaze ice shape on a NACA 0012 airfoil was considered. Although, the primary objective for this research was to simulate large-droplet ice accretion shapes, this shape provides a good comparison with the more commonly studied ice shape aerodynamics. This ice shape can be seen in the mesh shown in figure 48. The grid contained about 60,000 nodes and used far field conditions at the outer boundary. The experimental data of Bragg [63] was used for comparison. As described in the experimental data set, these runs probably did not have large regions of laminar flow due to the large and complex ice shape and therefore turbulence was modeled over the entire airfoil surface. Potapczuk [64] found that although modeling laminar regions around the ice shape influenced the velocity profiles along the airfoil surface, simulating laminar flow did not greatly influence the integrated aerodynamic forces. Therefore, modeling the entire surface as turbulent seems reasonable and appropriate. All runs were made at a Mach number of 0.12 and a Reynolds number of 1.5×10^6.

Figures 49 through 51 show aerodynamic predictions for angles of attack from -6 to +6 degrees. These predictions indicate that NSU2D was able to reasonably evaluate performance characteristics for an iced airfoil with large separation regions at low angles of attack. Calculations for -8 and +8 degrees failed to converge, which is attributed to inherent unsteadiness in the flow due to the presence of vortex shedding off the horns of the ice shape. The computed values for the lift coefficient (figure 49) agreed reasonably well with the experiments, although the lift curve slope was slightly underpredicted. This was a result of a more rapid predicted pressure recovery within the separated regions than was measured in the experiment. The drag (figure 50) and moment (figure 51) were also very well predicted, considering the large amount of separation on the airfoil.

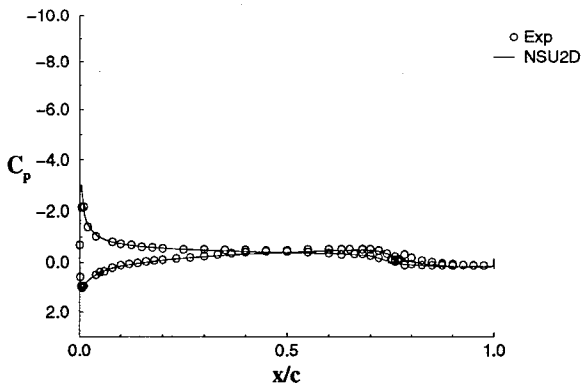

(a)

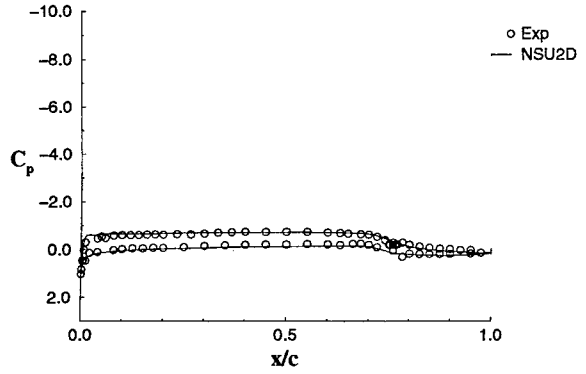

(b)

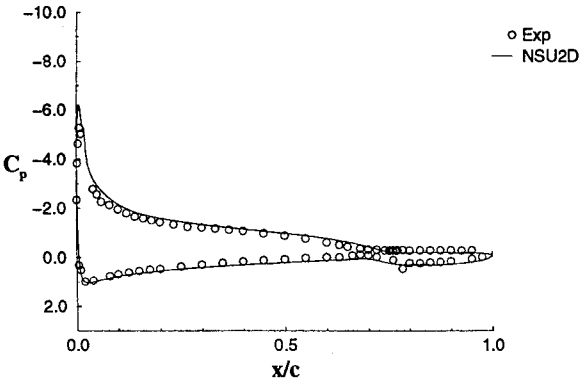

(c)

FIGURE 47. SURFACE PRESSURE DISTRIBUTION FOR A NLF 0414 AIRFOIL AT (a) $\alpha = -6°$, (b) $\alpha = 0°$, AND (c) $\alpha = 10°$

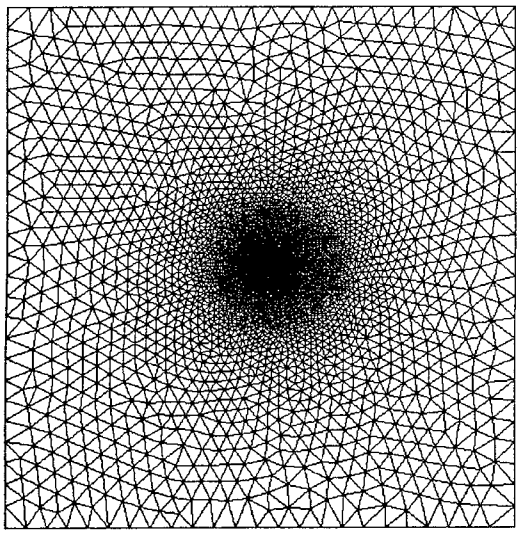

(a)

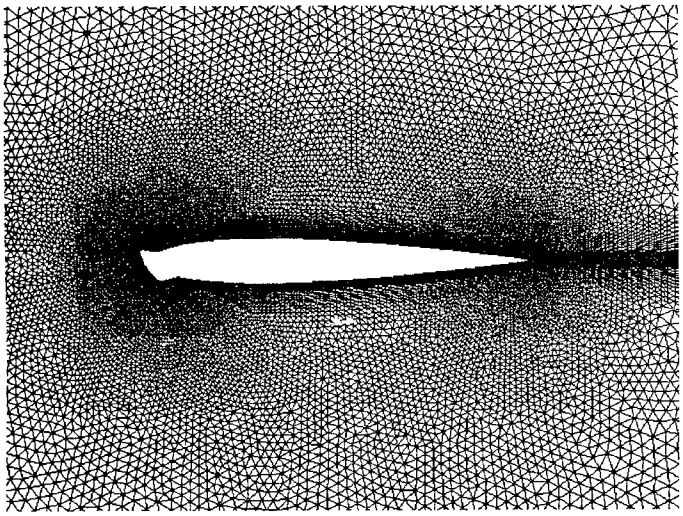

(b)

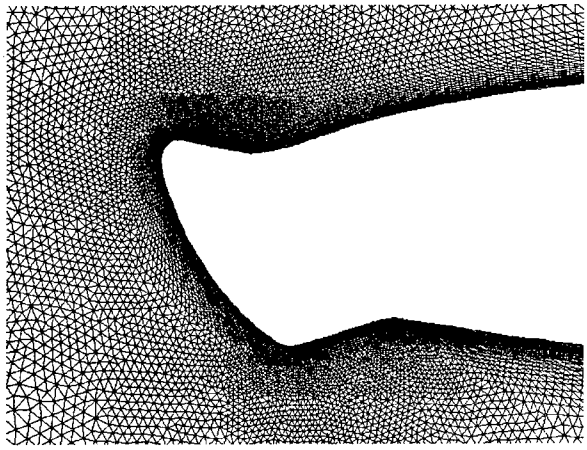

(c)

FIGURE 48. MESH FOR NACA 0012m (a) FAR FIELD WHERE AIRFOIL IS INSIDE THE CLUSTERED GRIDS, (b) CLOSEUP OF AIRFOIL, AND (c) CLOSEUP OF ICE SHAPE

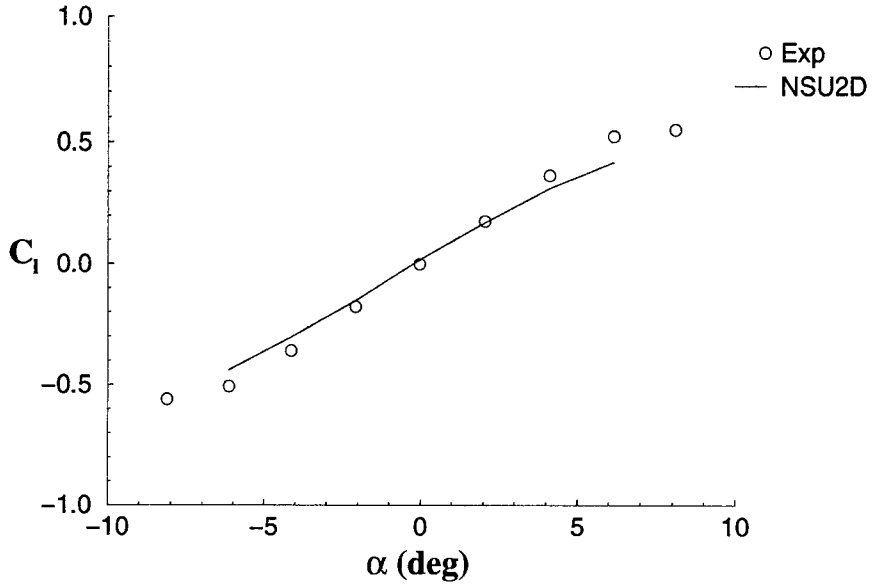

FIGURE 49. LIFT COEFFICIENTS FOR A NACA 0012m AIRFOIL WITH LEADING-EDGE GLAZE ICE

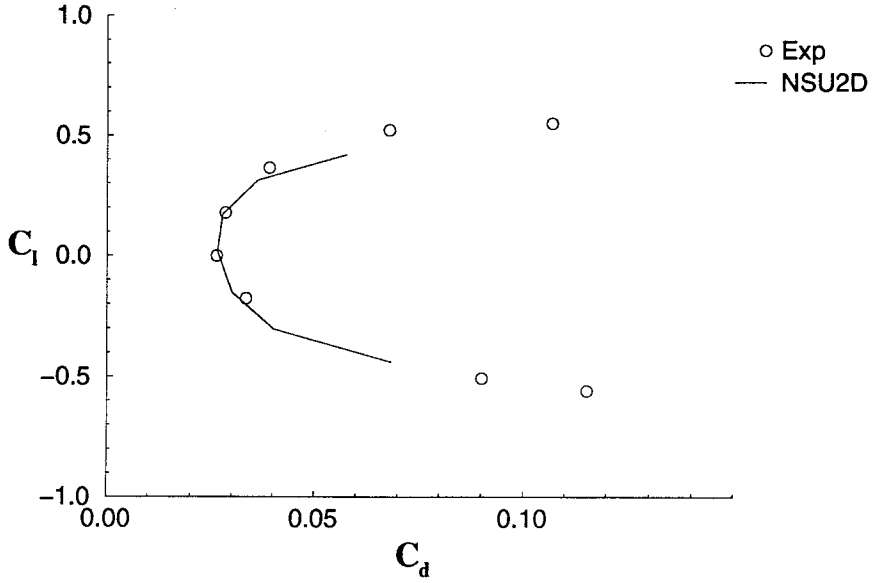

FIGURE 50. DRAG COEFFICIENTS FOR A NACA 0012m AIRFOIL WITH LEADING-EDGE GLAZE ICE

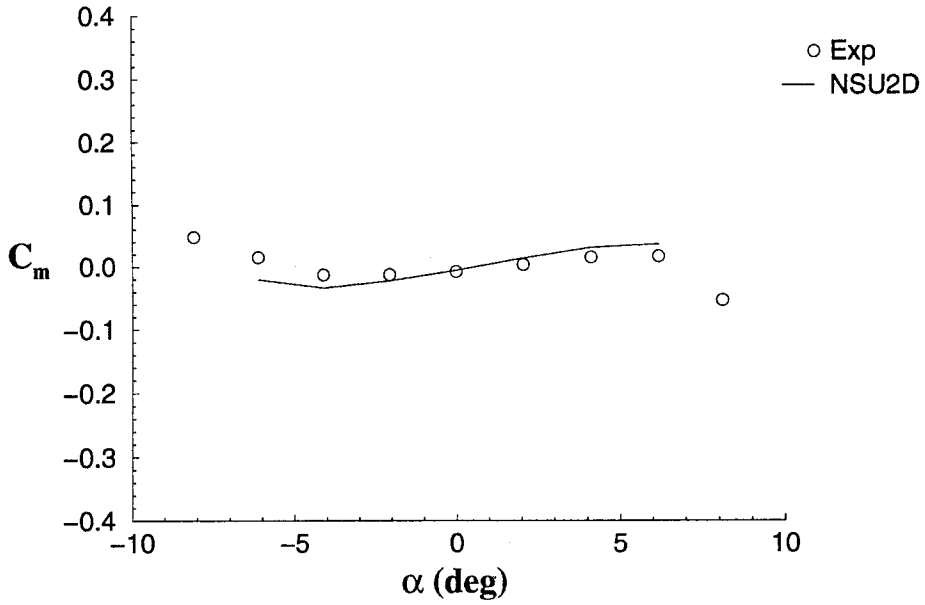

FIGURE 51. MOMENT COEFFICIENTS FOR A NACA 0012m AIRFOIL WITH LEADING-EDGE GLAZE ICE

Figure 52 shows the surface pressure distribution for $\alpha = 4.12°$. This figure shows good agreement in the attached regions of the flow, but the plot shows a faster pressure recovery within the separated regions on both the upper and lower surfaces. This is especially noticeable on the upper surface. The plots also reveal a small pressure spike/discontinuity on the lower surface ice horn. This maybe an indication of insufficient grid resolution within this region or a result of the surface slope discontinuity. The pressure distributions for this geometry at other angles of attack showed similar agreement.

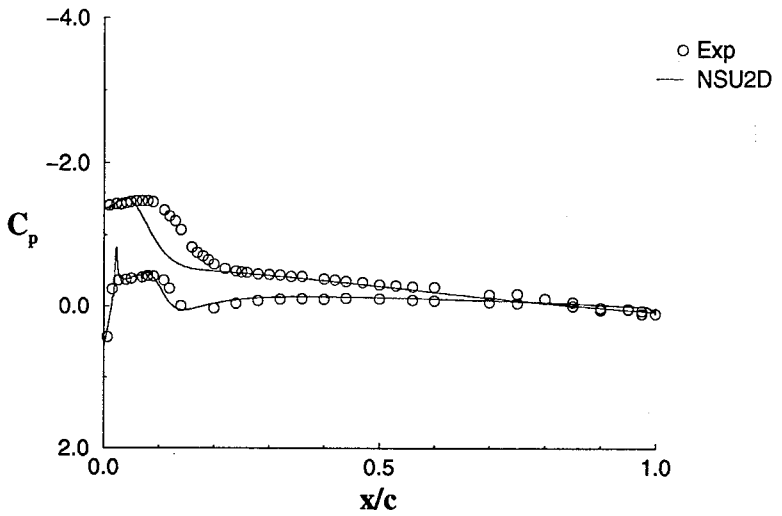

FIGURE 52. SURFACE PRESSURE DISTRIBUTION FOR A NACA 0012m AIRFOIL WITH LEADING-EDGE GLAZE ICE AT $\alpha = 4.12°$

3.4 AIRFOIL STALL TYPES.

There are three types of airfoil stall at low speeds: trailing-edge stall, leading-edge stall, and thin-airfoil stall. The type of stall an airfoil experiences is dependent on the where the boundary layer first separates and how the separated flow grows. This, in turn, is dependent primarily on the airfoil geometry, Reynolds number, surface roughness, and free-stream turbulence. McCullough and Gault provide a detailed explanation of the three types of airfoil stall [65].

The trailing-edge stall occurs when the flow separation starts from the trailing edge of the airfoil, and the separation point progresses upstream as the angle of attack is increased. This stall type is usually associated with thick airfoils with a thickness ratio greater than 0.15. An example of an airfoil that has a trailing-edge stall is the NACA 63_3-018. The lift curve of this airfoil is shown on figure 53 [66]. It shows a smooth and gradual stall, with a round peak in the lift curve. The lift curve became nonlinear at $\alpha = 10°$. This coincided with the angle of attack at which the flow started to separate at the trailing edge. The lift curve slope continued to decrease as the separation propagated upstream. The $C_{\ell,max}$ occurred when the flow was separated over half of the airfoil.

The leading-edge stall is typically found on airfoils with moderate thickness ratios (between 0.09 and 0.15). The NACA 63_3-012 is an example of this. On these types of airfoils, a small laminar separation bubble usually forms at moderate angles of attack just downstream of the suction peak (where the flow transitions). As the angle of attack is increased, the laminar separation bubble moves upstream. As the angle of attack is further increased, the bubble rapidly bursts (fails to reattach), leading to a sudden stall. The result of this is a very abrupt discontinuity in the lift curve at stall, as shown in figure 53. Another example of an airfoil that has a leading-edge stall is the NACA 23012m, which was used in this study.

The thin-airfoil stall occurs on all sharp-edge airfoils and some thin airfoils (with a thickness ratio less than 0.09). The double-wedge airfoil shown on figure 53 is an example of this. The thin-airfoil stall is characterized by a flow separation that forms on the leading edge of the airfoil that grows downstream with increasing angle of attack. This growth in the separation bubble is much more gradual than the sudden bubble burst that occurs on the leading-edge stall, resulting in a much more gradual stall. A "kink" in the lift curve is often observed when the leading-edge bubble starts to grow rapidly. On the double-wedge airfoil, this occurs at $\alpha = 2°$. The lift reaches a maximum when the bubble fails to reattach. The top of the curve is relatively flat with little lift loss after stall.

An airfoil can also have stall characteristics that are a combination of two of the types described above. An example of this is the combination of the thin-airfoil and the trailing-edge stall. Flow separation can form both at the leading and the trailing edge. As the angle of attack is increased, the separation will grow until the two bubbles join near stall.

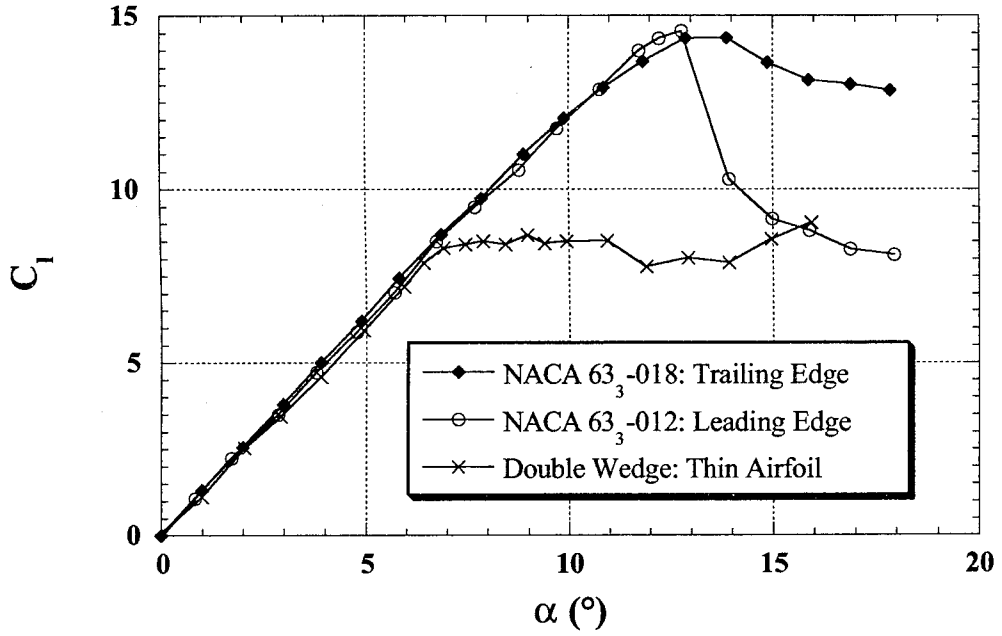

FIGURE 53. LIFT CHARACTERISTICS OF THE THREE AIRFOIL STALL TYPES

4. RESULTS AND DISCUSSION.

4.1 EXPERIMENTAL RESULTS.

The C_ℓ and C_m data in this section come from the integrated surface pressures and the C_d measurements were taken from the wake pressure data unless otherwise indicated. The C_h data were taken from the flap hinge balance measurements.

4.1.1 Effect of Simulated Ice Ridge Location.

Figure 54 shows the effect of the 0.25″ (k/c = 0.0139) forward-facing quarter-round ice simulation at three different x/c locations on the aerodynamic coefficients. The boundary layer was tripped (at 2% chord upper and 5% lower surface) for the cases with the simulated ice shapes at x/c = 0.10 and x/c = 0.20. All of the simulated ice cases showed reduced lift curve slopes in the linear regions (-5° < α < 1°) when compared to the clean case (figure 54(a)). Varying the ice shape location from x/c = 0.02 to 0.20 had large effects on the lift of the NACA 23012m. The simulated ice cases exhibited gradual stall characteristics typical of a thin-airfoil-type stall and not the leading-edge stall of the clean model. (See discussion of types of airfoil stall in section 3.4.) Of the three cases shown, the loss in lift was most severe when the ice shape was located at x/c = 0.10 (with $C_{\ell,max}$ = 0.27). It will be shown later that the worst ice shape location for $C_{\ell,max}$ degradation was at x/c = 0.12. When the ice shape was located at x/c = 0.02, $C_{\ell,max}$ was approximately doubled. A classical $C_{\ell,max}$ (as α is increased C_ℓ eventually reaches a maximum and then decreases) was not observed when the simulated ice shape was located at x/c = 0.20. Instead, only an inflection in the curve was observed at α = 4° (and C_ℓ = 0.42). Jacobs [12] observed similar lift curves (where a real $C_{\ell,max}$ was not observed) under certain conditions in his test of protuberances on a NACA 0012 airfoil.

Figure 54(b) shows the drag polars with the 0.25″ simulated ice shape at the three different x/c locations. Figure 54(b) shows significant increases in drag when the simulated ice shape was present. The largest increase in drag for $C_\ell > 0$ occurred when the simulated ice shape was at x/c = 0.10, which also corresponds to the case with the lowest C_ℓ. However, at $C_\ell < 0$, the largest increase in drag occurred when the simulated ice shape was located at x/c = 0.20.

The pitching moments with the three simulated ice shape locations are shown in figure 54(c). When the simulated ice shape was at x/c = 0.10 and 0.20, the pitching moment exhibited a large break in the slope at ℓ = -1°, becoming more negative, indicating that the airfoil was more aft loaded. When the simulated ice shape was located at x/c = 0.02, the pitching moment diverged at ℓ = 5°. However, between ℓ = 0° and 5°, the pitching moment was more positive than the clean case. Figure 54(d) shows the flap hinge moments with the simulated ice shape at the three different x/c locations. Between ℓ = -9° and ℓ = 1°, the hinge moments with a simulated ice shape present were higher than that of the non-iced case, indicating a larger trailing-edge down moment about the flap hinge. The cases with the simulated ice shape at x/c = 0.10 and 0.20 exhibited a large break in the ℓ slope at ℓ = 0°. The case with the simulated ice shape at x/c = 0.02 exhibited a large break in the slope ℓ = 6°. Figures 54(c) and 54(d) show that the sudden divergence in the flap hinge moment occurred at an angle of attack that was a few degrees higher than that of the pitching moment.

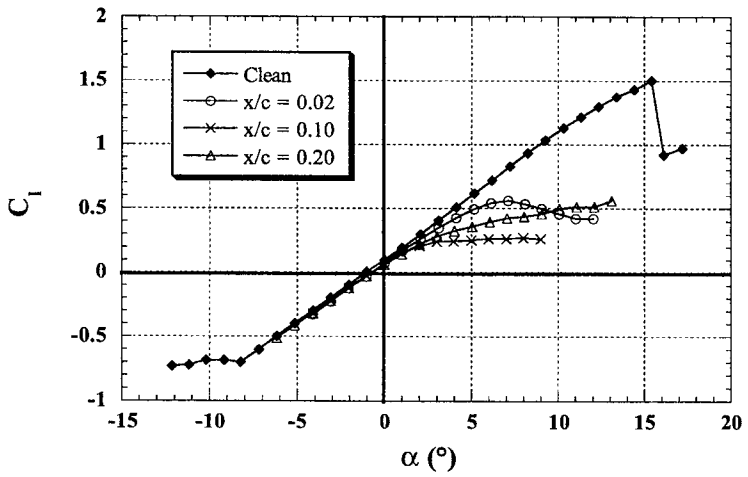

(a) Lift

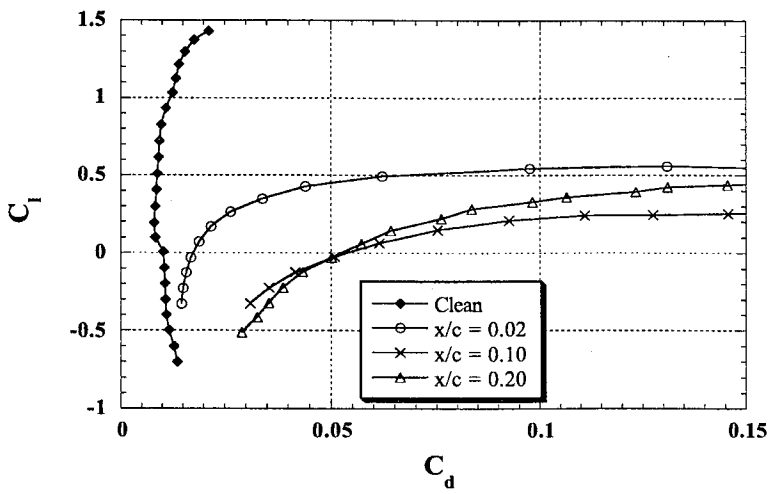

(b) Drag

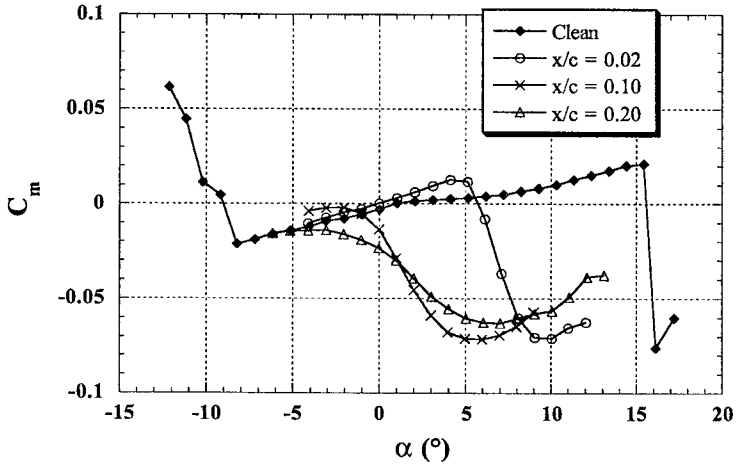

(c) Pitching Moment

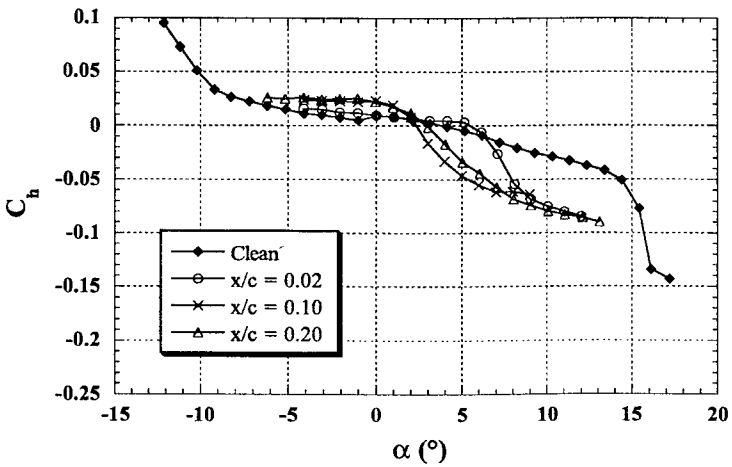

(d) Flap Hinge Moment

FIGURE 54. EFFECTS OF SIMULATED ICE SHAPE LOCATION ON AERODYNAMIC COEFFICIENTS
(NACA 23012m 0.25″ forwarded-facing quarter round, boundary layer tripped for $x/c = 0.10$ and $x/c = 0.20$ cases, $Re = 1.8$ million)

Figure 54 shows the summary of $C_{\ell,max}$ versus the chordwise location of the simulated ice accretion (0.25″ forward-facing quarter round) as well as the clean airfoil $C_{\ell,max}$ with natural transition. All of the cases with the simulated ice shapes at, down stream of, 4% chord had the boundary layer tripped at 2% chord upper and 5% chord lower surface. The cases with the simulated ice shapes upstream of 4% chord were not tripped. The lowest $C_{\ell,max}$ for the 0.25″ shape (k/c = 0.0139) was 0.25 and occurred at x/c = 0.12. The maximum lift increased rapidly as the simulated ice was moved forward of this location, reaching 0.97 at the leading edge. Thus, it is clear from figure 55 that in terms of maximum lift loss, the most critical location for this simulated ice shapes was at x/c = 0.12.

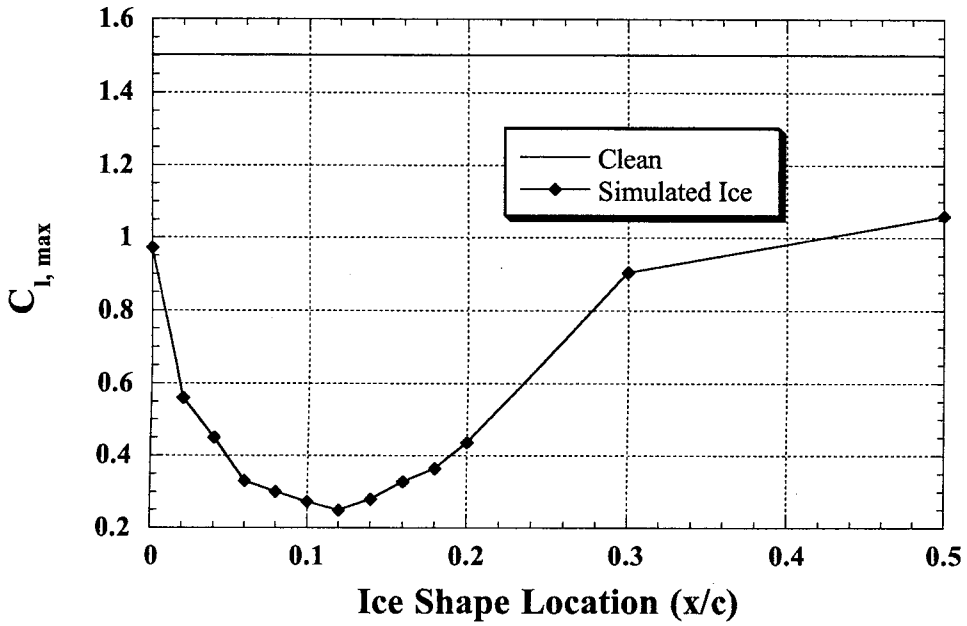

FIGURE 55. SUMMARY OF $C_{\ell,max}$ WITH SIMULATED ICE SHAPE AT VARIOUS LOCATIONS
(NACA 23012m, forward-facing quarter round, boundary layer tripped for case with simulated ice at $x/c \geq 0.04$, Re = 1.8 million)

As stated in the introduction, studies [12, 13] have shown that the effects of a spanwise surface protuberance (of $k/c < 0.005$) on lift, drag, and pitching moment became more severe as it was moved closer to the leading edge. Gregory and O'Reilly [67] showed that the k/c = 0.0004 surface roughness resulted in the most severe loss in $C_{\ell,max}$ (on a NACA 0012 airfoil) when it was placed at the leading edge. Bowden [13] observed that the maximum increase in the drag occurred when the protuberance was located near the location of maximum local surface velocity (or minimum Cp). A possible explanation for this is that the protuberance would extract the greatest amount of boundary layer momentum when placed at that location, which would thicken the boundary layer and increase drag. Figure 56 shows the drag increase (compared to the clean airfoil) due to the 0.25″ ice shape simulation. Each curve represents a fixed angle of attack, and the simulated ice shape location is depicted on the x axis. Also shown on the figure, by the solid

arrows, are the locations of maximum local air velocity (of the clean airfoil) for each angle of attack and, by the open arrows, the location of the maximum adverse pressure gradient (also of the clean airfoil). The figure shows that, as the angle of attack was increased, the chordwise location with the greatest increase in drag moved upstream and was approximately at the location of the maximum local air velocity. This is similar to what Bowden found on a NACA 0011 airfoil.

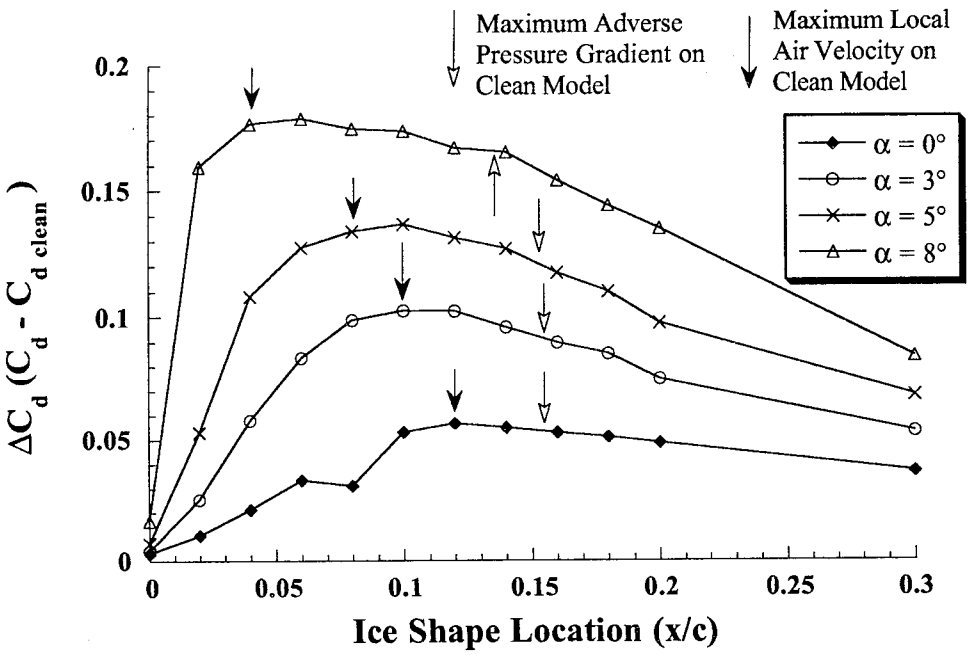

FIGURE 56. DRAG INCREASE DUE TO SIMULATED ICE SHAPE AT VARIOUS LOCATIONS
(NACA 23012m, forward-facing quarter round, boundary layer tripped for case with simulated ice at $x/c \geq 0.04$, $Re = 1.8$ million)

However, as shown in figure 57, the loss in lift due to the 0.25″ ice shape simulation did not follow this behavior. The figure shows that there were maxima in the lift loss as well. However, unlike the drag increase, the simulated ice shape location for maximum lift loss was well downstream of the maximum local air velocity and slightly upstream of the maximum adverse pressure gradient. Also, the maxima remained fixed near $x/c = 0.12$ and did not move upstream with increasing angles of attack. This was the same x/c location that produced the lowest $C_{\ell,max}$ as shown in figure 55. A detailed analysis of Jacobs' protuberance, the largest lift loss also occurred when it was located well downstream of the maximum local air velocity in the adverse pressure region. Thus, it is apparent that for the large protuberances tested here, the chordwise location with the most severe reduction in lift did not coincide with either the location of the maximum adverse pressure gradient nor the local maximum air velocity (although it was bounded by them). However, for this airfoil, the location of the maximum adverse pressure gradient seemed to be a better indicator.

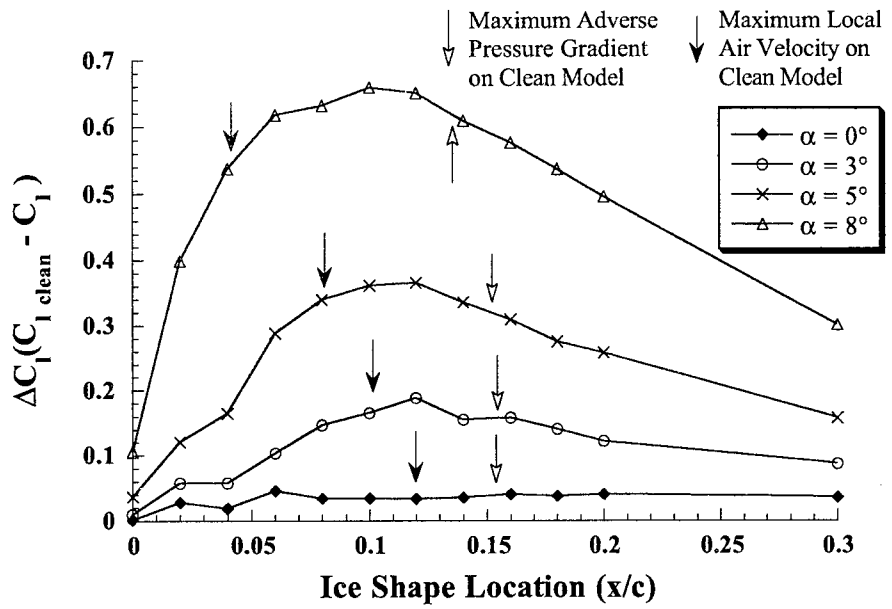

FIGURE 57. LIFT LOSS DUE TO SIMULATED ICE SHAPE AT VARIOUS LOCATIONS (NACA 23012m, forward-facing quarter round, boundary layer tripped for case with simulated ice at x/c ≥ 0.04. Re = 1.8 million)

4.1.1.1 Effects of Flap Deflection.

Figure 58 shows the effects of the flap deflection on integrated aerodynamic coefficients. Figure 58(a) shows that flap deflection did not significantly alter the lift characteristics of the airfoil with simulated ice. All three flap deflection cases show a very gradual stall characteristic of thin-airfoil stall. However, as the flap deflection was increased from -5° to 5°, the angle of attack at which the lift curve became nonlinear decreased from 3° to 1°. Also, as the flap deflection was increased, the linear region of the iced cases became increasing shifted vertically from the clean cases (i.e., reduced lift at a given α). At α = -5°, there was almost no vertical shift in the lift curve. However, at α = 5°, there was a 0.08 shift in between the iced and the clean cases.

Figure 58(b) shows the effect of flap deflection on drag. On the clean model, varying the flap deflection did not change the drag polars by a large amount. However, increasing the flap deflection did significantly decrease the drag at matched lift coefficients for the case with simulated ice accretion.

Figures 58(c) and 58(d) show the effect of flap deflection on the pitching and flap hinge moments. Increasing the flap deflection from -5° to 5° did not change where the breaks in the C_m curves (with simulated ice shapes) occurred, as it occurred at α = -1° for all three flap deflections. Varying the flap deflection from -5° to 5° decreased the angle of attack at which the C_h curves broke from 2° to 0°. Increasing the flap deflection also increased the differences in C_m and C_h between the clean and the iced case at negative angles of attack. This was similar to the vertical shift in the linear regions of the lift curve (figure 58(a)).

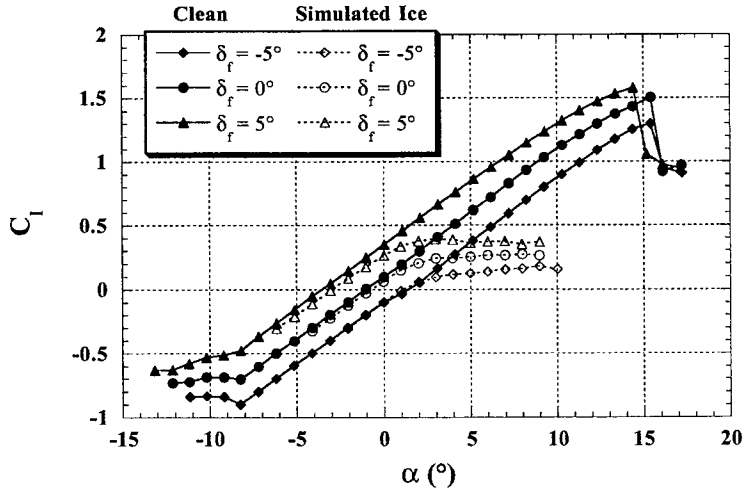

(a) Lift

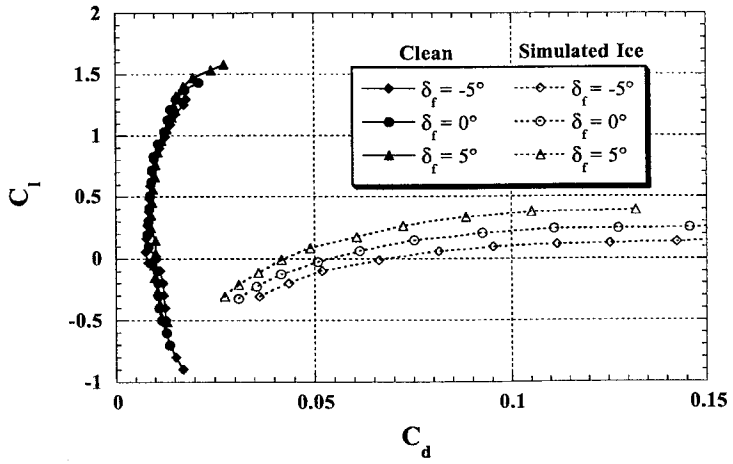

(b) Drag

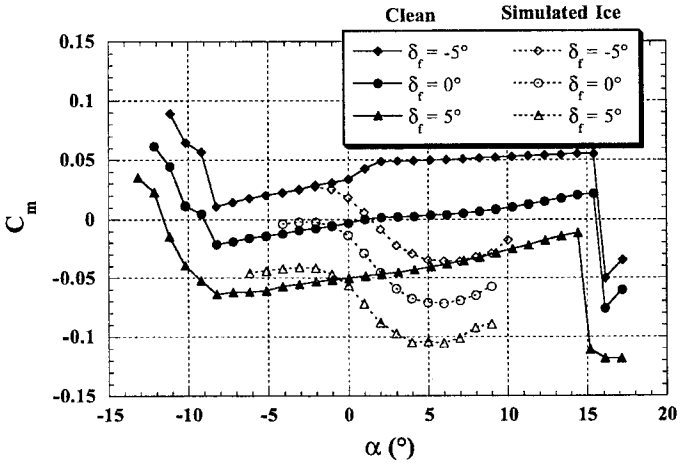

(c) Pitching Moment

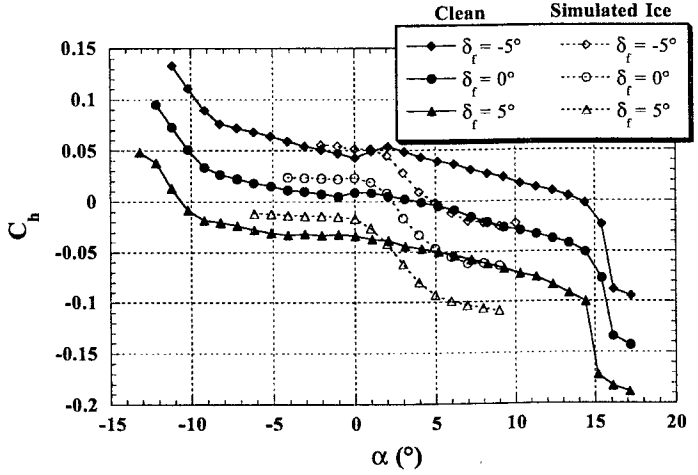

(d) Flap Hinge Moment

FIGURE 58. EFFECTS OF FLAP DEFLECTION ON AERODYNAMIC COEFFICIENTS
(NACA 23012m, 0.25″ forward-facing quarter round at $x/c = 0.10$, boundary layer tripped, $Re = 1.8$ million)

Figure 59(a) shows the plot of lift versus the flap deflection angle at constant angles of attack. This is a plot of the flap effectiveness as it shows how effective the flap is in changing lift. It shows that at α = -2° and 0°, the simulated ice shape did not greatly decrease the flap effectiveness. At α = -2°, the $C_{\ell_{\delta f}}$ was 5.17 for the clean case and 4.71 for the simulated ice case, a 9% reduction in flap effectiveness. However, at α = 2° and 4°, there were very large reductions in the flap effectiveness. On the clean model (at α = 4°), the $C_{\ell_{\delta f}}$ was 5.17 while on the simulated ice case, the $C_{\ell_{\delta f}}$ was 2.87, a 44% reduction. Thus, in the linear range of the lift curve, the simulated ice shape did not significantly alter the flap effectiveness. However, in the nonlinear regions, the flap effectiveness was cut almost in half.

Figure 59(b) shows the effect of flap deflection on the pitching moment at constant angles of attack. It shows that the simulated ice shape caused large changes in C_m, as much as 0.09 in the range of α's shown. However, it did not affect $C_{m,\delta f}$ as much as $C_{\ell_{\delta f}}$. In the worst case, the simulated ice shapes altered $C_{m,\delta f}$ by only 18%.

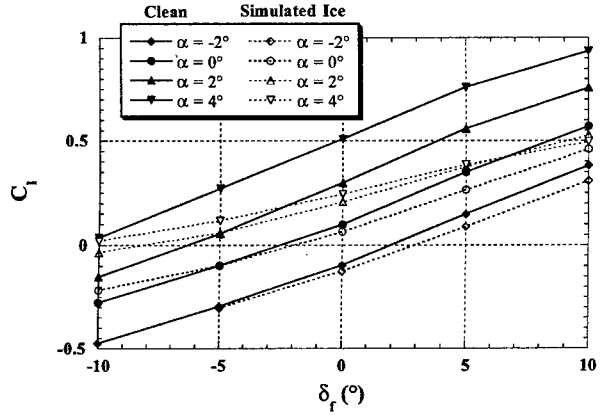

(a) Lift

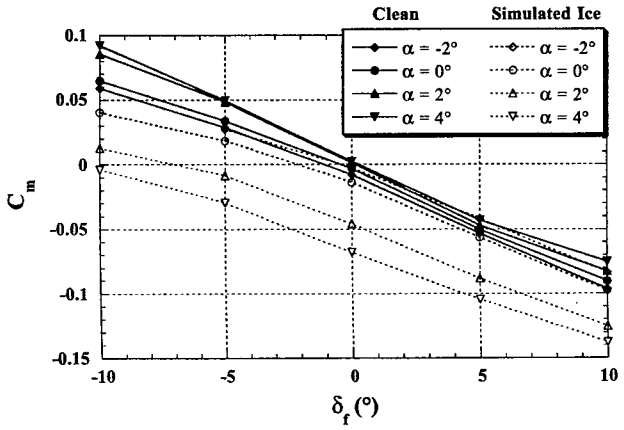

(B) Pitching Moment

FIGURE 59. EFFECTS OF SIMULATED ICE SHAPE ON FLAP EFFECTIVENESS (NACA 23012m, 0.25″ forward-facing quarter round at x/c = 0.10, boundary layer tripped, Re = 1.8 million)

4.1.1.2 Flow Field Analysis.

The flow field will be discussed next in order to provide a better understanding of the integrated results shown in the preceding section. Figure 60 summarizes the boundary layer state observed on the model using fluorescent oil flow visualization. The figure shows the progression of the separation bubbles upstream and downstream of the ice shape simulation as the angle of attack was increased. Here, the 0.25″ quarter-round ice simulation was located at $x/c = 0.10$ and the boundary layer was not tripped. The primary separation bubble upstream of the simulated ice shape formed at $x/c = 0.07$ at $\alpha = 0°$. The separation point moved gradually upstream to $x/c = 0.05$ at $\alpha = 3°$ and remained at this location to $\alpha = 5°$. Evidence of a secondary separation bubble upstream of the simulated ice shape was observed but was not shown because it could not be accurately measured. The primary downstream bubble reattachment region was located between $x/c = 0.40$ and $x/c = 0.44$ at $\alpha = 0°$. It was not clearly defined because the reattachment of the ice-induced bubble was seen in the oil flow as a band of relatively stagnant oil on the surface. The stagnant oil band was probably an indication of an unsteady reattachment process. The region moved downstream as α was increased and at $\alpha = 3.25°$ was located between $x/c = 0.75$ and the trailing edge. Thus, for the 0.25″ quarter round at $x/c = 0.10$, the stall was initiated by a rapidly growing separation bubble that eventually reached the trailing edge, which is characteristic of a thin-airfoil stall. Clearly, the separation bubble that formed downstream of the simulated ice shape was the most dominant feature in the flow field.

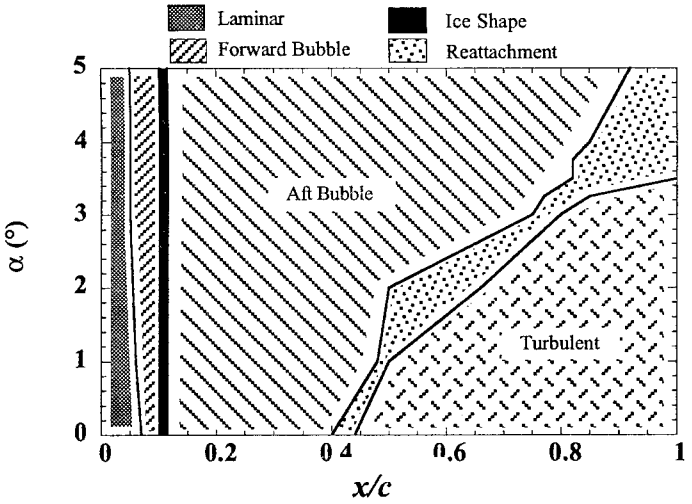

FIGURE 60. SUMMARY OF BOUNDARY LAYER STATE WITH THE SIMULATED ICE AT $x/c = 0.10$
(NACA 23012m, forward-facing quarter round, boundary layer not tripped, $Re = 1.8$ million)

Figure 61 shows the reattachment locations of the separation bubble with the simulated ice shapes at three chordwise locations. Again, this was obtained from flow visualization. Two reattachment location lines are shown for each of the cases because the reattachment location was not clearly defined for large bubbles. Figure 61 shows that when the simulated ice shape was located at $x/c = 0.02$, the bubble failed to reattach at $\alpha = 7°$. When the simulated ice was located at $x/c = 0.10$ and 0.20, the bubble failed to reattach at $\alpha = 2.5°$ and 3°, nearly the same angle of attack.

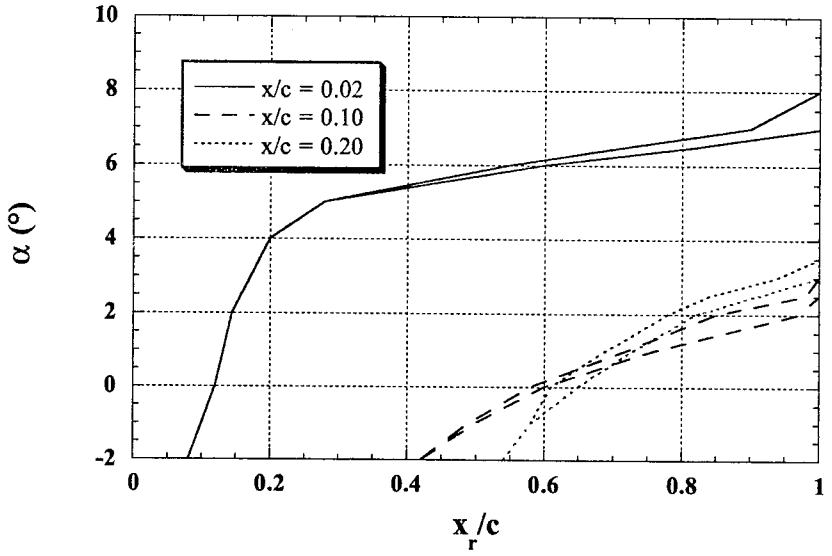

FIGURE 61. REATTACHMENT LOCATION OF SEPARATION BUBBLE THAT FORMED DOWNSTREAM OF SIMULATED ICE
(NACA 23012m, forward-facing quarter round, boundary layer tripped for $x/c = 0.10$ AND $x/c = 0.20$ CASES, $Re = 1.8$ million)

The large change in the flow field around the airfoil can be seen in the pressure distribution plots of figure 62. Figure 62(a) shows the surface pressure distribution with the 0.25″ ice shape simulation placed at various chordwise locations at $\alpha = 0°$ and compared to the clean case. The clean case shows the stagnation point at the leading edge with a suction peak at $x/c = 0.12$ on the upper surface and at $x/c = 0.02$ on the lower surface.

The pressure distributions with the simulated ice shape show a severely altered flow field, even at this angle of attack. It is first important to note that the surface pressure was not measured over the simulated ice shape. Thus, the C_p from the last pressure tap upstream of the simulated ice shape is connected in the figure to the first pressure tap downstream of the simulated ice shape by a straight line. The flow field became significantly altered when the simulated ice shape was at $x/c = 0.02$. There was a large suction peak ($C_p = -1.16$) immediately downstream of the simulated ice shape as the flow accelerated over it and separated. However, the simulated ice shape was located in a very favorable pressure gradient and the bubble was able to reattach quickly at $x/c = 0.12$ (as indicated by figure 61). This allowed another suction peak (due primarily to the airfoil geometry and not the simulated ice shape) to form at $x/c = 0.18$ with a C_p value of -0.51.

When the simulated ice shape was located at $x/c = 0.10$, the flow on the upper surface initially accelerated from the leading-edge stagnation point. However, the flow started to decelerate as it approached the simulated ice shape and experienced an adverse pressure gradient and flow separation. This resulted in a local $C_{p,min}$ of 0.52 located ahead of the simulated ice shape at $x/c = 0.03$, followed by a local $C_{p,max}$ of 0.58 at $x/c = 0.04$. Immediately downstream of the simulated ice shape, a longer separation bubble was formed, and the C_p was nearly constant at

-0.90 until x/c = 0.27, where it started to increase as the reattachment process began. Near x/c = 0.60, the C_p approached the clean model value and indicated that the flow had reattached. Although the simulated ice shape was located in a favorable pressure gradient, it was so close to the location of the onset of adverse pressure gradient that the separation bubble was forced to reattach in an adverse pressure gradient. Thus, the separation bubble for this simulated ice shape location was much larger than when the simulated ice shape was located at x/c = 0.02.

With the simulated ice shape located at x/c = 0.20, the local $C_{p,min}$ and $C_{p,max}$ upstream of the simulated ice shape became more clearly defined as there was a greater surface length along the model for the flow to first accelerate and decelerate upstream of the simulated ice shape. In this case, the simulated ice shape was located in an adverse pressure gradient and resulted in a very large separation bubble that did not reattach until near x/c = 0.70. In both the x/c = 0.10 and 0.20 cases, the C_p value at the constant pressure region downstream of the simulated ice shape was approximately -0.90. Also, the trailing-edge pressure was the lowest when the simulated ice shape was located at x/c = 0.10 indicating the least upper surface pressure recovery.

The separation bubbles described above were very similar to the long laminar separation bubble described by Tani [68]. The overall shapes of the pressure distributions were very similar to those observed by Mullins et al. [69] and Calay et al. [14]. However, the length of the separation bubble for this investigation was much longer because the simulated ice used in this test was much larger. The shape of the pressure distribution when the simulated ice shape was located at x/c = 0.02 compared very favorably to that observed by Bragg et al. [70] who performed extensive measurements on a NACA 0012 airfoil with a large leading-edge ice shape.

As Figure 62(b) shows, similar trends in the pressure distributions were observed for α = 5°. This was approximately the angle of attack at which $C_{p,max}$ occurred for many of the cases with a simulated ice shape. The pressure distribution for the clean case shows a suction peak (C_p = 1.68) at x/c = 0.08. Well over half of the lift occurred in the first 25% chord due to the large leading-edge suction. When the simulated ice shape was located at x/c = 0.02, the C_p in the separation bubble downstream of the simulated ice shape was even more negative than that of the clean model suction peak. The simulated ice shape was located in a favorable pressure gradient and, the resulting separation bubble was still relatively short (with reattachment at x/c = 0.30, figure 59).

When the simulated ice shape was located at x/c = 0.10, a very long separation bubble formed downstream of the simulated ice shape. In fact, the large suction peak that normally forms near x/c = 0.08 was completely replaced by this separation bubble. This was the case where the simulated ice shape was located near the suction peak of the clean model and almost all of the resulting separation bubble was located in the adverse pressure region. It was difficult to determine from the surface pressure values whether or not the separation bubble reattached. However, flow visualization results of figure 8 indicated that the flow was completely separated. When the simulated ice shape was located at x/c = 0.20, the resulting separation bubble was very similar to that of x/c = 0.10, with nearly identical C_p values. However, the local suction peak upstream of the simulated ice shape was larger. Again the x/c = 0.10 case shows the least upper surface pressure recovery as shown by the trailing-edge pressures.

It is apparent from the flow visualization and pressure distribution plots that the large loss in lift observed in figure 54(a) was due to the long separation bubble that formed downstream of the simulated ice shape. Figure 62 showed that the long separation bubbles formed when the simulated ice shape was located in the vicinity of, and downstream of, the suction peak (of the clean airfoil) in the pressure recovery region. This was because the separation bubble was unable to reattach quickly in the adverse pressure gradient. When this occurred, the large suction peak observed on the clean airfoil (where the bulk of the lift was generated) was eliminated. However, when the simulated ice shape was located far enough downstream, a smaller local suction region was able to form upstream of the simulated ice shape, recovering some of the lift. This explains why the region near $x/c = 0.12$ is so critical in terms of lift loss, as shown in figure 55.

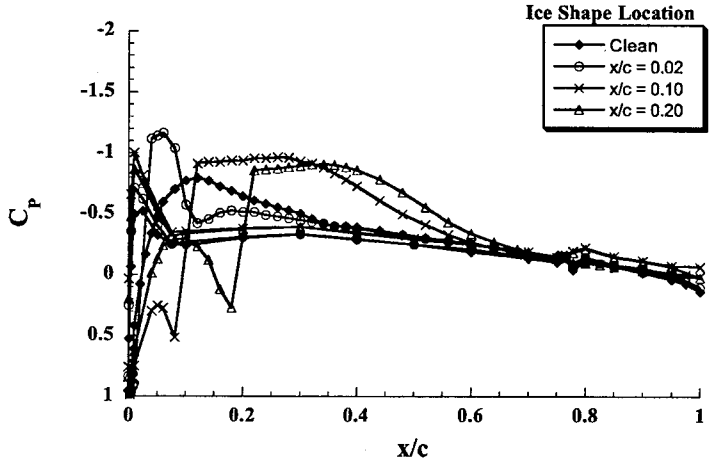

(a) $\alpha = 0°$

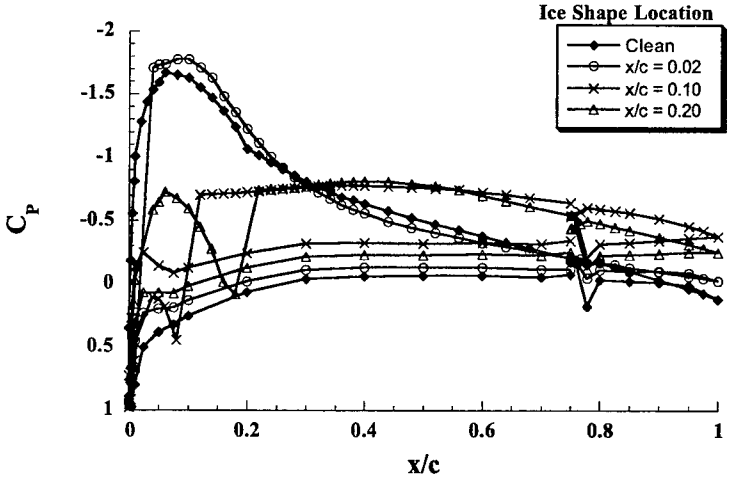

(b) $\alpha = 5°$

FIGURE 62. EFFECT OF ICE SHAPE LOCATION ON SURFACE PRESSURE DISTRIBUTION
(NACA 23012m, forward-facing quarter round, boundary layer tripped for $x/c = 0.10$ and $x/c = 0.20$ cases, $Re = 1.8$ million)

4.1.1.3 Pitching and Flap Hinge Moment Analysis.

By examining the pressure distribution, the trends seen in the integrated pitching and flap hinge moments of figure 54 can be better understood. NACA 23012 is a forward-loaded airfoil in which most of the lift is generated in the vicinity of the large suction peak that forms near the leading edge of the airfoil. At $\alpha = 0°$, when the simulated ice shape was located at $x/c = 0.10$ and 0.20, most of the lift was generated in the region of the long separation bubble that formed downstream of the simulated ice shape. In fact, negative lift was generated upstream of the simulated ice shape. Thus, it became more aft loaded than the clean airfoil. When the simulated ice shape was located at $x/c = 0.02$, most of the lift was also generated by the separation bubble. However, the separation bubble was very short and it was located upstream of the quarter-chord location, resulting in a more forward-loaded lift distribution than the clean airfoil. This can be seen in figure 54(c), which shows that at $\alpha = 0°$, when the simulated ice shape was located at $x/c = 0.02$, C_m was more positive (or nose up) than the clean case. However, when the simulated ice shape was located at $x/c = 0.10$ and 0.20, the pitching moments were more negative than the clean case at this angle of attack.

Similar trends were observed at $\alpha = 5°$. Figure 62(b) shows that when the simulated ice shape was located at $x/c = 0.10$ and 0.20, the large suction peak near the leading edge of the airfoil was essentially eliminated and a long separation bubble formed downstream of the simulated ice shape. Thus, the airfoil became much more aft loaded. When the simulated ice shape was located at $x/c = 0.02$, the suction peak that formed near the leading edge of the model was even larger than that of the clean case. Thus, the airfoil became more front loaded than the clean case. Again, the result of the large changes in the pressure distribution due to the simulated ice can be observed in the measured pitching moments of figure 54(c).

The break in the C_m curve, as shown in figure 54(c), was due to the rapidly growing separation bubble. When the simulated ice shape was located at $x/c = 0.02$, the break in the C_m curve occurred at $\alpha = 5°$. This is precisely the angle of attack at which the separation bubble started to grow rapidly, as figure 61 shows. Thus, the critical angle of attack at which the pitching moment becomes severely affected coincides with the start of the rapid bubble growth.

Figure 62(a) shows that at $\alpha = 0°$ the presence of the simulated ice shapes did not significantly alter the pressure distribution over the flap. However, as shown in figure 54(d), when the simulated ice shape was located at $x/c = 0.10$ and 0.20, the effect of the simulated ice shape was large when based on the clean value even though the changes are small in an absolute sense. At this angle of attack ($\alpha = 0°$), the simulated ice shape "unloaded" the flap (i.e., made C_h more positive). The relatively small absolute changes in C_h at this angle of attack may have been due to all of the separation bubbles reattaching upstream of the flap. At $\alpha = 5°$, the separation bubble did reach the flap when the simulated ice shape was located at $x/c = 0.10$ and 0.20. This resulted in a much larger pressure difference between the upper and lower surface of the flap, figure 62(b), when compared to the clean case. Figure 54(d) shows that at $\alpha = 5°$, the C_h for $x/c = 0.10$ and 0.20 cases were more than five times as negative as that of the clean case. When the simulated ice shape was located at $x/c = 0.02$, 0.10, and 0.20, the separation bubble reached the flap at $\alpha = 6.5°$, 1°, and 1°, respectively. These are approximately the angles of attack where the large breaks in C_h occurred. Thus from the analysis of the pressure distribution and flow

visualization, it is apparent that the critical angle of attack at which the C_h became severely affected coincided with the separation bubble reaching the flap. This explains why the critical angle of attack for C_m was 1° or 2° lower than that for C_h.

4.1.2 Effects of Simulated Ice Shape Size.

Figure 63 shows the effect of the simulated ice shape size on integrated aerodynamic coefficients of the NACA 23012m. Again, the forward-facing quarter round was used. The height of the simulated ice shape was varied from 0.10″ to 0.25″ (k/c = 0.056 to 0.0139) and were tested on the airfoil surface at x/c = 0.10. The boundary layer was tripped. Figure 63(a) shows significant variations in the lift curves with simulated ice shape height. As the simulated ice shape height was increased from 0.10″ to 0.25″, the $C_{\ell,max}$ decreased from 0.60 to 0.27. Also, the angle of attack at which the lift curve diverged rapidly from the clean case decreased from 5° to 2°. Increasing the ice shape height increased drag at all angles of attack as figure 63(b) shows. Figure 63(c) shows that the simulated ice shape height had a significant effect on the pitching moment as well. As the ice shape was increased from 0.10″ to 0.25″ the angle of attack at which the pitching moment started to diverge rapidly from the clean case decreased from 5° to -1°. Increasing the ice shape size from 0.10″ to 0.25″ decreased the angle of attack at which the flap hinge moment diverged rapidly from the clean case from 6° to 1°.

The reason for this behavior is that as the simulated ice shape height was increased, the separation bubble became larger in chordwise extent. This can be seen in the surface pressure plots of figure 64. The simulated ice shapes were located at x/c = 0.10 and the angle of attack was 5°. When the simulated ice shape was 0.10″ high, the separation bubble reattached near x/c = 0.45. When the ice shape was 0.15″ high, it was not clear where the reattachment location was because of the large effect on the flow field. However, it appeared that the reattachment took place near x/c = 0.65 because, downstream of this location, the C_p profile looked very similar to the clean case except for the 0.1 offset. When the simulated ice shape was 0.25″ high, the separation bubble did not reattach on the model. As the simulated ice shape height was increased, the C_p in the separation bubble increased as well. A reduction in the suction peak upstream of the ice shape was also observed as the ice shape height was increased. The higher C_p values in the separation bubble and the smaller suction peak decreased the lift (from to 0.51 to 0.25 as the ice shape height was increased from 0.10″ to 0.25″ at α = 5°). The longer separation bubble also resulted in earlier stall, higher drag, and an earlier divergence of the pitching and the flap hinge moments from the clean values, as figure 63 shows.

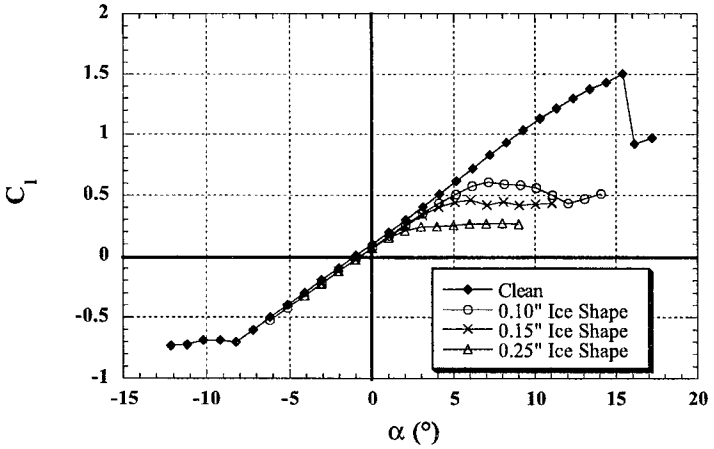

(a) Lift

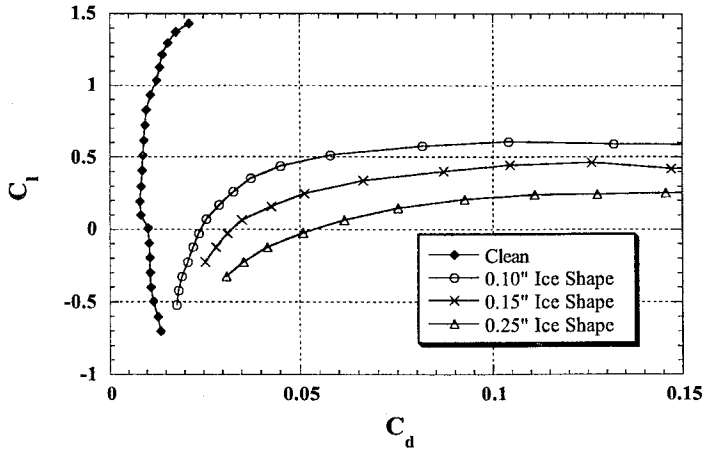

(b) Drag

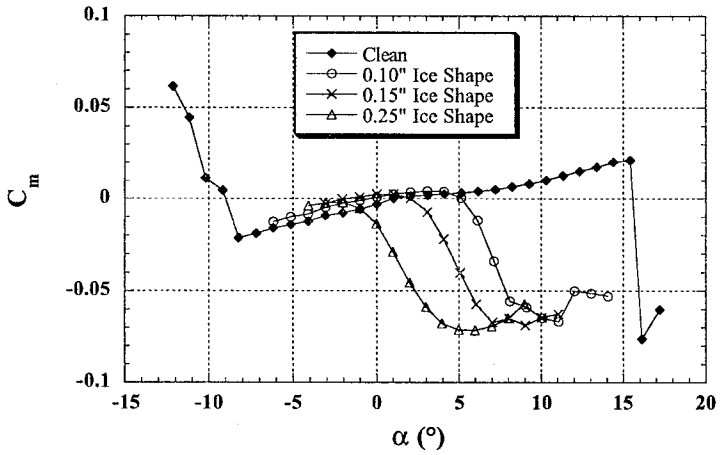

(c) Pitching Moment

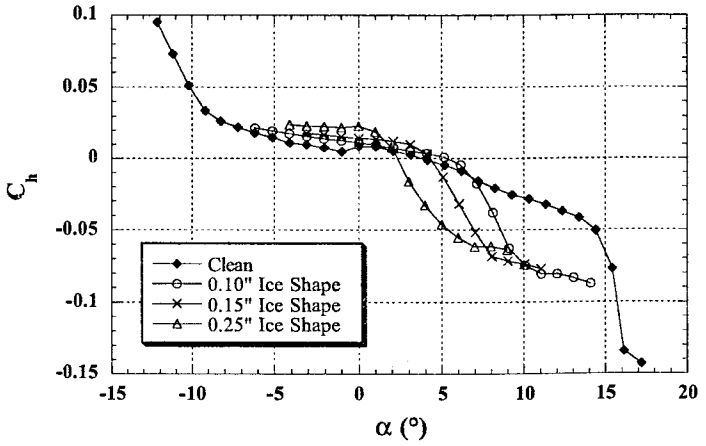

(d) Flap Hinge Moment

FIGURE 63. EFFECTS OF SIMULATED ICE SHAPE SIZE ON AERODYNAMIC COEFFICIENTS
(NACA 23012m, forward-facing quarter round at $x/c = 0.10$, boundary layer tripped, $Re = 1.8$ million)

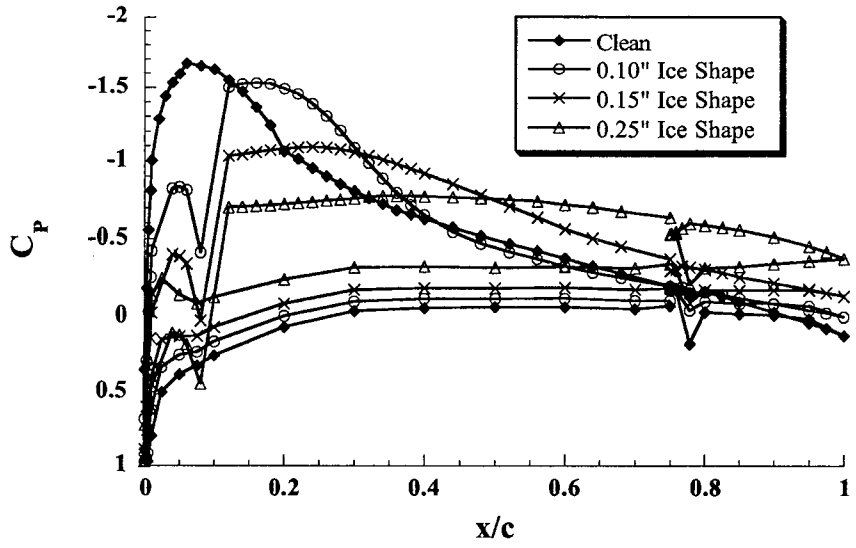

FIGURE 64. EFFECTS OF SIMULATED ICE SHAPE SIZE ON SURFACE PRESSURES (NACA 23012m, forward-facing quarter round at $x/c = 0.10$, boundary layer tripped, $\alpha = 5°$ $Re = 1.8$ million)

Figure 65 shows the summary of the $C_{\ell,max}$ with the three simulated ice shape sizes at various x/c locations. Also shown in the figure is the summary of $C_{\ell,max}$ with the 16-grit roughness (k/c = 0.0014, density = 30%) as described in section 2.1. It shows that increasing the simulated ice shape height decreased $C_{\ell,max}$ everywhere except at the leading edge. The simulated ice shape height did not have a large effect on $C_{\ell,max}$ at the leading edge, with the $C_{\ell,max}$ ranging from 0.92 to 1.01. In fact, the $C_{\ell,max}$ for the 0.15″ simulated ice shape was higher than that of the 0.10″ shape. Another interesting feature is that as the ice shape height was decreased from 0.25″ to 0.10″, the location of the minimum $C_{\ell,max}$ moved upstream from x/c = 0.12 to 0.10. This upstream movement of the minimum $C_{\ell,max}$ location with decreasing ice shape size is clearly evident in the roughness data. The 16-grit roughness had an average height of 0.025″, making it approximately 1/4 the height of the 0.10″ simulated ice shape (the smallest one that was tested). The minimum $C_{\ell,max}$ for the roughness occurred when it was located at x/c = 0.02 and continued the trend of the simulated ice shapes. When the roughness was placed at the leading edge, the $C_{\ell,max}$ was 0.90, which was similar to what was observed for the ice shapes. The upstream movement of the minimum $C_{\ell,max}$ location was probably due to the following reason. As the simulated ice shape size was decreased, the critical location became more sensitive to the location of the maximum local air velocity and less on the location of the maximum adverse pressure gradient. This was because as the simulated ice became smaller (with smaller separation bubbles), the momentum removal becomes more important than the separation bubble. Since the location of the maximum local velocity is closer to the leading edge than that of the maximum adverse pressure gradient, the ice shape location with the lowest $C_{\ell,max}$ moved upstream as the ice shape size was decreased.

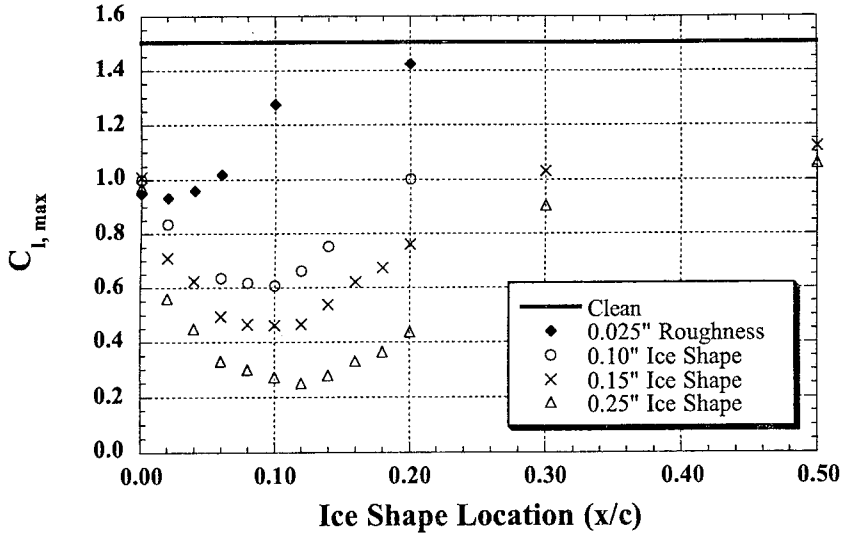

FIGURE 65. SUMMARY OF $C_{\ell,max}$ WITH VARIOUS SIMULATED ICE SHAPE SIZE AND LOCATIONS
(NACA 23012, forward-facing quarter round, boundary layer tripped for case with simulated ice at $x/c \geq 0.04$, $Re = 1.8$ million)

4.1.3 Effect of Simulated Ice Shape Geometry.

The effects of the simulated ice shape geometry on airfoil aerodynamics were also studied in order to understand what the critical features were. Figure 66 shows the effect of various geometries (as shown in figure 6) on integrated aerodynamic coefficients. All of the simulations shown in figure 66 had a height of 0.25″. Figure 66(a) shows that the forward-facing quarter round had a $C_{\ell,max}$ of 0.27 while the backward-facing quarter round had a $C_{\ell,max}$ of 0.34. The backward-facing quarter round had only a slightly less severe effect on lift than the forward-facing quarter round even though the side facing the flow was much more streamlined. The half round had a significantly higher $C_{\ell,max}$ (0.58) than the backward-facing quarter round even though they had an identical forward face exposed to the flow. Thus, the geometry of the downstream side had a significant effect on lift. However, this was the case only when the face exposed to the flow is streamlined (such as with the backward-facing quarter round and the half round). Figure 66(a) shows that the forward-facing quarter round and the ramp shape had nearly identical lift curves even though they had very different downstream sides. Thus, for the two shapes with very blunt forward faces, the shape of the backward face was not as important (for the shapes tested).

Figure 66(b) shows the effect of the simulated ice shape geometry on drag. It shows that the forward-facing quarter round and the ramp shape had nearly identical drag polars. Of the simulated iced cases, the half round had the least drag, followed by the backward-facing quarter round.

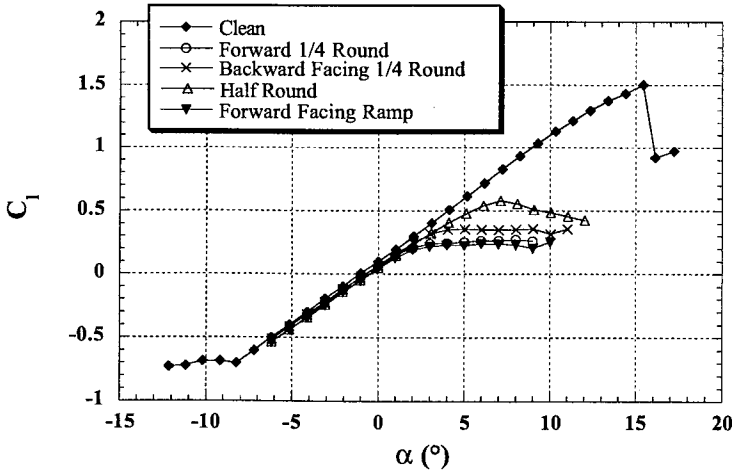

(a) Lift

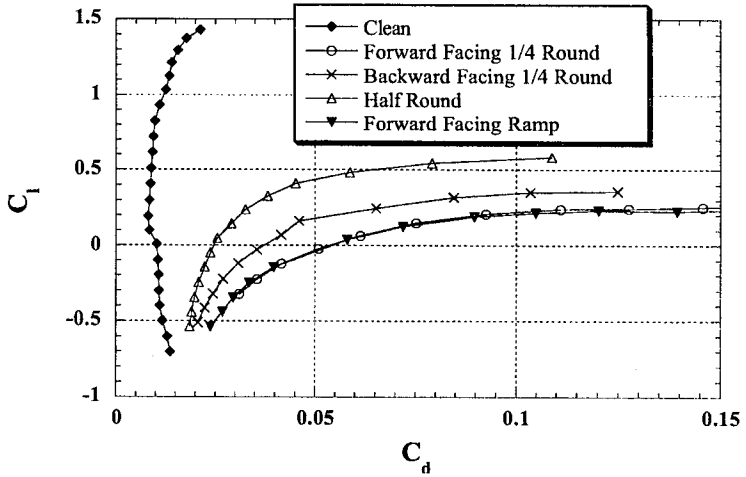

(b) Drag

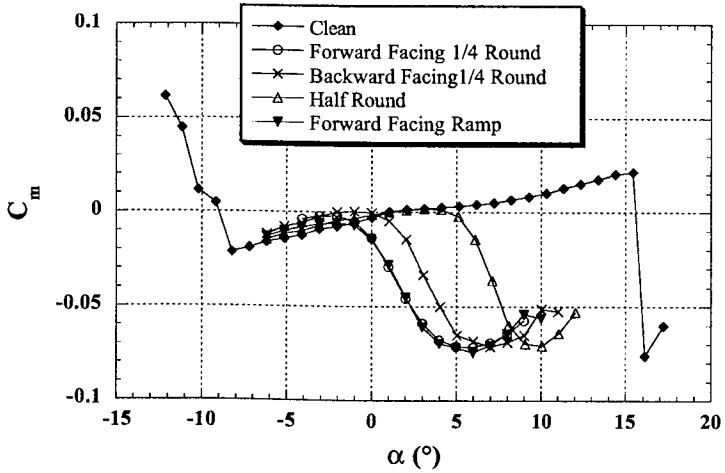

(c) Pitching Moment

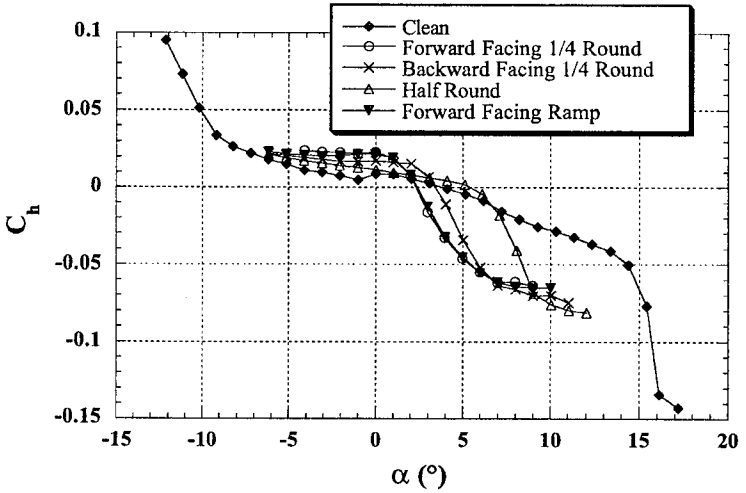

(d) Flap Hinge Moment

FIGURE 66. EFFECTS OF SIMULATED ICE SHAPE GEOMETRY ON AERODYNAMIC COEFFICIENTS (NACA 23012m, simulated ice shapes at $x/c = 0.10$, $k/c = 0.25''$, boundary layer tripped, $Re = 1.8$ million)

Similar effects were observed for the pitching and flap hinge moments, as shown in figures 66(c) and 66(d). It shows that the backward-facing quarter round experienced C_m and C_h divergence at a higher α than the forward-facing quarter round. The half round, in turn, had the divergence at a significantly higher α than the backward-facing quarter round. Finally, the forward-facing quarter round and the ramp shape had nearly identical flap hinge curves.

4.1.4 Effects of Roughness Near Ice Shape.

SLD icing flight tests have shown the presence of roughness-type accretion upstream and downstream of the spanwise ice shape. Thus, it was important to understand the effect of the roughness-type accretion on the iced airfoil aerodynamics. The roughness-type accretion was simulated using 16-grit roughness tape extending upstream and downstream from the simulated ice shape (with k/c = 0.0014, density = 30%). The size and density of the roughness was identical to the roughness only case in figure 65. Figure 67(a) shows the result of the roughness on lift. In all of the cases, a 0.25″ forward-facing quarter round was used at x/c = 0.10. Unlike in the other cases, the boundary layer on the upper surface was not tripped. That is the reason why the no-roughness $C_{\ell,max}$ shown in figure 67(a) was 0.37, and the $C_{\ell,max}$ shown in figure 54(a) was 0.27. The various extents of the roughness that were tested did produce large relative changes in lift, but they were not large in an absolute sense since the C_ℓ values were so low. Figure 67(a) shows that the lowest $C_{\ell,max}$ (0.31) resulted when the roughness extended 0.5″ in front of the ice shape. When the chordwise roughness extent was smaller than 0.25″, most or all of the roughness was located inside the separation bubble that formed upstream of the ice shape, lessening its effect ($C_{\ell,max}$ = 0.34). When the roughness extent was increased from 0.5″ to 2″, the $C_{\ell,max}$ increased from 0.31 to 0.37. This may have happened because the roughness decreased the effective height of the ice shape by displacing the boundary layer upwards. Figure 67(a) also shows that when the 2″ chordwise extent roughness was placed immediately downstream of the roughness in addition to the 1″ extent upstream, the resulting $C_{\ell,max}$ was 0.32. This was slightly lower than the case with only the 1″ extent upstream roughness ($C_{\ell,max}$ = 0.34). Thus, the roughness downstream of the ice shape had a measurable effect on lift even though it was completely submerged within the long separation bubble that formed downstream of the ice shape.

The effect of the surface roughness on drag is shown on figure 67(b). It shows that the surface roughness extent did have measurable effects on drag, although they were not large. Of the cases tested, the 2″ roughness extent had the least drag.

Figures 67(c) and 67(d) show the effects of surface roughness extent on the pitching and flap hinge moments. Again, they show that the surface roughness extent did not have a large effect on C_m and C_h. However, as before, the 2″ roughness extent had the least aerodynamic degradation, as the C_m and C_h curves diverged from the clean case at a higher α than the other cases tested.

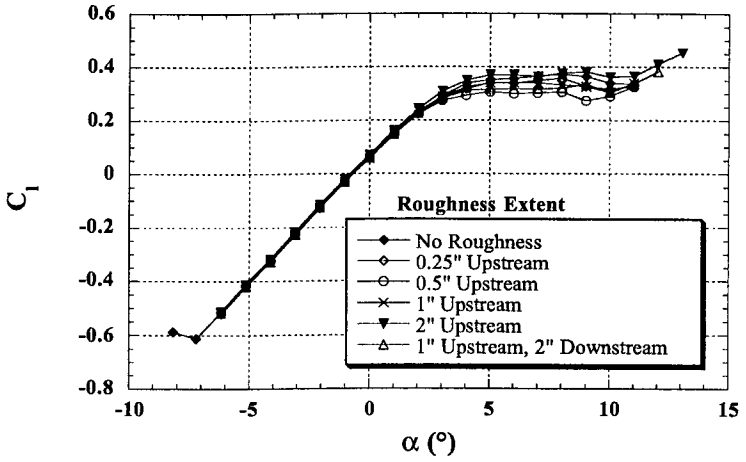

(a) Lift

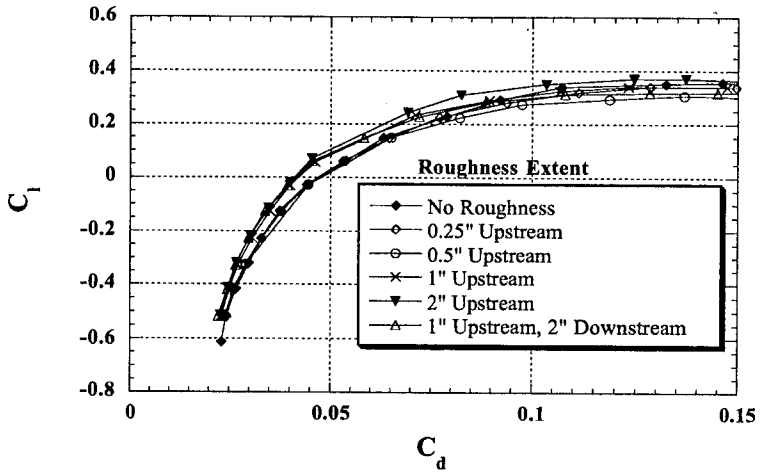

(b) Drag

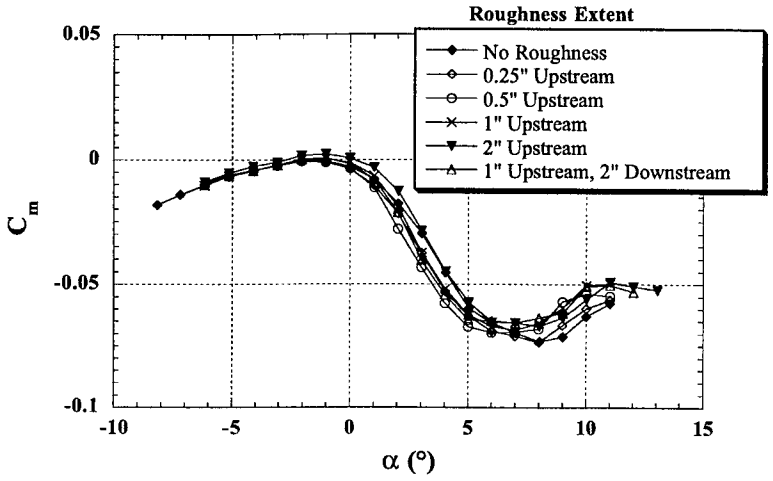

(c) Pitching Moment

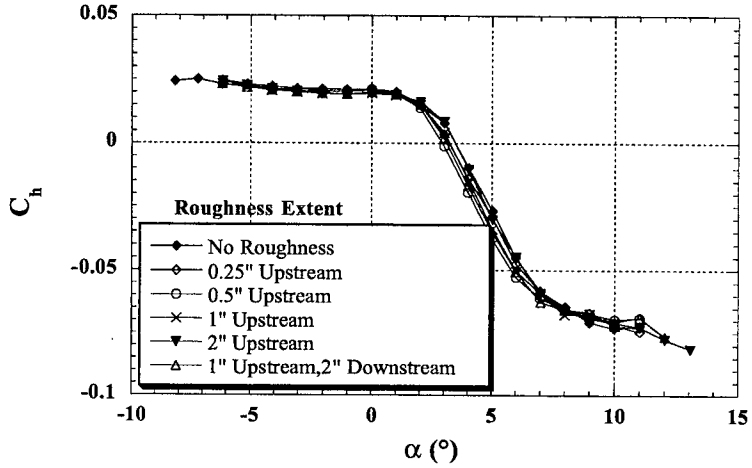

(d) Flap Hinge Moment

FIGURE 67. EFFECTS OF SURFACE ROUGHNESS IN ADDITION TO SIMULATED ICE SHAPE ON AERODYNAMIC COEFFICIENTS
(NACA 23012m, 0.25″ forward-facing quarter round at x/c = 0.10, Re = 1.8 million)

4.1.5 Effects of Spanwise Gaps.

In SLD aircraft icing tests [71], the spanwise ice accretion was observed to partially shed, leaving spanwise gaps. This causes the ice accretion and the associated flow field to be strongly three-dimensional. Because of this, cases were run in order to simulate the ice accretion after partial shedding. The baseline 0.25″ forward-facing quarter round was tested with nominal spanwise gaps of 2.5″ and 5″. The simulated ice accretion span was kept at 6″. The schematics of the spanwise gaps are shown in figure 15. The model on the left has 2.5″ spanwise gaps and the model on the right has 5″ spanwise gaps. The direction of the flow is from the left to the right. This particular arrangement was chosen in order to keep one of the simulated ice shape spans over the model's surface taps.

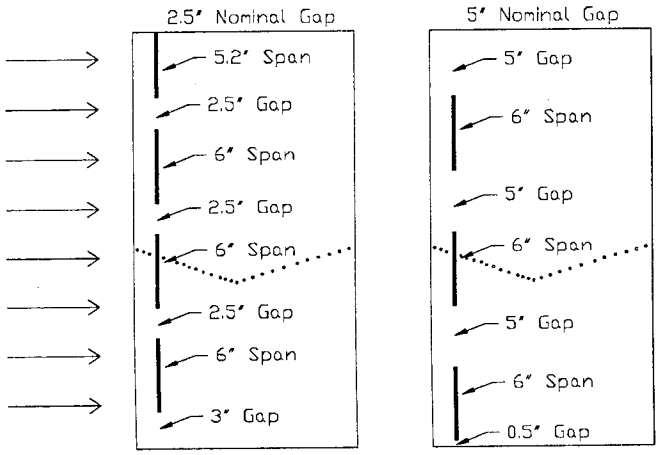

FIGURE 68. SPANWISE GAP GEOMETRY
(NACA 23012m, 0.25″ forward-facing quarter round at $x/c = 0.10$,
boundary layer tripped, $Re = 1.8$ million)

Figure 69 shows the effects of spanwise gaps on the aerodynamic coefficients. All of the data shown in this figure were derived from the force balance measurements because the pressure measurements cannot capture spanwise variations in highly 3-D flow. Figure 69(a) shows that the presence of the spanwise gaps significantly increased the lift in the nonlinear range when compared to the full-span simulated ice case. However, the lift curves became nonlinear at nearly the same angle of attack (3°). Also, there was not a large difference in the lift curve between the 2.5″ and 5″ gap cases (the 5″ gap case had slightly higher lift). Figure 69(b) shows the effect of spanwise gaps on drag. Again, it shows that the spanwise gaps significantly reduced drag when compared to the full-span case. The 5″ gap case had less drag than the 2.5″ case because it had less flow blockage.

Figures 69(c) and 69(d) show the effect of the spanwise gaps on pitching and flap hinge moments. The gaps significantly delayed the onset of the divergence of C_m and C_h from the clean model values. The divergence in C_m (for both 2.5″ and 5″ gap cases) occurred at $\alpha = 4°$, instead of $\alpha = 0°$ for the full-span case. The divergence in C_h occurred at $\alpha = 4°$, instead of $\alpha = 1°$.

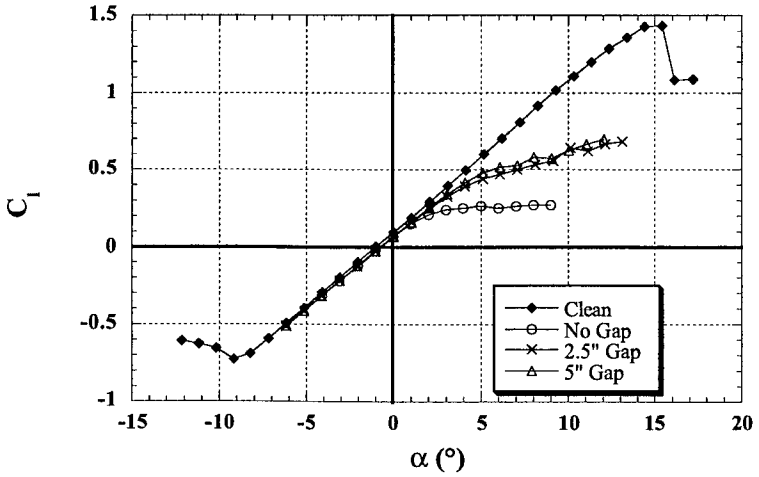

(a) Lift

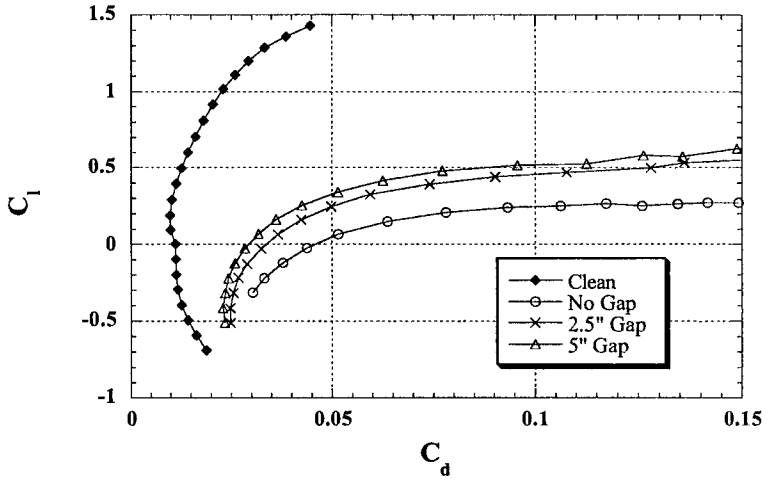

(b) Drag

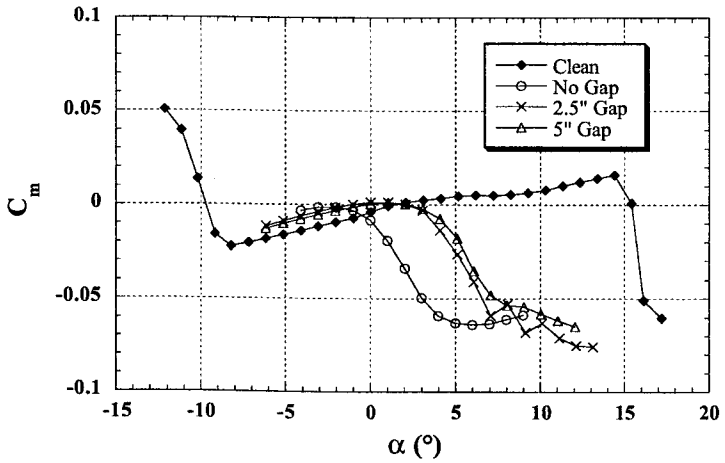

(c) Pitching Moment

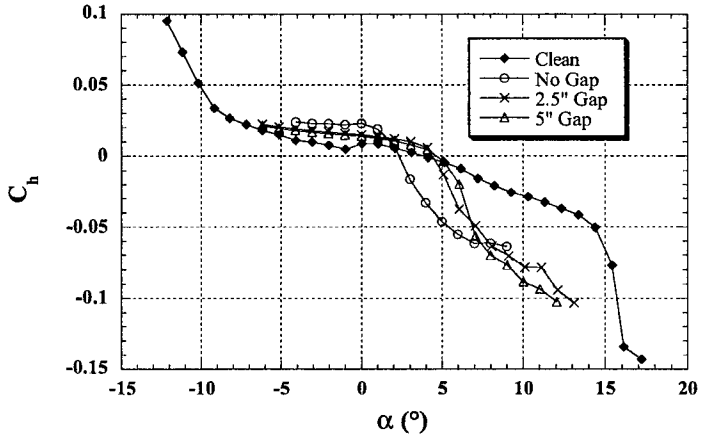

(d) Flap Hinge Moment

FIGURE 69. EFFECTS OF SPANWISE GAP ON AERODYNAMIC COEFFICIENTS
(NACA 23012m, 0.25″ forward-facing quarter round at x/c = 0.10, data derived from force balance, boundary layer tripped, Re = 1.8 million)

4.1.6 Effect of Simulated Ice Accretion on the Lower Surface.

In a typical icing encounter, ice accretes on the lower surface as well as the upper surface. Thus, the NACA 23012m was tested with the baseline 0.25″ quarter round on the upper and lower surface. Figure 70 shows the aerodynamic coefficients with the simulated ice shape placed at $x/c = 0.10$ on the upper and lower surfaces. The boundary layer was tripped on both upper and lower surfaces. The lift and pitching moment data shown were derived from the force-balance measurements. This was because when the simulated ice shape was located at $x/c = 0.10$ on the lower surface, there were not enough pressure taps left available on the lower surface to accurately generate lift and pitching moment (due to sparse pressure tap distribution on the lower surface). The drag data, however, were still derived from the wake pressure measurements.

Figure 70(a) shows that when the simulated ice shape was located only on the lower surface, its effect on lift much less severe than when it was located on the upper surface. The $C_{\ell,max}$ when the simulated ice accretion was placed only on the lower surface was 1.26. This was much greater than the $C_{\ell,max}$ of 0.27 when the simulated ice shape was located on the upper surface only. The worst lift degradation occurred when the simulated ice accretion was located on both the upper and the lower surface, with a $C_{\ell,max}$ of 0.21. However, the lift curve was very similar to the case where the simulated ice accretion was located only on the upper surface. The simulated ice shape on the lower surface did not have a large effect on lift because at positive angles of attack, the pressure gradient on the lower surface is very favorable. Thus, the separation bubble due to the simulated ice shape was much smaller than that on the upper surface.

Figure 70(b) shows the effect of the lower surface simulated ice accretion on drag. It shows that when the simulated ice accretion was located only on the upper surface, it produced large increases in drag only at positive lift (i.e., positive α). When the simulated ice accretion was located only on the lower surface, large increases in drag were observed only at negative lift. When the simulated ice shape was located at both the upper and lower surfaces, large increases in drag were observed at both negative and positive lift (and were close to the sum of the upper-only and lower-only cases).

Figure 70(c) and 70(d) show the effect of the lower surface ice accretion on pitching and flap hinge moments. It shows that when the simulated ice accretion was located only on the lower surface, the C_m and C_h curves were very similar to that of the clean model case. When the simulated ice accretion was located on both the upper and lower surfaces, the C_m and C_h curves were very similar to that of the case where the simulated ice accretion was located only on the upper surface.

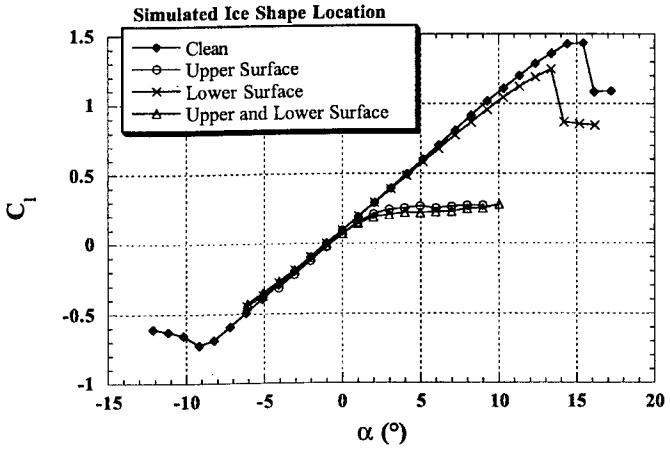

(a) Lift

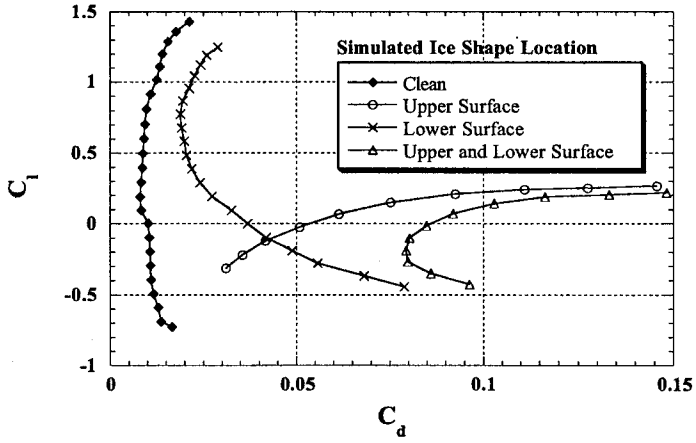

(b) Drag

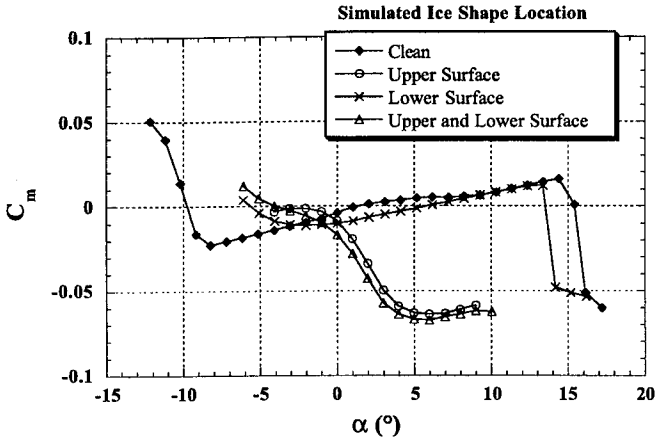

(c) Pitching Moment

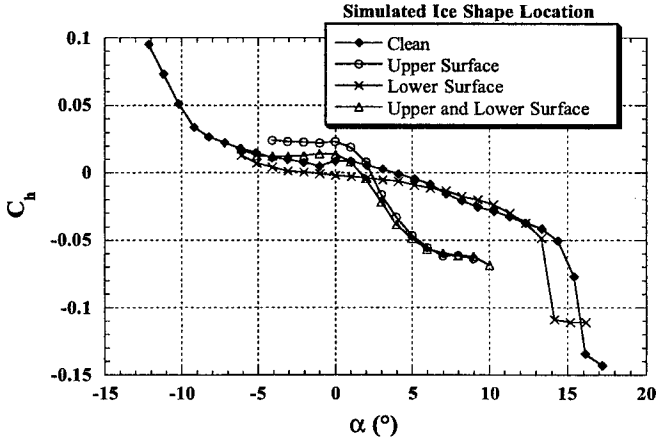

(d) Flap Hinge Moment

FIGURE 70. EFFECTS OF LOWER SURFACE SIMULATED ICE ACCRETION ON AERODYNAMIC COEFFICIENTS (NACA 23012m, 0.25″ forward-facing quarter round at $x/c = 0.10$. C_ℓ and C_M derived from force balance, boundary layer tripped, $Re = 1.8$ million)

4.1.7 Effects of Airfoil Geometry.

The importance of airfoil geometry on iced airfoil aerodynamics was investigated by testing the simulated ice shapes on the NLF 0414 airfoil, which has aerodynamic characteristics quite different from the NACA 23012m. Studying the effect of simulated ice shapes on two very different airfoils provided a clearer explanation of the aerodynamic factors that determine the critical ice shape location.

4.1.7.1 Comparison of Clean Models.

Large differences in the iced airfoil aerodynamics between the NACA 23012m and the NLF 0414 were observed. This was because these two airfoils have very different geometry and aerodynamic characteristics. Figure 71 shows the comparisons between the NACA 23012m and the NLF 0414 geometry. The NACA 23012m was designed to provide low pitching moment by generating most of the lift near the leading edge. The NLF 0414, however, was designed to achieve laminar flow over the airfoil by distributing the load over a large portion of the chord and delaying the onset of pressure recovery and the accompanying large adverse pressure gradient (where transition occurs) until around 70% chord.

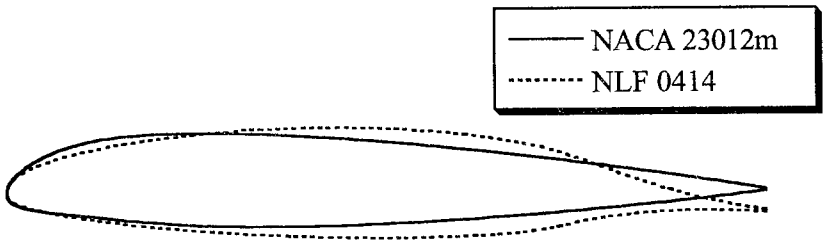

FIGURE 71. COMPARISON OF NACA 23012m AND NLF 0414 GEOMETRY

The different aerodynamic characteristics are quite apparent in the measured clean-model surface pressure of figure 72. In this figure, the surface pressures are compared at nearly identical lift coefficients. However, because the NLF 0414 is highly cambered, it's α was much lower than that of the NACA 23012m. On the NACA 23012m, there is a strong suction peak centered at $x/c = 0.08$, followed by an adverse pressure gradient that extended to the trailing edge. On the NLF 0414, a leading-edge suction peak was not present. Instead, after the initial acceleration around the leading edge to $x/c = 0.02$, the surface pressure was nearly constant ($C_p \approx -0.8$) to $x/c = 0.73$. The pressure recovery process began at this point and the adverse pressure gradient extended from here to the trailing edge. Since the flow around the nose on the NACA 23012m accelerated to a $C_{p,min} = -1.7$ versus only -0.9 for the NLF 0414, much more pressure recovery was required on the NACA 23012m airfoil.

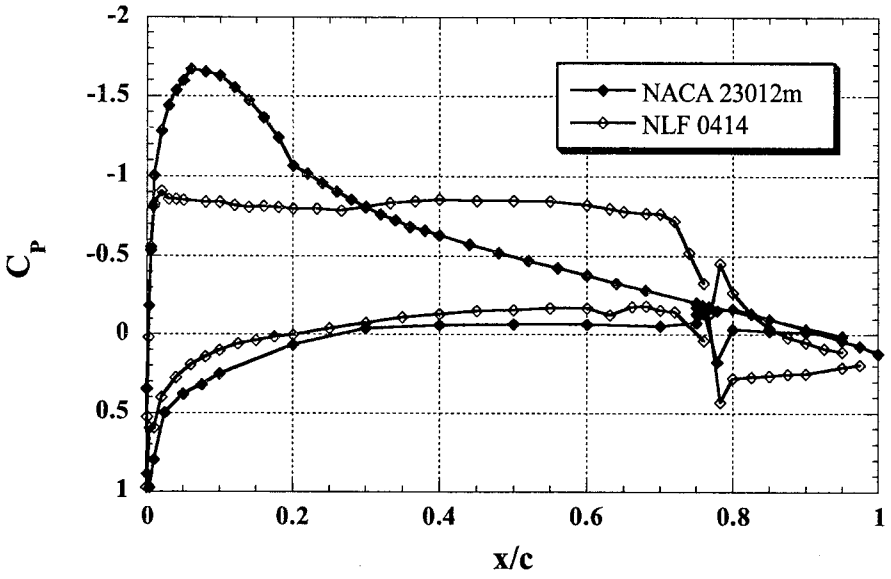

FIGURE 72. COMPARISON OF NACA 23012m AND NLF 0414 CLEAN MODEL PRESSURE DISTRIBUTION

4.1.7.2 Effect of Ice shape Locations.

All of the results in this section were with the 0.25″ forward-facing quarter-round ice shape simulation. The boundary layer was tripped at $x/c = 0.02$ on the upper surface and $x/c = 0.05$ on the lower surface. The boundary layer was not tripped for the clean model or when the ice shape was located at $x/c = 0.02$. The Reynolds number was 1.8 million.

The differences in the airfoil geometry (and the resulting clean airfoil aerodynamic characteristics) between the NACA 23012m and NLF 0414 led to large differences in behavior with simulated ice shapes. Figure 73 shows the effect of simulated ice shape on the lift of the two airfoils. Varying the ice shape location from $x/c = 0.02$ to 0.20 had large effects on the lift of the NACA 23012m (figure 73(a)). The loss in lift was most severe when the ice shape was located at $x/c = 0.10$ (with $C_{\ell,max} = 0.27$). When the ice shape was located at $x/c = 0.02$, $C_{\ell,max}$ was approximately doubled.

Figure 73(b) shows the effect of simulated ice on the lift of the NLF 0414. When the simulated ice shape location was varied from $x/c = 0.02$ to 0.20, the lift curves did not vary significantly, with only slight changes in the $C_{\ell,max}$ and α_{stall}. The maximum lift was also much higher than on the NACA 23012m, with a typical value of 0.70. When the ice shape was located at $x/c = 0.40$, the lift curve was significantly different as it did not have a clearly defined $C_{\ell,max}$. Instead, there was an inflection in the lift curve at $\alpha = 0°$ due to the separation of the flow downstream of the simulated ice shape.

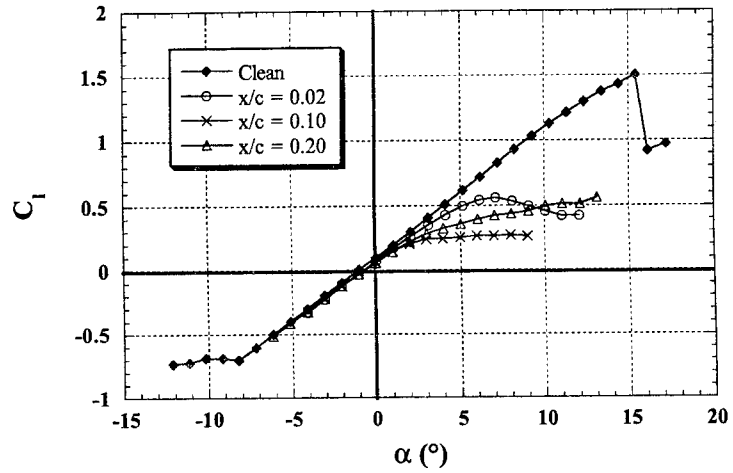

(a) NACA 23012m

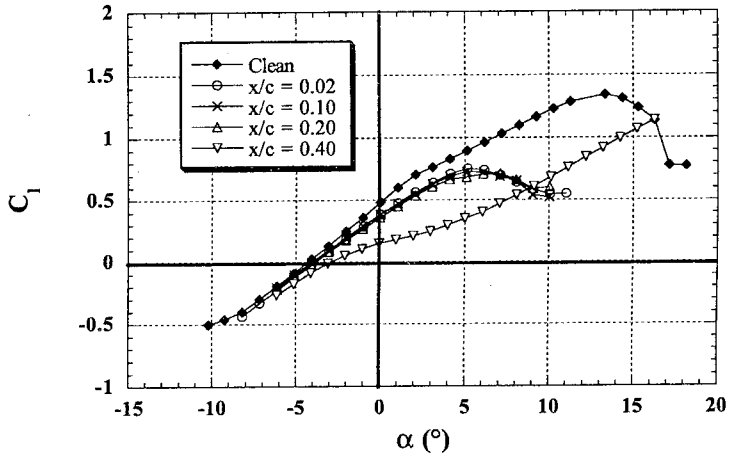

(b) NLF 0414

FIGURE 73. EFFECT OF SIMULATED ICE SHAPE LOCATION ON LIFT
(0.25″ forward-facing quarter round, $Re = 1.8 \times 10^6$, boundary layer tripped)

The large differences between the NACA 23012m and NLF 0414 airfoils can also be seen in figure 74, a summary of $C_{\ell,max}$ as a function of ice shape location. The lowest $C_{\ell,max}$ for the NACA 23012m was 0.25 (an 83% reduction from the clean value) when the simulated ice shape was located at $x/c = 0.12$. Thus, this was the critical ice shape location on the NACA 23012m as the maximum lift increased rapidly as the simulated ice was moved upstream and downstream of this location. Figure 74 shows that on the NLF 0414, the variations in the ice shape location did not have a large effect on $C_{\ell,max}$ between $x/c = 0.02$ and $x/c = 0.20$. The $C_{\ell,max}$ varied only between 0.68 and 0.79 when the ice shape was located in this region. These values were much higher than those observed for the NACA 23012m. When the simulated ice shape was located at $x/c = 0.30$, the $C_{\ell,max}$ dropped to 0.58 and then to 0.21 at $x/c = 0.50$. However, the lift curves for these cases did not have a true $C_{\ell,max}$ in the classical sense. Instead, only an inflection in the lift curve was observe where the flow downstream of the simulated ice shape had failed to reattach.

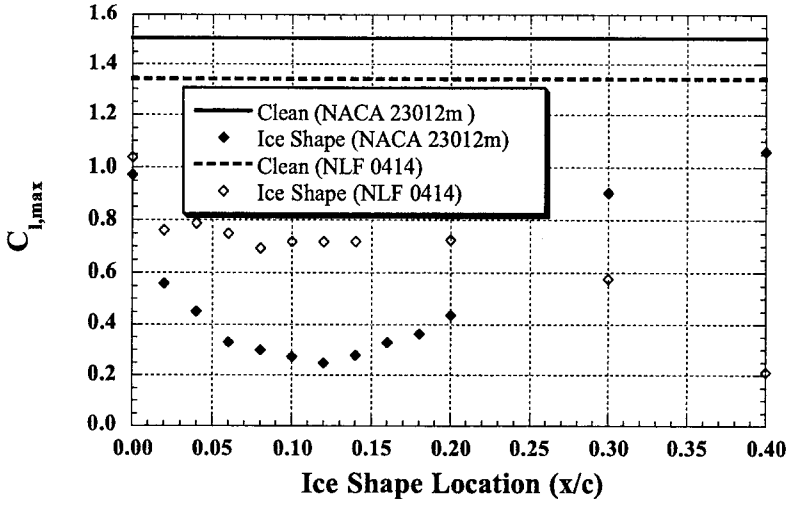

FIGURE 74. SUMMARY OF $C_{\ell,max}$ WITH 0.25″ FORWARD-FACING QUARTER-ROUND SIMULATED ICE SHAPE AT VARIOUS CHORDWISE LOCATIONS ($Re = 1.8 \times 10^6$)

Figure 75 shows the drag comparisons. Both of the models showed large increases in drag with the presence of the simulated ice shape. On the NACA 23012m, the drag increases were much smaller when the simulated ice shape was located at $x/c = 0.02$. On the NLF 0414, similar drag increases were observed when the simulated ice shape was located at $x/c = 0.02$, 0.10, and 0.20. However, much large increases were observed when the simulated ice shape was located at $x/c = 0.40$.

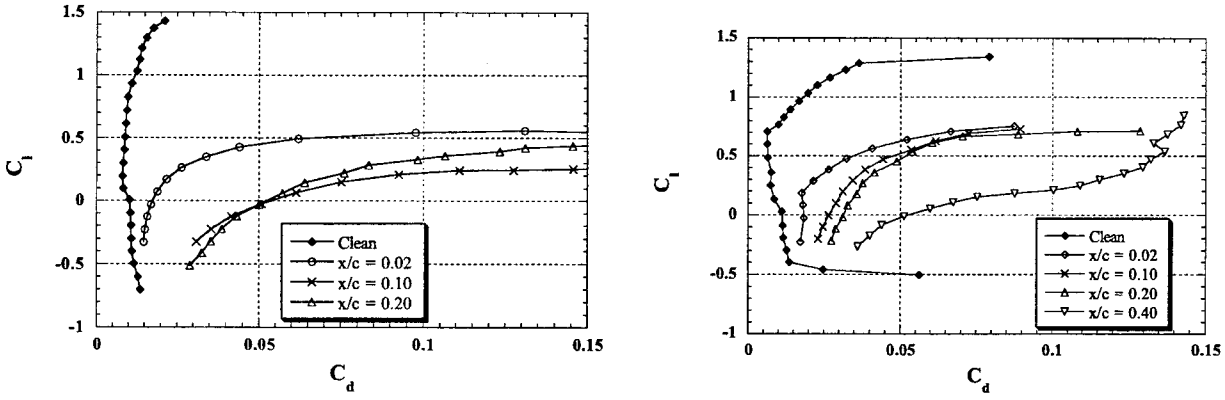

(a) NACA 23012m (b) NLF 0414

FIGURE 75. EFFECT OF SIMULATED ICE SHAPE LOCATION ON DRAG (0.25″ forward-facing quarter round, $Re = 1.8 \times 10^6$, boundary layer tripped)

The pitching moment comparisons are shown in figure 76. The simulated ice shapes caused large changes in the pitching moment on both airfoils. There were large breaks in the pitching

moment curves on both of the models. However, on the NLF 0414, this break in C_m was not present when the simulated ice shape was located at $x/c = 0.40$.

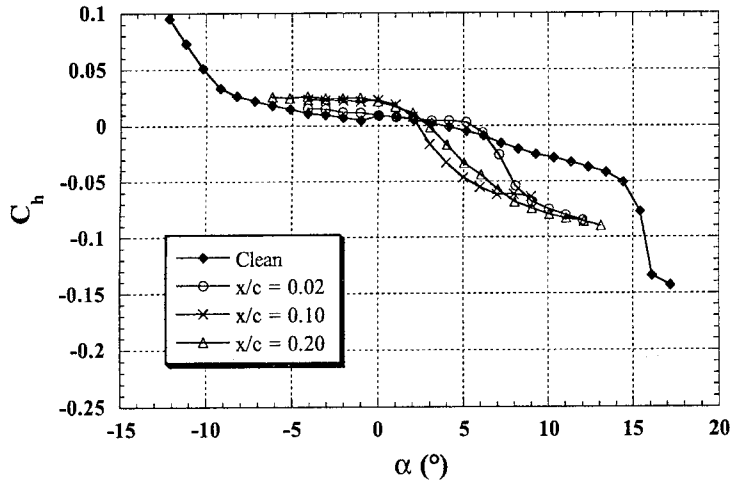

(a) NACA 23012m

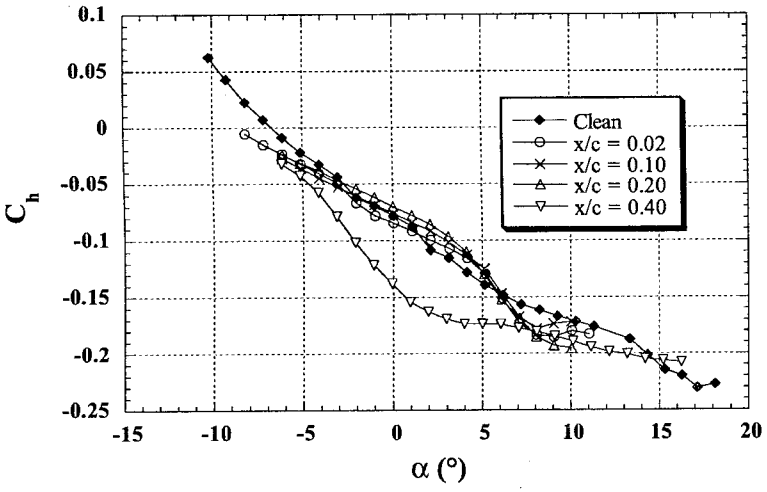

(b)

FIGURE 76. EFFECT OF SIMULATED ICE SHAPE LOCATION ON PITCHING MOMENT (0.25″ forward-facing quarter round, $Re = 1.8 \times 10^6$, boundary layer tripped)

Figure 77 shows the comparisons of the flap hinge moments. On the NACA 23012m (figure 77(a)), the ice shape produced a significant change in the C_h curve (compared to the clean case) at all ice shape locations. The rapid divergence of the flap hinge moment varied from $\alpha = 1°$ (for $x/c = 0.10$ and 0.20) to 6° (for $x/c = 0.02$). The ice shape did not produce significant changes in the C_h values for the NLF 0414 when it was located between $x/c = 0.02$ and 0.20 (figure 77(b)). However, the slope $C_{h,\alpha}$ was more negative at about $\alpha = 5°$, where the airfoil was stalling. When the ice shape was at $x/c = 0.40$, the C_h was significantly more negative (or flap up) than the clean case between $\alpha = -5°$ and 7°. At the other angles of attack, the values did not vary by a large amount.

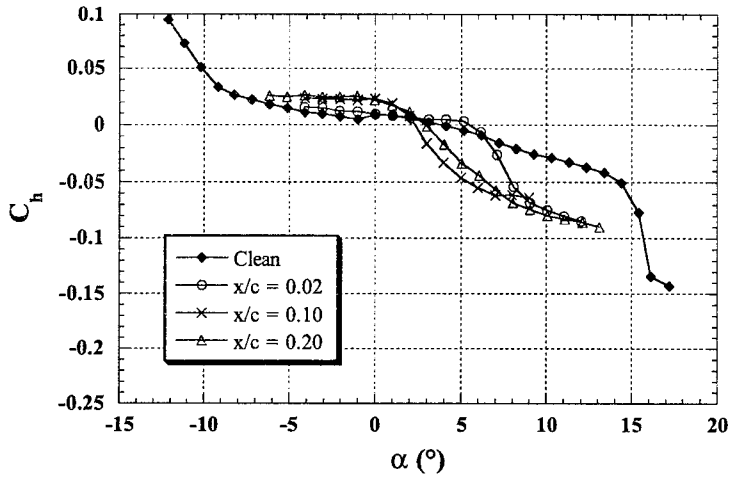

(a) NACA 23012m

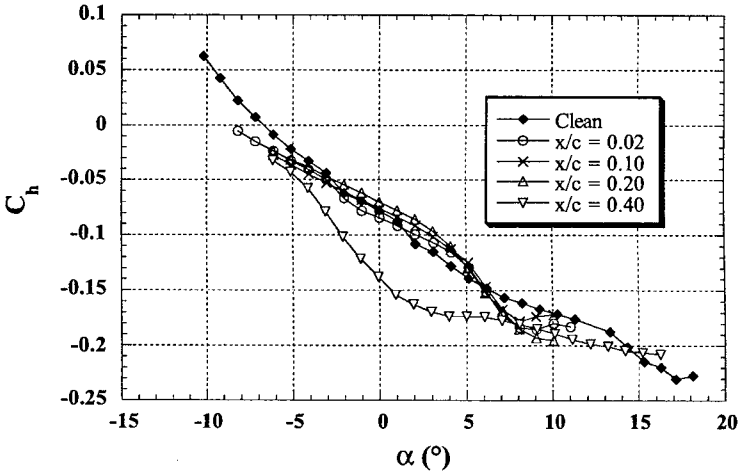

(b) NLF 0414

FIGURE 77. EFFECT OF SIMULATED ICE SHAPE LOCATION ON FLAP HINGE MOMENT
(0.25″ forward-facing quarter round, $Re = 1.8 \times 10^6$, boundary layer tripped)

Figure 78 shows ΔC_d, the drag increase due to the ice shape when compared to the clean airfoil, for the 0.25″ ice shape. Figure 78(a) shows the drag increase on the NACA 23012m. It shows that the most critical location of the simulated ice shape (in terms of ΔC_d) moved upstream with increasing angles of attack and closely coincided with the location of the maximum local air velocity. Figure 78(b) shows the drag increase on the NLF 0414. At angles of attack of -3° and 0°, a leading-edge suction peak was not observed. Instead, the highest local air velocity occurred near mid chord at $x/c = 0.55$ (for $\alpha = -3°$) and 0.45 (for $\alpha = 0°$). The location of maximum adverse pressure gradient was located at the trailing edge pressure recovery near $x/c = 0.75$. Because the simulated ice shape was not tested at $x/c > 0.50$, some of these points described above are not shown in figure 78(b). At angles of attack of 3° and 5°, a leading-edge suction

peak was present, with the location of the $C_{p,min}$ at $x/c = 0.01$. The location of the maximum adverse pressure gradient was located immediately downstream of the $C_{p,min}$ and not at the trailing edge pressure recovery. At angles of attack of -3° and 0° (where there was no leading-edge suction peak on the clean model), there was a gradual increase in ΔC_d as the ice shape was moved downstream from the leading edge to $x/c = 0.30$. As the ice shape was moved further downstream, ΔC_d increased at a much faster rate. At angles of attack of 3° and 5°, ΔC_d was relatively constant between $x/c = 0.02$ and $x/c = 0.20$, after which ΔC_d started to increase rapidly. The ΔC_d values eventually reached a maximum (at $x/c = 0.4$ for $\alpha = 3°$ and at $x/c = 0.35$ for $\alpha = 5°$) after which they decreased. Unlike the NACA 23012m, the location of the maximum local air velocity was not a good indicator of the most critical simulated ice shape location.

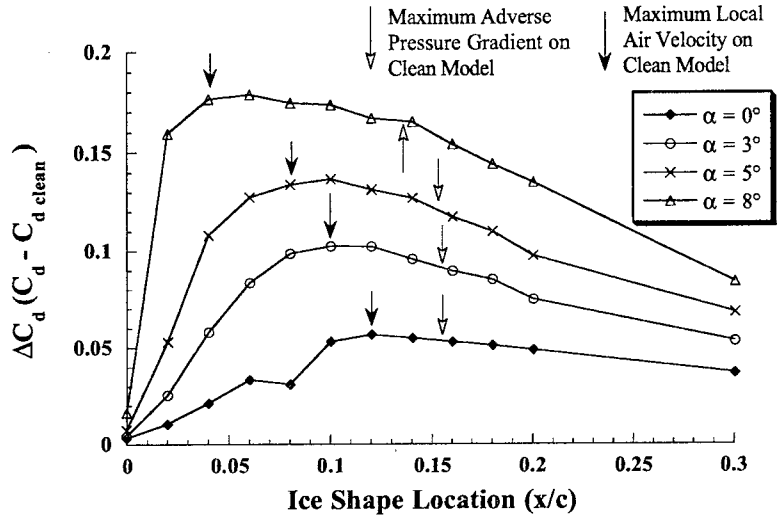

(a) NACA 23012m

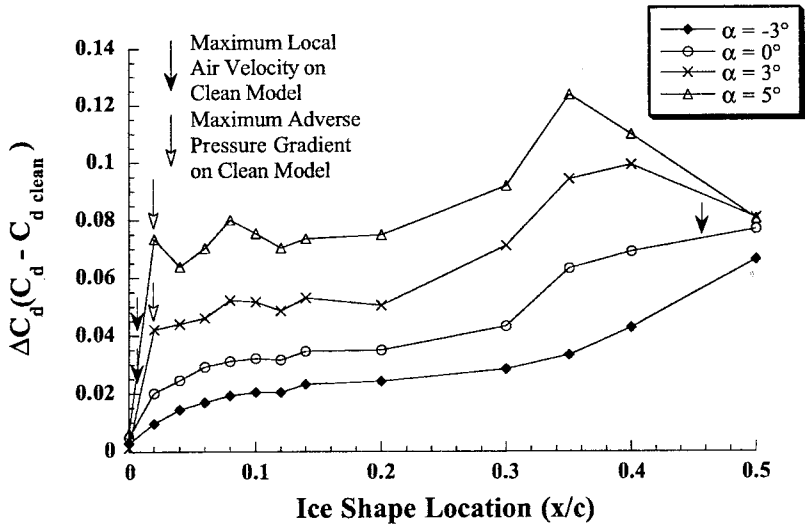

(b) NLF 0414

FIGURE 78. DRAG INCREASE DUE TO ICE SHAPE
(0.25″ forward-facing quarter round, $Re = 1.8 \times 10^6$, boundary layer tripped)

Figure 79 shows the lift loss ΔC_l (when compared to the clean airfoil) due to the 0.25″ ice shape simulation. On the NACA 23012m (figure 79(a)), the most critical location of the simulated ice shape (in terms of lift loss) was between x/c = 0.10 and 0.12 and did not vary significantly with angle of attack. This was the same location that resulted in the lowest $C_{\ell,max}$, as shown in figure 74. The most critical location was situated between the locations of the maximum local air velocity and the maximum adverse pressure gradient. Thus, it did appear that the most critical ice shape location was related to these flow features.

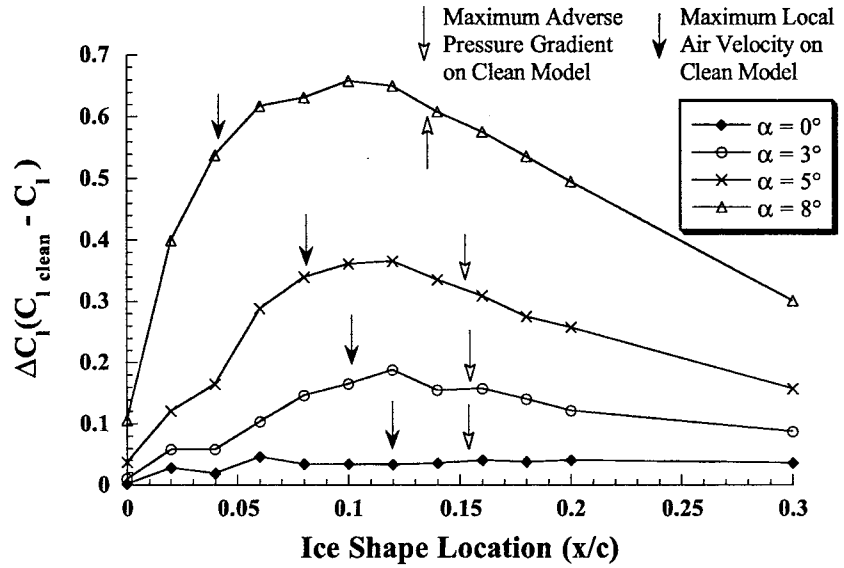

(a) NACA 23012m

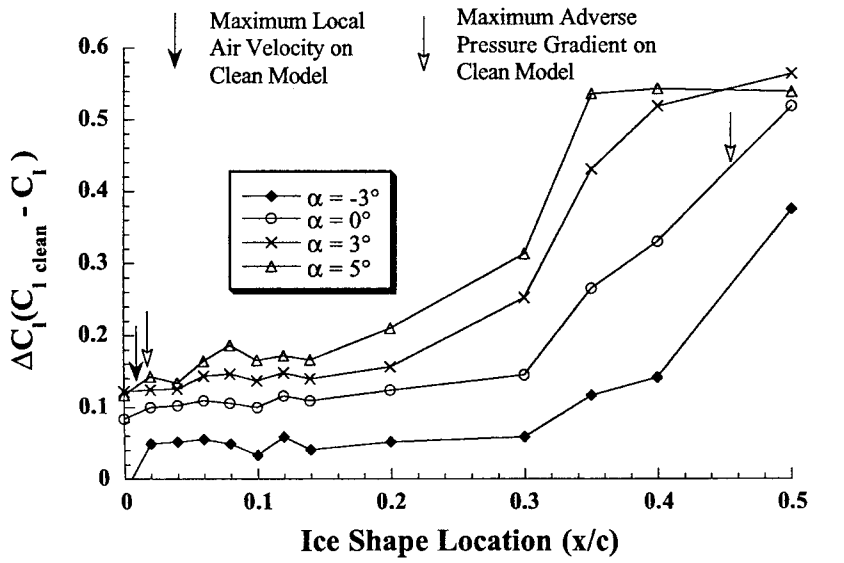

(b) NLF 0414

FIGURE 79. LIFT LOSS DUE TO ICE SHAPE
(0.25″ forward-facing quarter round, $Re = 1.8 \times 10^6$, boundary layer tripped)

The lift loss behavior of the NLF 0414 airfoil, as shown in figure 79(b), was quite different from that of NACA 23012m. Figure 79(b) shows that when the ice shape was placed between the leading edge and $x/c = 0.20$, there was not a large variation in the lift loss. This was similar to what was observed in the $C_{\ell,max}$ plot of figure 74. It was only when the ice shape was located downstream of $x/c = 0.30$ and closer to the adverse pressure gradient at the trailing-edge pressure recovery that a much larger increase in the lift loss was observed. This was even the case at $\alpha = 3°$ and 5° where the adverse pressure gradient associated with the leading-edge suction peak was more severe than the trailing-edge pressure recovery. Unlike the NACA 23012m, loss in lift increased with increasing chordwise location, and the locations of maximum local air velocity and adverse pressure gradient were not proper indicators for critical locations.

4.1.7.3 Flow Field Comparisons.

The flow field of the NACA 23012m and NLF 0414 airfoils will be discussed and compared in order to provide an explanation to the performance data of the previous section.

Figure 80(a) shows the surface pressure distribution on the NACA 23012m model with the 0.25″ simulated ice shape at various chordwise locations. The angle of attack was 5°. When the simulated ice shape was present on the airfoil, a long separation bubble usually formed immediately downstream. Figure 80(a) shows that when the simulated ice shape was at $x/c = 0.02$, it was still located in a favorable pressure gradient, and the separation bubble was relatively short. When the simulated ice shape was located at $x/c = 0.10$ and 0.20, a very long separation bubble formed downstream of the simulated ice shape. In fact, flow visualization indicated that the bubbles did not reattach.

Figure 80(b) shows the surface pressure distribution on the NLF 0414 model with the ice shape simulation at various chordwise locations. The angle of attack was 1°, where the clean airfoil had a C_ℓ similar to the NACA 23012m at $\alpha = 5°$. When the ice shape was located at and between $x/c = 0.02$ and 0.20, the suction region (due to separation) had similar C_p values (-1.3) and the separation length did not vary as much as it did for the NACA 23012m. The bubble length varied from 18% chord for the $x/c = 0.02$ case to 28% chord for the $x/c = 0.20$ case. After the flow had reattached, the C_p on all three cases dropped to approximately 0.50 and remained fairly constant until the pressure recovery over the flap occurred.

When the ice shape was located at $x/c = 0.40$, the surface pressure distribution looked significantly different than those of the other three iced cases. Also, based on the low trailing-edge pressures and flow visualization, the separation bubble was determined to not to have reattached, resulting in a separation length of 60% chord.

The reason for the similarities in the $x/c = 0.02$, 0.10, and 0.20 cases was that the ice shape and the resulting separation bubble was located in a region of relatively constant pressure (on the clean model). Thus, the separation bubbles in the three cases above were all allowed to reattach in a similar pressure gradient (which happened to be nearly zero in this case). The resulting separation bubbles all appeared similar, with relatively similar suction regions and separation lengths because the ice shape was in a similar flow field. The variation in the separation length

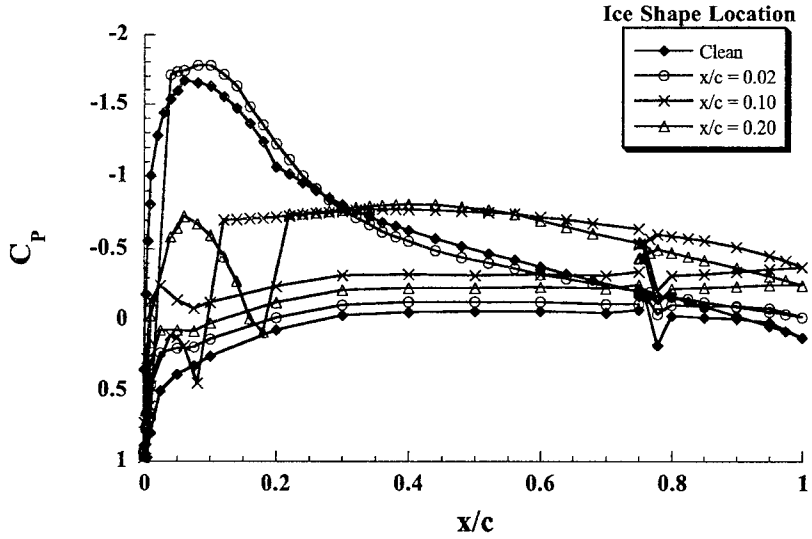

(a) NACA 23012m, $\alpha = 5°$

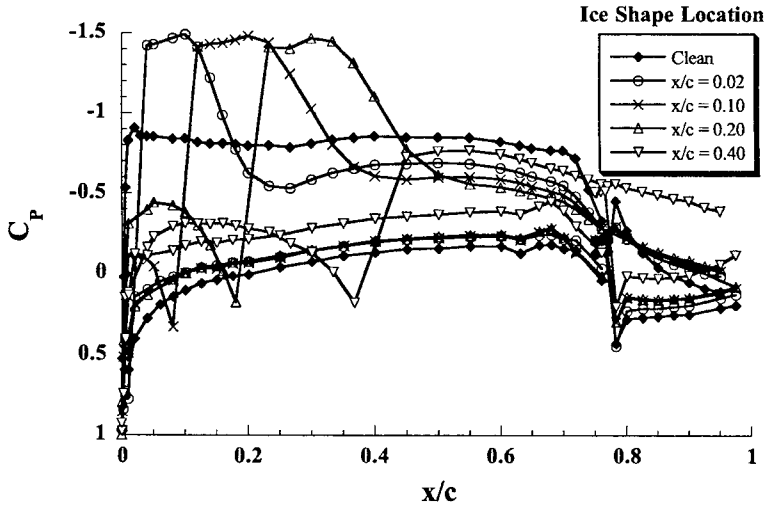

(b) NLF 0414, $\alpha = 1°$

FIGURE 80. EFFECT OF SIMULATED ICE SHAPE LOCATION ON SURFACE PRESSURE
(0.25″ forward-facing quarter round, $\alpha = 1°$, $Re = 1.8 \times 10^6$, boundary layer tripped)

may be due to the thicker boundary layer the ice shape encountered as it was moved downstream. The similarities ended when the ice shape was located at $x/c = 0.40$. Although the ice shape itself was in the region of constant pressure, it was located close to the clean model pressure recovery region (where there was a strong adverse pressure gradient). Thus, the separation bubble was forced to reattach in an adverse pressure gradient, resulting in a trailing-edge separation.

The simulated ice shape affected the NACA 23012m and the NLF 0414 very differently due to the differences in their geometries and clean airfoil aerodynamics. The NACA 23012m was a much more forward-loaded airfoil, which resulted in a very severe adverse pressure recovery downstream of a large, near-leading-edge suction peak. Thus, the separation bubble that forms downstream of the simulated ice shape had to reattach in a very adverse pressure gradient. This resulted in very long separation bubbles with severe performance degradations. On the other hand, the NLF 0414 had a much more evenly loaded pressure distribution. The separation bubbles that formed downstream of the simulated ice shape attached much quicker, which resulted in much less severe performance degradation.

4.2 COMPUTATIONAL RESULTS.

4.2.1 NACA 23012m Iced Airfoil Results.

In the following, the aerodynamic influence of a forward-facing quarter-round ice shape will be considered. The experimental data presented in section 4.1 will be used for comparison. The tunnel walls were modeled directly in all of these computations, so the experimental data have not been corrected for wall interference. The data were taken for $M = 0.2$ and $Re = 1.8 \times 10^6$ using the NACA 23012m airfoil described in section 3.1. The transition points on the upper surface for all iced cases were chosen to be the minimum of three quantities: the ice shape location, the transition point predicted by XFOIL for the clean case and the trip location which was 2% chord for all experimental runs used for comparison in this section. On the lower surface, again the transition point specified was the minimum of the one predicted by XFOIL for the clean case and the trip location which was 5% for all experimental runs. As before, the code was run for all experimental angles but only conditions which were fully converged are reported in the figures.

Due to the presence of the ice shape and flap, a much finer grid was used for the iced-airfoil calculations than was used in the validation calculations. Since the tunnel walls were modeled, each angle of attack required a separate grid. The initial grids contained approximately 100,000 nodes and 1300 points along the airfoil surface. The grid points were clustered around the ice shape and within the separation region. The spacing of the first grid point normal to the airfoil surface was 1×10^6 chord lengths with a 15% successive increase in grid size away from the wall. This grid was then adapted using the procedure of section 2.2.3. The final grids contained approximately 125,000 nodes.

The computations were completed on both the Department of Aeronautical and Astronautical Engineering (AAE) SGI workstations and the National Center for Supercomputing Applications (NCSA) SGI Power Challenge Array and Origin 2000. Iced-airfoil calculations on the SGI Origin 2000 using 3 multigrid levels took approximately 20 seconds of CPU time per cycle. Iced calculations required approximately 1000 cycles for convergence.

4.2.1.1 Computational Prediction Fidelity for Icing.

The ability of the current computational methodology to predict the flow field about an airfoil with a ridge ice accretion was first tested using $k/c = 0.0083$ forward-facing quarter-round protuberance located at a chordwise location of $x/c = 0.10$.

Figures 81 through 84 plot the aerodynamic coefficients for the iced NACA 23012m. Figure 81 shows the variation of lift coefficient as a function of angle of attack. At low angles of attack ($\alpha < 3°$), NSU2D gave good agreement with the experimental data, although the slope was underpredicted by approximately 8%. Starting at 3 degrees, the computations predicted a break in the slope and started to underpredict the experimental lift. Then as the experimental lift began to gradually level off, the computational lift continued to increase and no noticeable maximum lift condition was seen in the NSU2D predictions. This, as is discussed later in this section, can probably be attributed to large-scale unsteady separation bubble behavior in the measurements at fully separated angles of attack ($\alpha \geq 3°$), which the steady-state calculations cannot predict.

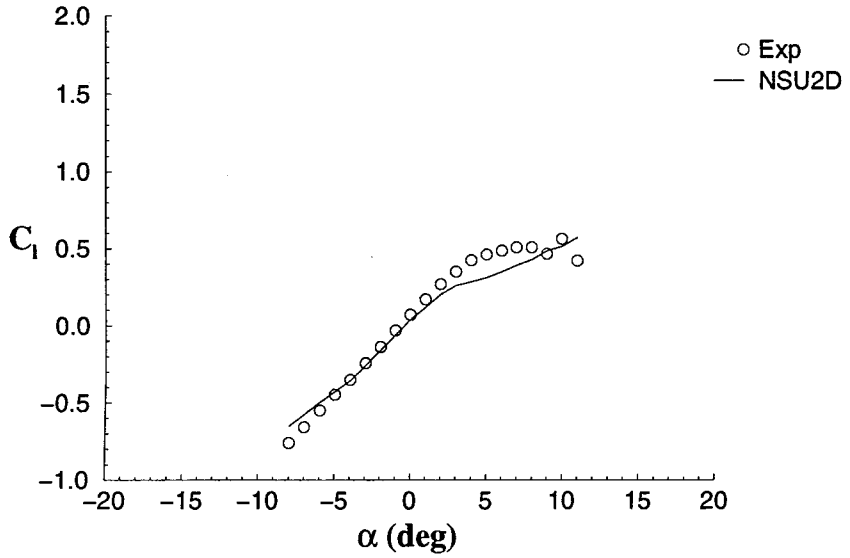

FIGURE 81. LIFT COEFFICIENTS FOR A NACA 23012m WITH $k/c = 0.0083$ QUARTER-ROUND ICE SHAPE LOCATED AT $x/c = 0.1$

Figure 82 shows the drag predictions. Despite the large amount of separation occurring on the upper surface of the airfoil, the performance of the simulations was reasonable, i.e., within 10%-20% of the experimental data. The drag at the lower angles was slightly underpredicted. At the upper angles, the large increase found in the experimental drag was also seen in the computations, although the exact magnitude was overpredicted. This is partially attributed to the behavior of the separation bubble predicted by the computations, which varied slightly from the actual bubble behavior expected in the experimental data.

The comparison of the predicted and experimental pitching moment is found in figure 83. Overall, NSU2D gives excellent correlation with experiment for the pitching moment. The large increase in negative moment caused by the growth of the separation bubble is well predicted both qualitatively and quantitatively, although the computations predict the break at a slightly earlier angle of attack than the experiments. The hinge moment predictions (figure 84) have similar agreement with the experimental data, although the earlier break is more dramatic than for the pitching moment.

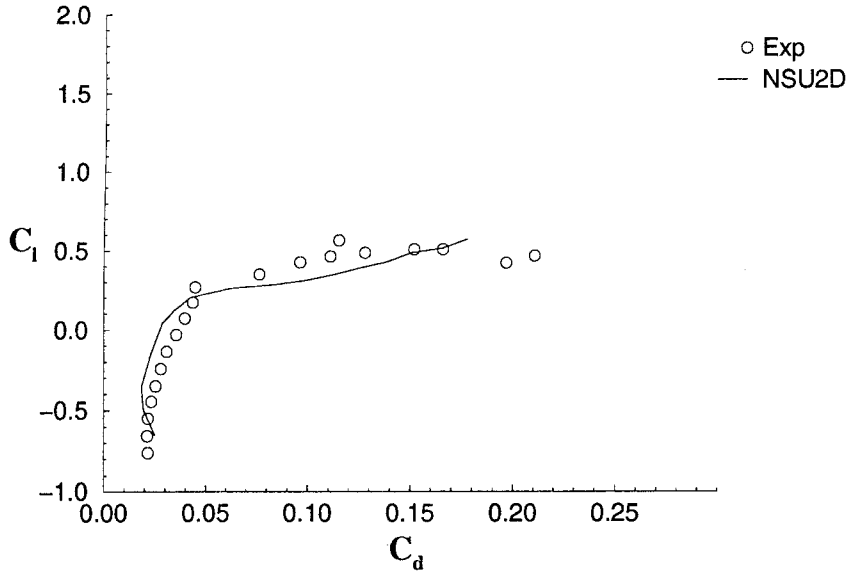

FIGURE 82. DRAG COEFFICIENTS FOR A NACA 23012m WITH $k/c = 0.0083$ QUARTER-ROUND ICE SHAPE LOCATED AT $x/c = 0.1$

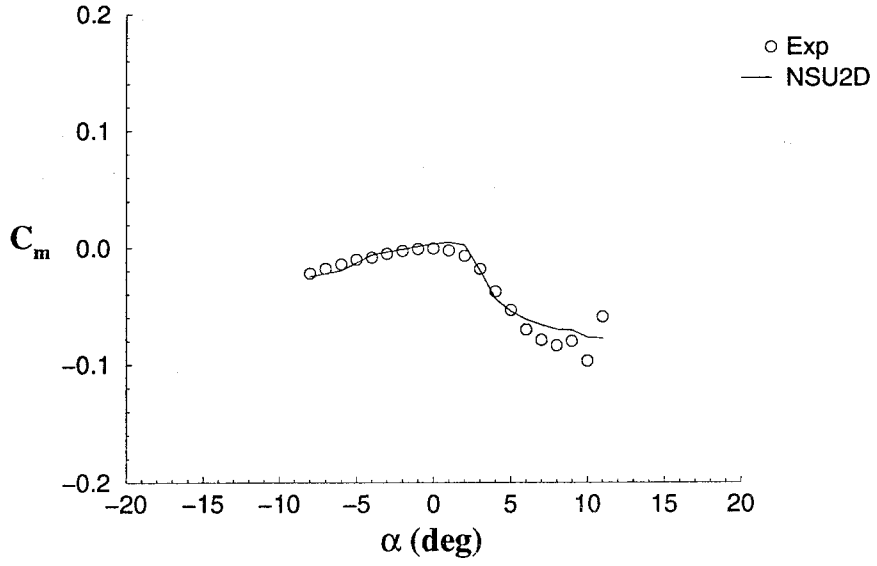

FIGURE 83. PITCHING MOMENT COEFFICIENTS FOR A NACA 23012m WITH $k/c = 0.0083$ QUARTER-ROUND ICE SHAPE LOCATED AT $x/c = 0.1$

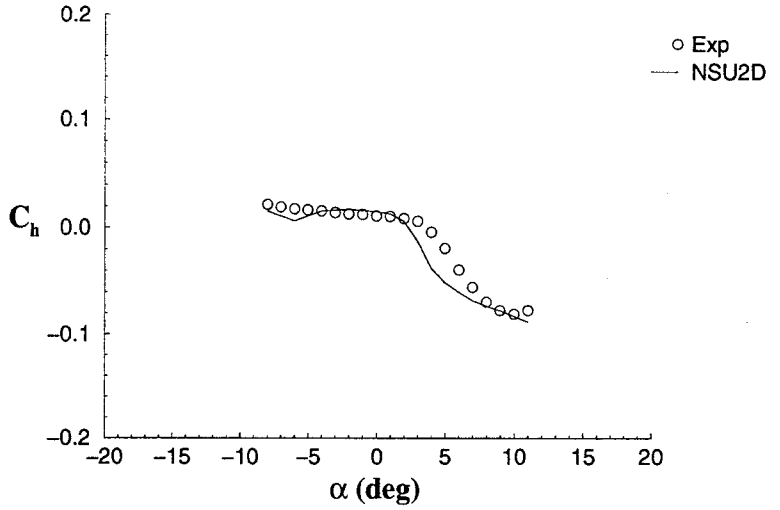

FIGURE 84. HINGE MOMENT COEFFICIENTS FOR A NACA 23012m WITH $k/c = 0.0083$ QUARTER-ROUND ICE SHAPE LOCATED AT $x/c = 0.1$

Finally, we consider some of the aerodynamic characteristics responsible for the integrated quantities discussed above. Figure 85 plots selected velocity vectors within the separation bubble for $\alpha = -6°$. Note that if all the velocity vectors were plotted the figure would be too dense to be clear. The velocity vectors show the large aft separation bubble extending from the top of the ice shape with an initial expansion upwards. At this low angle of attack the separation region was quite thin and remained fairly close to the airfoil. The small recirculation region upstream of the ice shape showed a vertical extent which was less than the top of the ice shape, a result which is consistent with the buff-body experiments of Winkler.

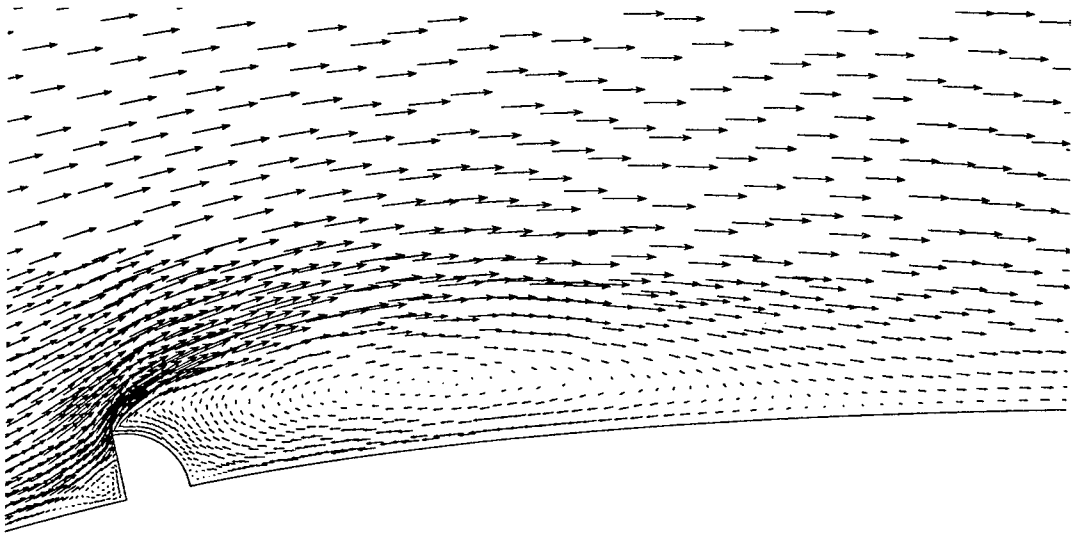

FIGURE 85. VELOCITY VECTORS AT SAMPLE LOCATIONS FOR A NACA 23012m WITH $k/c = 0.0083$ QUARTER-ROUND ICE SHAPE LOCATED AT $x/c = 0.1$ AND $\alpha = -6°$

Figure 86 plots the reattachment length for the separation bubble aft of the ice shape versus the airfoil's angle of attack. The computational reattachment locations were based on the point where the skin friction changed sign. Reattachment lengths obtained through analysis of the experimental pressure distributions are plotted for comparison. The computational reattachment lengths were determined using the predicted skin friction along the airfoil surface. The figure shows that the bubble has almost exponential growth, as the reattachment length grew slowly at the low angles then quickly at the larger angles until the bubble reached the trailing edge. The computations predicted a somewhat shorter reattachment length at the low angles, which is consistent with the backward-facing step results in figure 21. Between 2 and 3 degrees, the computations showed very rapid bubble growth, and the predicted separation region reached the trailing edge before the experimental bubble. This is the expected reason for the earlier break in the hinge moment predictions. The predictive differences found between the experimental and computational reattachment length at the higher angles are attributed to unsteady effects at the high angles and difficulties predicting the flow through the flap gap.

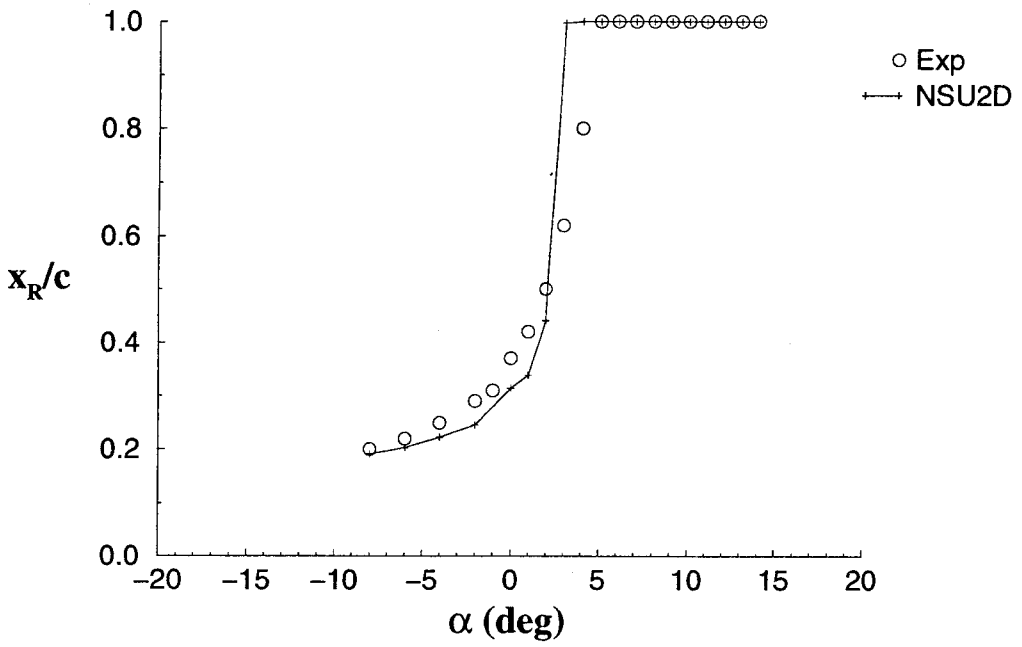

FIGURE 86. REATTACHMENT LOCATIONS OF THE AFT ICE SEPARATION BUBBLE FOR A NACA 23012m WITH $k/c = 0.0083$ QUARTER-ROUND ICE SHAPE LOCATED AT $x/c = 0.1$

Figures 87 and 88 plot the pressure distribution along the airfoil surface for α = -6 and 6°, respectively. Computationally predicted streamlines are also shown for each angle as a reference for the bubble behavior. For each of these plots, NSU2D accurately predicted the pressure over the majority of the airfoil surface. The code gave excellent agreement in the nonseparated regions of the flow, i.e., along the lower surface and along the upper surface in front of the ice

shape. This is especially noticeable in the $\alpha = -6°$ case, (figure 87) where the pressure spike at the leading edge of the lower surface was well predicted. The code accurately predicted the pressure increase in the stagnation region ahead of the ice shape, as well as the magnitude of the suction peak occurring downstream of the ice shape. However, similar to the results for the backward-facing step and the glaze-iced airfoil (figure 52), NSU2D displayed a much faster pressure recovery than the experimental data in the large separation region aft of the ice shape. This discrepancy in the separation region became more severe as the angle of attack was increased. This error in pressure recovery is thought to be due to the turbulence model inadequately predicting the amount of entrainment within the shear layer. This is an area which should be investigated further and may require modification of the current turbulence model or freestream turbulence values.

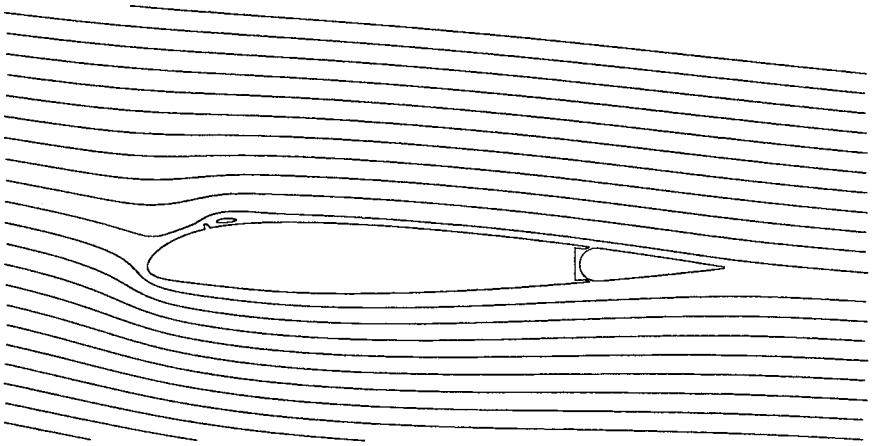

(a)

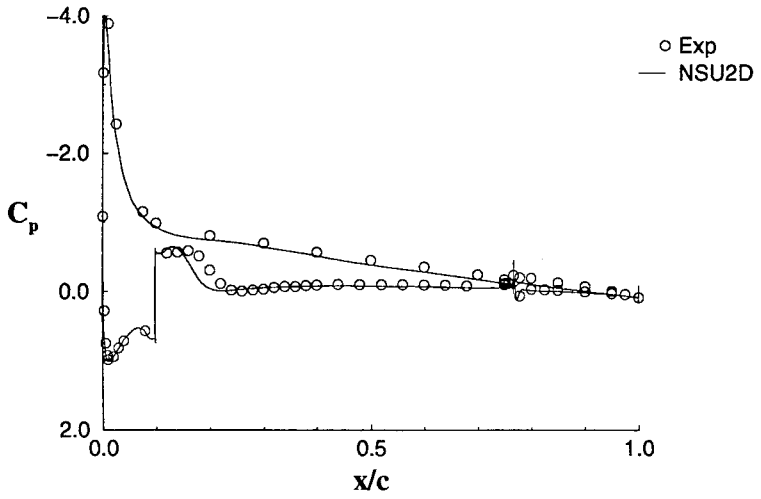

(b)

FIGURE 87. (a) STREAMLINES AND (b) SURFACE PRESSURE DISTRIBUTIONS FOR A NACA 23012m WITH $k/c = 0.0083$ QUARTER-ROUND ICE SHAPE LOCATED AT $x/c = 0.1$ AND $\alpha = -6$

Comparisons of the pressure distribution at higher angles (figure 88) revealed a similar level of discrepancy despite having a fully separated flow. This was attributed to the fact that the reattachment point had become fixed at the trailing edge for both the experiments and the computations (a reattachment condition more easily predicted). It is remarkable that in all of these cases the errors in the pressure distribution did not significantly affect the aerodynamic moment coefficient predictions. This was because the pressure discrepancies were centered primarily around the quarter-chord location and therefore tended to cancel themselves out once levered about the hinge line.

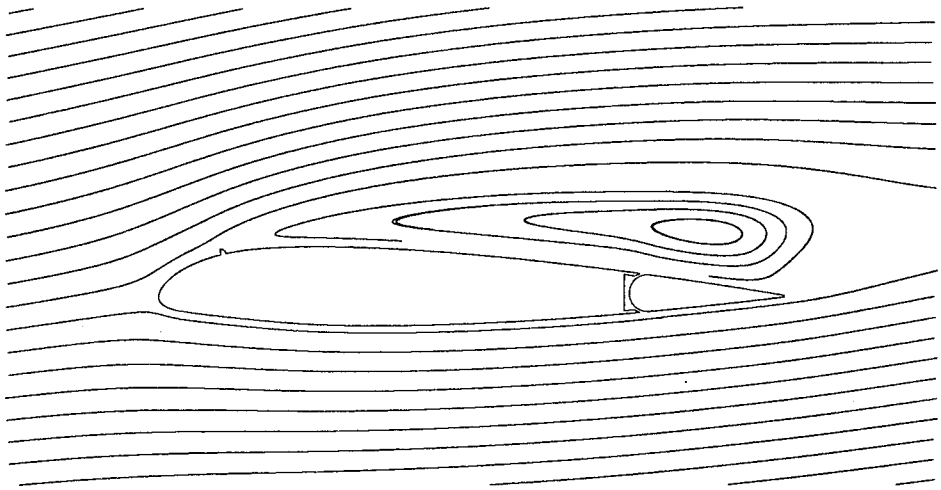

(a)

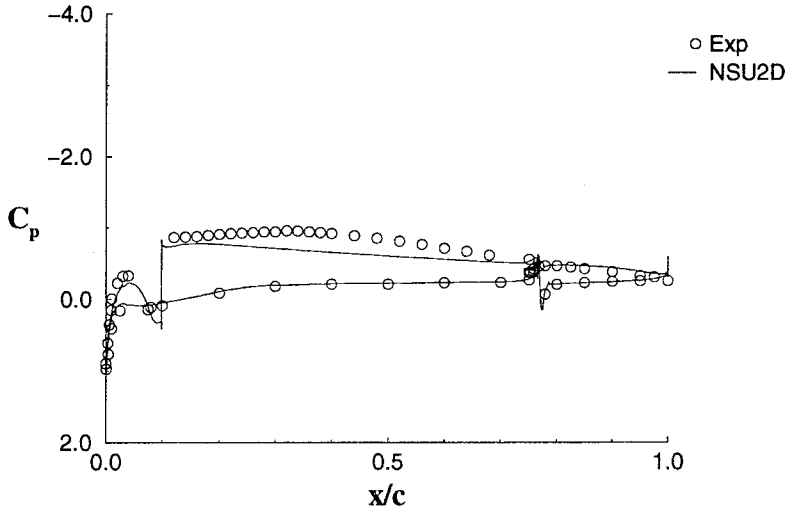

(b)

FIGURE 88. (a) STREAMLINES AND (b) SURFACE PRESSURE DISTRIBUTIONS FOR A NACA 23012m WITH $k/c = 0.0083$ QUARTER-ROUND ICE SHAPE LOCATED AT $x/c = 0.1$ AND $\alpha = 6°$

Analysis of the aerodynamic coefficients, reattachment lengths, pressure distributions, and flow field plots indicates three general regimes of flow phenomena which can be isolated to aid in future discussion: linear, nonlinear, and fully separated. The *linear* regime is associated with low angles of attack (approximately less than 0° in this case). Here, the separation bubble remains close to the airfoil surface and the chordwise growth of the bubble, as the angle of attack is increased, is fairly slow. At higher angles of attack (around 0-4°), the airfoil displays behavior of the *nonlinear* regime, yielding a break in the aerodynamic forces and moments. Here the bubble displays rapid growth over a relatively small range of angle of attack. Unsteady flow behavior is expected to start developing in this regime. Once the separation region reaches the trailing edge, the airfoil is in the *fully separated* regime $\alpha > 4°$. Here the bubble quickly begins to extend away from the airfoil and into the outer flow field. With this type of bubble, large-scale vortex shedding is more likely to occur. This type of unsteady phenomenon can not be captured with the current steady-state computational strategy, and therefore, the computational results are questionable at these angles.

The next sections will study the influence of the quarter-round simulated ice accretion by varying its size and location. Although experimental data will also be shown, the effects predicted in the computations will primarily be discussed. In general, correlation between computational and experimental data was found for each of the cases considered to be similar to that described above.

4.2.1.2 Effects of Variation in Size.

In the following section, the aerodynamic influence of a quarter-round ice shape is considered computationally by varying its maximum height. The ice location was held constant at 10% chord and two sizes were studied: $k/c = 0.0083$ and $k/c = 0.0139$. In addition, a case with no ice shape ($k/c = 0.0$) which included only the boundary layer trip was used as a reference condition. The geometries of the three configurations are depicted in figure 89.

The lift curves for these configurations are shown in figure 90. The significant reduction in lift curve slope and the dramatic reductions in maximum lift coefficient and maximum lift angle caused by the ice shape presence were predicted reasonably well by NSU2D. However, for both iced cases, the NSU2D predictions exhibited a weaker, although more abrupt, break in the lift curve slope than that shown by the experiments. Although no noticeable maximum lift condition was seen in the NSU2D predictions, the break in the lift curve slope can be used to estimate the trends for loss in maximum lift. Here the break does occur at an earlier angle for the larger ice case (at $\alpha = 1°$) than for the smaller ice case (at $\alpha = 3°$), which corresponds well with the start of the experimental breaks.

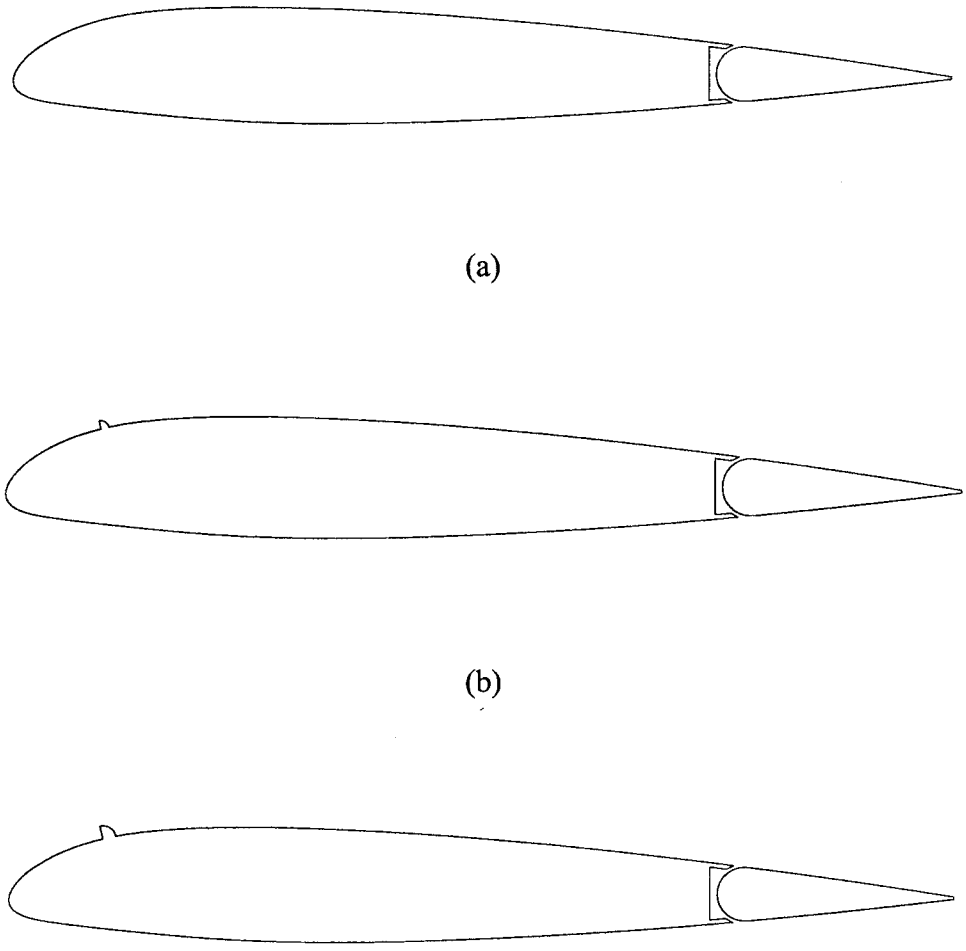

(a)

(b)

(c)

FIGURE 89. GEOMETRY OF NACA 23012m WITH AN ICE SHAPE LOCATED AT $x/c = 0.1$ WITH HEIGHTS (a) $k/c = 0.0$, (b) $k/c = 0.0083$, AND (c) $k/c = 0.0139$

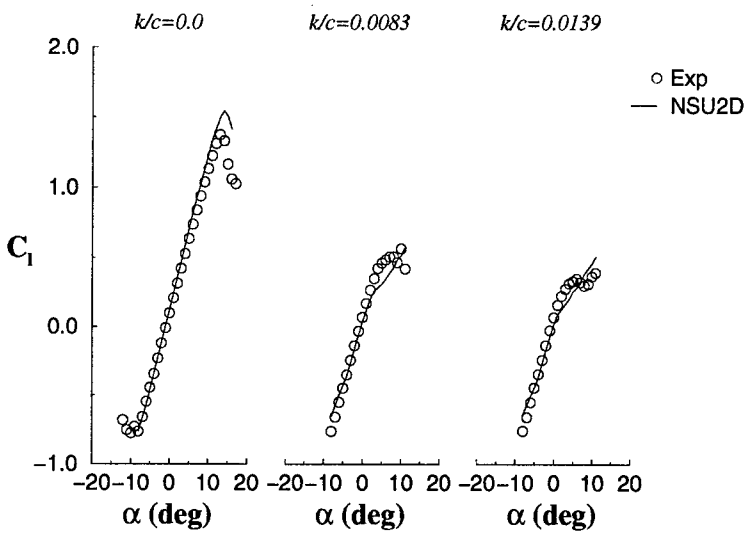

FIGURE 90. EFFECT OF SHAPE HEIGHT ON LIFT FOR AN ICE SHAPE LOCATED AT $x/c = 0.1$

Figure 91 shows the drag predictions. The trends due to the presence and height change of the ice shape were well predicted by NSU2D, considering the large amount of separation occurring for the iced-airfoil flows. At low angles of attack, NSU2D predicted the small increase in drag as the ice size was increased, although the magnitude was slightly underpredicted. Both the computations and the experiments showed a significant increase in drag for the iced cases at large angles of attack. However, unlike the clean case, the large increases in drag for the iced cases occurred a couple of degrees before the maximum lift point.

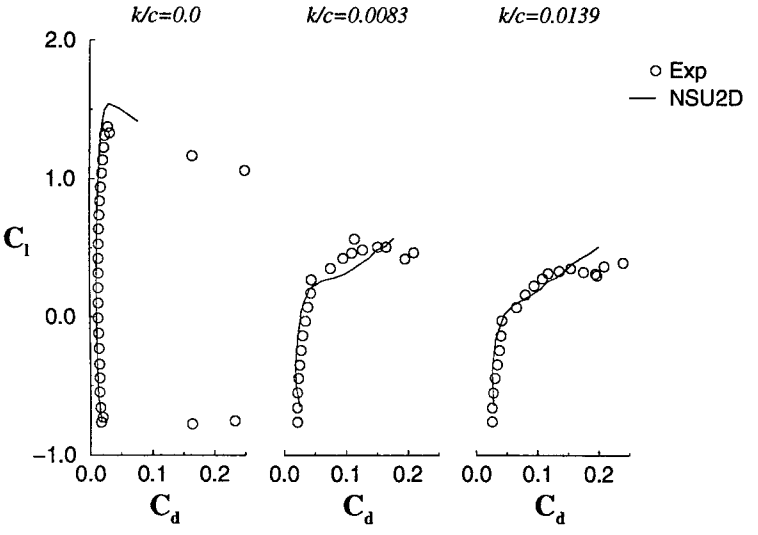

FIGURE 91. EFFECT OF SHAPE HEIGHT ON DRAG FOR AN ICE SHAPE LOCATED AT $x/c = 0.1$

Figure 92 shows the pitching moment coefficient distribution with angle of attack. The trends caused by the presence of the ice shapes were well reproduced by NSU2D. In fact, the NSU2D results for the iced cases had better agreement with the experiments than the clean case (perhaps due to the decrease in flow through the flap gap). NSU2D performed remarkably well for predicting the strong drop-off in moment at positive angles of attack as the ice shape was increased in size. However, the computations did not predict the subsequent increase in moment coefficient seen in the experimental data for angles past stall.

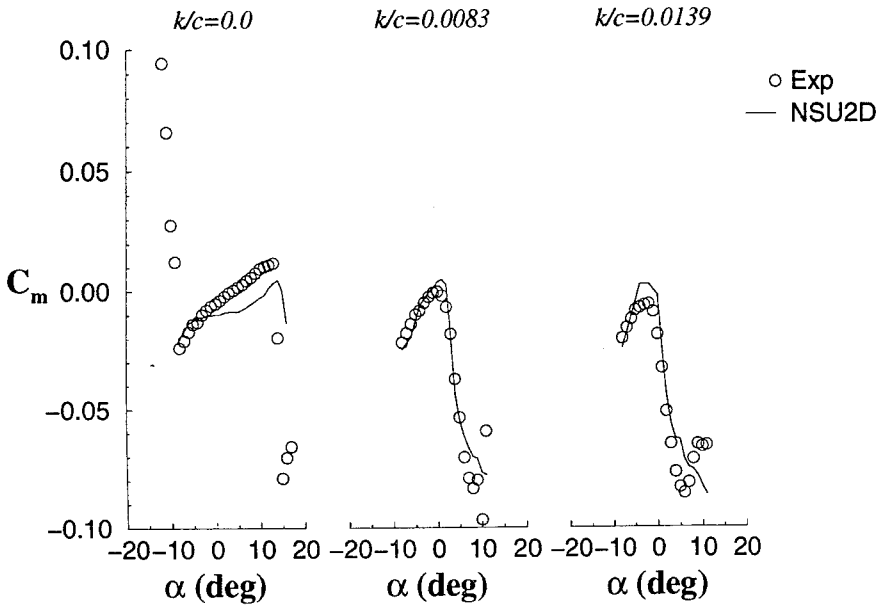

FIGURE 92. EFFECT OF SHAPE HEIGHT ON PITCHING MOMENT FOR AN ICE SHAPE LOCATED AT $x/c = 0.1$

Perhaps the most import aerodynamic coefficient with respect to aircraft control is the hinge moment. The comparison between computation and experiment of this critical parameter is shown in figure 93. Again, NSU2D successfully predicted the qualitative trends resulting from the presence and change in height of the ice shape. In particular, the increased drop-off in C_h at high angles of attack was reproduced both qualitatively and quantitatively.

The pressure distribution for each of the three configurations at $\alpha = 3°$ is plotted in figure 94. The plots show that the presence of the ice shape caused an increase in pressure at the leading edge, i.e., the suction peak was reduced. This created a much more rear-loaded airfoil with a subsequent change in the pitching moment and loss in lift. Also, the pressure along the lower surface decreased as the ice shape size was increased, resulting in a further loss in lift.

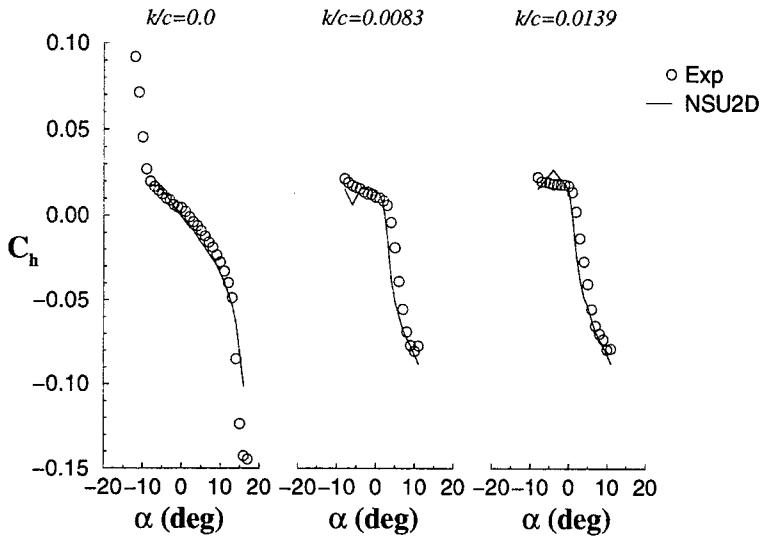

FIGURE 93. EFFECT OF SHAPE HEIGHT ON HINGE MOMENT FOR AN ICE SHAPE LOCATED AT $x/c = 0.1$

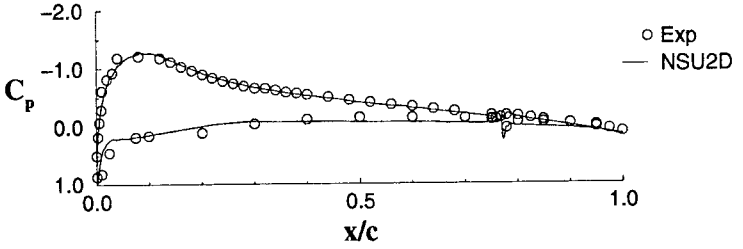

(a)

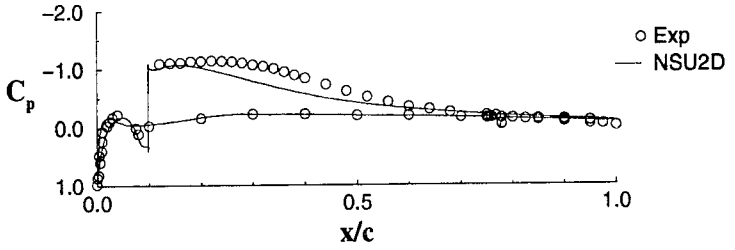

(b)

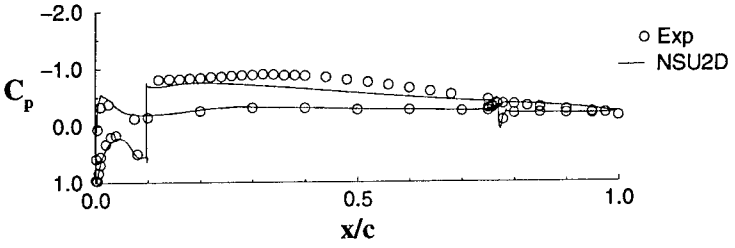

(c)

FIGURE 94. EFFECT OF SHAPE HEIGHT ON PRESSURE DISTRIBUTION AT $\alpha = 3°$ FOR AN ICE SHAPE LOCATED AT $x/c = 0.1$ FOR HEIGHTS (a) $k/c = 0.0$, (b) $k/c = 0.0083$, AND (c) $k/c = 0.0139$

The above results indicate that NSU2D correctly predicts the trends of all the major aerodynamic features associated with the ice shape presence for the present conditions. In addition, the quantitative comparison was reasonable for many of these cases.

4.2.1.3 Effects of Variation in Ice Shape Location.

The effect on the aerodynamic coefficients due to a quarter-round ice shape of size $k/c = 0.0083$ located at 10%, 20%, and 30% chord is shown in figures 96 through 99. These geometries are depicted in figure 95. As will be shown in the following paragraphs, the computational results agreed well with the experimental data for angles of attack within the linear range. For the three

locations tested, the 10% chord location had the strongest influence on the aerodynamic characteristics of the airfoil.

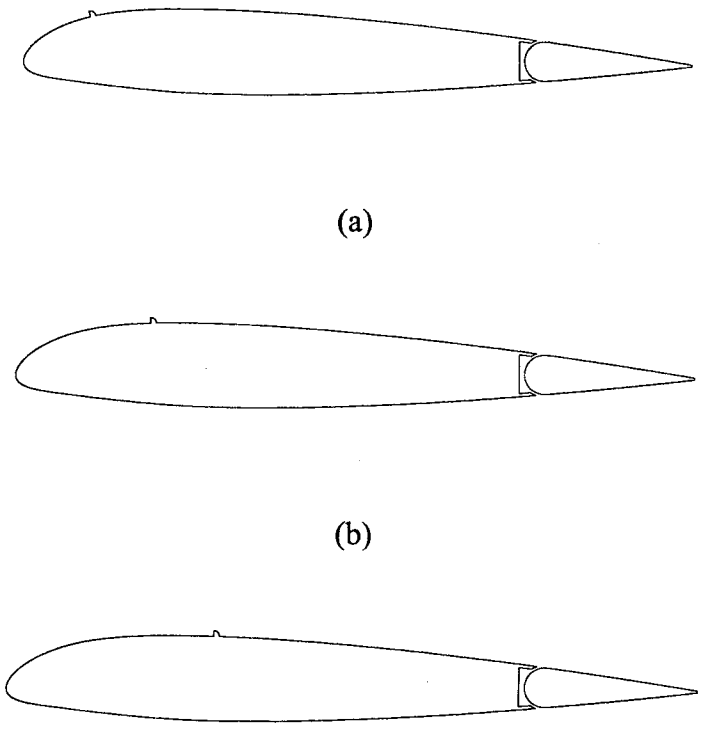

(a)

(b)

(c)

FIGURE 95. GEOMETRY OF NACA 23012m WITH $k/c = 0.0083$ ICE SHAPE LOCATED AT (a) $x/c = 0.1$, (b) $x/c = 0.2$, AND (c) $x/c = 0.3$

The effect of the protuberance at the three locations on the lift coefficient is shown in figure 96. The cases when the ice shape were located at $x/c = 0.1$ resulted in the largest reduction in the lift curve slope. The 10% chord location was also the first to experience the break in the lift curve, indicating the earliest stall (although the computations did not predict the actual stall). Figure 97 shows the drag predictions. Once again the 10% chord location appears to be the worst. This was primarily caused by the earlier onset of stall, as there was very little difference in the drag of the three configurations at the lower angles of attack. The $x/c = 0.1$ had the most severe effect on the pitching moment (figure 98) and hinge moment (figure 99). As the ice shape was moved rearward on the airfoil, the moment curves displayed a much more gradual break. This gradual effect is much more desirable regarding the controllability of the aircraft.

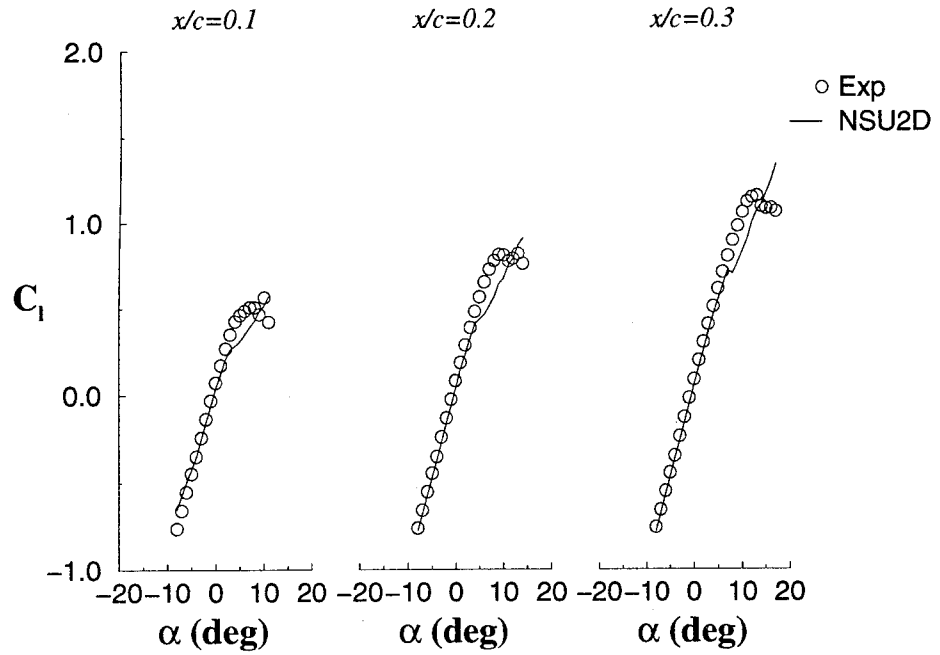

FIGURE 96. EFFECT OF SHAPE LOCATION ON LIFT FOR $k/c = 0.0083$ ICE SHAPE

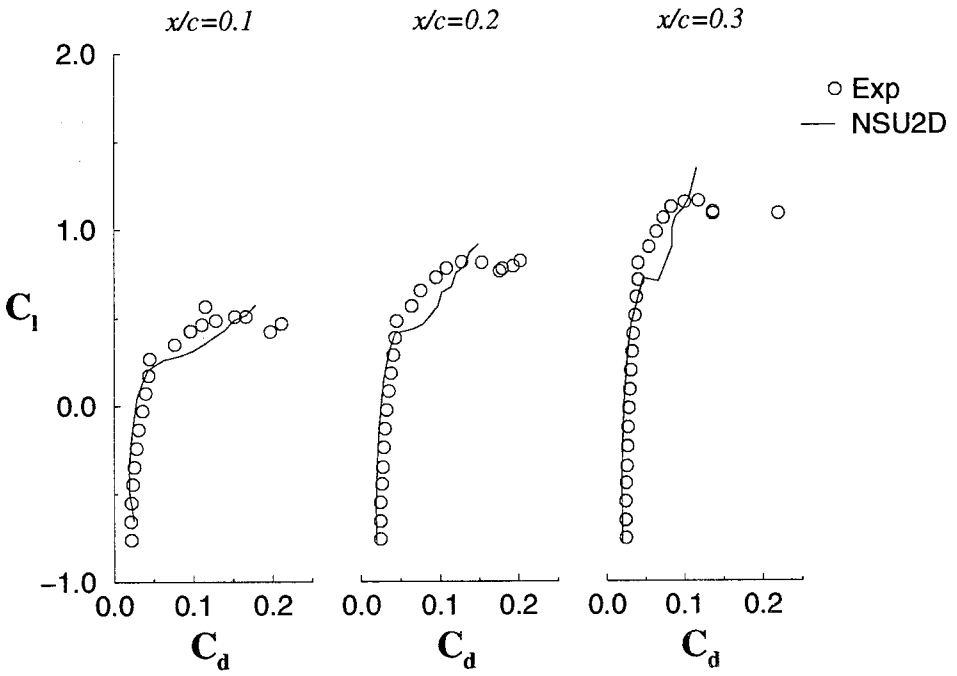

FIGURE 97. EFFECT OF SHAPE LOCATION ON DRAG FOR $k/c = 0.0083$ ICE SHAPE

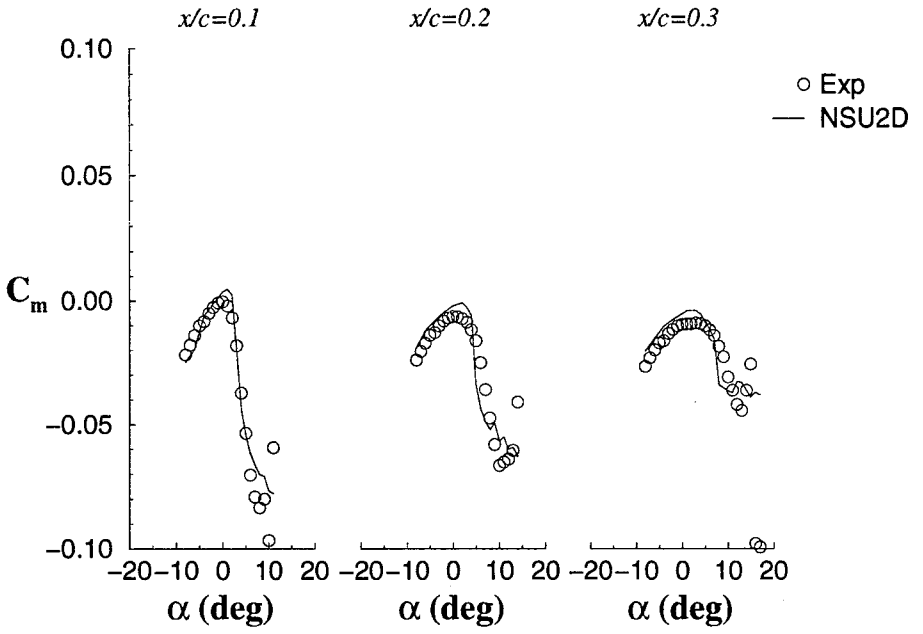

FIGURE 98. EFFECT OF SHAPE LOCATION ON PITCHING MOMENT FOR k/c = 0.0083 ICE SHAPE

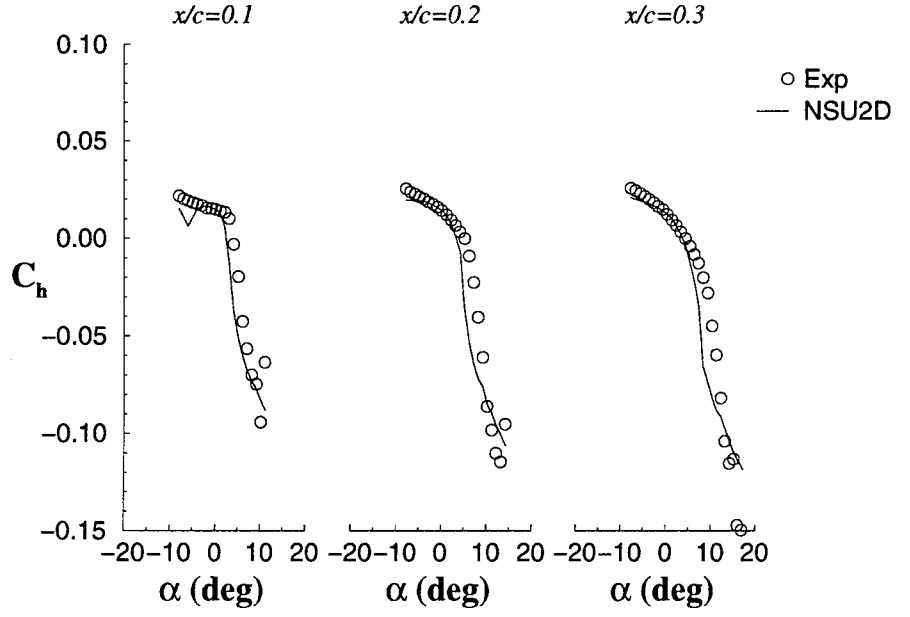

FIGURE 99. EFFECT OF SHAPE LOCATION ON HINGE MOMENT FOR k/c = 0.0083 ICE SHAPE

Figure 100 displays the pressure distribution along the airfoil surface at $\alpha = 3°$ for the three ice shape locations. As expected, the stagnation region followed the ice shape as it was moved rearward. The airfoil with the ice shape at 10% chord did not display a suction peak at the leading edge, while the geometries with the ice shape moved farther back did possess a peak (although not as large as in the clean case seen in figure 94(a)). This appears to be the reason why the 10% chord location produced the greatest decrease in lift as well as the strongest influence on the moment coefficients.

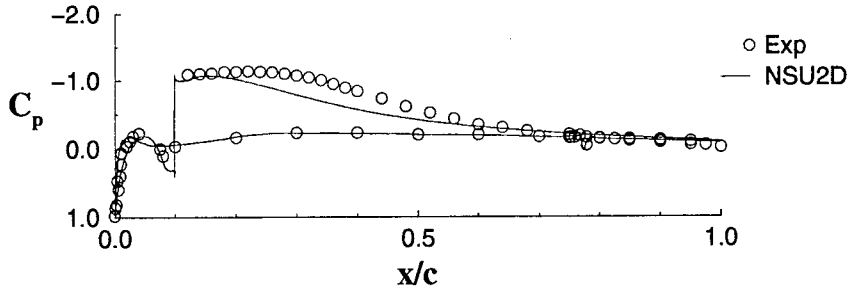

(a)

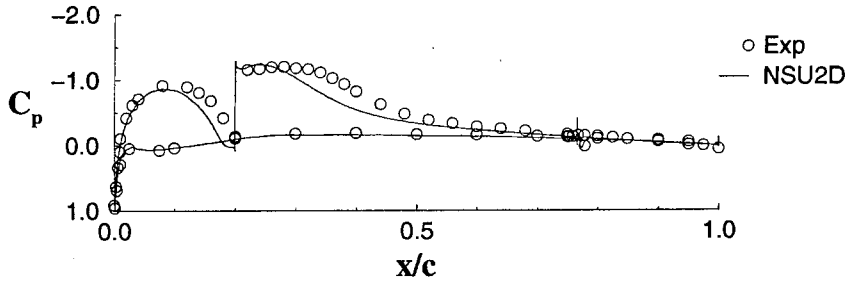

(b)

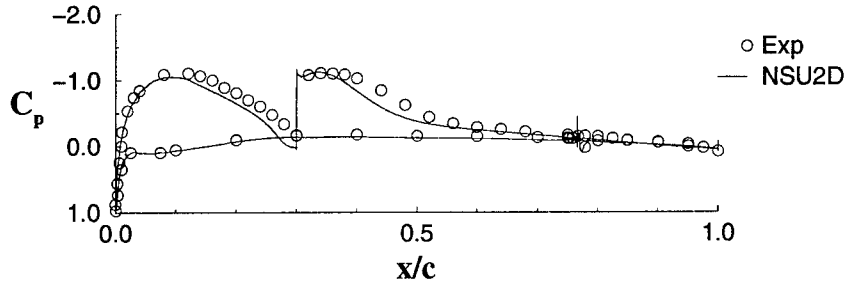

(c)

FIGURE 100. EFFECT OF SHAPE LOCATION ON PRESSURE DISTRIBUTION AT $\alpha = 3°$ FOR $k/c = 0.0083$ ICE SHAPE LOCATED AT (a) $x/c = 0.1$, (b) $x/c = 0.2$, AND (c) $x/c = 0.3$

Flow field analysis results are presented for the 2%, 10%, and 20% ice locations. Figures 101 through 103 plot the reattchment length for the separation bubble aft of the ice shape versus the airfoil's angle of attack. The computational reattachment lengths were determined using the predicted skin friction along the airfoil surface. For the 2% ice location case, there is significant flow separation at the trailing edge for angle of attack as low as $\alpha = 0°$. As the angle of attack increases, the reattachment point of the bubble and the flow separation point which was initially at the trailing edge moves closer to each other until at about $\alpha = 7°$ where the two points meet. Hence, we observe a rapid break in the plot at $\alpha = 7°$. Therefore, this geometry exhibits a combination of thin airfoil and trailing edge type of stall. Beyond $\alpha = 7°$, the flow became unsteady. The 10% and the 20% case exhibits a thin airfoil type of stall as seen from figures 103 and 104.

Figure 104 plots the C_ℓ when the flow first becomes fully separated versus the location of simulated ice accretion. We see that the most detrimental effect on the lift occurs close to the 10% location, as also seen from the C_ℓ - α plots. This is consistent with the experimental results presented in the previous section, which noted the critical location as 12% also shown in the figure.

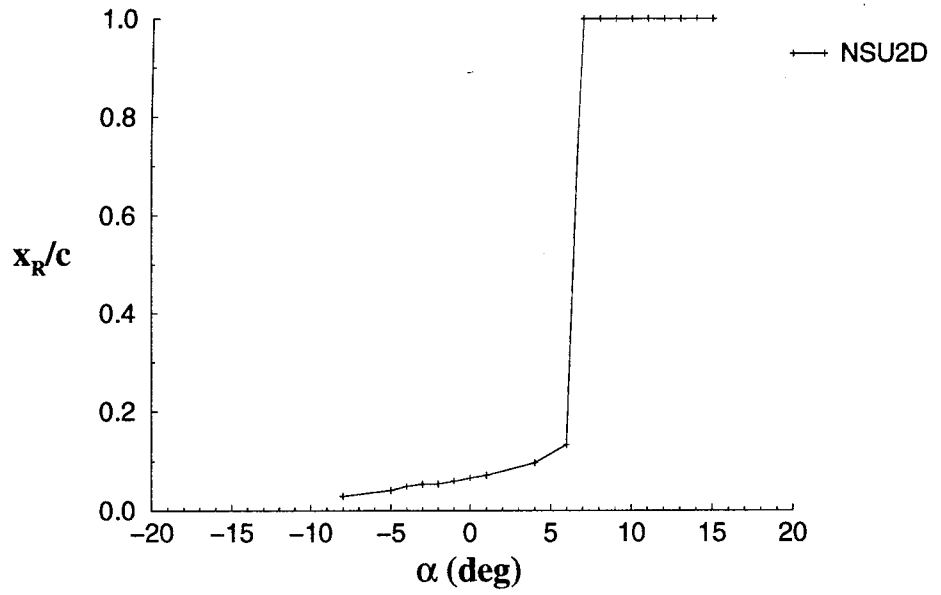

FIGURE 101. REATTACHMENT LOCATIONS OF THE AFT ICE SEPARATION BUBBLE FOR A NACA 23012m WITH $k/c = 0.0083$ QUARTER-ROUND ICE SHAPE LOCATED AT $x/c = 0.02$

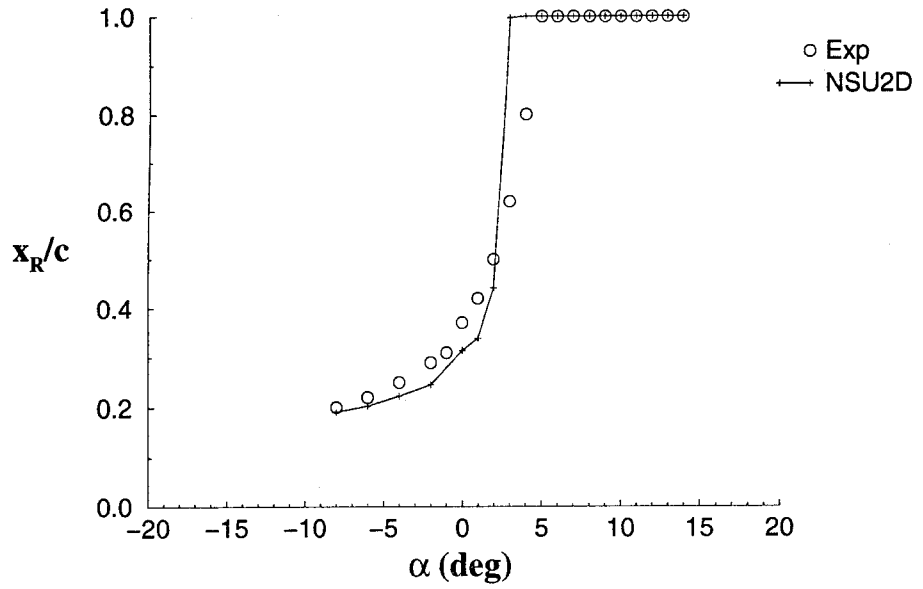

FIGURE 102. REATTACHMENT LOCATIONS OF THE AFT ICE SEPARATION BUBBLE FOR A NACA 23012m WITH $k/c = 0.0083$ QUARTER-ROUND ICE SHAPE LOCATED AT $x/c = 0.1$

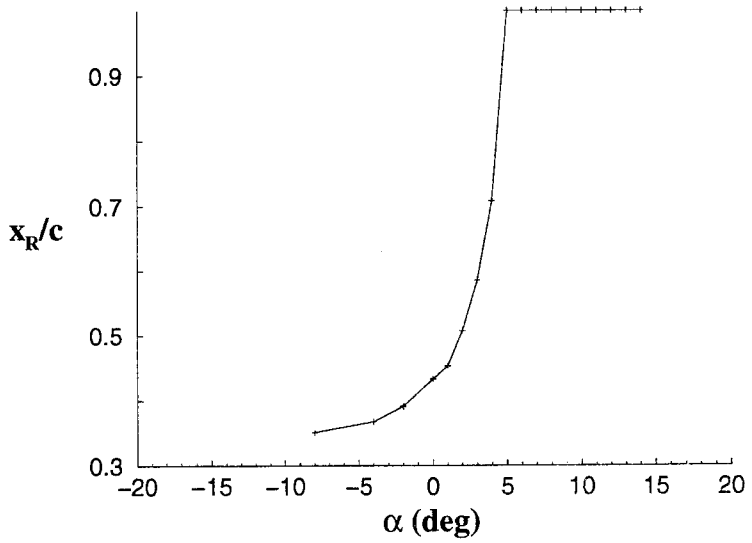

FIGURE 103. REATTACHMENT LOCATIONS OF THE AFT ICE SEPARATION BUBBLE FOR A NACA 23012m WITH $k/c = 0.0083$ QUARTER-ROUND ICE SHAPE LOCATED AT $x/c = 0.2$

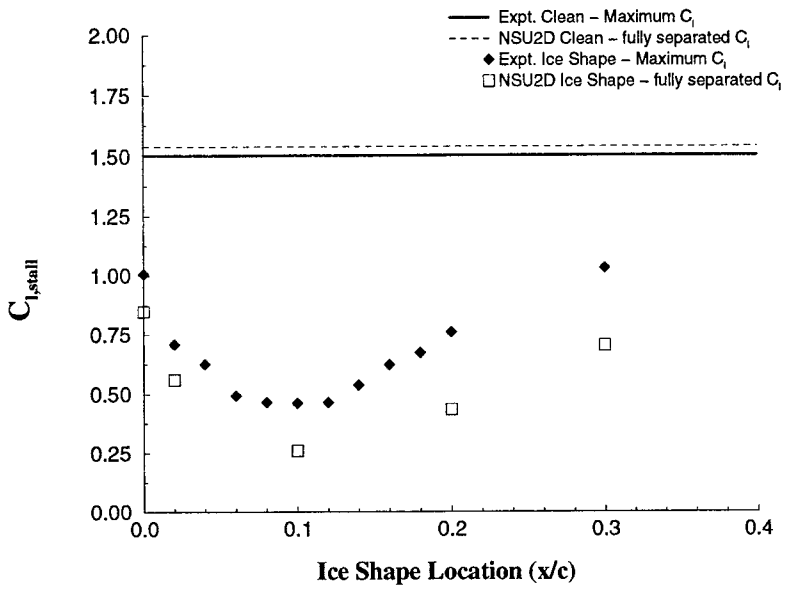

FIGURE 104. LIFT COEFFICIENT FOR ANGLE OF ATTACK AT WHICH FLOW FIRST FULLY SEPARATES VS. *x/c* FOR A NACA 23012m AIRFOIL WITH *k/c* = 0.0083 QUARTER-ROUND ICE SHAPE

4.2.1.4 Effects of Variation in Ice Shape Geometry.

Figures 105 through 108 show the effects due to variation in the shape of the ice protuberance. All of the shapes considered are located at 10% chord and have a maximum height of *k/c* = 0.0139. Shape A is the same forward-facing quarter round discussed in section 4.2.1.1, Shape B is a backward-facing quarter round, and Shape C is a forward-facing triangular ramp. The shapes are presented in figure 7. The comparison with experiment for all three shapes was similar to that discussed previously for Shape A. As can be seen in the figures, all of the shapes have very similar effects on the aerodynamic coefficients, but it appears that the two forward-facing shapes (A and C) have a slightly more detrimental effect on the performance than the backward-facing quarter round (Shape B).

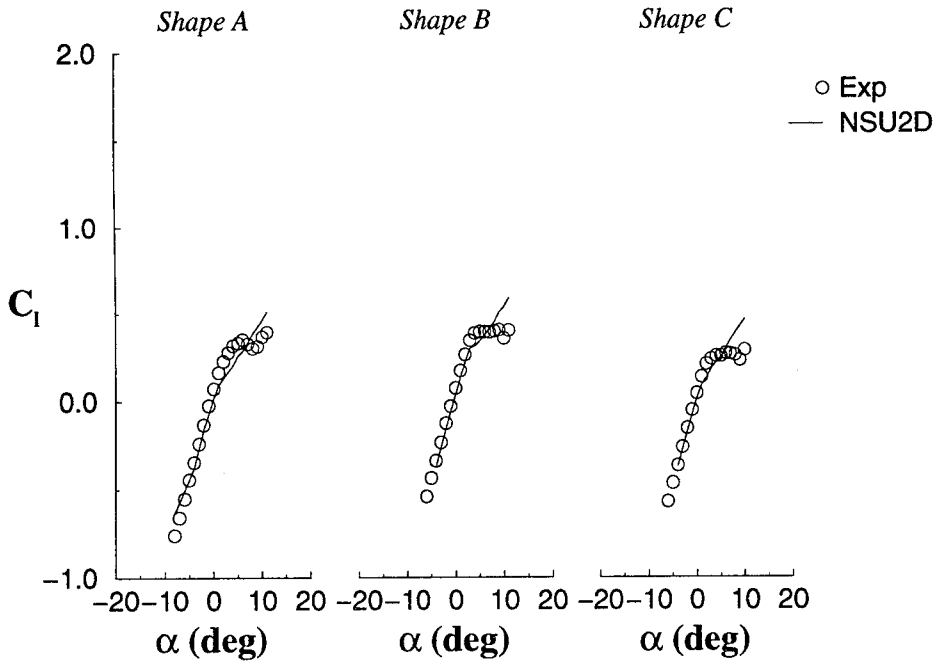

FIGURE 105. EFFECT OF ICE SHAPE GEOMETRY ON LIFT FOR $k/c = 0.0139$ ICE SHAPES LOCATED AT $x/c = 0.1$

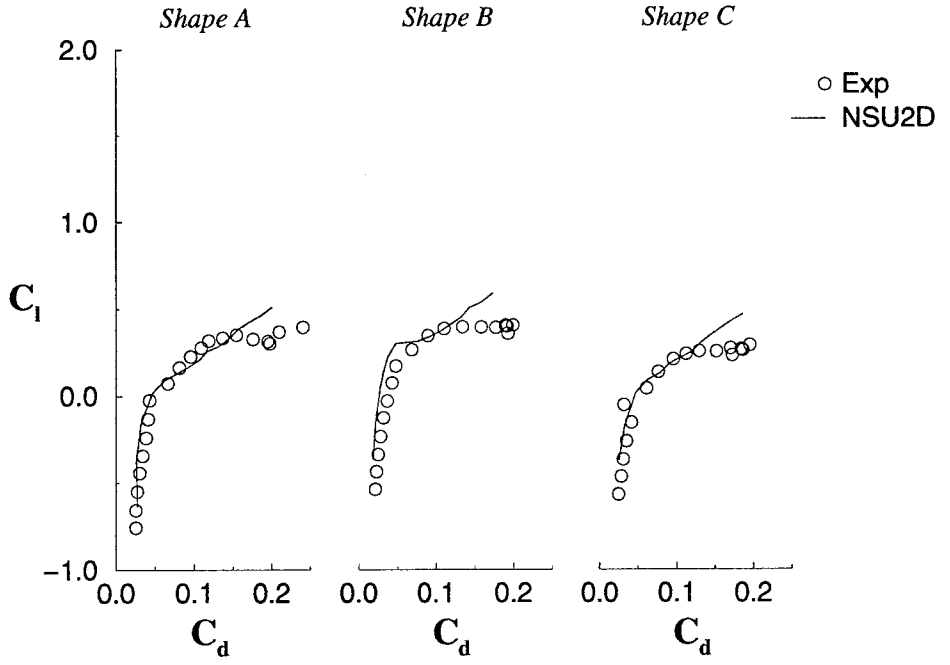

FIGURE 106. EFFECT OF ICE SHAPE GEOMETRY ON DRAG FOR $k/c = 0.0139$ ICE SHAPES LOCATED AT $x/c = 0.1$

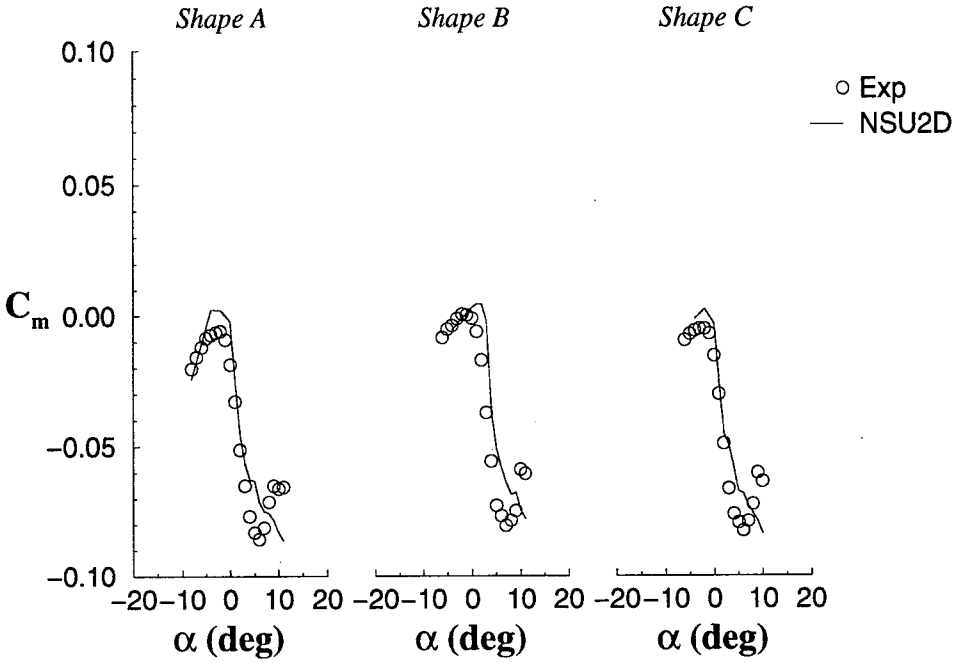

FIGURE 107. EFFECT OF ICE SHAPE GEOMETRY ON PITCHING MOMENT FOR $k/c = 0.0139$ ICE SHAPES LOCATED AT $x/c = 0.1$

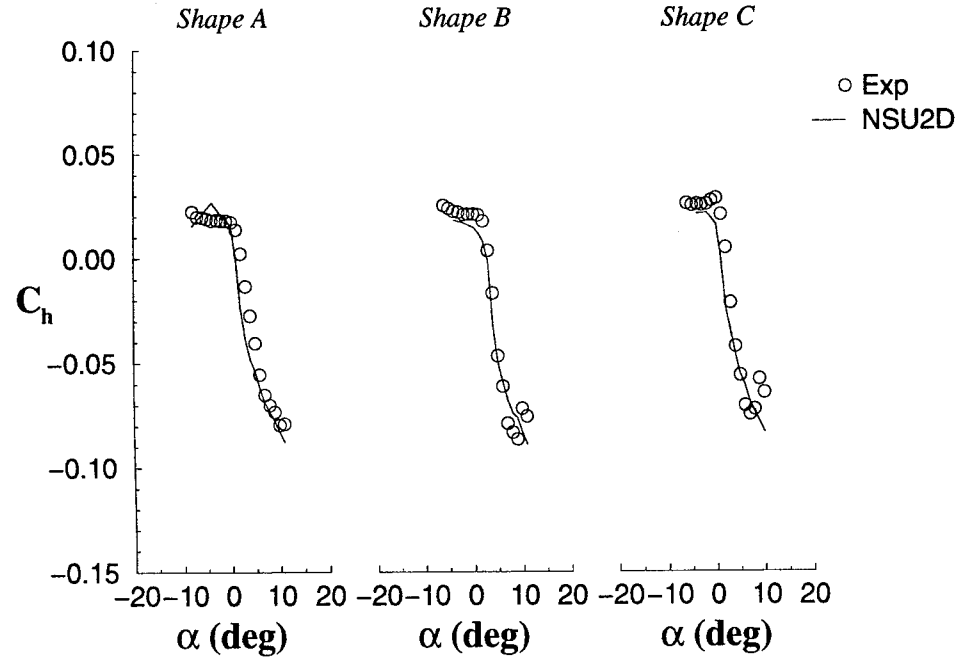

FIGURE 108. EFFECT OF ICE SHAPE GEOMETRY ON HINGE MOMENT FOR $k/c = 0.0139$ ICE SHAPES LOCATED AT $x/c = 0.1$

4.2.1.5 Effects of Flap Deflection.

Calculation for the clean NACA 23012m airfoil were studied for the flap deflections of 0, 5, and 10 degrees. Figures 109 through 112 show the effects due to flap deflection for the clean case. The computational predictions are compared with UIUC experimental data. We see that the NSU2D predictions for the non-iced cases exhibited good comparison with the experimental results, although the slope of the lift curve and maximum lift coefficient were overestimated. The code is generally able to robustly predict trends due to flap deflection on the lift curve slope and the maximum lift for the non-iced NACA 23012m airfoil. The effect on drag, pitching moment, and hinge moment, due to flap deflection, show that computational predictions agreed well with the experimental data.

The effect on the forces and moments due to variation in flap deflection is shown in figures 113 through 116 for the $k/c = 0.0083$ iced case located at 10% chord. The computations agree well with the experimental data throughout the linear range. However, the prediction of lift and drag, in the nonlinear range, is only qualitatively correct.

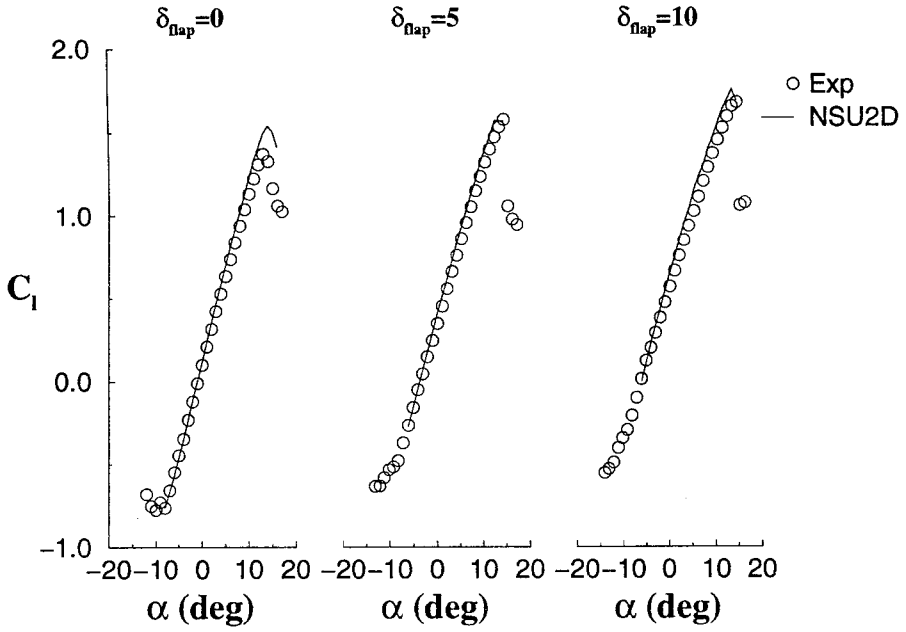

FIGURE 109. EFFECT OF FLAP DEFLECTION ON LIFT FOR $k/c = 0.0$

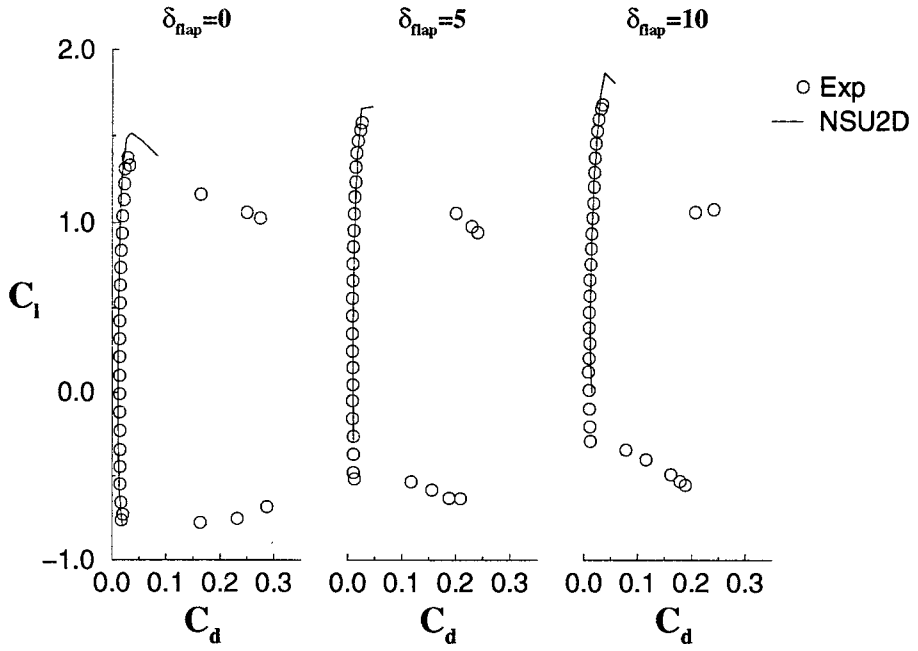

FIGURE 110. EFFECT OF FLAP DEFLECTION ON DRAG FOR $k/c = 0.0$

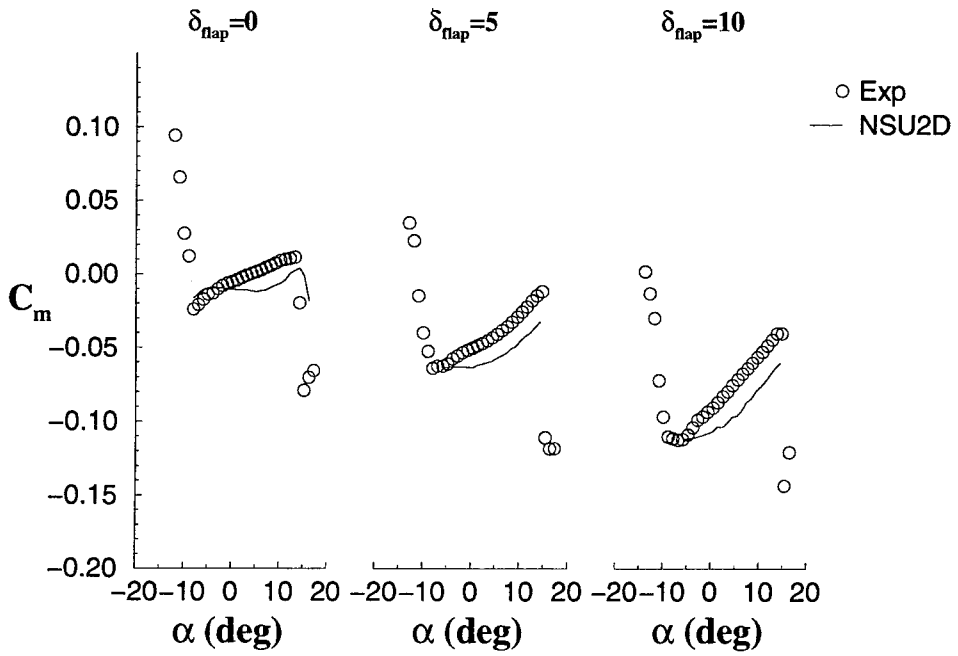

FIGURE 111. EFFECT OF FLAP DEFLECTION ON PITCHING MOMENT FOR $k/c = 0.0$

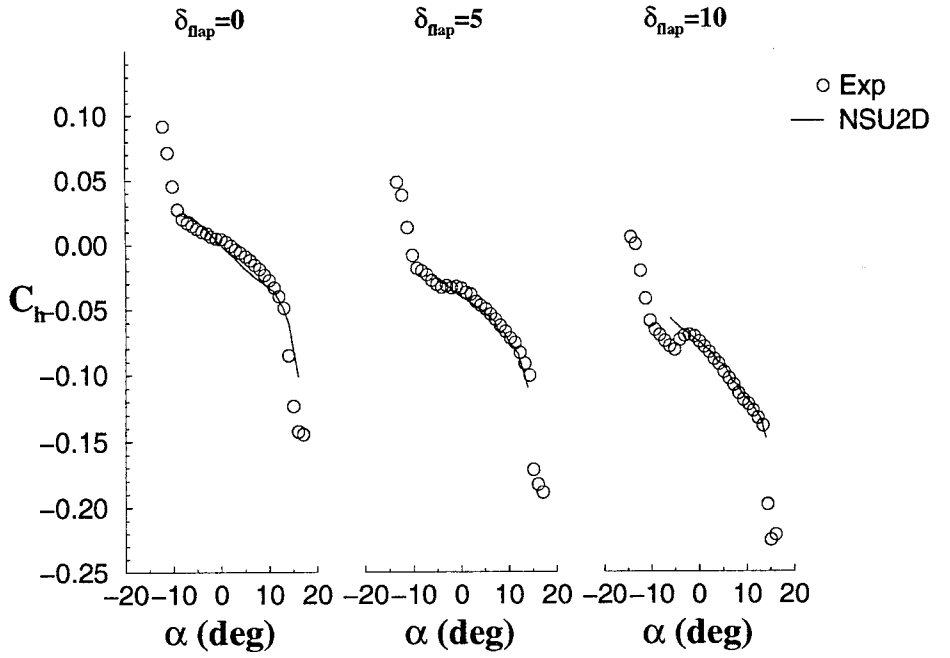

FIGURE 112. EFFECT OF FLAP DEFLECTION ON HINGE MOMENT FOR $k/c = 0.0$

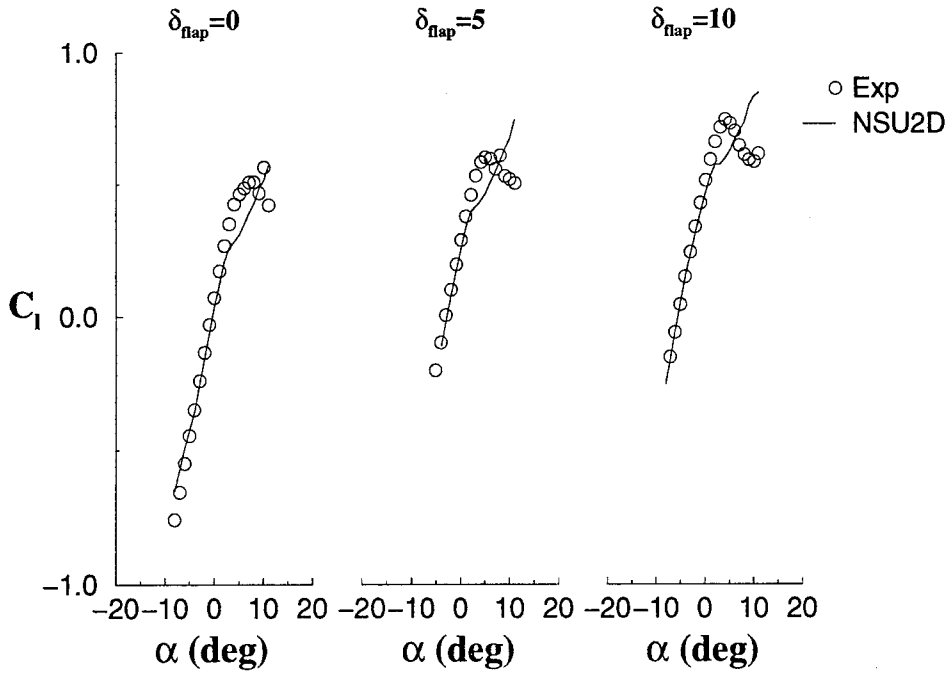

FIGURE 113. EFFECT OF FLAP DEFLECTION ON LIFT FOR ICED CASE WITH $k/c = 0.0083$ LOCATED AT $x/c = 0.1$

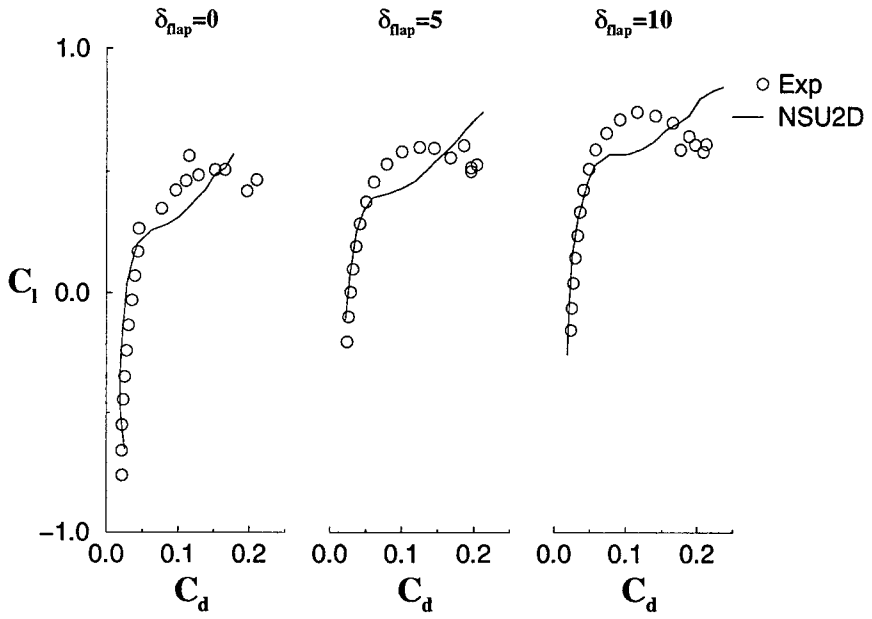

FIGURE 114. EFFECT OF FLAP DEFLECTION ON DRAG FOR ICED CASE WITH $k/c = 0.0083$ LOCATED AT $x/c = 0.1$

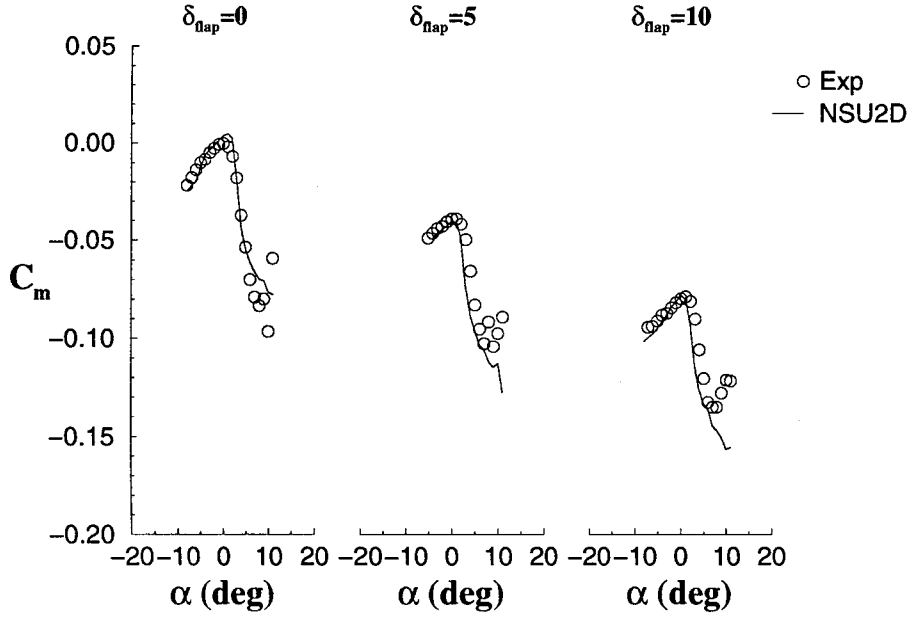

FIGURE 115. EFFECT OF FLAP DEFLECTION ON PITCHING MOMENT FOR ICED CASE WITH $k/c = 0.0083$ LOCATED AT $x/c = 0.1$

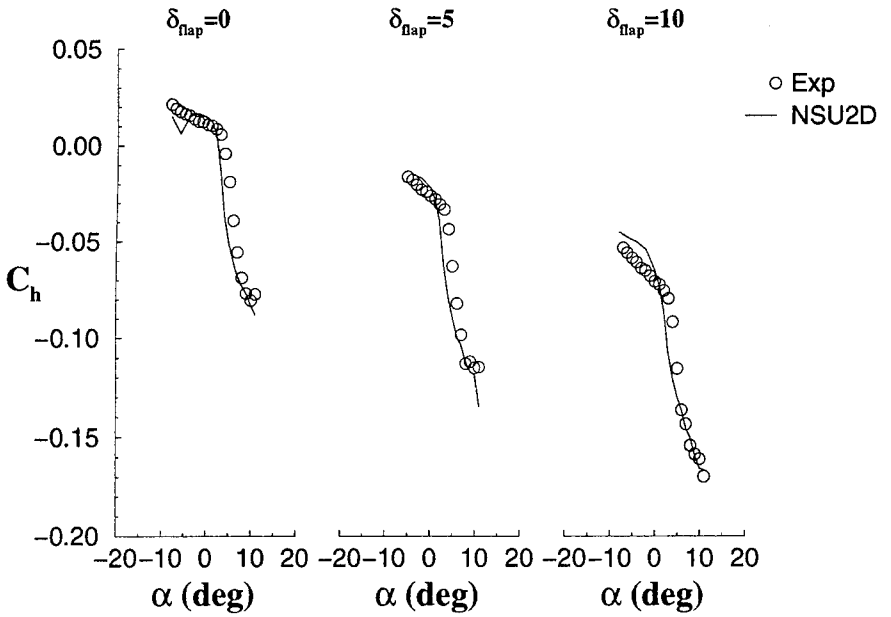

FIGURE 116. EFFECT OF FLAP DEFLECTION ON HINGE MOMENT FOR ICED CASE WITH $k/c = 0.0083$ LOCATED AT $x/c = 0.1$

4.2.1.6 Effects of Variation in Reynolds Number.

The effects on the aerodynamic performance of an iced NACA 23012m, due to variations in Reynolds number, are shown in figures 117 through 120. The $k/c = 0.0083$ quarter-round protuberance located at $x/c = 0.1$ was chosen for this study. Since there was no experimental data available for the larger Reynolds numbers, only computations are presented for the higher Reynolds number cases. Simulations for Reynolds numbers of 1.0, 1.8, 4, 6, and 8 million are compared. Note, in order to save computation time, only the positive angles of attack were run for the $Re = 6 \times 10^6$ and $Re = 8 \times 10^6$ and no unstructured grid adaption was used for the higher Reynolds numbers. None of the aerodynamic coefficients plotted here showed a significant Reynolds number influence. As such, the minor variation in the computed results for the four Reynolds numbers could be attributed to computational uncertainties in the simulations. The lack of a Reynolds number influence is consistent with the assertion of Bragg [72] that Reynolds number effects are critical for the clean case but are not discernible for the iced case. The reason is being that the separated shear flow is insensitive to the details of the approaching boundary layer at these conditions.

For very low angles of attack, the predictions did exhibit a slight reduction in drag at the higher Reynolds number due to the decrease in skin friction (figure 118). However, the upper angles did not exhibit this behavior as the influence of the pressure drag began to dominate the skin friction. Comparison of the pressure coefficient distributions for these cases (not shown) also reveals no significant differences caused by Reynolds number variation. It should be noted, however, that most Reynolds number effects become apparent close to stall (see section 3.3.2.1,

and as noted earlier, stall is not accurately predicted with the current steady-state methodology due to the expected large-scale unsteady behavior in the separation bubble. Therefore, the applicability of the results in the fully separated regime is not certain.

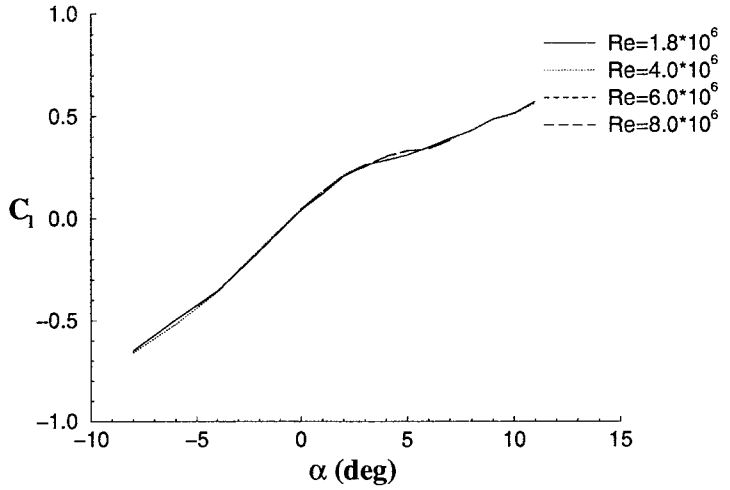

FIGURE 117. EFFECT OF REYNOLDS NUMBER ON LIFT FOR $k/c = 0.0083$ ICE SHAPE LOCATED AT $x/c = 0.1$

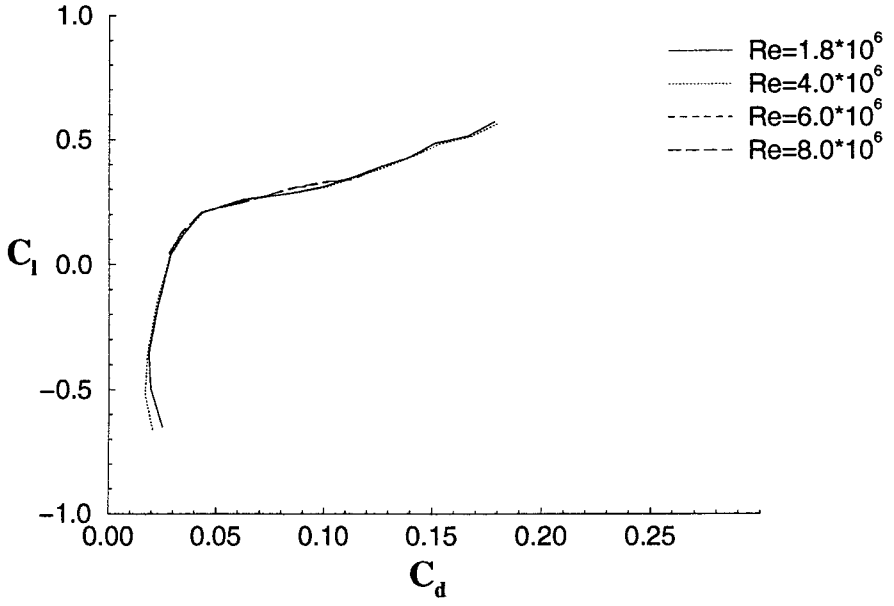

FIGURE 118. EFFECT OF REYNOLDS NUMBER ON DRAG FOR $k/c = 0.0083$ ICE SHAPE LOCATED AT $x/c = 0.1$

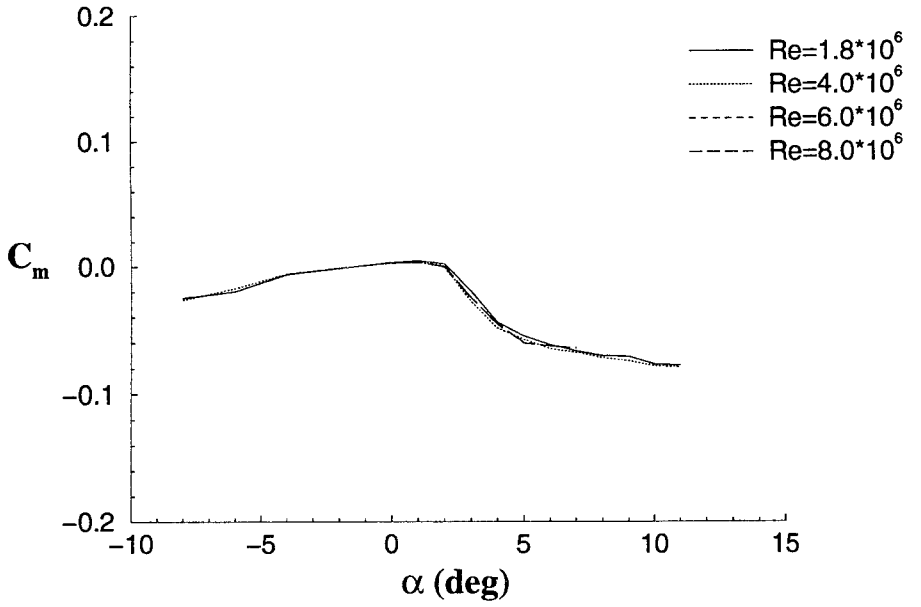

FIGURE 119. EFFECT OF REYNOLDS NUMBER ON PITCHING MOMENT FOR $k/c = 0.0083$ ICE SHAPE LOCATED AT $x/c = 0.1$

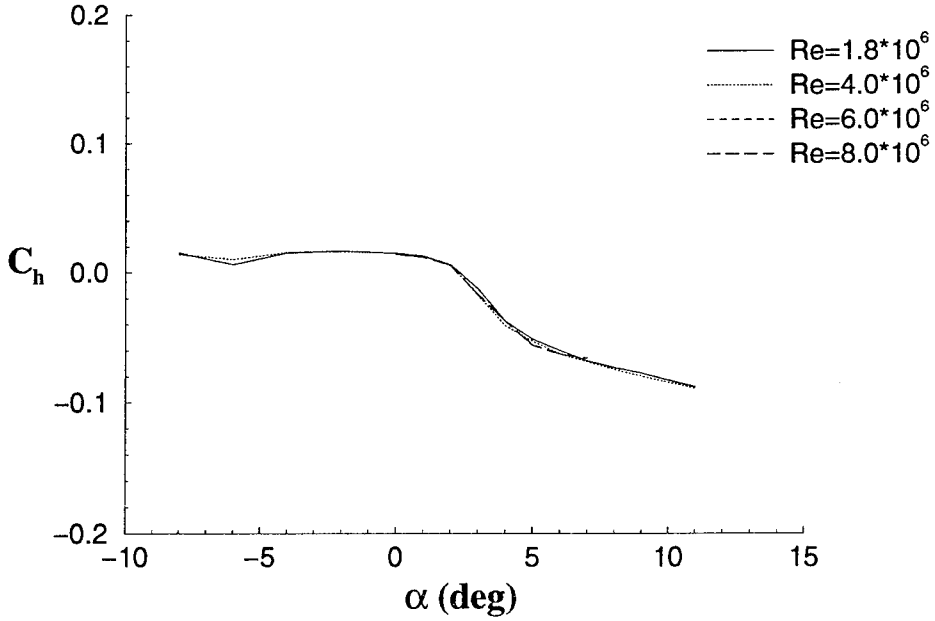

FIGURE 120. EFFECT OF REYNOLDS NUMBER ON HINGE MOMENT FOR $k/c = 0.0083$ ICE SHAPE LOCATED AT $x/c = 0.1$

4.2.2 Other Iced Airfoil Simulations.

The effect on the aerodynamic coefficients due to the variation in airfoil geometry was studied. Three other airfoils, in addition to the NACA 23012m, were chosen for this study. The coordinates for all three were provided by NASA Glenn, which has used them in other studies. The NLF 0414 was included as representative of a general aviation aircraft main wing. A business jet model was included as representative of a business jet main wing. The business jet model is referred to as the GLC 305 in some NASA publications, although its coordinates differ slightly from the GLC 305 airfoil. Finally, a large transport horizontal stabilizer (LTHS), was included as representative of a commercial large transport tailplane. We wish to thank Mr. Gene Addy of NASA's John H. Glenn Research Center at Lewis Field for providing us with the airfoil geometries of the above airfoils. The geometries used for results in this section had a quarter-round ice shape size of $k/c = 0.0083$, located at 10% chord.

Figures 121 through 124 shows the surface pressure distribution for the clean case for all the four airfoils at an equivalent C_ℓ of approximately 0.5. The business jet model and the LTHSs were run at a $Re = 8 \times 10^6$, while the data for $Re = 1.8 \times 10^6$ is presented for the NACA 23012m and the NLF 0414, since the experimental runs were conducted at this Reynolds number for these airfoils. It can be seen from these figures that the NACA 23012m is a forward-loaded airfoil with a light loading of the flap. The NLF 0414 has a relatively uniform chordwise loading until the pressure recovery near the trailing edge. Both the business jet model and the LTHSs have the same type of loading, both are forward-loaded airfoils with a light loading of the flap in the clean case. Both the business jet model and the LTHS airfoils have large suction peaks.

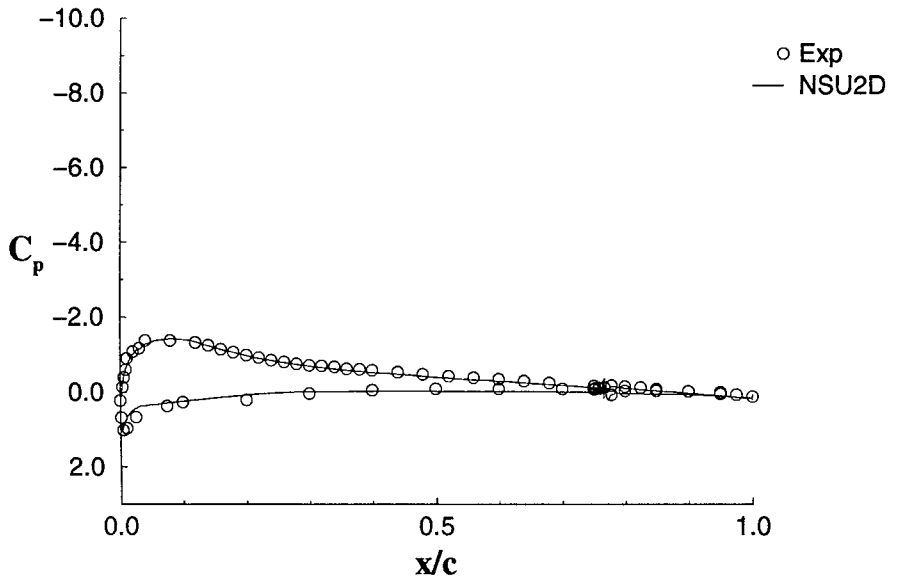

FIGURE 121. SURFACE PRESSURE DISTRIBUTION FOR A CLEAN NACA 23012m AIRFOIL FOR AN EQUIVALENT $C_\ell = 0.5$ AT $\alpha = 4°$

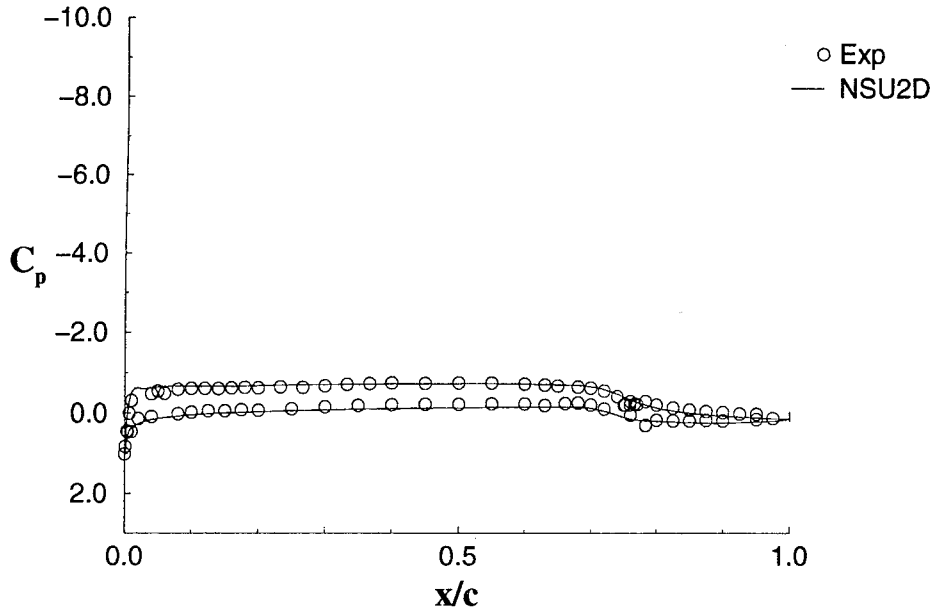

FIGURE 122. SURFACE PRESSURE DISTRIBUTION FOR A CLEAN NLF 0414 AIRFOIL FOR AN EQUIVALENT $C_\ell = 0.5$ AT $\alpha = 0°$

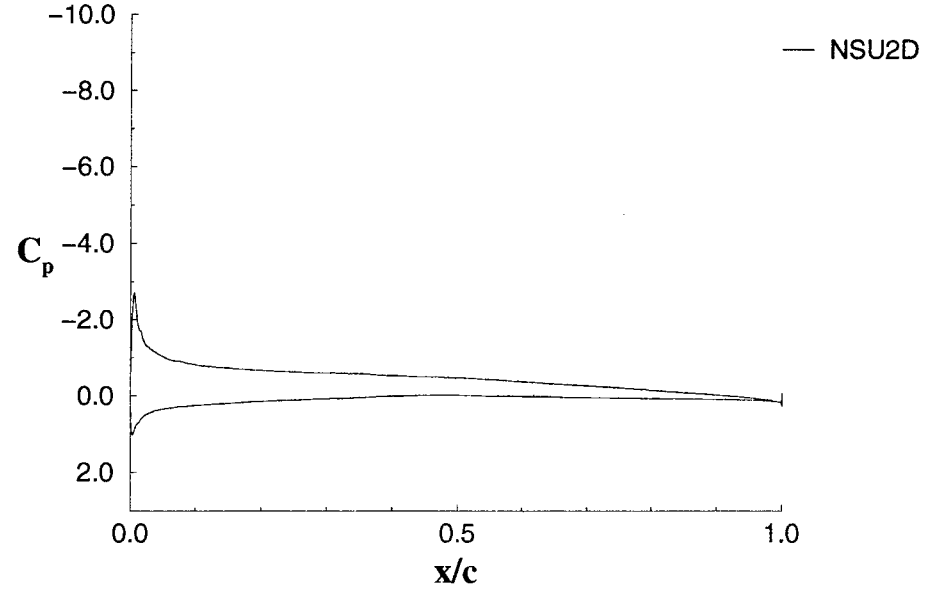

FIGURE 123. SURFACE PRESSURE DISTRIBUTION FOR A CLEAN BUSINESS JET MODEL AIRFOIL FOR AN EQUIVALENT $C_\ell = 0.5$ AT $\alpha = 4°$

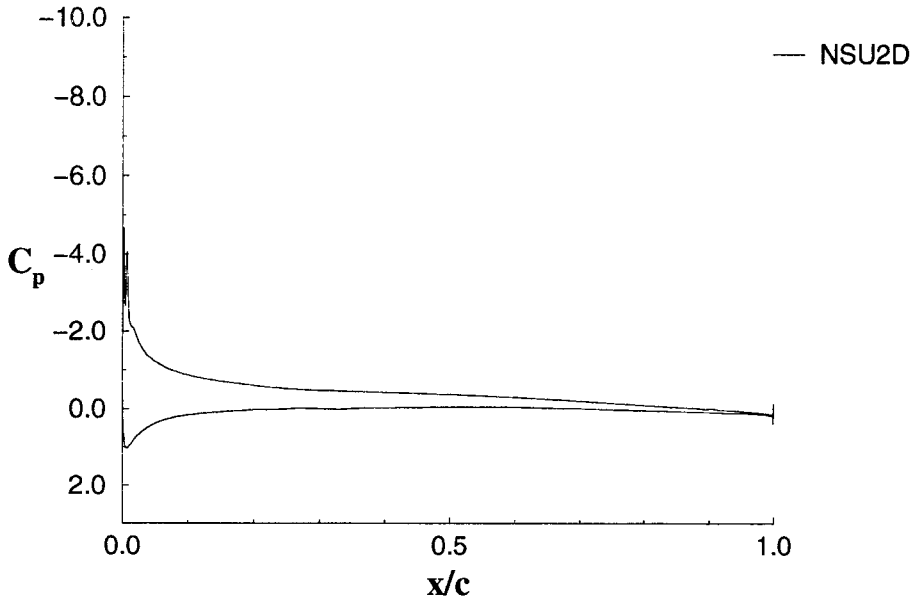

FIGURE 124. SURFACE PRESSURE DISTRIBUTION FOR A CLEAN LARGE TRANSPORT HORIZONTAL STABILIZER AIRFOIL FOR AN EQUIVALENT $C_\ell = 0.5$ AT $\alpha = 4°$

4.2.2.1 NLF Airfoil Results.

4.2.2.1.1 NLF Airfoil Results: Effect of Ice Shape Location.

Figures 125 through 128 show the effect on the aerodynamic coefficients due to variation in ice shape location for the NLF 0414 airfoil with a quarter-round ice shape size of $k/c = 0.0083$. The locations chosen for the study were $x/c = 0.02$, $x/c = 0.1$, and $x/c = 0.3$. The computations predict a much earlier stall and a much lower C_ℓ. The peculiar shape of the NLF airfoil makes it a very difficult candidate to obtain good agreement with the experimental results. The NLF 0414 airfoil is highly cambered near the trailing edge, where the pressure recovery occurs. The load is distributed over a large portion of the chord and the onset of pressure recovery and the accompanying large adverse pressure gradient is delayed until around 70% chord. As seen from figure 75, NSU2D predicts a much smaller pressure spike near the leading edge in presence of the ice and a larger pressure recovery to occur immediately after the pressure spike compared to the experiment. This could be a reason why there was a discrepancy in both lift and moment coefficients, especially at higher angles of attack.

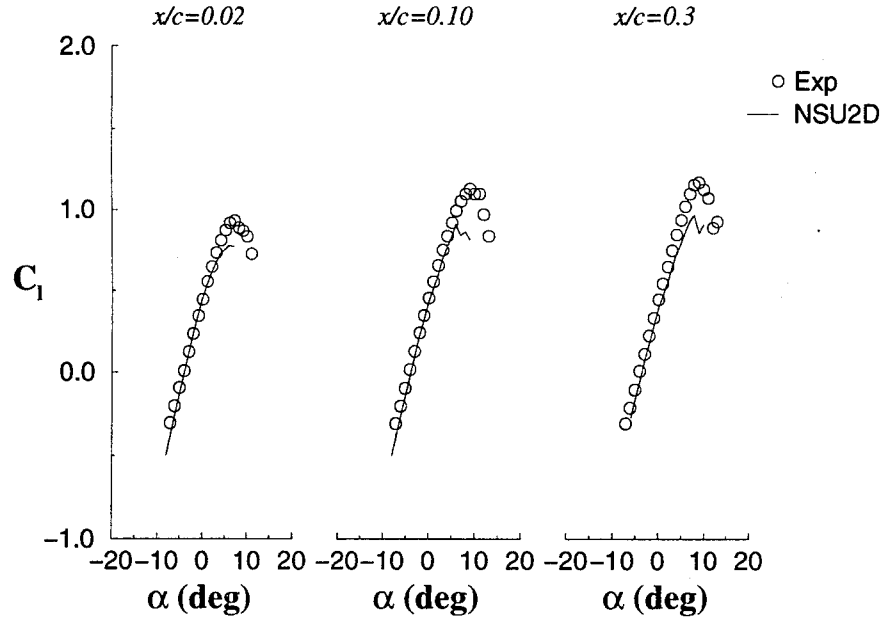

FIGURE 125. EFFECT OF ICE SHAPE LOCATION ON LIFT FOR k/c = 0.0083 ICE SHAPES FOR THE NLF AIRFOIL

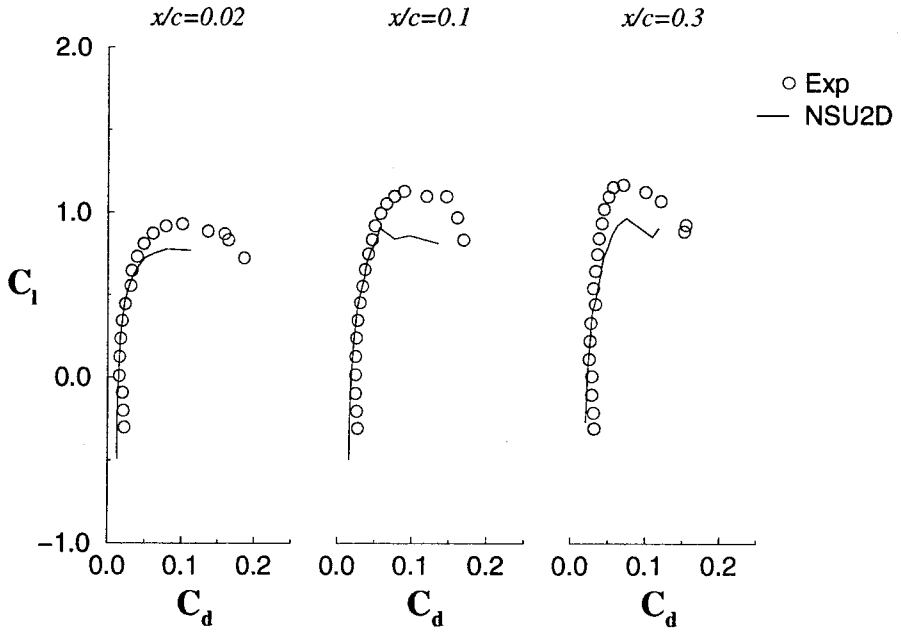

FIGURE 126. EFFECT OF ICE SHAPE LOCATION ON DRAG FOR k/c = 0.0083 ICE SHAPES FOR THE NLF AIRFOIL

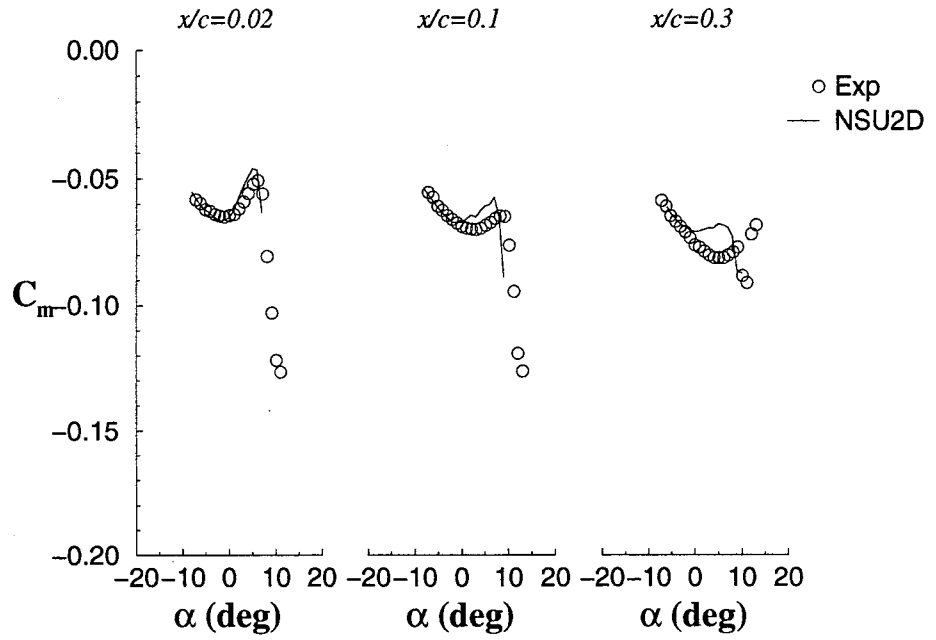

FIGURE 127. EFFECT OF ICE SHAPE LOCATION ON PITCHING MOMENT FOR k/c = 0.0083 ICE SHAPES FOR THE NLF AIRFOIL

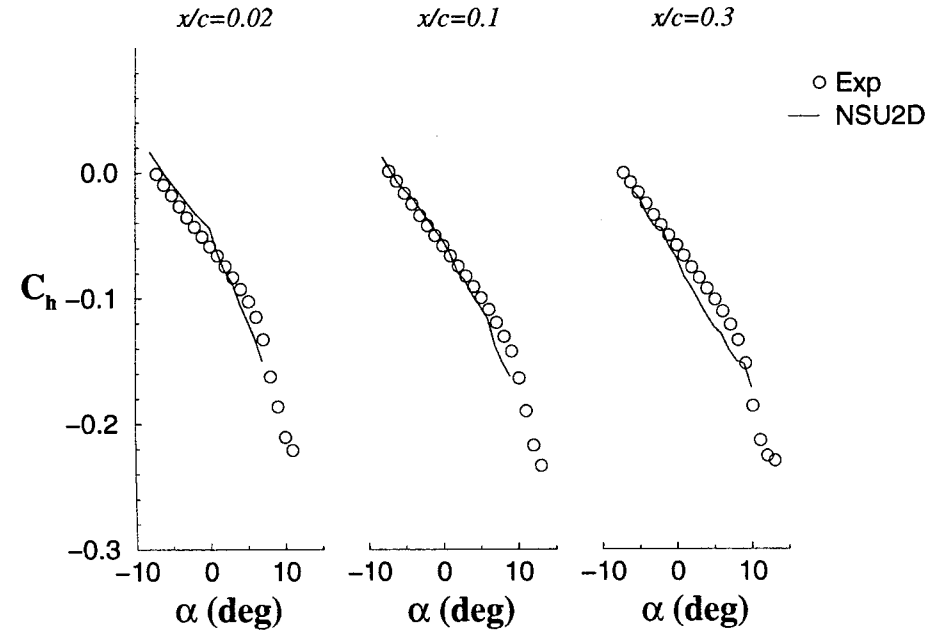

FIGURE 128. EFFECT OF ICE SHAPE LOCATION ON HINGE MOMENT FOR k/c = 0.0083 ICE SHAPES FOR THE NLF AIRFOIL

The plot of predicted lift coefficients, shows that the computational predictions of the 2%, 10%, and the 30% cases agreed reasonably well with the experimental results. Both the computations and experiments indicate large detrimental effects for all the ice shape locations tested. However, the leading-edge location appears to be the worst. The drag coefficient plot (figure 126) indicated reasonably good agreement with the experimental results at low angles of attack. However, the angle at which the drag suddenly increases was underpredicted, especially for $x/c = 0.1$. The break in the pitching moment curve (figure 127), occurred earlier for the computations. This could be because the bubble reattached earlier, compared to the experiment. The hinge moment predictions (figure 128) which is an important parameter with respect to aircraft control, agreed surprisingly well with experimental results. However, a distinctive break was observed in the computational predictions of the hinge moment $x/c = 0.02$ case, which was substantially delayed in the experimental results.

Figures 129 through 131 show the reattachment length for the separation bubble aft of the ice shape versus the airfoil's angle of attack for the 2%, 10%, and 30% iced cases of the NLF 0414 airfoil. The computational reattachment lengths were determined using the predicted skin friction along the airfoil surface. The reattachment lengths grew slowly at low angles, e.g., at $\alpha < 5°$, in all the three cases, then quickly grew at the larger angles until the bubble reached the trailing edge. The plots show that the bubble almost has an exponential growth. All the cases have a combination of a thin-airfoil type of stall and a trailing-edge type of stall. In fact, there was trailing-edge separation even at negative angles of attack. Comparison with figure 125 shows that the prediction of lift is reasonable up until full separation after which it can underpredict the lift. This is consistent with the NACA 23012m results. From figure 132, both computations and experiments indicate that for $k/c = 0.0083$, the near leading-edge locations, e.g., $x/c = 0.02$, have the most detrimental effect. However, the experimental results for $k/c = 0.0139$ shows that the $x/c = 0.3$ is the most critical. As such, the simulated ice shape location with the largest detrimental effect is not easily determined. All the locations tested seem to have a significant detrimental effect compared to the clean case.

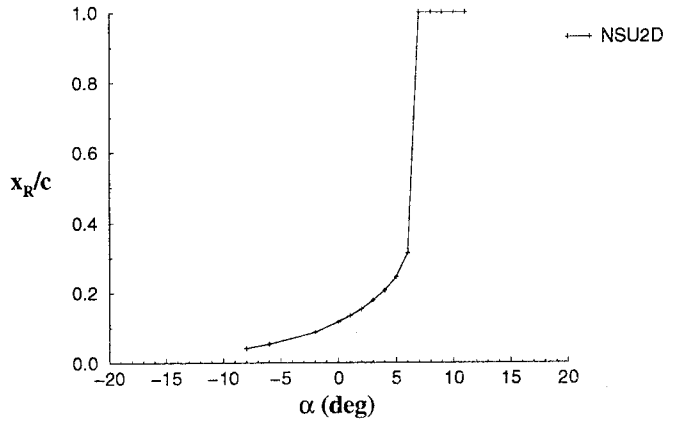

FIGURE 129. REATTACHMENT LOCATIONS OF THE AFT ICE SEPARATION BUBBLE FOR A NLF 0414 AIRFOIL WITH $k/c = 0.0083$ QUARTER-ROUND ICE SHAPE LOCATED AT $x/c = 0.02$

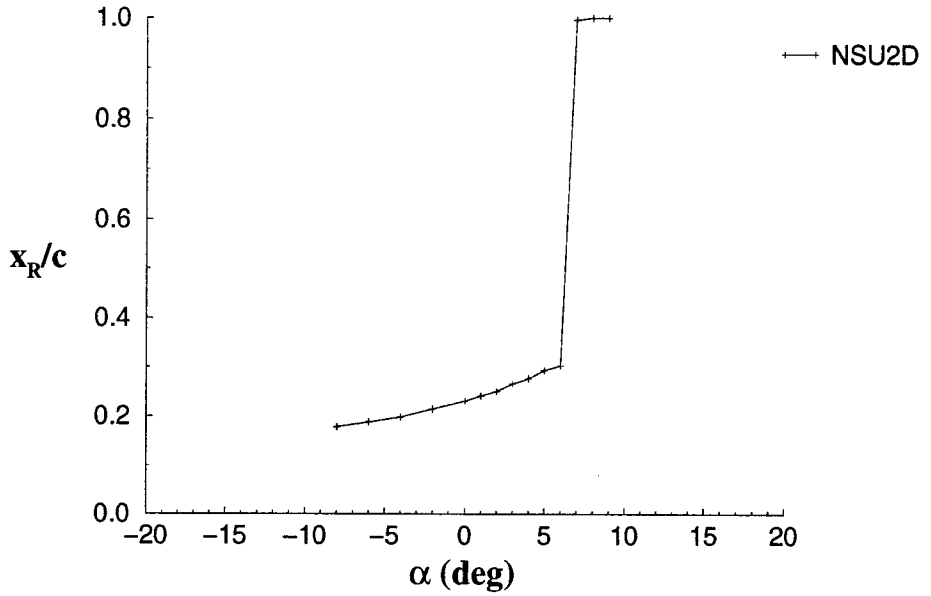

FIGURE 130. REATTACHMENT LOCATIONS OF THE AFT ICE SEPARATION BUBBLE FOR A NLF 0414 AIRFOIL WITH $k/c = 0.0083$ QUARTER-ROUND ICE SHAPE LOCATED AT $x/c = 0.1$

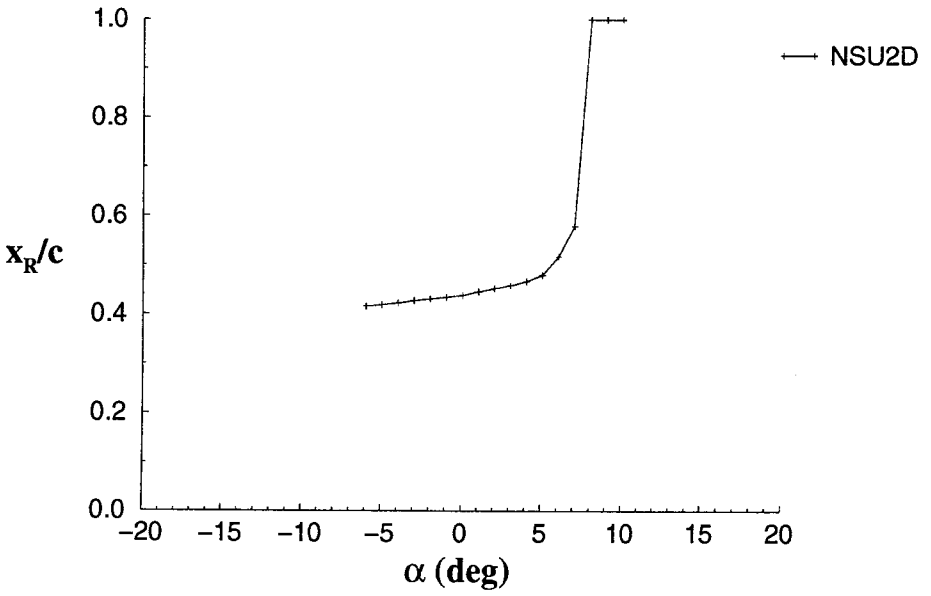

FIGURE 131. REATTACHMENT LOCATIONS OF THE AFT ICE SEPARATION BUBBLE FOR A NLF 0414 AIRFOIL WITH $k/c = 0.0083$ QUARTER-ROUND ICE SHAPE LOCATED AT $x/c = 0.03$

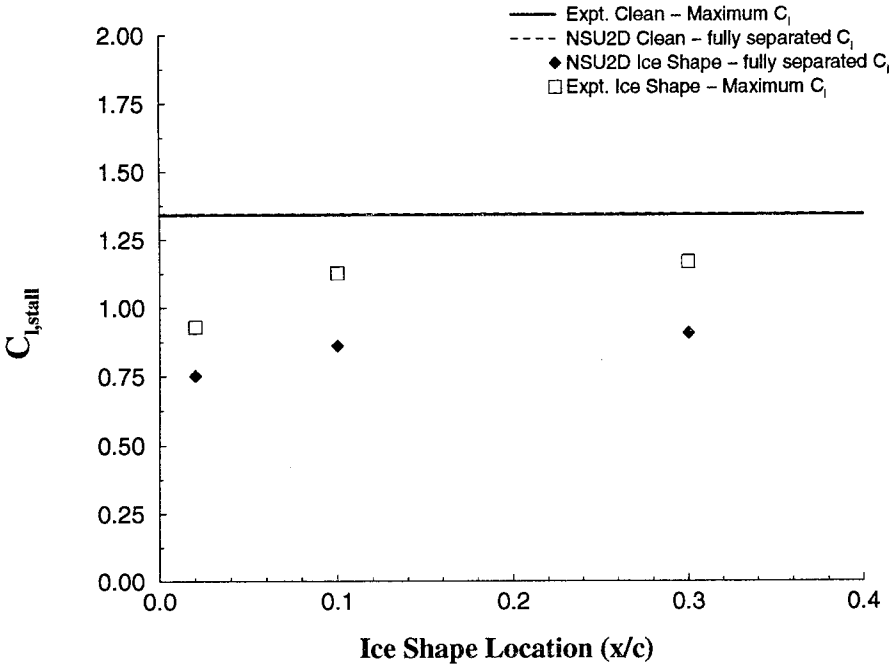

FIGURE 132. LIFT COEFFICIENT FOR ANGLE OF ATTACK AT WHICH FLOW FIRST FULLY SEPARATES VS. *x/c* FOR A NLF 0414 WITH *k/c* = 0.0083 QUARTER-ROUND ICE SHAPE

4.2.2.1.2 NLF Airfoil Results: Effects of Variation in Size.

In the following section, the aerodynamic influence of a quarter-round ice shape is considered computationally by varying its maximum height for the NLF 0414 airfoil. The ice location was held constant at 10% chord and two sizes were studied: *k/c* = 0.0083 and *k/c* = 0.0139. In addition, a case with no ice shape (*k/c* = 0.0) which included only the boundary layer trip was used as a reference condition.

The lift curves for these configurations are shown in figure 133. The significant reduction in lift curve slope, the maximum lift coefficient and maximum lift angle caused by the ice shape presence were predicted reasonably well by NSU2D. However, for both iced cases, the NSU2D predictions exhibited an earlier, more abrupt break in the lift curve slope than that shown by the experiments.

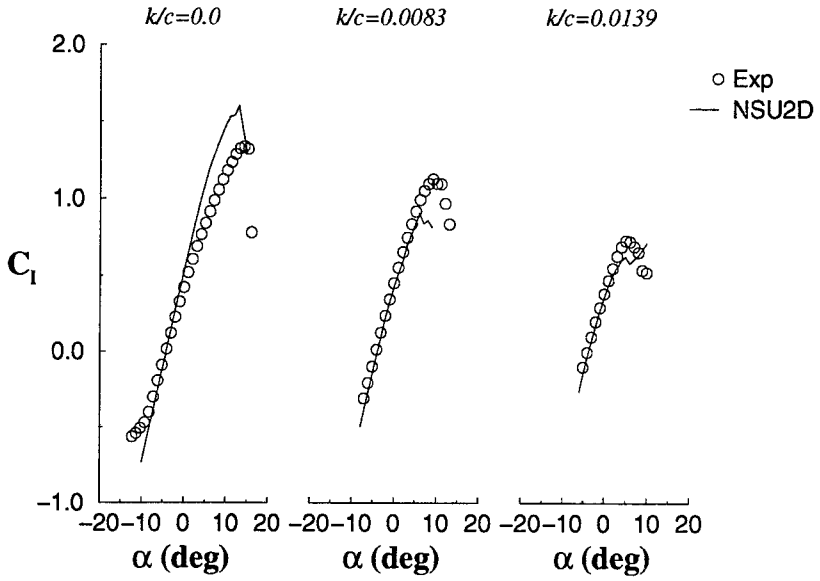

FIGURE 133. EFFECT OF ICE SHAPE ON LIFT FOR A NLF 0414 AIRFOIL WITH QUARTER-ROUND ICE SHAPE LOCATED AT $x/c = 0.1$

Figure 134 shows the drag predictions. The trends due to the presence and height change of the ice shape were well predicted by NSU2D, considering the large amount of separation occurring for the iced airfoil flows. At low angles of attack, NSU2D predicted the small increase in drag as the ice size was increased, although the magnitude was slightly underpredicted. Both the computations and the experiments showed a significant increase in drag for the iced cases at large angles of attack.

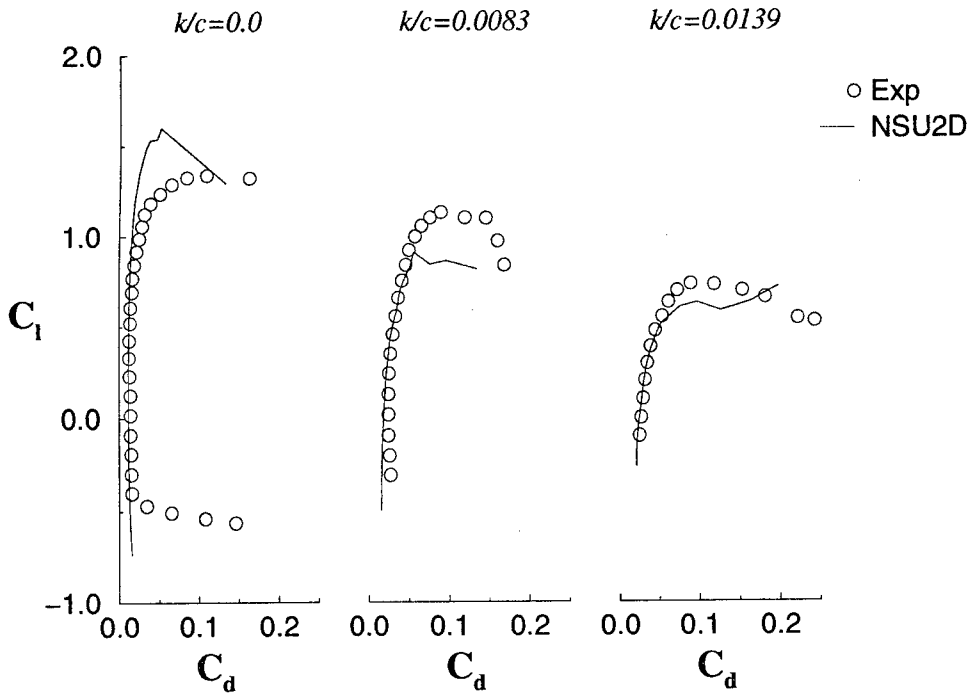

FIGURE 134. EFFECT OF ICE SHAPE HEIGHT ON DRAG FOR A NLF 0414 AIRFOIL WITH A QUARTER-ROUND ICE SHAPE LOCATED AT $x/c = 0.1$

Figure 135 shows the pitching moment coefficient distribution with angle of attack. The trends caused by the presence of the ice shapes were well reproduced by NSU2D. In fact, the NSU2D results for the iced cases had better agreement with the experiments than the clean case. NSU2D performed remarkably well for predicting the strong drop-off in moment at positive angles of attack as the ice shape was increased in size.

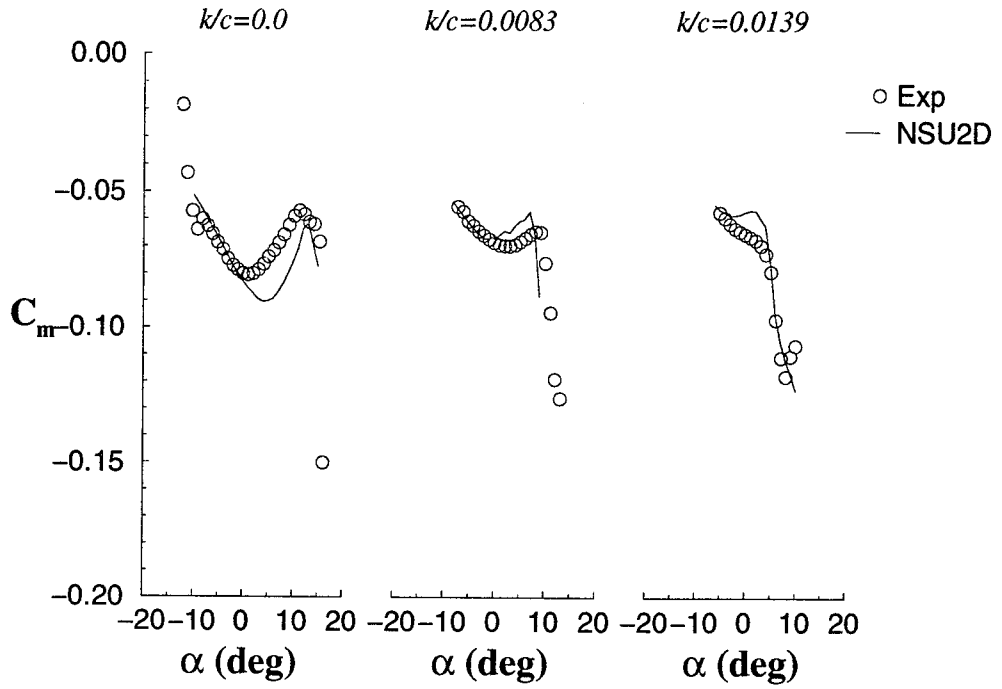

FIGURE 135. EFFECT OF ICE SHAPE HEIGHT ON PITCHING MOMENT FOR A NLF AIRFOIL WITH A QUARTER-ROUND ICE SHAPE LOCATED AT $x/c = 0.1$

Perhaps the most important aerodynamic coefficient, with respect to aircraft control, is the hinge moment. The comparison between computation and experiment of this critical parameter is shown in figure 136. Again, NSU2D successfully predicted the qualitative trends resulting from the presence and change in height of the ice shape. In particular, the increased drop-off in C_h at high angles of attack was reproduced both qualitatively and quantitatively.

In conclusion, it can be stated that the larger ice shape had a more detrimental effect (as expected) and NSU2D predictions agree with the experimental data more closely for the iced case of NLF 0414 than for the clean case. This is primarily due to the problem of prediction of a large transitional flow region in the clean case. (See discussion in section 3.3.2.5.)

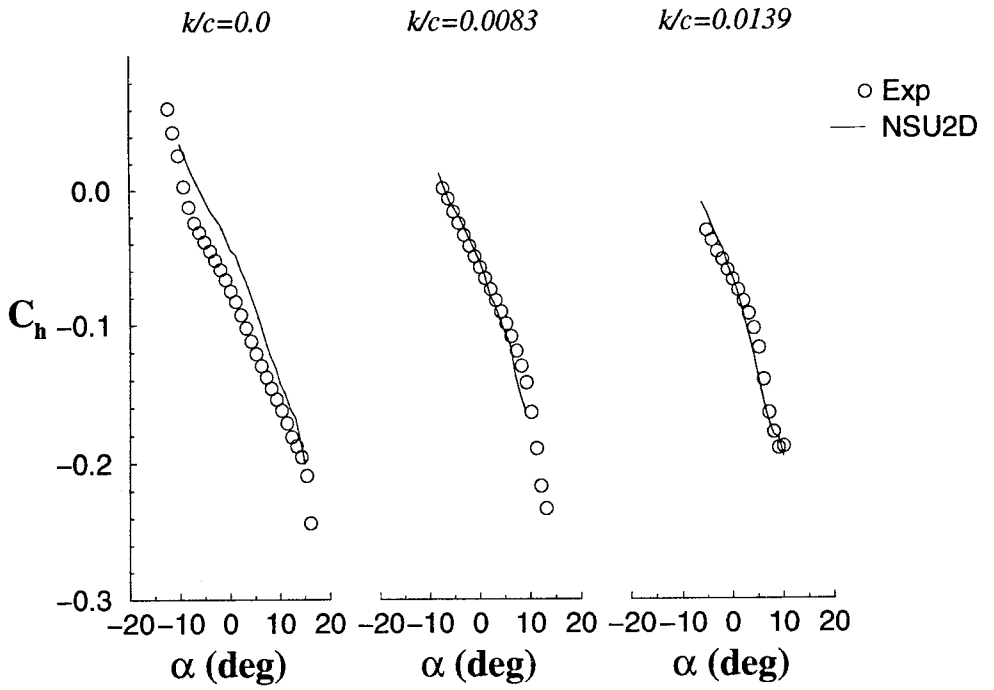

FIGURE 136. EFFECT OF ICE SHAPE HEIGHT ON HINGE MOMENT FOR A NLF 0414 AIRFOIL WITH A QUARTER-ROUND ICE SHAPE LOCATED AT $x/c = 0.1$

4.2.2.2 Business Jet Model Airfoil Results.

The business jet model clean airfoil is forward loaded. As observed earlier in the case of the forward-loaded NACA 23012m, a large detrimental effect of the ice shape is also expected in the case of the business jet model.

Figures 137 through 140 show the effect of ice shape location on aerodynamic coefficients for a $k/c = 0.0083$ ice shape for the business jet model airfoil. The locations chosen were $x/c = 0.02$, $x/c = 0.1$, and $x/c = 0.2$. The clean case results are also presented for comparison. It was observed from the lift and drag plots that the most detrimental effect of the ice shape on lift and drag would occur if the ice shape was placed close to $x/c = 0.02$. This is close to the location of minimum pressure for the clean airfoil condition, which was further upstream compared to the NACA 23012m (see figure 121 and 123).

The pitching moment and hinge moment plots (figures 139 and 140 show that the sharpest breaks occur for ice shape locations of $x/c = 0.02$ and $x/c = 0.1$. Consider the hinge moment plot shown in figure 140. On the clean business jet model, the flap is lightly loaded. When the separation bubble, due to the ice shape, reaches the flap, the flap became heavily loaded and caused a change in the hinge moment curve slope.

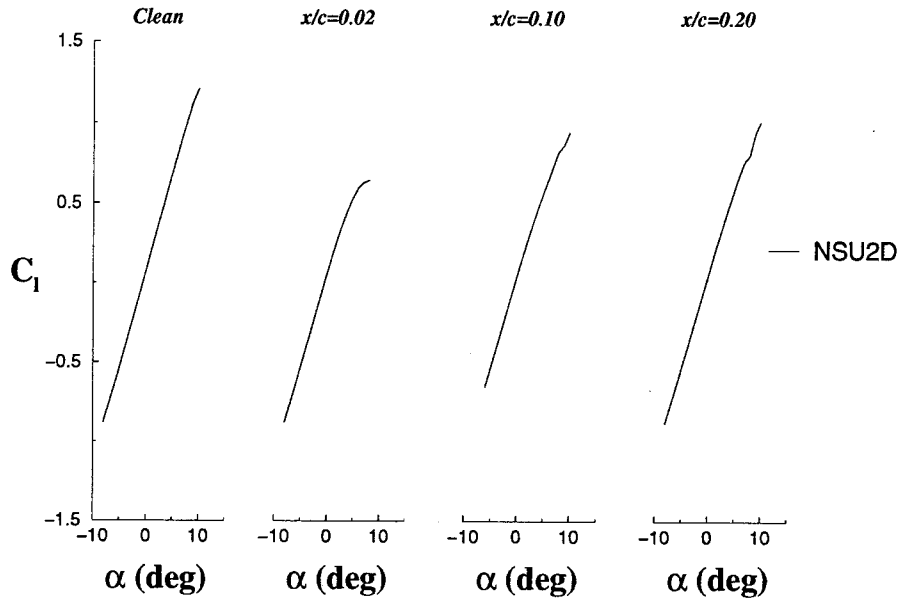

FIGURE 137. EFFECT OF ICE SHAPE LOCATION ON LIFT FOR k/c = 0.0083 ICE SHAPES FOR THE BUSINESS JET MODEL AIRFOIL

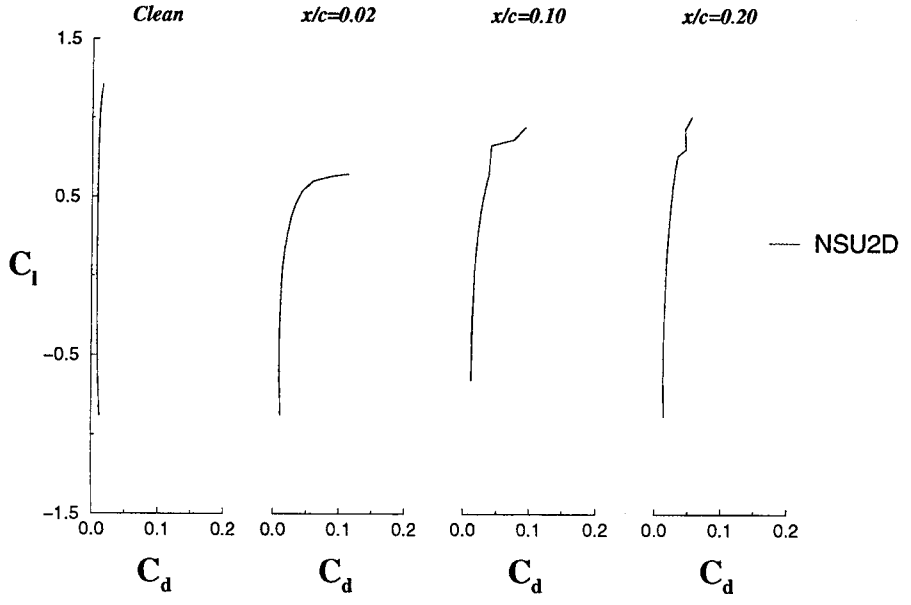

FIGURE 138. EFFECT OF ICE SHAPE LOCATION ON DRAG FOR k/c = 0.0083 ICE SHAPES FOR THE BUSINESS JET MODEL AIRFOIL

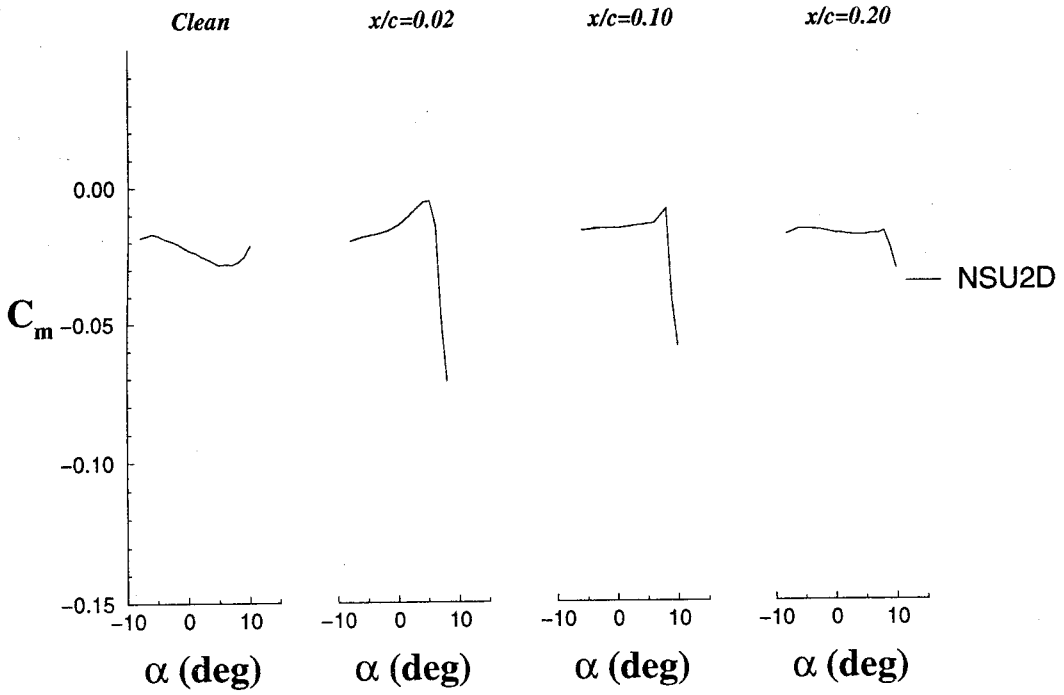

FIGURE 139. EFFECT OF ICE SHAPE LOCATION ON PITCHING MOMENT FOR k/c = 0.0083 ICE SHAPES FOR THE BUSINESS JET MODEL AIRFOIL

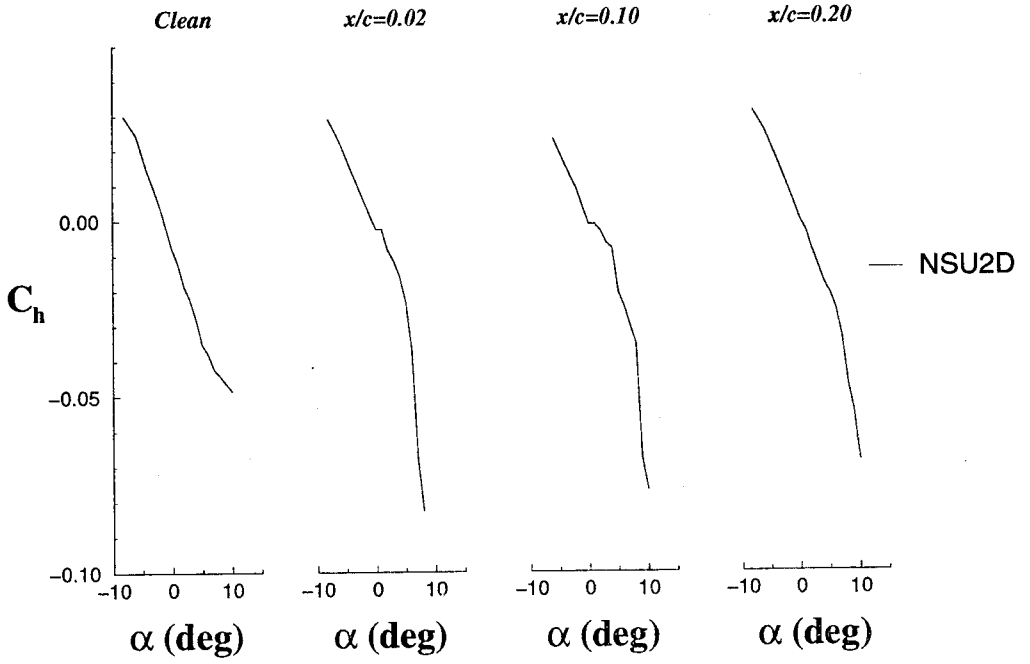

FIGURE 140. EFFECT OF ICE SHAPE LOCATION ON HINGE MOMENT FOR k/c = 0.0083 ICE SHAPES FOR THE BUSINESS JET MODEL AIRFOIL

Figures 141 through 143 show the plot of the reattachment length versus the airfoil angle of attack for the cases when the ice is located at 2%, 10%, and 20%. The 2% case has the largest detrimental effect on $C_{\ell,max}$. For this location the airfoil stalls at an angle of attack of 7 degrees which is the lowest stall angle among all the ice shape locations on this airfoil. As with the NACA 23012m, the worst location for the lift performance is close to the peak of C_p distribution. Also, the drag increases rapidly for this $C_{\ell,max}$. The $x/c = 0.02$ iced case exhibits a combination of a thin-airfoil type of stall and a trailing-edge type of stall; wherein, the trailing-edge separation point moves closer to and merges with the reattachment point of the bubble. The $x/c = 0.10$ iced case also had a detrimental effect on the airfoil performance. It has a low C_ℓ when the flow first fully separates and this occurred at an angle of attack of 8 degrees.

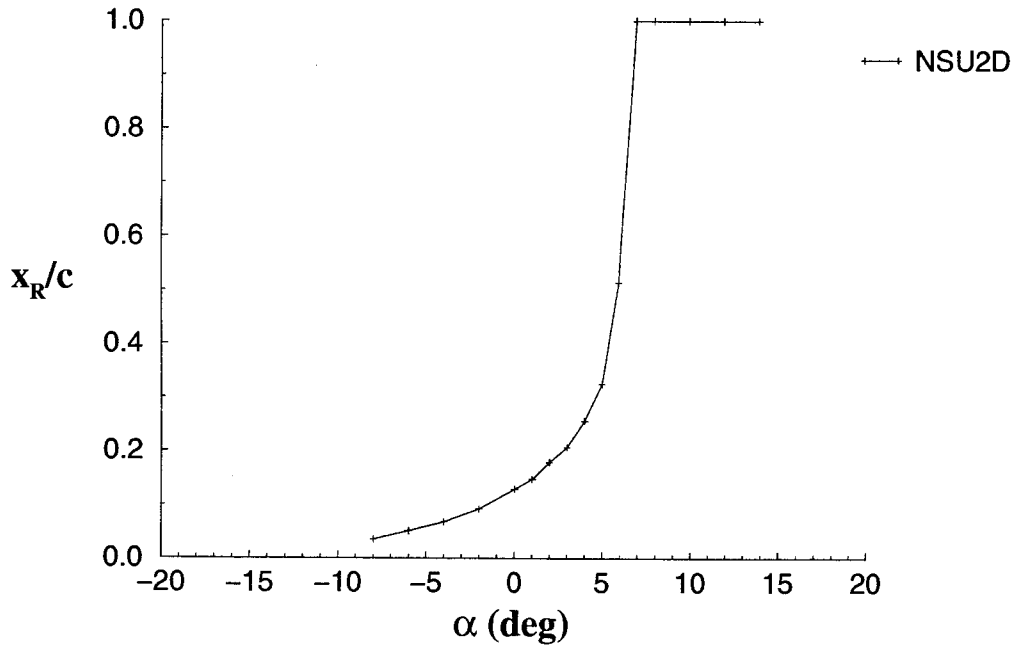

FIGURE 141. REATTACHMENT LOCATIONS OF THE AFT ICE SEPARATION BUBBLE FOR A BUSINESS JET MODEL AIRFOIL WITH $k/c = 0.0083$ QUARTER-ROUND ICE SHAPE LOCATED AT $x/c = 0.02$

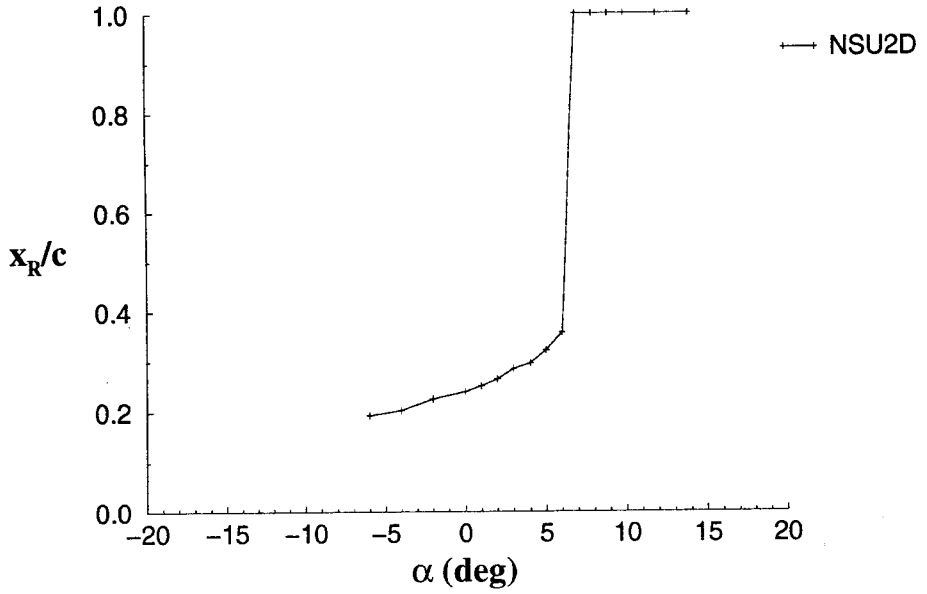

FIGURE 142. REATTACHMENT LOCATIONS OF THE AFT ICE SEPARATION BUBBLE FOR A BUSINESS JET MODEL AIRFOIL WITH $k/c = 0.0083$ QUARTER-ROUND ICE SHAPE LOCATED AT $x/c = 0.1$

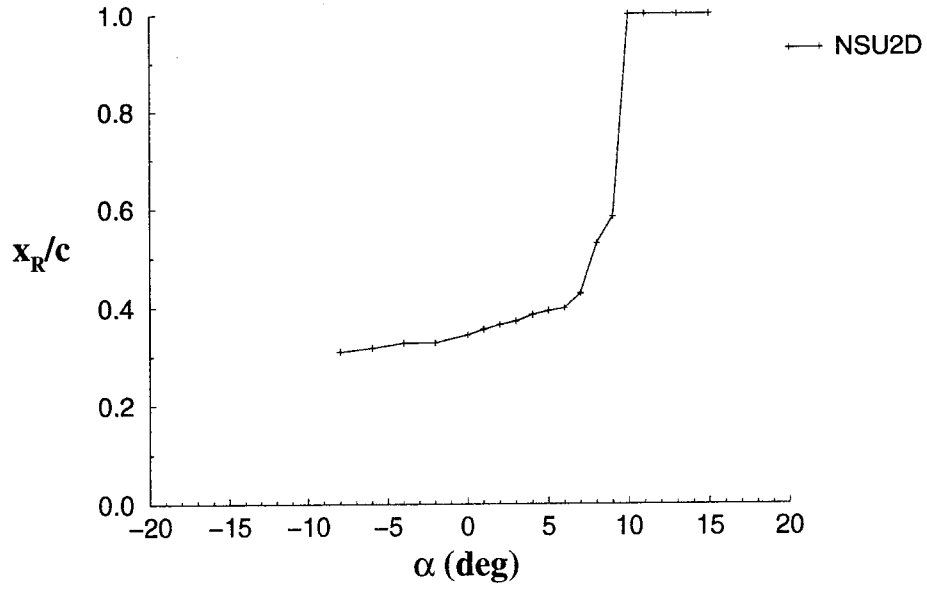

FIGURE 143. REATTACHMENT LOCATIONS OF THE AFT ICE SEPARATION BUBBLE FOR A BUSINESS JET MODEL AIRFOIL WITH $k/c = 0.0083$ QUARTER-ROUND ICE SHAPE LOCATED AT $x/c = 0.2$

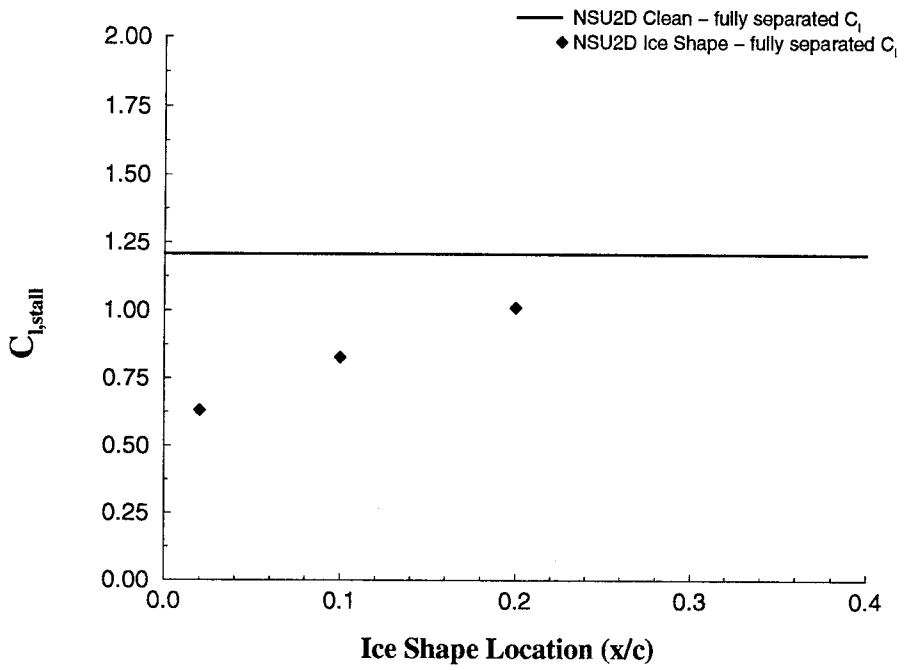

FIGURE 144. LIFT COEEFICIENT FOR ANGLE OF ATTACK AT WHICH FLOW FIRST FULLY SEPARATES VS. *x/c* FOR A BUSINESS JET MODEL WITH *k/c* = 0.0083 QUARTER-ROUND ICE SHAPE

4.2.2.3 Large Transport Horizontal Stabilizer Airfoil Results.

The clean LTHS airfoil is forward loaded. Hence even in this case we expect large detrimental effects due to the ice shape for the locations tested. Also, all the LTHS cases had a very strong suction peak close to stall. In the iced cases, the pressure recovery occurred very close to the ice shape location. Convergence of computational runs was achieved up to very low angles of attack for the clean and the iced cases. For the clean case, convergence could be achieved only up to an angle of attack of 5 degrees.

Figures 145 through 148 show the effect of ice shape location on aerodynamic coefficients for *k/c* = 0.0083 ice shape for the LTHS airfoil. The locations chosen were *x/c* = 0.02, *x/c* = 0.1, and *x/c* = 0.2. The clean case results are also presented for comparison.

Figures 145 and 148 show the lift and drag coefficients predicted by the computations for those cases which converged. Since the clean and the iced cases converged only for low angles of attack (up to 4°), it cannot be said with certainty as to which location was the most critical for this airfoil. From the drag plot, it is seen that the 2% case had very large drag increases even at low angles of attack. This is because of a large separation bubble even at such low angles of attack.

Figure 147 shows very sharp breaks in the pitching moment for all the iced cases. This could be attributed to the separation bubble behavior. Moreover, there was large-scale unsteadiness beyond the angles for which the results converged. Compared to this, the hinge moment plot is smoother. This is because there is a trailing-edge separation even at low angles; hence, the separation bubble growth and reattachment point does not affect the hinge moment curve as much.

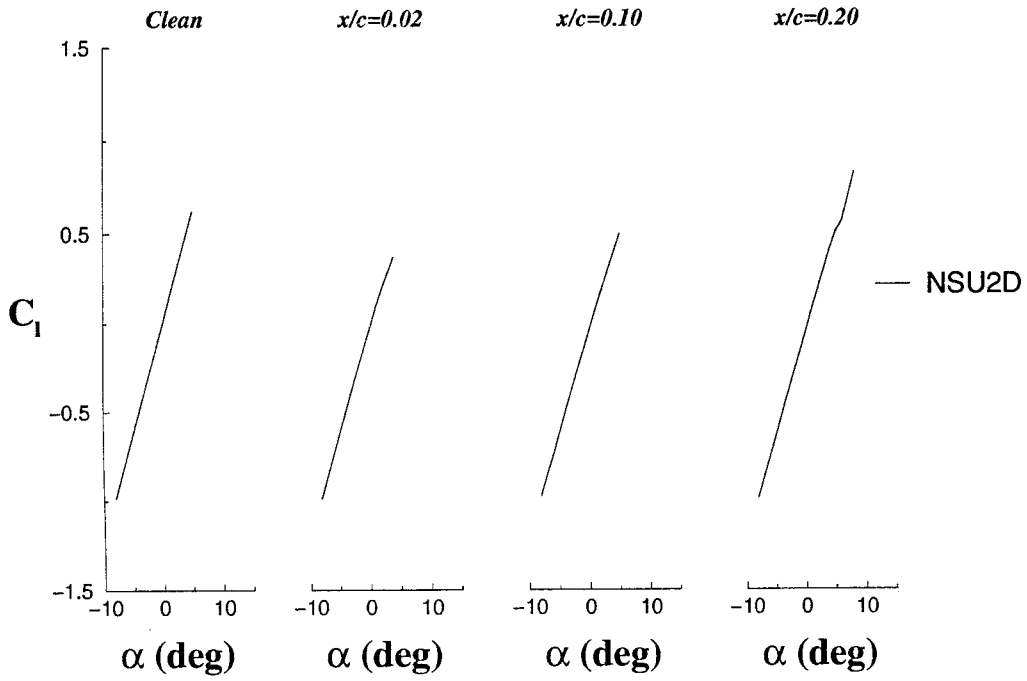

FIGURE 145. EFFECT OF ICE SHAPE LOCATION ON LIFT FOR k/c = 0.0083 ICE SHAPES FOR THE LARGE TRANSPORT HORIZONTAL STABILIZER

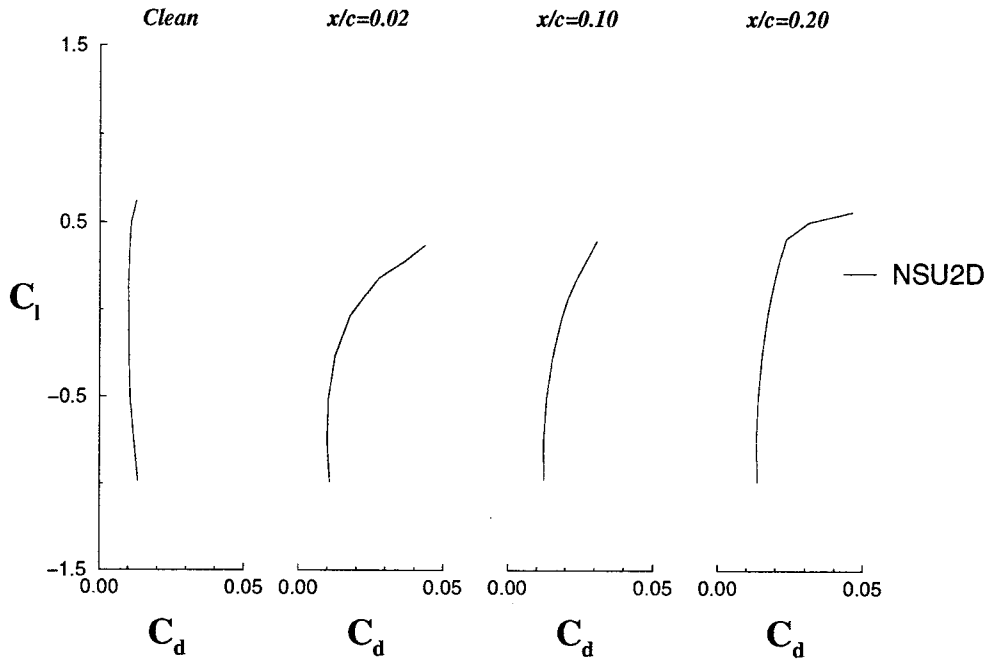

FIGURE 146. EFFECT OF ICE SHAPE LOCATION ON DRAG FOR k/c = 0.0083 ICE SHAPES FOR THE LARGE TRANSPORT HORIZONTAL STABILIZER

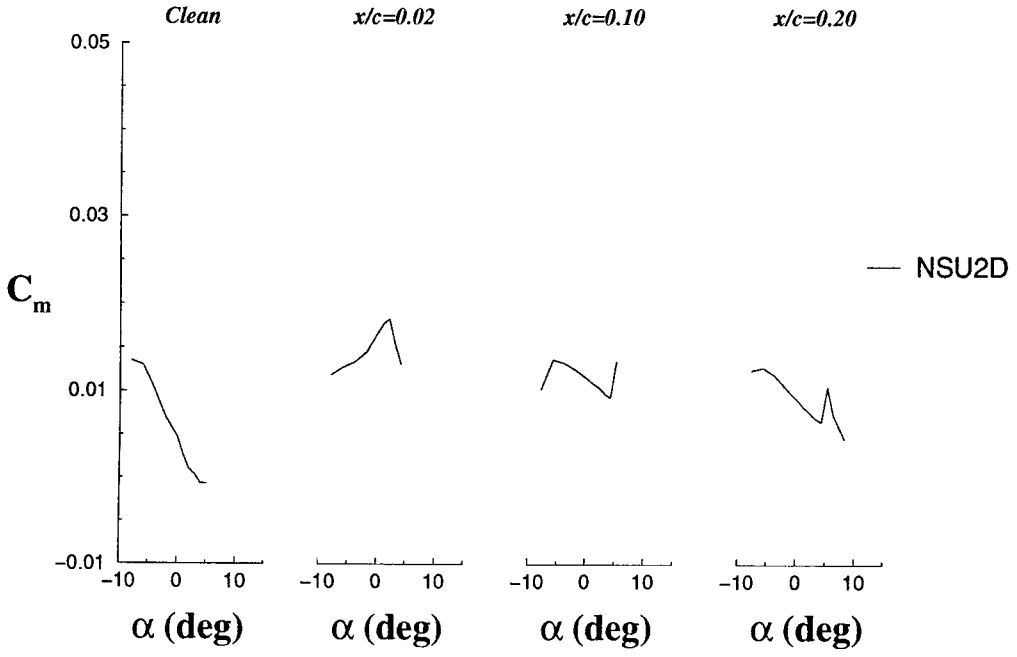

FIGURE 147. EFFECT OF ICE SHAPE LOCATION ON PITCHING MOMENT FOR k/c = 0.0083 ICE SHAPES FOR THE LARGE TRANSPORT HORIZONTAL STABILIZER

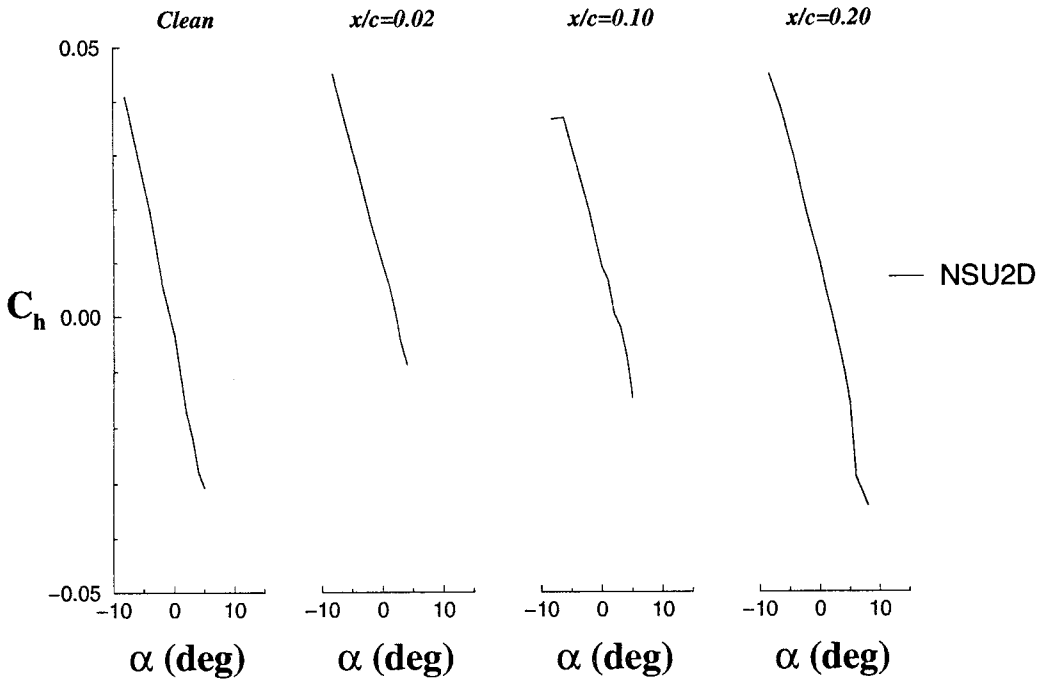

FIGURE 148. EFFECT OF ICE SHAPE LOCATION ON HINGE MOMENT FOR k/c = 0.0083 ICE SHAPES FOR THE LARGE TRANSPORT HORIZONTAL STABILIZER

4.2.2.4 Comparative Study of the Four Airfoils.

The following paragraphs discuss large differences observed in aerodynamic characteristics between the NACA 23012m and NLF 0414 airfoil with ridge ice simulations and some marked similarities observed in the aerodynamic characteristics of the business jet model and the LTHS airfoils.

The effect on the aerodynamic coefficients due to variation in airfoil geometry was first studied. Comparison of NACA 23012m, NLF 0414, business jet model, and the LTHS airfoil geometries with a quarter-round ice shape size of k/c = 0.0083 located at 10% chord is shown in figure 149.

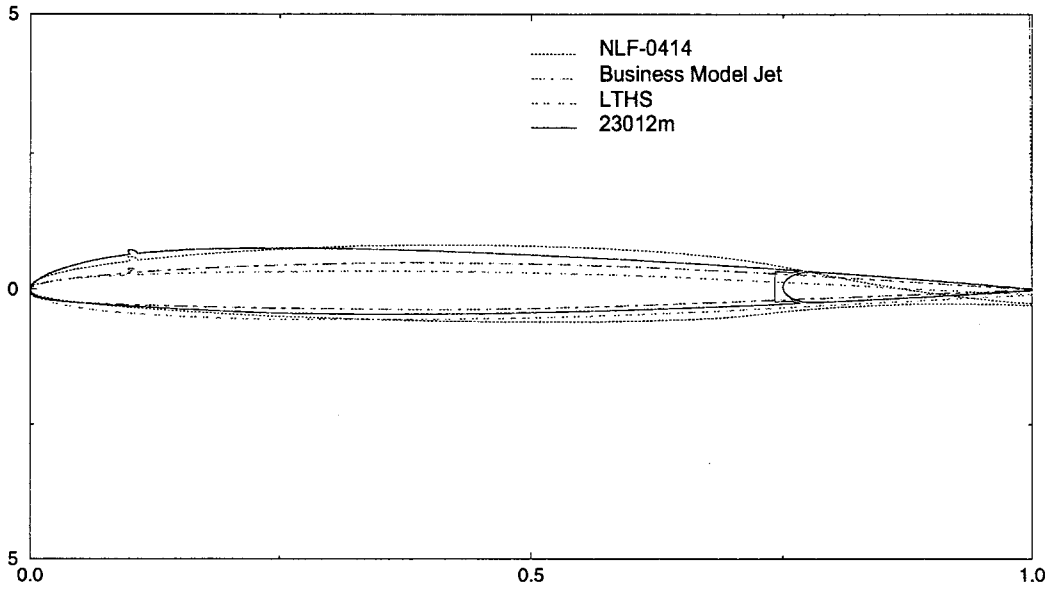

FIGURE 149. COMPARISON OF AIRFOIL GEOMETRIES WITH $k/c = 0.0083$ ICE SHAPE LOCATED AT $x/c = 0.1$

Figures 150 through 153 show the aerodynamic coefficients of four airfoils. The experimental data is presented only for NACA 23012m and NLF 0414. The business jet model and the LTHS were run at $Re = 8 \times 10^6$. The $x/c = 0.1$ was chosen mainly because from the results presented in the previous sections, the 10% location has a very strong detrimental effect on the performance. The computational results generally agreed well with the experimental data for angles of attack within the linear range. Large drag increases were observed for all the iced cases close to stall. At higher angles of attack the flow becomes unsteady. For the LTHS airfoil, computational predictions are shown for angles for which the computational results converged. Due to large scale unsteadiness, for clean and the iced cases, convergence could be achieved for angles of attack up to 5 degrees.

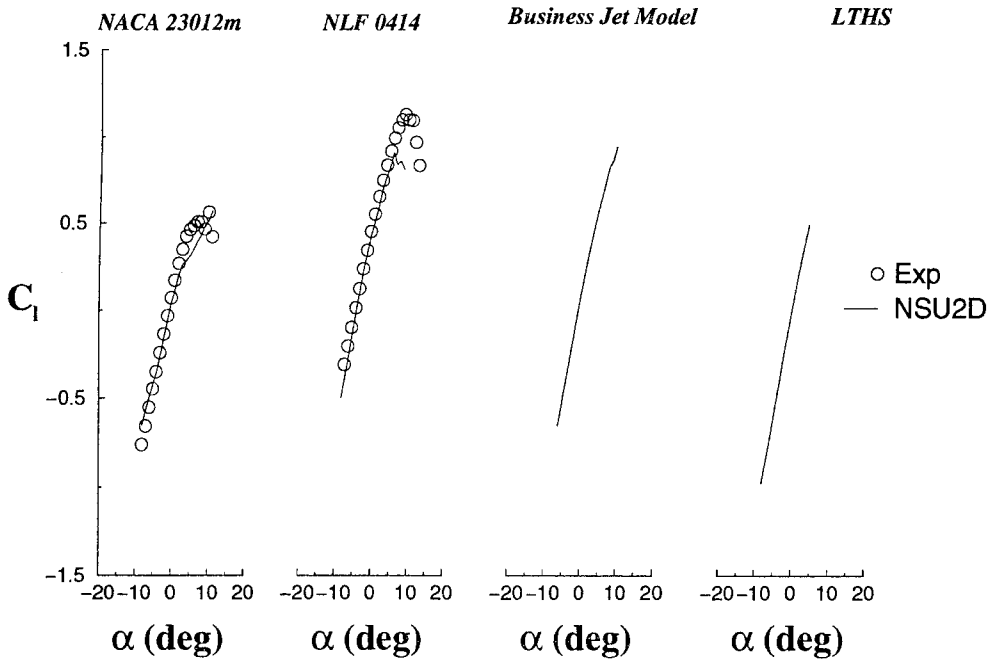

FIGURE 150. EFFECT OF AIRFOIL GEOMETRY ON LIFT FOR $k/c = 0.0083$ ICE SHAPE LOCATED AT $x/c = 0.1$

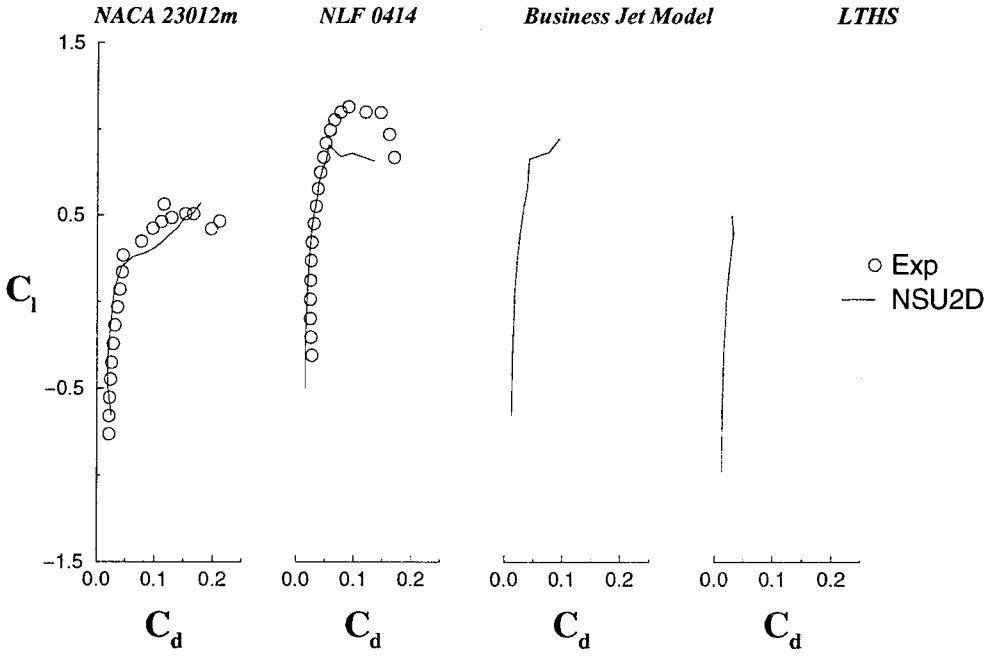

FIGURE 151. EFFECT OF AIRFOIL GEOMETRY ON DRAG FOR $k/c = 0.0083$ ICE SHAPE LOCATED AT $x/c = 0.1$

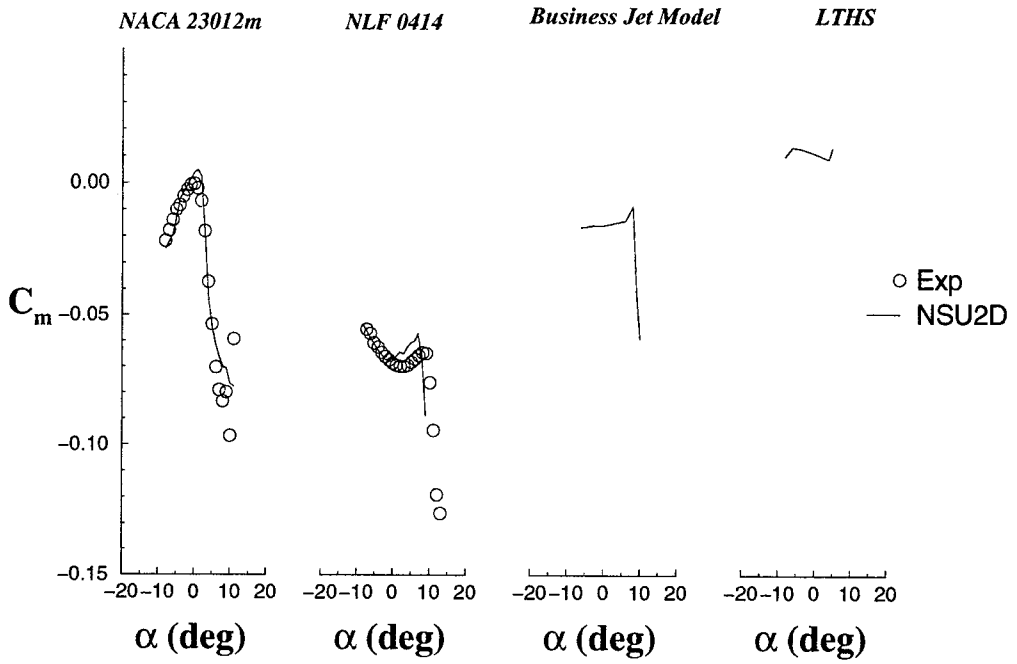

FIGURE 152. EFFECT OF AIRFOIL GEOMETRY ON PITCHING MOMENT FOR $k/c = 0.0083$ ICE SHAPE LOCATED AT $x/c = 0.1$

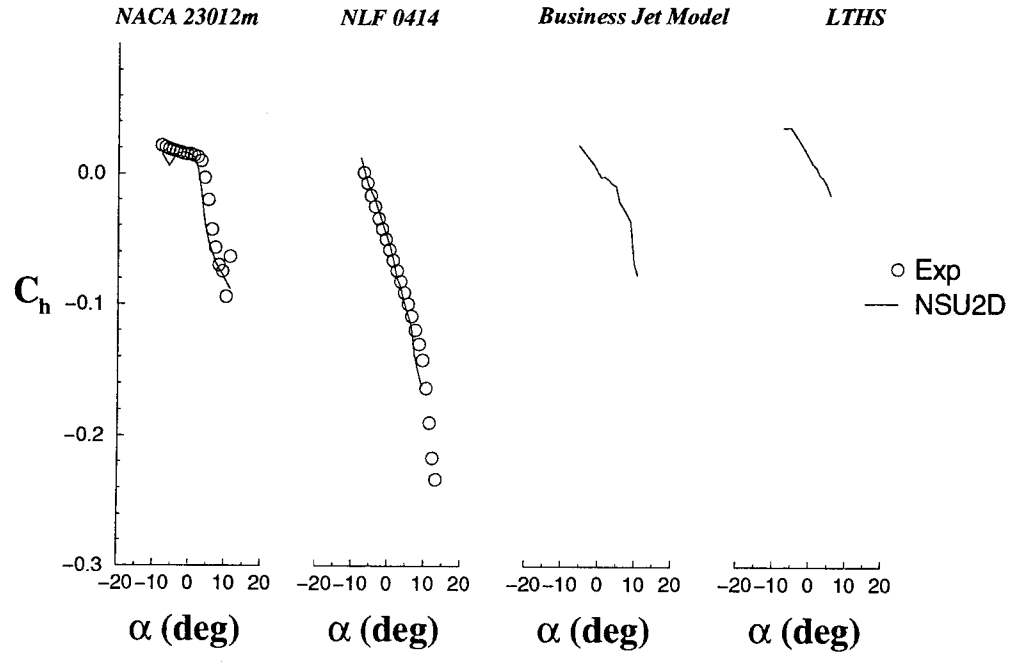

FIGURE 153. EFFECT OF AIRFOIL GEOMETRY ON HINGE MOMENT FOR $k/c = 0.0083$ ICE SHAPE LOCATED AT $x/c = 0.1$

From the lift and drag plots in figures 150 and 151, it can be seen that the effects of the ice shape simulation were much more severe on the NACA 23012m than on the NLF 0414. This may be attributed to the large differences in their clean model pressure distributions. The clean NACA 23012m is a very forward-loaded airfoil, with a very large leading-edge suction peak. The NLF 0414 has a relatively uniform chordwise loading until the pressure recovery near the trailing edge. On the NACA 23012m, the largest penalties occurred when the simulated ice shape prevented the leading-edge suction peak from forming. On the NLF 0414, it was found that all the locations had detrimental effects on the aerodynamic parameters, but no location could be pinpointed as causing the largest aerodynamic penalty.

From figures 150 and 151, it can be observed that the business jet model and the LTHS airfoils exhibit similar iced aerodynamic performance. This may be attributed to the fact that both the airfoils have the same type of loading in the clean case. Both are forward-loaded airfoils with very light loading of the flap in the clean case and have large suction peaks. On both the airfoils, the pressure recovery region was located very close to the ice shape location. It appears that this may be the reason why these airfoils did not have as much of a performance degradation as noted with the NACA 23012m.

Figure 152 shows the effect of ice shape on the pitching moment. For both NACA 23012m and the NLF 0414, NSU2D predicts the large increase in the negative moment caused by the growth of the separation bubble both qualitatively and quantitatively. This occurs first for the NACA 23012m airfoil. In the case of the business jet model too, a strong break in the slope of the pitching moment curve can be seen. In the case of the LTHS airfoil, due to failure of convergence, results corresponding only to a small range of angles is presented. It is, hence, difficult to ascertain whether it will have as strong a break as shown by the other airfoils.

The ice shape affected the C_h (figure 153) much more on the NACA 23012m than on the NLF 0414. On the clean NACA 23012m, the flap is lightly loaded. When the separation bubble, due to the ice shape, reached the flap, the flap became heavily loaded and caused a large change in the hinge moment slope. On the NLF 0414, the flap was heavily loaded even on the clean model due to early flap separation. Thus, even when the bubble reached the flap, it did not alter the C_h. The flap loading was very light in the clean case of the business jet model and the loading increased greatly when the separation bubble reached the flap causing breaks in the hinge moment curve which were not observed in the case of NLF 0414 airfoil. In the case of the LTHS airfoil, there was trailing-edge separation even at very low angles of attack, hence, the bubble did not dramatically change the slope of the hinge moment curve.

Figures 153 through 157 show the streamlines and the pressure distribution for all the four airfoils for an equivalent $C_\ell = 0.261$. The iced NACA 23012m has the largest bubble. The reattachment point lies close to the trailing edge. The NLF 0414 and the business jet model have nearly equal reattachment lengths of 0.27% chord. The LTHS airfoil had a much larger bubble extending up to 0.343% chord. In general, the pressure distributions are predicted reasonably well for the NACA 23012m and the NLF 0414 airfoils especially for the latter.

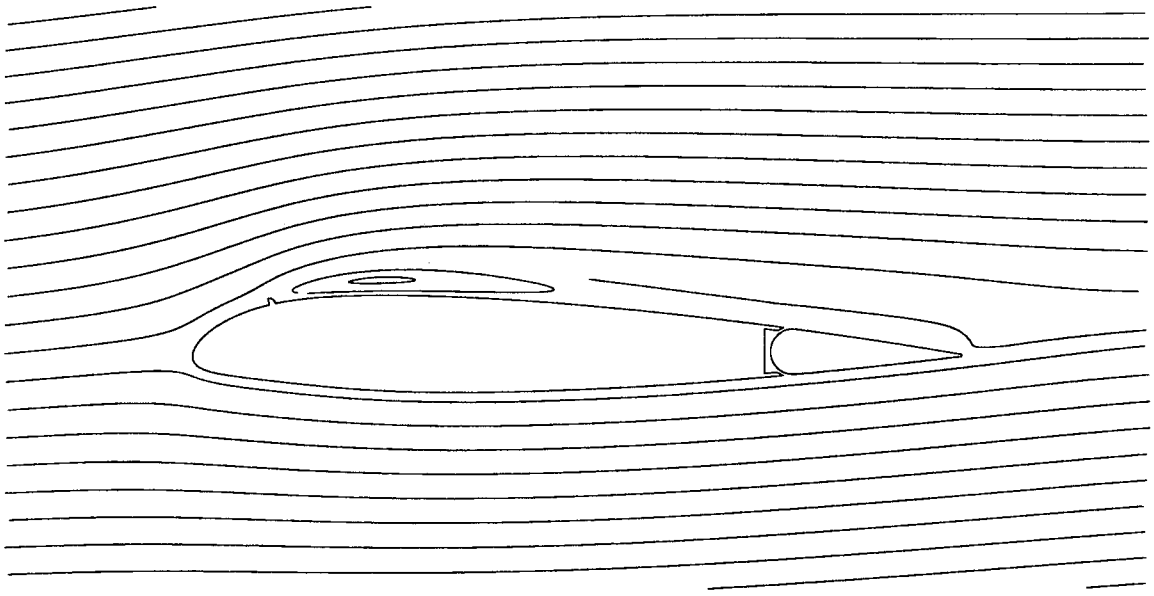

(a)

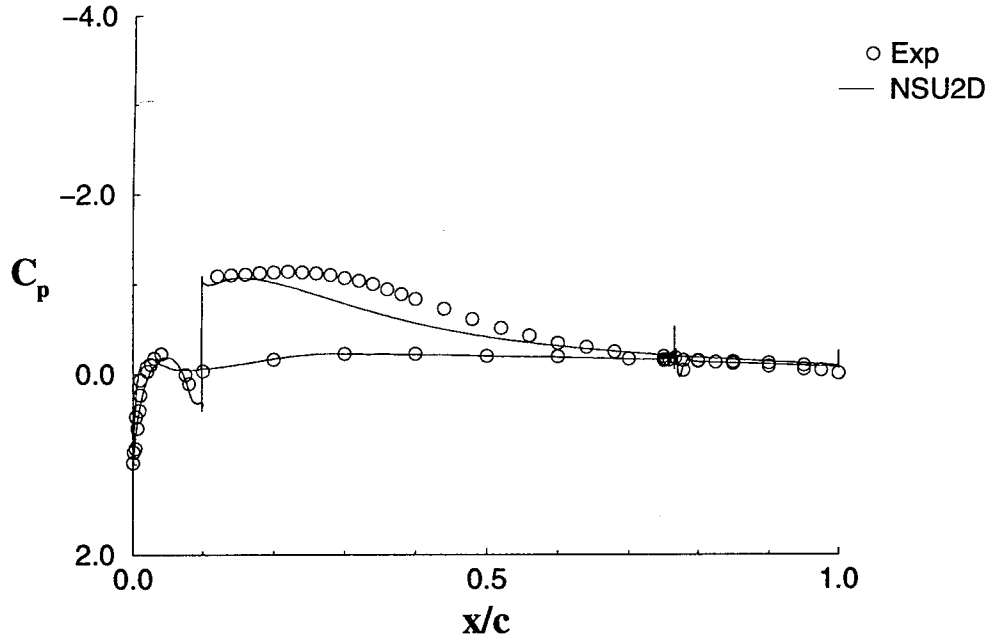

(b)

FIGURE 154. STREAMLINES AND SURFACE PRESSURE DISTRIBUTIONS FOR A NACA 23012m AIRFOIL WITH $k/c = 0.0083$ QUARTER-ROUND ICE SHAPE LOCATED AT $x/c = 0.1$ AND $\alpha = 3°$

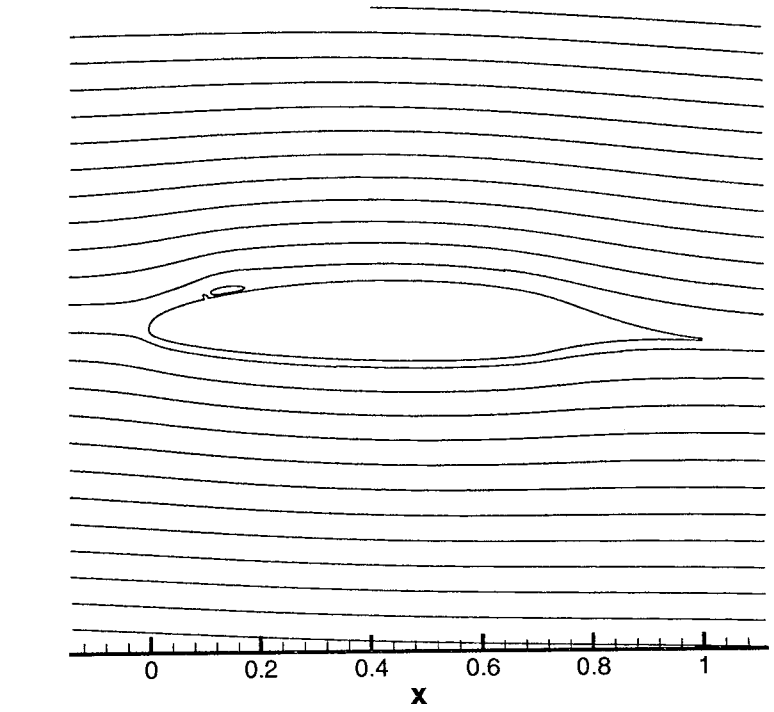

FIGURE 155. STREAMLINES AND SURFACE PRESSURE DISTRIBUTIONS FOR A NLF 0414 AIRFOIL WITH $k/c = 0.0083$ QUARTER-ROUND ICE SHAPE LOCATED AT $x/c = 0.1$ AND $\alpha = -2°$

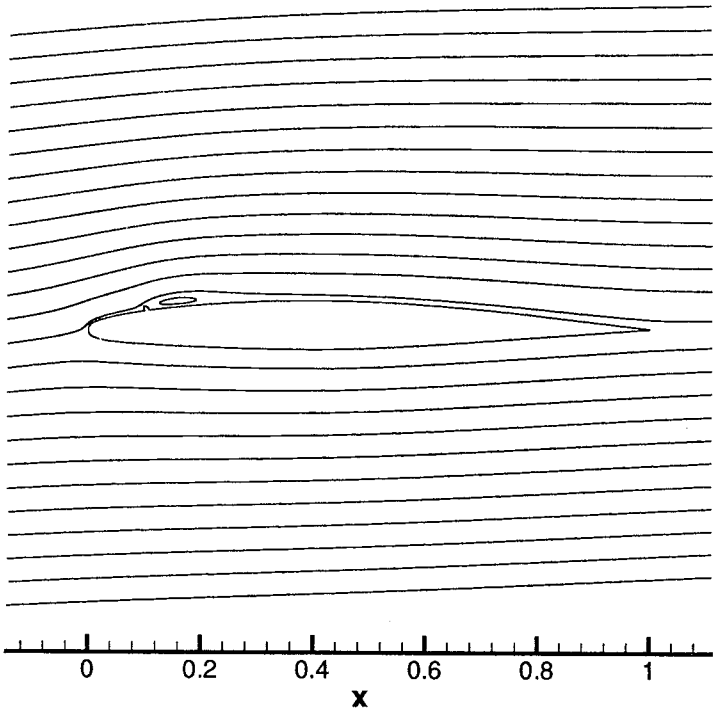

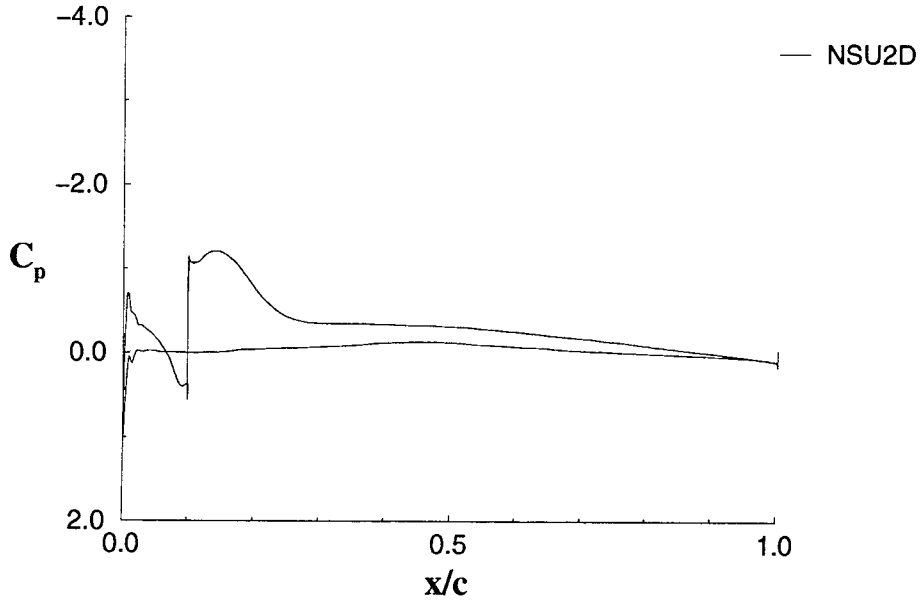

FIGURE 156. STREAMLINES AND SURFACE PRESSURE DISTRIBUTIONS FOR A BUSINESS JET MODEL AIRFOIL WITH $k/c = 0.0083$ QUARTER-ROUND ICE SHAPE LOCATED AT $x/c = 0.1$ AND $\alpha = 2°$

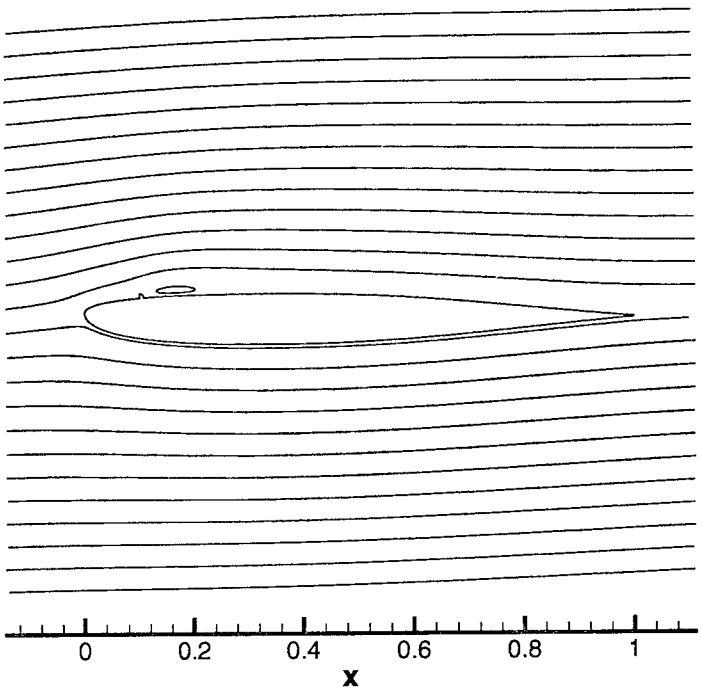

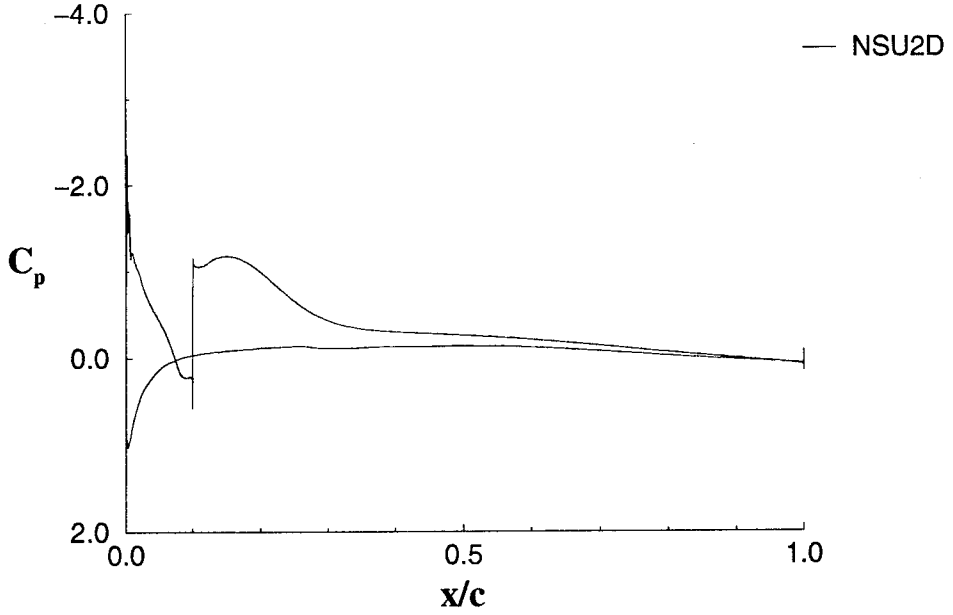

FIGURE 157. STREAMLINES AND SURFACE PRESSURE DISTRIBUTIONS FOR LARGE TRANSPORT HORIZONTAL STABILIZER AIRFOIL WITH $k/c = 0.0083$ QUARTER-ROUND ICE SHAPE LOCATED AT $x/c = 0.1$ AND $\alpha = 3°$

4.3 EXPERIMENTAL DATA CD-ROM.

All of the experimental data taken in this experiment are archived in reduced format on a CD-ROM titled *UIUC/FAA SLD Experimental Data* that is provided with this report. The CD-ROM is formatted for IBM-compatible computers. The data files are organized by run numbers. Each run number represents one angle of attack sweep (with 5 flap deflections, -10° to 10° in 5° increments) for a particular case.

There are six files associated with each run number. The first five are the separate integrated aerodynamic coefficient-reduced data files. There is a separate file for each flap deflection. The names of these files have the following format:

run[run number].[flap deflection]

An underscore "_" is used for negative flap angles. For example, the file for run 149 with flap = -5 would be named "run149._05". The sixth file contains the surface pressure coefficient data. There is only one file for each run number because the C_p file contains the data for all five of the flap deflections. The names of these files have the following format:

run[run number].cp

The surface pressure file for run 149 would be named "run149.cp."

The integrated aerodynamic coefficient data file contains both the pressure and balance data. The format for these files is shown on table 3. It is in a very simple format that does not require much further explanation.

The format for the C_p data files, shown on table 4, is more complicated and requires more explanation. The first column is the model angle of attack and the second column is the flap angle. The first row is the *x/c* location of the surface pressure taps. The taps are ordered so that it first goes from the trailing edge of the flap to the leading edge of the flap on the upper surface. Then it goes back to the trailing edge of the flap through the lower surface. It then starts at the trailing edge of the main element and goes to the leading edge of the main element on the upper surface. Finally, it goes to the trailing edge of the main element through the lower surface. The surface pressure coefficients for each angle of attack (and flap angle) are laid out as rows.

The descriptions of the run numbers are shown on tables 3 through 12. Each run contains all five flap deflections unless otherwise indicated.

TABLE 3. FORMAT OF INTEGRATED AERODYNAMIC COEFFICIENT DATA FILES

α	δ_f	C_l Pressure	C_l Balance	C_d Wake	C_d Balance	C_m Pressure	C_m Balance	C_h Pressure	C_h Balance
-1	-5	-0.19982	-0.20051	0.01266	0.01382	0.0320174	0.029917	0.047709	0.0425
-0	-5	-0.09934	-0.10109	0.01168	0.013007	0.0349076	0.031836	0.046128	0.04017
1.02	-5	-0.03239	-0.032	0.00813	0.010971	0.0434285	0.039401	0.056013	0.04901
2.05	-5	0.059542	0.05787	0.00792	0.010666	0.0479164	0.043759	0.059882	0.05296
...	...	.....	.....	.....	.....	.....	.....	.....	.....

TABLE 4. FORMAT OF THE SURFACE PRESSURE COEFFICIENT DATA FILES

α	δ_f	1.000	0.975	0.950	0.900	0.850	0.825	0.800
-14.14005	10	-0.391348	-0.3756646	-0.3826813	-0.4320879	-0.5211259	-0.6092398	-0.793896
-13.1566	5	-0.448579	-0.3796391	-0.3570982	-0.3573129	-0.3822463	-0.4188318	-0.4783181
-13.17717	10	-0.279054	-0.2910371	-0.3079561	-0.3683629	-0.4647658	-0.558174	-0.7547
-12.15366	0	-0.453074	-0.3471015	-0.3055085	-0.2647324	-0.2422265	-0.2366001	-0.2135846
-12.17024	5	-0.300933	-0.2794443	-0.2716719	-0.2876566	-0.3200359	-0.3620474	-0.4430255
-12.18361	10	-0.182122	-0.2173451	-0.2428358	-0.3131109	-0.4175242	-0.5141504	-0.7081167
-11.17022	-5	-0.44934	-0.3081256	-0.2457377	-0.1686718	-0.09942628	-0.06236112	0.02385377
-11.17773	0	-0.32633	-0.2634404	-0.2341093	-0.2074372	-0.1922189	-0.1912069	-0.1712768
-11.19327	5	-0.198598	-0.2035625	-0.2043917	-0.2294305	-0.2648219	-0.3181002	-0.4384505
-11.20465	10	-0.084211	-0.1393681	-0.1735512	-0.2536339	-0.3640028	-0.4626516	-0.6440821
-10.17031	-10	-0.456743	-0.2689758	-0.1864233	-0.07531165	0.03366091	0.09702635	0.2330594
-10.18207	-5	-0.346246	-0.2359919	-0.184264	-0.1196632	-0.05869595	-0.02547282	0.05577896
-10.19254	0	-0.218269	-0.184678	-0.1656577	-0.1516682	-0.1440809	-0.1465283	-0.1301576

TABLE 5. NO SIMULATED ICE AIRFOIL DATA

Airfoil	Ice Shape Geometry	*Re* (x10^6)	Trip	Run Number
NACA 23012m	None	1.8	No	run412
NACA 23012m	None	1.8	Yes	run424
NACA 23012m	None	1.0	No	run413
NACA 23012m	None	1.0	Yes	run483
NLF 0414	None	1.8	No	
NLF 0414	None	1.8	Yes	run301

TABLE 6. FORWARD-FACING QUARTER ROUND, $k = 0.25''$, NACA 23012m

Re (x10^6)	Trip	*x/c*	Run Number	Comments
1.8	No	0	run478	flap = -10 deg only
1.8	No	0	run479	flap = -5 deg only
1.8	No	0	run480	flap = 0 deg only
1.8	No	0	run481	flap = 5 deg only
1.8	No	0	run482	flap = 10 deg only
1.8	No	0.02	run476	
1.8	No	0.04	run501	
1.8	No	0.06	run505	
1.8	No	0.1	run502	
1.8	No	0.14	run504	
1.8	No	0.2	run503	
1.8	Yes	0.04	run500	
1.8	Yes	0.06	run485	
1.8	Yes	0.08	run486	
1.8	Yes	0.1	run487	
1.8	Yes	0.12	run490	
1.8	Yes	0.14	run492	
1.8	Yes	0.16	run494	
1.8	Yes	0.18	run495	
1.8	Yes	0.2	run497	
1.8	Yes	0.3	run498	
1.8	Yes	0.5	run499	
1	No	0	run477	
1	No	0.02	run475	
1	Yes	0.06	run484	
1	Yes	0.1	run488	
1	Yes	0.14	run493	
1	Yes	0.2	run496	

TABLE 7. FORWARD-FACING QUARTER ROUND, $k = 0.15''$, NACA 23012m

Re (x10^6)	Trip	*x/c*	Run Number	Comments
1.8	No	0	run471	
1.8	No	0.02	run469	
1.8	No	0.04	run430	
1.8	No	0.06	run431	
1.8	No	0.08	run432	
1.8	No	0.1	run435	
1.8	No	0.12	run436	
1.8	No	0.14	run437	
1.8	No	0.16	run439	
1.8	No	0.18	run440	
1.8	No	0.2	run438	
1.8	No	0.3	run441	
1.8	No	0.3	run442	completion of run441
1.8	No	0.5	run443	
1.8	Yes	0.04	run468	
1.8	Yes	0.06	run466	
1.8	Yes	0.08	run465	
1.8	Yes	0.1	run455	
1.8	Yes	0.12	run459	
1.8	Yes	0.14	run460	
1.8	Yes	0.16	run461	
1.8	Yes	0.18	run462	
1.8	Yes	0.2	run457	
1.8	Yes	0.3	run463	
1.8	Yes	0.5	run464	
1	No	0	run472	flap = -10,-5,0
1	No	0	run473	flap = 5,10
1	No	0.02	run470	
1	Yes	0.06	run467	
1	Yes	0.1	run456	
1	Yes	0.12	run458	

TABLE 8. FORWARD-FACING QUARTER ROUND, $k = 0.10''$, NACA 23012m

Re (x10^6)	Trip	*x/c*	Run Number
1.8	No	0	run530
1.8	No	0.02	run529
1.8	No	0.1	run528
1.8	Yes	0.06	run525
1.8	Yes	0.08	run526
1.8	Yes	0.1	run522
1.8	Yes	0.12	run527
1.8	Yes	0.14	run524
1.8	Yes	0.2	run523

TABLE 9. VARIOUS SIMULATED ICE SHAPE GEOMETRY, $k = 0.25''$, $Re = 1.8 \times 10^6$, NACA 23012m

Ice Shape Geometry	Trip	x/c	Run Number	Comments
Backward-Facing 1/4 Round	No	0.02	run506	
Backward-Facing 1/4 Round	Yes	0.10	run507	
Backward-Facing 1/4 Round	Yes	0.20	run508	
Forward-Facing Ramp	No	0.02	run517	
Forward-Facing Ramp	No	0.02	run518	completion of run517
Forward-Facing Ramp	Yes	0.10	run516	
Forward-Facing Ramp	Yes	0.20	run515	
Half Round	No	0.02	run519	
Half Round	Yes	0.10	run520	
Half Round	Yes	0.20	run521	

TABLE 10. FORWARD-FACING QUARTER ROUND ON UPPER AND LOWER SURFACE OF THE MODEL AT $x/c = 0.10$, $k = 0.25''$, $Re = 1.8 \times 10^6$, NACA 23012m

Upper	Lower	Height	*Re* (x10^6)	Trip	x/c	Run Number
No	Yes	0.25″	1.8	No	0.10	run509
Yes	Yes	0.25″	1.8	No	0.10	run510

TABLE 11. SPANWISE GAPS IN THE SIMULATED ICE SHAPES, FORWARD-FACING QUARTER ROUND, $k = 0.25''$, $Re = 1.8 \times 10^6$, NACA 23012m

Trip	Gap	*x/c*	Run Number	Comments
No	5″	0.02	run531	
Yes	5″	0.10	run532	
Yes	5″	0.20	run533	flap = -10, -5
Yes	5″	0.20	run534	flap = 0 to 10
Yes	2.5″	0.10	run535	

TABLE 12. ROUGHNESS UPSTREAM AND DOWNSTREAM OF SIMULATED ICE SHAPE, FORWARD-FACING QUARTER ROUND, $k = 0.25''$, $Re = 1.8 \times 10^6$, NACA 23012m

Trip	Upstream	Downstream	*x/c*	Run Number	Comments
No	0.25″	none	0.10	run544	
No	0.50″	none	0.10	run543	
No	1″	none	0.10	run546	flap = -10, -5
No	2″	none	0.10	run545	flap = 0 to 10
No	1″	2″	0.10	run547	

TABLE 13. SIXTEEN-GRIT ROUGHNESS, 0.25″ CHORDWISE EXTENT, $Re = 1.8 \times 10^6$, NACA 23012m

x/c	Run Number
0.00	run537
0.02	run538
0.04	run542
0.06	run539
0.10	run540
0.20	run541

TABLE 14. FORWARD-FACING QUARTER ROUND, $K = 0.25''$, NLF 0414

Re (x10^6)	Trip	*x/c*	Run Number	Comments
1.8	No	0.00	run317	
1.8	No	0.00	run318	completion of run317
1.8	No	0.02	run316	
1.8	No	0.04	run315	
1.8	No	0.06	run314	
1.8	No	0.10	run313	
1.8	No	0.20	run319	
1.8	No	0.20	run320	completion of run319
1.8	No	0.06	run309	
1.8	No	0.08	run310	
1.8	No	0.10	run302	
1.8	No	0.12	run311	
1.8	No	0.14	run303	
1.8	No	0.20	run304	
1.8	No	0.30	run305	
1.8	No	0.40	run306	
1.8	No	0.40	run307	completion of run306
1.8	No	0.50	run308	

5. CONCLUSIONS.

5.1 PRIMARY CONCLUSIONS.

The main conclusions drawn from this integrated experimental and computational study were that large separation bubbles form downstream of the simulated ridge ice accretions that severely degrade the airfoil performance. This degradation was primarily a function of ice shape size and location and nearly independent of Reynolds number and ice shape geometry. For the forward-loaded NACA 23012m airfoil, the loss of performance included an 80% loss of $C_{\ell,max}$ for an upper surface ice shape location of $x/c = 0.12$. This behavior was associated with a thin-airfoil type of stall which effectively eliminated the lift upstream of the ice shape. The separation bubble aft of the ice shape became significant at about 0° angle of attack and quickly engulfed the airfoil, at which point, large, trailing-edge up hinge moments developed. The more evenly loaded NLF 0414 suffered smaller aerodynamic losses and tended to exhibit a combination trailing-edge/thin-airfoil type of stall for the upper surface simulated ice shapes. The business jet model and the large horizontal tailplane stabilizer which had large suction peaks (forward loaded) suffered large aerodynamic losses when the ice shape was placed close to the leading edge.

In the following, additional conclusions and details are given first for the experimental study and then for the computational study.

5.2 EXPERIMENTAL STUDY CONCLUSIONS.

An experimental study was conducted in order to understand the effects of ridge ice accretion on aircraft aerodynamics.

- The simulated ice shape produced a large separation bubble, drastically changed the airfoil pressure distributions, and changed the NACA 23012m airfoil stall type from leading-edge to thin-airfoil stall.

- The simulated spanwise-ice accretion severely reduced $C_{\ell,max}$.

- The severe loss in lift at positive angles of attack was due to the simulated ice shape preventing the suction peak from forming near the leading edge. Most of the lift on a clean NACA 23012m is generated in this suction peak. When the simulated ice shape was at critical chordwise locations, this suction peak was eliminated by a long separation bubble, which formed downstream of the simulated ice shape. The separation bubble failed to reattach at angles of attack as low as 2°, which led to the very low $C_{\ell,max}$ values observed.

- The most critical simulated ice shape location (in terms of reduction in $C_{\ell,max}$ was 12% chord for a forward-facing quarter round with height-to-chord ratio of 0.0139. It resulted in a $C_{\ell,max}$ of 0.25 as compared to an un-iced airfoil $C_{\ell,max}$ of 1.50. In general, this critical location of the simulated ice shape was near (but upstream of) the location of largest adverse pressure gradient on the clean airfoil and downstream of the location of the minimum surface pressure. However, the most critical location of the simulated ice shape, in terms of drag, increase for a given α was at the location of maximum local air velocity (or the minimum surface pressure) of the clean model.

- The simulated ice shape severely altered pitching and flap hinge moments. A large break in $C_{h,\alpha}$ was observed a few degrees angle of attack after a break in $C_{m,\alpha}$. This resulted in a large nose down, trailing-edge up pitching and flap hinge moments that were generated well before, and continued through, stall.

- The effect of the simulated ice shape on C_ℓ, C_d, C_m, and C_h became more severe as the ice shape size was increased. The C_m and C_h diverged from the clean model values at an earlier α as the ice shape size was increased. The simulated ice shape location at which the lowest $C_{\ell,max}$ occurred moved upstream with decreasing ice shape size.

- The variations in the geometry of the ice shape simulation had some effect on airfoil aerodynamics, with the half-round shape having a significantly higher $C_{\ell,max}$.

- The presence of roughness immediately upstream of the ice shape had measurable (although not large) effects on airfoil aerodynamics. The presence of roughness downstream of the ice shape had much less effect than the upstream roughness.

- The flap deflection did not significantly alter the ice-airfoil aerodynamics. The presence of the simulated ice shape cut the flap effectiveness in half in severe cases.

- The results showed that the ice shape protuberance affected the NLF 0414 very differently than the NACA 23012m. The following conclusions can be drawn based on the measured comparisons between the two airfoils.

- The effects of the simulated ice shapes were much more severe on the NACA 23012m. With the 0.25″ (k/c = 0.0139) ice shape simulation, the lowest $C_{\ell,max}$ on the NACA 23012m was 0.25 (simulated ice shape at x/c = 0.12). On the NLF 0414, the lowest $C_{\ell,max}$ was 0.68 (simulated ice shape at x/c = 0.08).

- On the NLF 0414, the largest increase in drag did not occur when the simulated ice shape was located at the location of the maximum local air velocity of the clean model. Also, the largest loss in lift on the NLF 0414 did not occur when the simulated ice shape was located in the region between the largest local air velocity and the maximum adverse pressure gradient of the clean model.

- The bubble lengths were usually shorter on the NLF 0414 than on the NACA 23012m due to a much more favorable pressure gradient downstream of the simulated ice shape.

- The ice shape affected C_h much more on the NACA 23012m than on the NLF 0414. On the clean NACA 23012m, the flap is lightly loaded. When the separation bubble, due to the ice shape, reached the flap, the flap load increased and caused a large change in the $C_{h,\alpha}$ slope. On the NLF 0414, the flap was heavily loaded even on the clean model due to early flap flow separation. Thus, even when the bubble reached the flap, it did not significantly alter the C_h at $\alpha > 5°$.

- The most critical ice shape location (in terms of lift loss) for the NACA 23012m and the NLF 0414 were very different. On the NACA 23012m, it was near x/c = 0.12. On the NLF 0414, the $C_{\ell,max}$ did not vary by a large amount when the simulated ice shape was located between x/c = 0.02 and 0.20.

The differences described above were due to large differences in the clean model pressure distribution between the NACA 23012m and the NLF 0414. The NACA 23012m is very forward-loaded airfoil, with a very large leading-edge suction peak. The NLF 0414 has relatively uniform chordwise loading until the pressure recovery near the trailing edge. On the NACA 23012m, the largest penalties occurred when the simulated ice shape prevented the leading-edge suction peak from forming. On the NLF 0414, the largest aerodynamic penalties occurred when the simulation ice shape (and the associated separation bubble) was located just upstream of the trailing-edge pressure recovery region.

5.3 COMPUTATIONAL STUDY CONCLUSIONS.

The NSU2D code (as used in this study) was first validated with several clean airfoil conditions and was found to accurately predict Mach and Reynolds number effects up to stall conditions. In addition, it was also found to reasonably accurately predict a backward-facing step flow with a moderate adverse pressure gradient. The ice shape airfoils investigated included a NACA 0012 with a leading-edge glaze ice shape, a modified NACA 23012m airfoil, a NLF 0414 airfoil, a business jet model airfoil, and LTHS airfoil with upper surface spanwise-step protuberances. The following conclusions can be drawn based on the results with the NACA 23012m airfoil.

- NSU2D predicts all the experimental trends of the major aerodynamic forces and moments associated with the ice shape presence. In particular hinge moments, curves including the ice shape effects on the breaks, were very accurately predicted. In addition, many of the more detailed flow measurements, such as pressure distributions and reattachment lengths, were also reasonably correlated with experimental results. However, the lift force was only quantitatively predicted up to fully separated conditions, after which the steady Reynolds Averaged Navier-Stokes approach may no longer be reasonable because of highly unsteady vortex shedding. Similarly, the drag force was also only qualitatively predicted once the separation covered a majority of the airfoil surfaces; however, pitching moment and hinge moment predictions were found to be reasonable even after separation.

- As in the experiments, the simulated upper surface ice shape airfoils produced a large separation bubble, drastically changed the airfoil pressure distributions and changed the airfoil stall type from leading-edge to thin-airfoil stall.

- Dramatic changes in the sectional aerodynamic characteristics were found as a function of ice shape location and ice shape size. The most critical ice shape location (in terms of lift loss) for the NACA 23012m was around $x/c = 0.1$, which was consistent with the experimental results. Ice shapes of size $k/c = 0.0083$ and $k/c = 0.0139$ were tested and compared with a clean airfoil configuration for the NACA 23012m. As expected, the larger shape produced the greatest detriment in lift curve slope performance and the angle for fully separated flow occurred sooner.

- The ice shape geometry had only a small influence on performance degradation, although shapes with a blunt leading-edge had a slightly larger effect than shapes with a rounded leading edge. Reynolds number effects (unlike the case for clean airfoils) were negligible, between 1 and 8 million.

- The code was able to reasonably predict the trends of forces and moments due to flap deflection both for the NACA 23012m at $k/c = 0$ (clean) and $k/c = 0.0083$ (ice) at $x/c = 0.1$. However, in the clean case, the simulations overestimated the lift curve slope and the maximum lift coefficient, while in the iced case the simulations slightly underpredicted the lift curve slope and did not predict a maximum lift coefficient.

- The ice shape simulations resulted in some substantial differences (and some similarities) among the other airfoils (NLF 0414, business jet model, LTHS, and NACA 0012) as

compared to the NACA 23012m. The following conclusions can be drawn based on the comparisons between the airfoils.

- The ridge shapes had a greater effect than the NACA 0012 leading-edge glaze-ice shape, despite being several times smaller in size. This was attributed to the reduced amount of flow separation since the protuberance was located well in front of the strong adverse pressure gradient.

- Large differences in aerodynamic characteristics were observed between the NACA 23012m and the NLF 0414 airfoils (as also noted experimentally), while some trends common to the business jet model and the LTHS airfoils were exhibited. The NACA 23012m airfoil is a forward-loaded airfoil while the NLF 0414 has a relatively uniform chordwise loading until the pressure recovery near the trailing edge. The business jet model and the LTHS model are both forward-loaded airfoils like the NACA 23012m, and they have very strong suction peaks.

- The most critical ice shape location (in terms of lift loss) for the NACA 23012m was found to be the 10% location which is nearest to the point of minimum C_p among the locations tested. However, the more evenly loaded NLF 0414 airfoil did not exhibit a distinctive critical ice shape location, i.e., the lift loss at fully separated conditions was roughly the same for x/c values ranging from 0.02 to 0.3. The most critical ice shape location for the business jet model upper surface iced airfoil was close to the leading edge, around $x/c = 0.02$, i.e., it produced the greatest detriment in performance as compared to $x/c = 0.1$ and $x/c = 0.20$. This is attributed to a large decrease in the pressure suction peak at the leading edge for this airfoil, which are highly forward loaded and has high suction peak in clean conditions. The LTHS airfoil which also has high suction peak near the leading edge showed detrimental performance when the ice shape was located near the leading edge ($x/c = 0.02$). The 2% case showed the earliest tendencies to stall. However, because of the limited range of angles of attack for which the results converged, it cannot be said with certainty that this location was the most detrimental to airfoil performance.

All the airfoils with ice shape locations of 2% (or at the leading edge) exhibited a combination of thin-airfoil/trailing-edge stall. However, only the NLF 0414 and LTHS exhibited this combination thin-airfoil/trailing-edge stall at ice shape chordwise locations of 10% and more, while at these aft locations, the forward-loaded NACA 23012m and the business jet model airfoils exhibited a more severe thin-airfoil type of stall.

6. REFERENCES.

1. National Transportation Safety Board, "Icing Tanker Test Factual Report," Docket No: SA-512, Exhibit No: 13B, DCA95MA001, Washington D.C., February 16, 1995.

2. Addy, H.E., Jr. and Miller, D.R., "A Study of Large-Droplet Ice Accretion in the NASA Lewis IRT at Near-Freezing Conditions, Part 2," NASA TM 107424, May 1996.

3. Dow, John P., Sr., "Roll Upset in Severe Icing," Federal Aviation Administration - Aircraft Certification Service, September 1995.

4. Johnson, C. L., "Wing Loading, Icing, and Associated Aspects of Modern Transport Design," *Journal of the Aeronautical Sciences,* vol. 8, no. 2, December 1940, pp. 43-54.

5. Morris, D. E., "Design to Avoid Dangerous Behavior of an Aircraft Due to the Effects on Control Hinge Moments of Ice on the Leading Edge of the Fixed Surface," Aeronautical Research Council, Technical Note No. Aero. 1878, current paper no. 66, London, March 1947.

6. Thoren, R. L., "Icing Flight Tests on the Lockheed P2V," ASME Paper No. 48-SA-41, 1948.

7. Trunov, O. K. and Ingelman-Sundberg, M., "On the Problem of Horizontal Tail Stall Due to Ice," Report JR-3, The Swedish Soviet Working Group on Scientific-Technical Cooperation in the Field of Flight Safety, 1985.

8. Ashenden, R. and Marwitz, J., "Turboprop Aircraft Performance Response to Various Environmental Conditions," AIAA Paper 97-0305, *Journal of Aircraft,* Vol 34, no. 3, May-June 1997, pp. 278-287.

9. Ashenden, R., Lindberg, W., and Marwitz, J., "Two-Dimensional NACA 23012 Airfoil Performance Degradation by Super-Cooled Cloud, Drizzle, and Rain Drop Icing," AIAA 34th Aerospace Sciences Meeting, Reno, NV, January 15-18, 1996.

10. Bragg, M.B., "Aircraft Aerodynamic Effects Due to Large-Droplet Ice Accretions," Paper No. 96-0932, AIAA 34th Aerospace Sciences Meeting, Reno, NV, January 15-18, 1996.

11. Bragg, M.B., "Aerodynamics of Super-Cooled Large-Droplet Ice Accretion and the Effect on Aircraft Control," *Proceedings of the FAA International Conference on Aircraft Inflight Icing*, Volume II, DOT/FAA/AR-96/81,II, August 1996, pp. 387-399.

12. Jacobs, E.N., "Airfoil Section Characteristics as Affected by Protuberances," NACA Report No. 446, 1932 Council, Technical Note No. Aero. 1878, current paper no. 66, London, March 1947.

13. Bowden, D.T., "Effect of Pneumatic De-Icers and Ice Formations on Aerodynamic Character of an Airfoil," NACA Technical Note 3564, February 1956.

14. Calay, R.K., Holdù, A.E., and Mayman, P., "Experimental Simulation of Runback Ice," *Journal of Aircraft*, Vol. 34, No. 2, March-April 1997, pp. 206-212.

15. Potapczuk, M.G. and Gerhart, P.M., "Progress in Development of a Navier-Stokes Solver for Evaluation of Iced Airfoil Performance," AIAA Paper 85-0410, January 1985.

16. Potapczuk, M., "Numerical Analysis of a NACA 0012 Airfoil with Leading-Edge Ice Accretions," AIAA Paper 87-0101, January 1987.

17. Baldwin, B.S. and Lomax, H.J., "Thin-Layer Approximation and Algebraic Model for Separated Turbulent Flows," AIAA Paper 78-0257, January 1978.

18. Bragg, M.B. and Spring, S.A., "An Experimental Study of the Flow Field About an Airfoil with Glaze Ice," AIAA Paper 87-0100, January 1987.

19. Caruso, S.C., "Development of an Unstructured Mesh/Navier-Stokes Method for Aerodynamics of Aircraft With Ice Accretions," AIAA Paper 90-0758, January 1990.

20. Caruso, S.C. and Farschi, M., "Automatic Grid Generation for Iced Airfoil Flow Field Predictions," AIAA Paper 92-0415, January 1992.

21. Cebeci, T., "The Calculation of Flow Over Iced Airfoils," AIAA Paper 88-0112, January 1988.

22. Caruso, S.C. and Farschi, M., "Automatic Grid Generation for Iced Airfoil Flow Field Predictions," AIAA Paper 92-0415, January 1992.

23. Kwon, O.J. and Sankar, L.N., "Numerical Study of the Effects of Icing on Finite Wing Aerodynamics," AIAA Paper 90-0757, January 1990.

24. Kwon, O.J. and Sankar, L.N., "Numerical Study of the Effects of Icing on Fixed Wing Rotary Wing Performance," AIAA Paper 91-0662, January 1991.

25. Kwon, O.J. and Sankar, L.N., "Numerical Investigation of Performance Degradation of Wings and Rotors Due to Icing," AIAA Paper 92-0412, January 1992.

26. Wright, W.B. and Potapczuk, M.G., "Computational Simulation of Large-Droplet Icing," Proceedings of the FAA International Conference on Aircraft Inflight Icing, Vol. II, DOT/FAA/AR-96/81,II, August 1996, pp. 545-555.

27. Dompierre, J., Cronin, D.J., Bourgault, Y., Baruzzi, G.S., Habashi, W.G., and Wagner, G.A., "Numerical Simulation of Performance Degradation of Ice Contaminated Airfoils," AIAA Paper 97-2235, 1997.

28. Lee, S., Dunn, T., Gurbacki, H.M., Bragg, M.B., and Loth, E., "An Experimental and Computational Investigation of Spanwise-Step Ice Shapes on Airfoil Aerodynamics," AIAA Paper No. 98-0490, Reno, NV, January 12-15, 1998.

29. Lee, S. and Bragg, M.B., "Effects of Simulated Spanwise Ice Shapes on Airfoils: Experimental Investigation," AIAA Paper No. 99-0092, Reno, NV, January 11-14, 1999.

30. Dunn, T. and Loth, E., "Effect of Simulated Spanwise Ice Shapes on Airfoils: Computational Investigation," AIAA Paper No. 99-0093, Reno, NV, January 11-14, 1999.

31. Lee, S. and Bragg, M.B., "An Experimental Investigation of Simulated Large-Droplet Ice Shapes on Airfoil Aerodynamics," accepted for publication, *Journal of Aircraft*, 1999.

32. Dunn, T., Loth, E. and Bragg, M.B., "A Computational Investigation of Simulated Large-Droplet Ice Shapes on Airfoil Aerodynamics," accepted for publication, Journal of Aircraft, 1999.

33. Noe, S., "Force Balance Measurements of Wind-Turbine Airfoil Performance with Simulated Leading-Edge Ice Accretions," M.S. Thesis, University of Illinois at Urbana-Champaign, Urbana, IL, 1996.

34. Jones, B.M., "The Measurement of Profile Drag by Pilot Traverse Method," Aeronautical Research Council, R&M 1688, 1936.

35. Lambert, M., ed., *Jane's All the World's Aircraft 1990-1991*, Jane's Information Group, Inc., 1990.

36. Rae, W. H. and Pope, A., *Low-Speed Wind Tunnel Testing*, John Wiley & Sons, New York, 1984.

37. Winkler, J.F., "Local Flow Field about Large Distributed Roughness Elements in a Laminar Boundary Layer," Ph.D. Dissertation, University of Illinois at Urbana-Champaign, Urbana, IL, 1996.

38. Mavriplis, D., "A CFD Package for Multi-Element Airfoil High-Lift Analysis (Revision 4)," Scientific Simulations, December 1996.

39. Mavriplis, D. and Venkatakrishnan, V., "Agglomeration Multigrid for Two-Dimensional Viscous Flows," Computers and Fluids, Vol. 24, No. 5, 1995, pp. 553-570.

40. Mavriplis, D., "Multigrid Solution of Compressible Turbulent Flow on Unstructured Meshes Using a Two-Equation Model," NASA CR-187513, January 1991.

41. Mavriplis, D., "Turbulent Flow Calculations Using Unstructured and Adaptive Meshes," NASA CR-182102, September 1990.

42. Mavriplis, D., "Multigrid Solution of Compressible Turbulent Flow on Unstructured Meshes using a Two-Equation Model," NASA CR-187513, January 1991.

43. Valarezo, W.O. and Mavriplis, D., "Navier-Stokes Applications to High-Lift Airfoil Analysis," AIAA Paper 93-3534, August 1993.

44. Mavriplis, D. and Venkatakrishnan, V., "Agglomeration Multigrid for Two-Dimensional Viscous Flows," Computers and Fluids, Vol. 24, No. 5, 1995, pp. 553-570.

45. Mavriplis, D., "Algebraic Turbulence Modeling for Unstructured and Adaptive Meshes," AIAA Paper 90-1653, June 1990.

46. Baldwin, B.S. and Barth, T.J., "A One-Equation Turbulence Transport Model for High Reynolds Number Wall-Bounded Flows," AIAA Paper 91-0610, January 1991.

47. Spalart, P.R. and Allmaras, S.R., "A One-Equation Turbulence Model for Aerodynamic Flows," AIAA Paper 92-0439, January 1992.

48. Mentor, F., "Improved Two-Equation k-omega Turbulence Models for Aerodynamic Flow," NASA TM-103975, October 1992.

49. Spalart, P.R. and Shur, M., "On the Sensitization of Turbulence Models to Rotation and Curvature," Aerospace Science and Technology, 1997, No. 5, pp. 297-302.

50. Drela, M. and Giles, M.B., "Viscous-Inviscid Analysis of Transonic and Low Reynolds Number Airfoils," AIAA Journal, Vol. 25, No. 10, October 1987, pp. 1347-1355.

51. Drela, M., "XFOIL 6.6 User Primer," MIT Aero and Astro Engineering, March 14, 1996.

52. Drela, M. and Giles, M.B., "A Two-Dimensional Viscous Aerodynamic Design and Analysis Code," AIAA Paper 87-0424, January 1987.

53. Oakley, T., Loth, E., and Adrian, R., "Cinematic Particle Image Velocimetry of a Turbulent Free Shear Layer," AIAA Journal, Vol. 34, No. 2, pp. 299-308, February 1996.

54. Pirzadeh, S., "Unstructured Viscous Grid Generation by the Advancing-Layers Method," AIAA Journal, Vol. 32, No. 8, August 1994, pp. 1735-1737.

55. Althaus, D. and Wortmann, F., "Stuttgarter Profilkatalog I: Experimental Results From the Laminar Wind Tunnel of the Institut fur Aero- und Gasdynamik der Univeritat Stuttgart," Friedr. Vieweg & Sohn, Braunschweig/Wiesbaden, 1981.

56. Abbott, I. H. and von Doenhoff, A.E., *Theory of Wing Sections*, Dover Press, 1959.

57. White, F.M., *Viscous Fluid Flow*, 2nd Edition, McGraw-Hill, 1991.

58. Driver, D.M. and Seegmiller, H.L., "Features of a Reattaching Turbulent Shear Layer in Divergent Channel Flow," AIAA Journal, Vol. 23, No. 2, pp. 163-171, February 1985.

59. Harris, C.D., "Two-Dimensional Aerodynamic Characteristics of the NACA 0012 Airfoil in the Langley 8-Foot Transonic Pressure Tunnel," NASA TM-81927, 1981.

60. McCroskey, W.J., "A Critical Assessment of Wind Tunnel Results for the NACA 0012 Airfoil," AGARD, Aerodynamics Data Accuracy and Quality: Requirements and Capabilities in Wind Tunnel Testing, July 1988.

61. Holst, T.L., "Viscous Transonic Airfoil Workshop Compendium of Results," AIAA Paper 87-1460, June 1987.

62. Ladson, C.L., "Effects of Independent Variation of Mach and Reynolds Numbers on the Low-Speed Aerodynamic Characteristics of the NACA 0012 Airfoil Section," NASA TM-4074, 1988.

63. Bragg, M., "An Experimental Study of the Aerodynamics of a NACA 0012 Airfoil With a Simulated Glaze Ice Accretion, Vol. II," NASA CR-191007, March 1993.

64. Potapczuk, M., "Numerical Analysis of a NACA 0012 Airfoil With Leading Edge Ice Accretions," AIAA Paper 87-0101, January 1987.

65. McCullough, G.B. and Gault, D.E., "Examples of Three Representative Types of Airfoil-Section Stall at Low Speed," NASA TN-2502, September 1951.

66. Mullins, B.R., Smith, D.E., and Korkan, K.D., "Effect of Icing on the Aerodynamic Performance of a Flapped Airfoil," AIAA Paper 95-0449, Reno, NV, January 1995.

67. Gregory, N. and O'Reilly, C.L., "Low-Speed Aerodynamic Characteristics of NACA 0012 Aerofoil Section, Including the Effects of Upper-Surface Roughness Simulating Hoar Frost," ARC R&M 3726, January 1970.

68. Tani, I., "Low-Speed Flows Involving Bubble Separations," *Progress in Aeronautical Sciences*, Pergamon, New York, 1964, pp. 70-103.

69. Mullins, B.R., Smith, D.E., and Korkan, K.D., "Effect of Icing on the Aerodynamic Performance of a Flapped Airfoil," AIAA Paper 95-0449, Reno, NV, January 1995.

70. Bragg, M.B., Khodadoust, A., and Spring, S.A., "Measurements in a Leading-Edge Separation Bubble due to a Simulated Airfoil Ice Accretion," AIAA Journal, Vol. 30, No. 6, June 1992, pp. 1462-1467.

71. "Freezing Drizzle: Towards a Better Knowledge and Better Prediction," published by Avions de Transport Regional, November 5, 1995.

72. Winkler, J.F., "Local Flow Field About Large Distributed Roughness Elements in a Laminar Boundary Layer," Ph.D. Dissertation, University of Illinois at Urbana-Champaign, Urbana, IL, 1996.